QUANTUM CONFINEMENT III
QUANTUM WIRES AND DOTS

Edited by

M. Cahay
S. Bandyopadhyay
J.P. Leburton
M. Razeghi

REPORT DOCUMENTATION PAGE

Form Approved
OMB NO. 0704-0188

1. AGENCY USE ONLY *(Leave blank)*	2. REPORT DATE	3. REPORT TYPE AND DATES COVERED
		Book

4. TITLE AND SUBTITLE	5. FUNDING NUMBERS
Quantum Confinement III. Quantum Wires and Dots	DAAH04-95-1-0495

6. AUTHOR(S)

M. Cahay (principal Investigator)

7. PERFORMING ORGANIZATION NAMES(S) AND ADDRESS(ES)	8. PERFORMING ORGANIZATION REPORT NUMBER
Electrochemical Society, Inc. Pennington, NJ 08534-2896	

9. SPONSORING / MONITORING AGENCY NAME(S) AND ADDRESS(ES)	10. SPONSORING / MONITORING AGENCY REPORT NUMBER
U.S. Army Research Office P.O. Box 12211 Research Triangle Park, NC 27709-2211	ARO 34437.3-EL-CF

11. SUPPLEMENTARY NOTES

The views, opinions and/or findings contained in this report are those of the author(s) and should not be construed as an official Department of the Army position, policy or decision, unless so designated by other documentation.

12a. DISTRIBUTION / AVAILABILITY STATEMENT	12 b. DISTRIBUTION CODE
Approved for public release; distribution unlimited.	

13. ABSTRACT *(Maximum 200 words)*

See Preface

14. SUBJECT TERMS

	15. NUMBER IF PAGES
	16. PRICE CODE

17. SECURITY CLASSIFICATION OR REPORT	18. SECURITY CLASSIFICATION OF THIS PAGE	19. SECURITY CLASSIFICATION OF ABSTRACT	20. LIMITATION OF ABSTRACT
UNCLASSIFIED	UNCLASSIFIED	UNCLASSIFIED	UL

NSN 7540-01-280-5500

Standard Form 298 (Rev.
Prescribed by ANSI Std. 239-
298-102

PROCEEDINGS OF THE THIRD
INTERNATIONAL SYMPOSIUM ON

QUANTUM CONFINEMENT:
PHYSICS AND APPLICATIONS

Editors

M. Cahay
University of Cincinnati
Cincinnati, Ohio

S. Bandyopadhyay
University of Notre Dame
Notre Dame, Indiana

J.P. Leburton
Beckman Institute
University of Illinois
Urbana, Illinois

M. Razeghi
Northwestern University
Chicago, Illinois

19960812 020

DTIC QUALITY INSPECTED 1

PREFACE

This book is a collection of the some of the papers presented at the Third International Symposium on Quantum Confinement: Physics and Applications, held October 8-13 in Chicago, USA, as part of the 188th Meeting of the Electrochemical Society. The symposium was sponsored by the Dielectric Science and Technology, the Electronics, and the Luminescence and Display Materials divisions of the Electrochemical Society.

The symposium was organized to address the most recent advances in nanoscale and quantum confined structures, including growth and characterization, device modeling, proposals for new devices, studies of electrical and optical properties, etc. Some of the papers also addressed issues related to fundamental aspects of superconductivity. This Proceedings Volume includes 35 of the 44 papers presented at the meeting.

The symposium was organized into eight sessions of oral presentations that spanned three days. Invited papers are indicated by an asterisk in the Table of Contents. In addition to the oral presentations, a pannel discussion was organized in the evening of the second day of the meeting. The panel session was organized to address the outstanding issues in the field of high-T_c superconductivity.

The editors thank all the speakers and session chairpersons for their contributions to the success of the symposium. We also thank the Electrochemical Society staff for their constant support and for their help in preparing the volume for publication.

Finally, we would like to conclude by expressing our appreciation for the financial support provided by the Army Research Office, the National Science Foundation, and the Electro-Chemical Society.

<div style="text-align:right">

M. Cahay
S. Bandyopadhyay
J. P. Leburton
M. Razeghi

</div>

TABLE OF CONTENTS

Self-Assembled Quantum Structures

Quantum Wires and Dots

Nanostructures

Devices

High-T_c Superconductivity

* Invited Speaker

FACTS ABOUT THE ELECTROCHEMICAL SOCIETY, INC.

The Electrochemical Society, Inc., is an international, nonprofit, scientific, educational organization founded for the advancement of the theory and practice of electrochemistry, electrothermics, electronics, and allied subjects. The Society was founded in Philadelphia in 1902 and incorporated in 1930. There are currently over 6000 scientists and engineers from more than 60 countries who hold individual membership; the Society is also supported by more than 100 corporations through Patron and Sustaining Memberships.

The Technical activities of the Society are carried on by Divisions and Groups. Local Sections of the Society have been organized in a number of cities and regions.

Major international meetings of the Society are held in the Spring and Fall of each year. At these meetings, the Divisions and Groups hold general sessions and sponsor symposia on specialized subjects.

The Society has an active publications program which includes the following:

Journal of The Electrochemical Society - The Journal is a monthly publication containing technical papers covering basic research and technology of interest in the areas of concern to the Society. Papers submitted for publication are subjected to careful evaluation and review by authorities in the field before acceptance, and high standards are maintained for the technical content of the JOURNAL.

Interface - Interface is a quarterly publication containing news, reviews, advertisements, and articles on technical matters of interest to Society Members in a lively, casual format. Also featured in each issue are special pages dedicated to serving the interests of the Society and allowing better communication between Divisions, Groups, and Local Sections.

Meeting Abstracts *(formerly Extended Abstracts)* - Meeting Abstracts of the technical papers presented at the Spring and Fall Meetings of the Society are published in serialized softbound volumes.

Proceedings Series - Papers presented in symposia at Society and Topical Meetings are published from time to time as serialized Proceedings Volumes. These provide up-to-date views of specialized topics and frequently offer comprehensive treatment of rapidly developing areas.

Monograph Volumes - The Society has, for a number of years, sponsored the publication of hardbound Monograph Volumes, which provide authoritative accounts of specific topics in electrochemistry, solid state science, and related disciplines.

For more information on these and other Society activities, visit the ECS Home Page at the following address on the World Wide Web:

http://www.electrochem.org.

Self-Assembled Quantum Structures

2

CONDUCTIVITY IN THREE DIMENSIONAL SELF-ORGANISED LATTICES OF QUANTUM DOTS

S. G. Romanov, D. V. Shamshur
A. F. Ioffe Physico-Technical Institute, St. Petersburg, 193021, Russia

C. M. Sotomayor Torres
Nanoelectronics Research Centre
Department of Electronics and Electrical Engineering
University of Glasgow, Glasgow G12 8QQ, UK

ABSTRACT

Magneto resistance and Hall resistance were measured in self-organised three-dimensional lattices of quantum dots. The density of the dots was around $10^{14}cm^{-3}$ and they were prepared within the pores of artificial opal by impregnating opal with molten InSb and Te. Aharanov-Bohm oscillations with periodicity corresponding to the smallest loops in the lattice were observed for both materials, thus confirming the regularity of the lattice. The current circulating around these loops is also thought to be responsible for the negative magneto resistance observed in the low-field region. Depending on the strength of the interdot coupling, the Hall effect in the lattice undergoes saturation, which is enhanced with decreasing temperature due to the lack of carriers participating in the effect. An order-disorder transition was found to occur in the lattice of InSb quantum dots containing few electrons ascribed to the Coulomb blockade.

INTRODUCTION

Composite materials are widely used for fabrication of three-dimensional (3D) arrays of nanostructures. To approach a regular array it is necessary to have a method to control the formation of nanostructures. Starting with an ordered matrix, the arrangement in space of quantum dots should follow that of the matrix during the in-situ growth of the quantum dots in the voids of the matrix. One pioneering method of this type is to use zeolite-type materials containing free nanometer-size voids as part of their crystalline structure (1). Usually zeolite-type materials are wide gap dielectrics, the porous framework of which can be infilled with a guest material of another type, e.g., a semiconductor. Depending on the void geometry nanostructures of different type (quantum wires or dots) can be designed within the host ordered matrix. Moreover, the host matrix determines the space symmetry of the lattice of guest nanostructures. This method is known as one of the self-organising strategies.

Among the variety of the porous matrices precious opal provides a matrix able to host nanoparticles of around 100 nm in size (2). This size is very attractive since such particles are large enough to neglect the particle-to-matrix interaction and small enough to demonstrate size-dependent quantisation of their energy structure. An early study of semiconductor-opal composites revealed the correlation between the geometrical structure and transport properties (3), describing the lattice of semiconductor grains in opal as array of quantum dots (QD) coupled via quantum point contacts (QPC). Correspondingly, three regimes of conductivity as a function of temperature or applied voltage were found pointing to the decisive role of: (i) QPCs - interdot tunnelling combined with thermal

activation, (ii) QDs - Coulomb blockade and, (iii) residual disorder of the lattice - manifested in percolation conductivity (4).

This paper reports on magneto transport properties in these QD lattices. Arrays of QD were prepared in opal containing InSb and Te, to obtain a comparative picture of the conductivity in these nanostructures. They will be referred to as O-InSb and O-Te, respectively. With nearly the same geometrical structure O-InSb and O-Te differ in the type and effective mass of their main charge carriers as well as in the sign of the magneto resistance.

MATERIAL PREPARATION

Precious opal is the ensemble of identical silica balls closely packed in the space lattice with the fcc symmetry (5). The diameter of balls D in the opals used for composite preparation was 250 nm (for impregnation with InSb) and 200 nm (for Te) with a size fluctuation of less than 5% within one sample. Balls in the opal structure are glued together with additional amorphous silica for improved structural strength. Typically, the size of the artificially grown samples is in the centimetre range, although they are of polycrystalline nature with crystallites of hundreds micrometers. Between adjacent balls there are nearly spherical voids of two different sizes: (i) large voids between 8 neighbouring balls the size of which is characterised by an inscribed sphere of diameter $d_1=0.41D$ and (ii) small voids between 4 adjacent balls with diameter $d_2=0.23D$. Thus, the large voids are octahedrally co-ordinated with 8 smaller ones, which in turn connected with 4 large voids. Windows between voids have a diameter of $d_3=0.15D$, but in the real structure these windows are squeezed due to the excess amount of amorphous silica distorting the spherical shape of the opal balls (6). This effect is stronger for O-InSb, since its opal matrix was additionally overgrown with amorphous silica. Consequently, the semiconductor structure consists of small quantum dots joined up by quantum wire-like constrictions which are degenerate in one-dimensional channels formed between larger quantum dots, as has been observed directly by scanning electron microscopy of O-InSb (4).

In order to transfer the regularity of the opal matrix to the semiconductor network of quantum dots, it is necessary to fill almost completely the internal volume of the host matrix with the guest semiconductor. In the present work this was achieved by impregnation of the opal with molten semiconductor under high hydrostatic pressure and temperature. InSb and Te were used since they are semiconductors with low melting point. The semiconductor material was poured in a steel ampoule containing the piece of dehydrated opal. Then this ampoule was hermetically closed and placed in a high-pressure cell. The sample was subjected to a pressure of 5 kbars and 600 C^o for 5 minutes. Then it was cooled down while keeping the same pressure. As a result the semiconductor is encapsulated in the opal voids forming a lattice of nanometer-size grains (dots) multiply coupled with each other via bottleneck-like constrictions (6). The concentration of semiconductor grains is roughly 10^{14} cm^{-3} for a given D. These samples are rather stable under normal atmospheric conditions, since the tightly loaded semiconductor prevents the penetration of gases into the volume of the material.

MEASUREMENT TECHNIQUES

The opal impregnated with the semiconductor was shaped and polished to obtain a bar with typical dimensions 3 x 3 x 0.5 mm^3. Six contact pads in the Hall bar

configuration were defined by lithographically and deposited by evaporation of Au-Ni-Ge films on one side of the sample. The spacing between the voltage contacts was about 0.3 mm. These contacts were subjected to thermal cycling tests with no detectable changes in the sample resistance. The magneto resistance R_{xx} and the Hall resistance R_{xy} were measured from 250 to 1.7 K in a superconducting magnet using alternative current bias and magnetic fields up to 5 T. The signal was detected using lock-in techniques. The data obtained in the range from 4.2 to 0.4 K were collected under dc current bias in a He^3 cryostat with a 1T magnet.

RESULTS AND DISCUSSION

The magneto resistance of O-InSb QD lattice depends upon temperature as shown in Fig.1. R_{xx} and R_{xy} were extracted as symmetric and antisymmetric parts from the data collected using voltage and Hall contacts, respectively. At high temperature the resistance of the lattice is almost independent of the applied magnetic field and a positive magneto resistance (PMR) $\Delta r/r$ of about 1% was observed in the whole range up to 5T. With decreasing temperature the PMR slightly increases and below 6 K it grows rapidly to 13% at 1.7 K. In addition, a negative magneto resistance (NMR) emerges in the low field region. Two features are distinguishable at low temperatures: (i) short-range oscillations of R_{xx} with magnetic field with period $\Delta B=0.18$ T (Fig.2a) and, (ii) long-range oscillations with period $\Delta B=1.6$ T (Fig.2b). Moreover, Hall resistance curves are also different in low and high temperature regimes (Fig.1b). Above 60 K one can see a linear dependence of the antysymmetric component of Rxy upon B corresponding to a concentration of the electrons of 10^{15} cm^{-3} and below 60K the saturation of this curve starts. The onset of the Hall resistance saturation shifts towards lower fields as the temperature decreases.

The lattice of O-Te QDs exhibits a magneto resistance which is quite different from that of the O-InSb QD lattice since: (i) the NMR is observed over the whole field range (Fig.3a) and, (ii) the amplitude of the NMR increases slightly with decreasing temperature. In addition, weak but discernible oscillations are superimposed on the monotonous background. As for O-InSb two periods of oscillations were found: the first derivative of R_{xx} reveals the oscillations with short-range period of $\Delta B=0.28$ T and differential curve in Fig.4a demonstrates the long-range oscillations with $\Delta B=0.75$ T. In contrast to the case obtained in O-InSb, R_{xy} in O-Te has a small symmetric component which does not depend upon temperature and which corresponds to the hole concentration $p=10^{17}$ cm^{-3} (Fig.3b).

It is has been shown before, analysis of the potential profile is an adequate technique to reveal transport properties of opal-based materials (2,4). Since the energy level of the ground state depends on the size of the grain and the effective mass of the carrier it is expected that different parts of the opal voids - grain (QD) and constriction (QPC) - will have different energy levels. Using a simple quantum box approximation, the shift of the ground level of a 30 nm diameter InSb QPC is estimated to be 120 meV and that of a 120 nm QD as 7.5meV. Thus, we may visualise the O-semiconductor structure as a system where constrictions form potential barriers between adjacent quantum dots.

<u>Comparison of O-InSb and O-Te</u>
Comparing O-InSb and O-Te, the barrier height is expected to be approximately 10 times higher in O-InSb than in O-Te due to the factor of 10 difference in effective masses of InSb and Te, 0.014 m$_0$ and 0.1-0.2 m$_0$, respectively. This would result in an energy

difference between the ground states of QPC with those of QD being much higher in O-InSb than in O-Te. In this case the potential relief felt by the carriers should lead to group carriers in the dots forming pools of electrons in O-InSb (holes in O-Te) separated by energy barriers. This arrangement is probably helped by the difference in dielectric permittivities between the SiO_2 matrix and semiconductor dots. The opposite trend would be the overlapping of states from neighbouring dots.

Dot-to-Dot Coupling. The strength of interdot coupling depends on the barrier height, the Fermi wavelength λ_F and the lattice parameter. Taking into account the carrier concentration estimated in these samples, we expect the interdot coupling to be stronger in O-InSb than in O-Te, since the barrier height is larger and λ_F is about 100 nm longer than the dot spacing in O-InSb. In contrast, the O-Te QD lattice has a shallower potential relief with lower energy barrier and dots are overfilled with holes. The resulting conductivity in the high temperature regime is tunnelling of electrons combined with thermal activation of carriers from the ground level in the case of O-InSb, considered in detail in (4), and classical diffusion of carriers in the case of O-Te. As a result, the resistivity of O-InSb is about 100 times higher than in O-Te, and the dependence of the conductivity on the temperature is stronger in O-InSb than in O-Te. We propose that in the high temperature regime the magneto resistance of O-InSb is weak because the magnetic field cannot distort dramatically the main part of the charge density distribution and only squeezes the area where wavefunctions overlap, i.e., the extended states of adjacent dots. The NMR observed in O-Te is typical of bulk Te and originates from the weak localisation phenomenon. In addition, the Hall resistance is a linear function of the field, thus yielding a reasonable value of the carrier concentration. However, the hole mobility in O-Te is lower than in the bulk because the artificial potential relief acts as a scattering centre arrangement. The geometrical structure of the 3D QD lattice allows intermixing of the longitudinal and transverse components of magneto resistance due to zigzag current paths through the lattice, therefore no single conductivity path across the sample along the current direction exists and as a result R_{xy} and R_{xx} are likely to be mixed.

Coulomb Blockade regime. The electron-electron repulsion is expected to be much stronger in O-InSb than in O-Te dots since, based on the carrier concentration estimates and the number of dots in the sample, we estimate that on average there are nearly 10 electrons in each InSb QD and about 100 electrons in each Te QD. The small number of free electrons in each InSb dot favours conditions for Coulomb blockade in O-InSb. The charging energy for a 120 nm QD is approximately 4 meV, therefore below 50 K the homogeneous current distribution in the dot lattice will be disturbed by the emergence of insurmountable Coulomb barriers. Such barriers vanish only at resonance conditions resulting in conductance peaks at characteristic voltages. Resonances occur when there is matching of energy levels from adjacent dots. To understand the charge transfer in this lattice one should take into account the random distribution of electrons over the QDs in the array. The, there is no reason to expect conductivity peaks for the lattice as a whole, since a number of low resistance paths through the lattice are available at any applied voltage. This means that the geometrically ordered lattice with a low electron population becomes disordered with respect to carriers and the current distribution at low temperatures. Under the Coulomb blockade the magneto resistance does not change significantly except for a slight increase of its relative magnitude, whereas the Hall resistance saturates.

Saturation of the Hall voltage. The saturation of the Hall resistance can be explained as follows: In the presence of a magnetic field, electrons flow under the Lorentz force though

high conductance paths to the side of the sample. Each transition of a given electron from one dot to another results in a redistribution of charge among dots thereby opening and closing complementary paths around this electron. This charge rearrangement is characterised by the irreversibility of the carrier movement. If all electrons, which are allowed to drain, approach the same side of the sample, a saturation of the Hall voltage will occur. With decreasing temperature, the number of available low conductance paths diminishes due to the smaller thermal broadening of conductance peaks for each particular pair of dots. Thus, the accessible electron reservoir becomes smaller resulting in a shift of the saturation onset towards the lower magnetic field. The diffusive redistribution of electrons over the lattice is prohibited by Coulomb barriers and a non- equilibrium state is formed. Increasing the magnetic field changes the relative position of energy levels in the QD and can open a connection to another electron reservoir. If the path to a more populated electron reservoir becomes open, the Hall voltage will drop correspondingly by the difference in electron concentration, leading to deviations from the saturated value. Due to the intermixing of the transverse and longitudinal resistance the same features are superimposed onto the monotonous trace of the magneto resistance in Fig.1a..

Impact of non-uniformity of QDs. In the low temperature regime, the conductivity in the QD lattice is additionally restricted by the effect of non-uniformity of dots in the lattice which results in different energy levels from dot to dot, thus diminishing the probability of occurrence of high conductance paths. Consequently, in this temperature range a faster increase of resistance is observed, with a corresponding non-linear I-V characteristic (4). In this regime, the enhancement of R_{xy} saturation is also observed and the high field features become more pronounced due to the lack of free electrons in reservoirs participating in the Hall voltage. Therefore, we suggest that the high-field features of R_{xy} are due to field-induced switching of the isolated electron reservoirs.

Aharanov-Bohm oscillations. A common feature of O-Te and O-InSb 3D quantum dot arrays is the magneto resistance oscillations at low temperatures. In both cases they are interpreted as Aharanov-Bohm oscillations with a periodicity corresponding to the quantization of the magnetic flux (7). The short-range oscillations in O-InSb strictly correspond to the smallest loop in [100]- type planes of the QD lattice having a diameter near 170 nm (see Figure1 in (4)). The long-range oscillations could be explained by a loop of 60nm in diameter. The smallest loop in the [110] set of planes has approximately 80 nm diameter is a good candidate (see fig.2 in (6)) if account is taken of the non-zero thickness of its frame. In O-Te the short-range oscillations correspond to loops of about 140 nm diameter. This loop is of the same configuration as for O-InSb but smaller in proportion to the ratio of diameters of silica balls forming the matrix for both materials: 250 nm in O-InSb and 200 nm in O-Te. As for the long-range oscillations, the magnetic flux is enclosed in the wider loop of 80 nm diameter with the same assignment as for O-InSb. The magnitude of oscillations depends on the lattice ordering, i.e., on the co-addition of the effect from individual loops. In these partly inhomogeneous QD lattices, the existence of loops with different orientations and possible polycrystalline structure of the sample are expected to diminish the magnitude of the Aharanov-Bohm oscillations. The magneto resistance oscillations in 3D QD lattices are accompanied with the NMR nearby zero field (Figs. 1a and 3a). It is worth noting that the NMR has a similar characteristic field as the short-range oscillations, suggesting that its characteristic length is of the same order as the loop perimeter. This phenomenon appears in both O-InSb and O-Te. The destruction of the phase coherence for carriers circulating around the lattice loops with increasing magnetic field is typical for weak localisation. It results in the peak of NMR in the R_{xx} curve of O-

InSb (Fig.2a) and the non-monotonous behaviour (additional peak of NMR) for O-Te near zero field (Fig.3a).

CONCLUSIONS

Two regimes of magneto transport were distinguished in the 3D lattice of QDs embedded in precious opal depending on the interdot coupling. In the case of strong coupling (O-Te) R_{xx} and R_{xy} are nearly the same as for bulk semiconductor. In the case of weakly coupled dots (O-InSb) the appearance of magneto transport depends on the regime of conductivity. For a homogeneous lattice, R_{xx} is expected to depend weakly on the applied magnetic field due to the shrinkage of overlapping wave functions of states from neighbouring dots and R_{xy} is expected to exhibit no peculiarities. Since the lattices studied here are partly inhomogeneous, Coulomb blockade effects are observed, the Hall voltage is seen to saturate, but no qualitative change of the magneto resistance occurs. R_{xy} is seen to be sensitive to changes of the potential relief as, for example, when the magnetic field alters the electronic reservoirs participating in the Hall voltage. A common feature found for both lattices is the Aharonov-Bohm oscillations with the period corresponding to the smallest loop in the lattice. The existence of this effect confirms the geometrical 3D ordering of the quantum dot lattice in opal matrices. The most important result concerns the ordering of the QD lattice: lattices with dots containing few electrons (O-InSb) show a order-disorder transition when the temperature decreases due to the electron-electron repulsion (Coulomb blockade), whereas in lattice where the QD have more carriers (O-Te) the physical ordering of the charge is more stable.

ACKNOWLEDGEMENTS

REFERENCES

1. V. N. Bogomolov, Sov. Physics Uspehi, **21**, 77 (1978)
2. V. N. Bogomolov, Y. A. Kumzerov and S. G. Romanov, in Physics of Nanostructures, J. H. Davies and A. R. Long, Editors, p317, Instituto of Physics Publishing, Bristol, (1992)
3. S. G. Romanov, to appear in Zeolites and Related Materials: State of Art 1994, J.Weitkamp, H.G.Karge, H.Pfeifrand and W.Holdreich, Editors.
4. S. G. Romanov, A. I. Larkin and C. M. Sotomayor Torres, to be published
5. J. V. Sanders, Nature, **204**, 35 (1964)
6. V. Balakirev, V. Bogomolov, V. Zhuravlev at al, Kristallografia **38**, 111 (1993) (in Russian)
7. see, for example, Localisation and Interaction in disordered metals and doped semiconductors, Editor D M Finlayson, Scottish Universities Summer School of Physics Publications, Proceeding No 31, Edinburgh (1986)
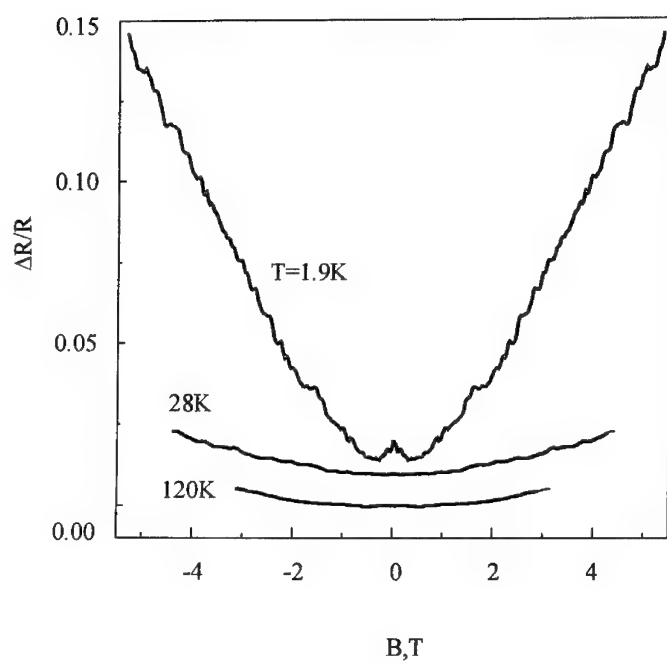
Fig.1a   O-InSb: Magnetoresistance curves at T=120, 28 and 1.9K.
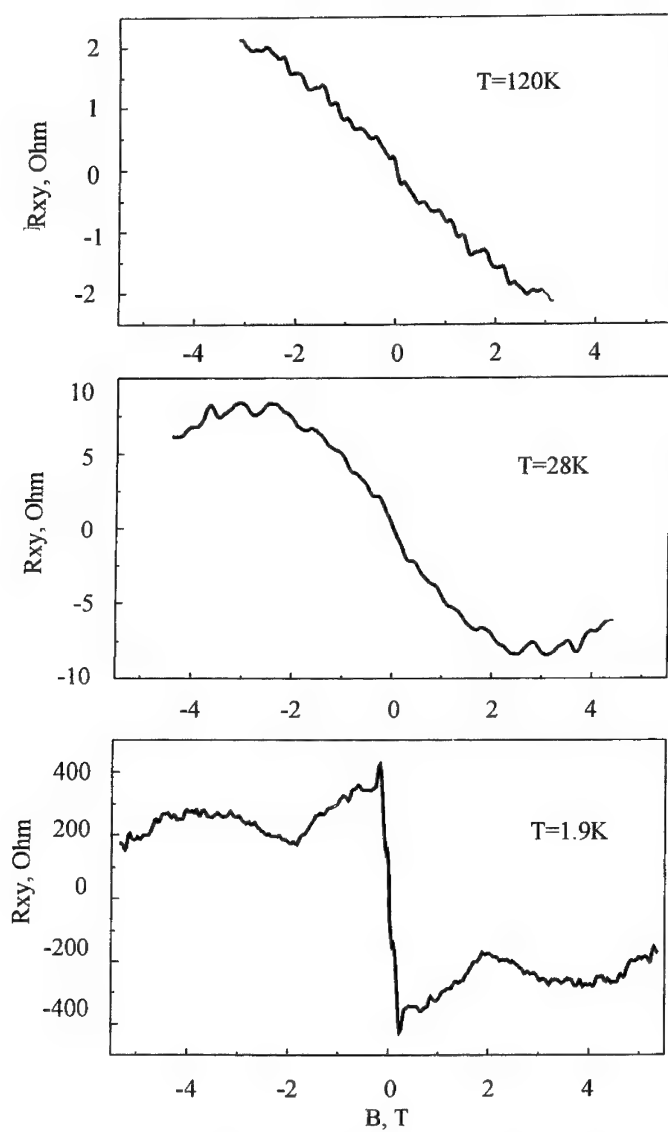
Fig.1b   O-InSb: Hall resistance at T=120, 28 and 1.9K.
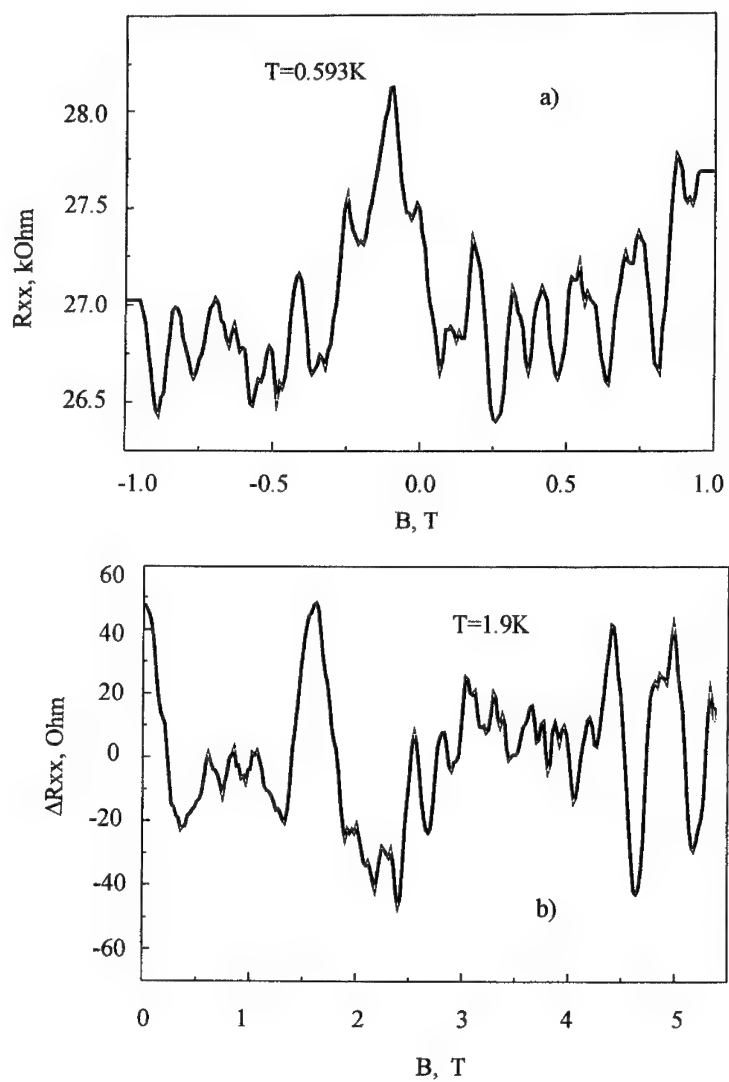
Fig.2 O-InSb: Short-range (a) and long-range (b) magnetoresistance oscillations.
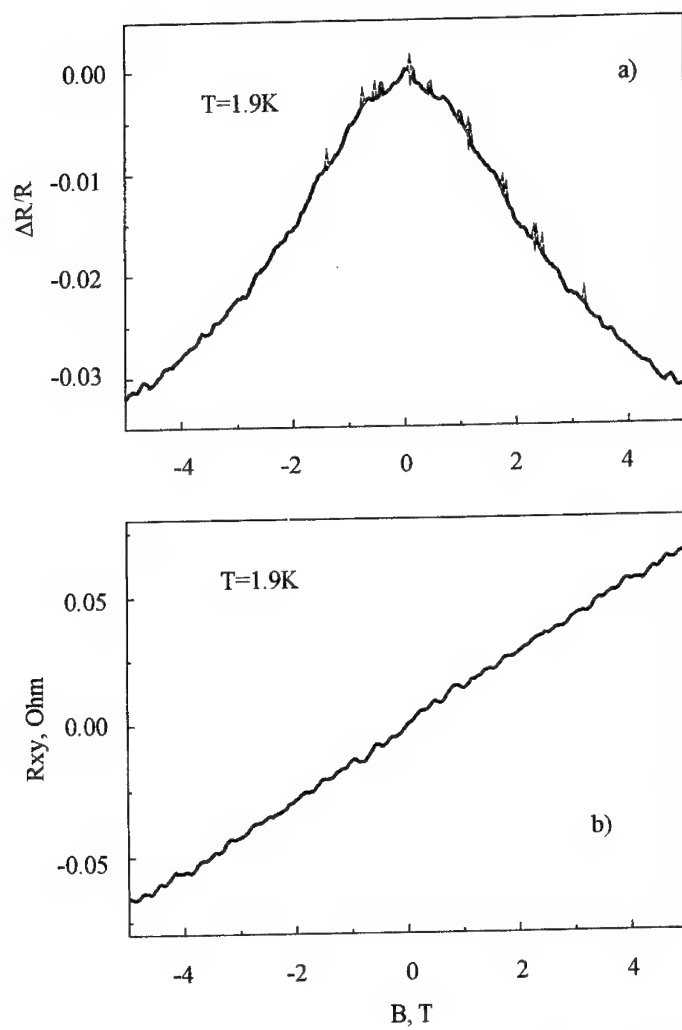
Fig.3   O-Te: (a) Magnetoresistance and (b) Hall resistance at T=1.9K
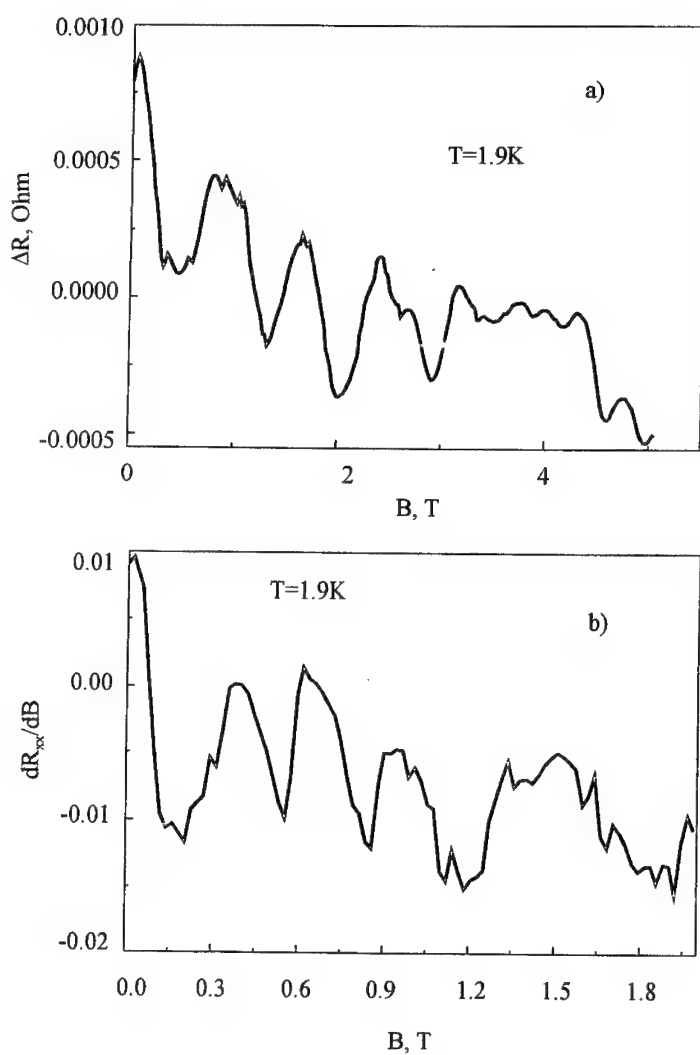
Fig.4   O-Te: long-range (a)-differential curve and (b)-first derivative short-range
oscillations of the magnetoresistance.

SELF-ASSEMBLED 3- DIMENSIONAL ARRAYS OF InP QUANTUM WIRES:
IMPACT OF THE TEMPLATE GEOMETRY UPON THE OPTICAL PROPERTIES

S.G. Romanov*, N.P. Johnson, C.M. Sotomayor Torres
Department of Electronics and Electrical Engineering,
University of Glasgow,
Glasgow, G12, 8QQ, UK
H.M. Yates, J.Agger, M.E. Pemble, M.W.Anderson A.R. Peaker
Department of Chemistry, UMIST, PO Box 88,
Manchester, M60 1QD, UK
V. Butko
*Permanent address
A.F.Ioffe Physical Technical Institute,
St. Petersburg, 194021, Russia

Abstract

3D arrays of quantum wires were prepared by InP MOCVD in channels of dielectric hosts: chrysotile asbestos (channel diameter 8 nm), MCM-41 (3 nm) and ALPO-5 (0.7 nm). The decrease of the Raman phonon frequencies, blue shift of absorption band-edges and photoluminescence bands with respect to bulk InP demonstrate quantum confinement for all composites. Competition between energy relaxation at the wire-host interface and in the wires themselves, result in different photoluminescent properties.

1 Introduction

Higher packing density of quantum nanostructures has pushed the search for novel materials to 3-dimensional arrays of quantum wires. Assembling nanostructures in an ordered array increases the strength of optical signals while maintaining control of their size. There are several approaches to achieve quantum confinement of electrons. The traditional approach has been to use lithography and etching in combination with either bulk material or electrically defined 2 dimensional electron gases to remove material and

so leave behind structures such as wires or dots [1]. This maybe viewed as a physical approach. Recently, this approach was improved to design large arrays of nanostructures without lithography by using crystalline substrates with high index planes [2]. The last method is called a self-organising strategy. Alternative chemical approaches include metal organics which form ligands to define dots and wires [3]. Porous crystalline structures may be employed as templates (or matrices) as an alternative to the commonly used nanolithographic fabrication of nanostructures. In this physical chemical approach a template provides a predefined surface on to which is grown a semiconductor. This kind of self organising strategy was proposed long ago [4] for elemental semiconductors and then extended towards compound semiconductors [5,6]. However, in cavity growth processes have usually been restricted to the zeolite matrix. This strongly limits the ability to vary the size parameters of the nanostructures.

Crystalline matrices whose empty voids are in the form of parallel channels may be infilled by guest semiconductor. The object is to produce structures with reduced dimensionality in that the electron waves propagate only in the dimension available. Some degree of coupling between molecules is desirable, as the zero dimensional case of isolated molecules or indeed purely one-dimensional (1-D) case offers almost no advantage over its gaseous counterpart. Two ways to approach quasi-1-D systems may be used: coupling between 1-D wires in an array, or coupling within wires of thickness greater than one molecule cross-section.

Three classes of host matrices were used in this study each with wire like channels which allows us to vary both the channel size and the channel spacing over a wide range not possible with one matrix alone. All host matrices are filled with the same guest semiconductor, InP using the same process. This enables us to distinguish between three types of different interactions existing in quantum wires confined in the matrix: (a) within the nanosize-wire, (b) between wires, and (c) between the wires and the dielectric matrix. The balance of these interactions defines the appearance of some optical properties, such as photoluminescence, since the shape of the potential along which energy relaxation occurs is determined by these interactions.

2 Host Material

2.1 Chrysotile Asbestos (CA) is a type of naturally occurring asbestos which consists of long thin tubes up to a few cm long. Each tube is made of a spiral roll (external diameter of 20-50 nm) of double SiO_2-MgO planes with an empty channel of 2-15 nm diameter inside. Tubes are arranged hexagonally and stuck together in bundles with the amorphous silica. Asbestos mined from different sites processes different channel diameter and spacing, however there is less than 10% variation [7] in channel diameter within a bundle of several mm diameter. A schematic diagram is shown in figure 1a. Further samples of asbestos were given a chemical treatment before infill to remove the MgO component of the mineral. This leaves a pure silica framework which keeps the original main channels along the their axis but has nearly 100 times more surface area [8]. This can be explained by assuming the removal of MgO creates additional channels in each tube which are smaller in diameter than the inner diameter of the unetched tubes. These etched samples are denoted EA-InP after infilling with InP.

2.2 MCM-41 is synthesised by use of surfactant micelles. Each surfactant molecule is made up of a long hydrocarbon chain with a hydrophilic and hydrophobic end, in sufficient concentration the heads turn in and form micelles, which in turn stack up to form micelia rods in hexagonal arrays [9]. Silicate added into solution covers the rods. After calcination by heating the material in air, the organic component is removed leaving a regular honeycomb network made from an amorphous silicate skeleton. The typical size of MCM particles is around several micrometers. The channels with diameter typically 3 nm are separated by the silica walls of 0.4 nm thickness. The great advantage of MCM-41 is the ability to vary the channel diameter by changing the carbon chain length of the surfactant. Three different materials with channels of 2.8, 3.2 and 3.6 nm diameters were used. A schematic diagram of MCM-41 is shown in figure 1b.

2.3 AlPO-5 is a zeolite framework formed from aluminium, phosphorus and oxygen, with crystallites of 60- 80 μm long [10]. This matrix has a relatively short channel diameter and spacing of 0.73 and 1.0 nm respectively. A schematic diagram showing the cross section is shown in figure 1c.

3 Infill Method

An MOCVD reactor is used in a two-step growth sequence to grow InP within the hosts using the reactants trimethyl indium (TMIn) and phosphine. Prior to growth the samples are dehydrated by heating overnight in flowing nitrogen. In the first stage of growth, TMIn in a carrier gas of hydrogen is passed over the samples for several hours at $52^{\circ}C$. Secondly, phosphine is passed through the reactor for several hours at $350^{\circ}C$ which allows decomposition of the phosphine at the absorbed In sites. This method [11] limits the amount of semiconductor growth on the external surfaces of the matrix.

To confirm the presence of InP inside the channels, X -ray diffraction (XRD) was performed on empty and asbestos with low InP loading. The outer surface was first etched in a solution of 1:4 H_2SO_4: H_2O_2 to remove this InP. However the X-ray diffraction patterns showed only the asbestos without evidence of InP. Electron micro probe analysis (EPMA) reveals only 0.25 and 0.3 atomic % of In and P, respectively. This appears too low to provide a detectable signal. Samples etched to remove the MgO component produce an amorphous diffraction pattern. After infill with InP into the etched matrix a typical crystalline InP pattern is superimposed on the amorphous X-ray pattern. Asymmetric line width broadening of the InP lines in the powdered EA-InP samples suggest that the InP lattice is distorted. EPMA shows the content of In and P has increased to 3.2 and 3.0 atomic % respectively. The colour of the asbestos changes from white (empty) through light brown (low loading) to dark brown (EA-InP) as the InP content is increased.

MCM-InP composites demonstrate both superimposed patterns of MCM and InP. A similar broadening of InP peaks was observed. Low InP loading and a relatively complex AlPO-5 XRD pattern combined to make it difficult to see the InP XRD pattern. However the XRD confirmed that the zeolite framework was still crystalline after InP inclusion.

NMR using ^{31}P shows the presence of InP for all three matrices, AlPO5, MCM and CA.

The content of InP in the matrices is relatively low, compared with the free volume of pores in MCM and CA matrices. Considering the nature of the deposition process we

expect, that InP forms a thin layer coating inner surface of the channels. Thus MCM-InP and CA(EA)-InP contains arrays of parallel InP wires in the form of thin-wall cylinders.

4 Optical Techniques

Photoluminescence (PL) and Raman spectra where excited with an Ar^+ laser at 2.408 eV and analysed using a 1-m double monochromater and a cooled photomultiplier operating in photon counting mode. Orientated bundles of asbestos fibre, pelletised MCM and ALPO where mounted in He flow cryostat for PL. Raman scattering was performed at room temperature in nearly back scattering mode. The absorption spectra were extracted from diffuse reflectance spectra obtained from powdered samples analysed by a single monochromator under the excitation of tungsten lamp.

5 Results and discussion

5.1 Raman Scattering

Raman Spectra for EA-InP, MCM-InP and AlPO-InP are shown in figure 2 (the signal was too weak to observe for unetched CA-InP). In each case two broad lines are seen which correlate well with 303.7 cm^{-1} and 345 cm^{-1} TO and LO phonons of bulk InP confirming its presence in the samples under study. The positions of LO and TO are 298 and 334 cm^{-1} for EA-InP, 303 and 336 cm^{-1} for MCM-InP, 279 and 338 cm^{-1} for ALPO-InP. The high degree of line broadening correlates with broadening of X-ray patterns and may be ascribed to randomisation of the InP lattice. In all cases there is a shift to lower frequencies of around 10 cm^{-1} for the LO phonon. This indicates the identity of the lattice parameters for InP grown under the same method and conditions.

The TO phonon, however, is very sensitive to the template used. The TO phonon is unchanged from the bulk for MCM-InP but is again shifted to lower frequencies for the EA-InP and ALPO-InP. A possible explanation is as follows: The common dimension to all samples over the range of a few microns is the channel. As the InP is attached to the channel matrix the chemical bonding within InP lattice is reduced compared to bulk InP due to the potential interaction with surrounding field of the template and thus leads to common decrease in the force constants and, therefore, frequency of phonons. For the MCM-InP and EA-InP cases where there is little shift in the TO phonon, enough lateral

InP molecules exist to make them behave similar to the bulk. The ALPO5 however has only space for one InP molecule before it reaches the matrix, in effect the lateral dimension is made up of alternating InP and matrix thus the effect of reduced force constants compared to the bulk could be responsible for lowering the TO phonon frequency. The fact that the EA is shifted more than MCM may reflect that the additional channels in the EA make the channel spacing smaller.

5.2 Absorption Spectra

The absorption spectra near the band edge are similar for each of the original three templates (figure 3). There is no sharply defined absorption edge as the density of InP is low. This similarity reflects the uniformity of the electronic band structure of the InP grown by the same method. The absorption is first determined by the chemical bonding between In and P atoms and then by the density of states combined from valence and conduction bands. It is difficult to define an absorption edge with these relatively low concentrations of InP. In the special case of EA-InP with 100 times the surface area an absorption edge of 1.42 eV was using Fochs's criterion [12] for edge position determination of the fundamental gap, compared to the bulk value of 1.35 eV. It is surprising that there is no evidence for the size dependent shift of the band edge for templates with very different diameters. Apparently, randomisation of the InP lattice in the vicinity of template surface together with long tails of the defect states is strong enough to dominate in the absorption in the edge region. The difference in the absorption coefficient corresponds to the difference in the InP content in each matrix.

5.3 Photoluminescence

The photoluminescence spectra for the three hosts are quite different (figures 4,5 and 6). The CA-InP has both high and low energy bands at 2.15 and 1.51 eV, AlPO-InP has a large high energy band around 2 eV, and MCM-InP has a low energy band and a mid energy peak that shifts with channel width at 1.4 and 1.6 eV respectively. Assignment of the CA-InP emission bands were made in [13]. It was shown, that the band just after the excitation line is due to the recombination occurring by means of transmission of the excitation from semiconductor component to the defect states of the asbestos matrix. In the absence of InP the PL is at least 100 times weaker. We argue that this process has a common character for all structurally confined materials grown by the

physical chemical method, and the intensity of this process depends on the strength of the interaction of the deposited species with supporting surface and the chemical bonding within these species.

The process of the wire formation inside the channel starts with the attachment of the metal-organic molecule on the sites where the defects of the matrix wall create a singularity of the electric field distribution [10]. This is followed by transformation to the compound semiconductor species with suitable chemical treatment, this provides the spatial coordination of the InP species and defects. The absorption spectrum of empty asbestos [13] beginning at 2 eV shows very weak absorption due to defect states in the 10 eV asbestos band gap. The Fermi level of the matrix should be determined by these defect states. We assume alignment between Fermi levels of matrix and InP near the middle of the host energy gap. Thus, if the states of guest and host materials are tightly bound, effective energy exchange is possible. In the case of low loading the molecule-to-matrix interaction is higher than molecule-to-molecule interaction, thus it results in preference for adsorbed energy (electron-hole pairs created under the illumination) to relax via defect energy states. This is exactly the case of AlPO-InP material. The diameter of channels in this matrix is too low to allow the deposition of two molecules in the wire cross-section. That is why the observed PL spectrum demonstrates only the band at the same region as bare AlPO. In the case of CA-InP material by increasing the loading the molecules covering the matrix surface interact with each other and thus form a layer of semiconductor on which to form the next layer and so on. In this case the balance between wire-to-matrix and in-wire interaction moves in favour of the latter. Both bands corresponding to the relaxation within InP and via asbestos defects are clearly seen. With the further increase of InP content the relaxation within semiconductor dominates and the photoluminescence spectra show only the band in the range of InP fundamental gap[13] this is the case for MCM shown in figure 6.

For macroscopic bundles of wires as in the case of asbestos it is possible to resolve an anisotropy in the PL by means of a linear polariser as shown in figure 4. Anisotropy in the absorption spectra has been reported earlier for GaAs wires in asbestos [14]. The conditions for electronic structure formation across the wire direction can result in a specific excitation of states which do not mix with those along the wire and results in the single peak from across the wires. The shift of this peak compared with PL

due to band to band transitions in direction along the wires reflects the confinement of electrons in the cross-wire direction.

In the case of MCM embedded wires we believe, that 3 nm diameter is enough to form quasi-one-dimensional wires whose in-wire interaction is large comparable with the wire-to-matrix interaction. However, because the walls separating adjacent wires are only 0.8 nm thick, the effect of the interaction between adjacent wires should be included in the analysis. This interaction is strong enough to affect the energy structure of the wire ensemble and thus change the energy relaxation process. As discussed in the asbestos based wires, there should be the different energy structure along and across the wire direction. However, the micro size of the MCM particles does not allow the PL bands in perpendicular directions to be resolved. Thus the observed spectra are the superposition of both polarisations. Based on the CA-InP spectra we assign the peak from the high energy side of the PL band onset to the PL band from the band across the wire direction. The width of this peak corresponds to the width of the energy band and, apparently, to the scattering caused by the variation the channel diameter from one particle to another. The position of this peak depends on two factors. First the confinement condition across the wire - this factor shifts this PL band to the blue side. The second is the interwire interaction resulting in the red shift of the peak. In figure 7 one can see that this PL peak is shifted with a small change of wire diameter from 3.6 via 3.2 to 2.8 nm correspondingly from 1.95 via 1.7 to 1.6 eV. This unusual tendency and extremely strong dependence may be explained by a dominating superlattice effect over the electron confinement. Decreasing the wire diameter allows an increase in the filling factor of the matrix, as there are more wires per unit surface of the cross section in the direction across the wires. The model assigning this band to the PL from confined electron energy structure is particularly suitable as this band is most sensitive to the interaction between wires in the ensemble.

6 Conclusions

The similarity of the electronic band structure near the fundamental gap of the wire ensemble geometry for InP MOCVD grown on the surface of channels of dielectric templates was demonstrated by comparison of the absorption spectra for three different templates. In this case the absorption does not depend on the confinement condition but rather corresponds to the case of incomplete formation of the InP lattice, resulting in the

reduced density of states near the gap region and long tails of the defect states. The appearance of the dynamic response of these arrays to the incident light - light scattering (Raman process) and light emission (photoluminescence) - is much more influenced by the ensemble geometry. The origin of this dependence is the relative strength of three characteristic energies, in-wire interaction (coupling of InP species between themselves), wire-to-matrix interaction (coupling of InP species with defects on the template surface) and wire-to-wire interaction (overlapping of the wire wave functions from adjacent channels). The equilibrium point of these couplings may be easy shifted by changing the wires' ensemble and interface conditions, this will allow the design materials with controllable optical properties by choosing matrices of different geometry or a matrix surface of different nature.

References

1   See, e.g., Papers in: Physics of Nanostructures ", eds. J. H. Davies and A.R.Long,
I   nst. of Phys Publishing Bristol, UK (1992)
2   P.D. Wang, N.N. Ledentstov, C.M. Sotomayor Torres, P.S. KopÕev,V.MUstinov,
        Appl. Phys. Lett. 64 1526 (1994)
3   L.D. Steingerwald et al J. Am Chem. Soc. 110 3046 (1986)
4   V.N.Bogomolov, S.V.Kholodkevich, S.G.Romanov, A.L.Agroskin. Sol. State
        Commun. 47 181 (1983)
5   Y.A.Alekseev,V.N.Bogomolov,T.B.Zhukova,V.P.Petranovskii, S.G.Romanov,
        S.V.Kholodkevich, Izvestija AN SSSR, ser.fiz. 50   418 (1986) (in Russian)
6   V.I. Srdanov, N.P. Blake, D. Markgraber, H. Metiu, G.D. Stuky. in
        Advanced Zeolite Science and Applications, Studies in Surface Science and
        Catalysis. Eds.J.C.Jamsen et al, (Elsiever B.V.,1994) vol.85,. p115.
7   V.N. Bogomolov, Yu. A. Kumzerov. JETP Lett.,   21 434 (1975)
8   V.P. Petranovskii, private communication

9   MCM41 C.T. Kresge, M.E. Leonowicz, W.J. Roth, J.C. Vartuli, patent no. 5 098 684, March 1992,

10   G. Finger, J. Richter-Mendau, M. Bulow, J. Kornatowski, Zeolites 11, 443, 1991.

11   M.W. Anderson, G.K. Logothetis, A.G. Taylor, N. Wallace, H.M. Yates, Adv. Mater. for Optics and Electronics 2 3134 (1993)

12   P.D. Fochs Proc. Phys. Soc. B 60 70 (1956)

13   S.G.Romanov, C.M.Sotomayor Torres, H.M.Yates, M.E.Pemble, V.Y.Butko. Submitted to J. Appl. Phys.

14   V.V.Poborchii,M.S.Ivanova,I.A.Salamatina Microstructures and Superlattices, 16, 133 (1194)
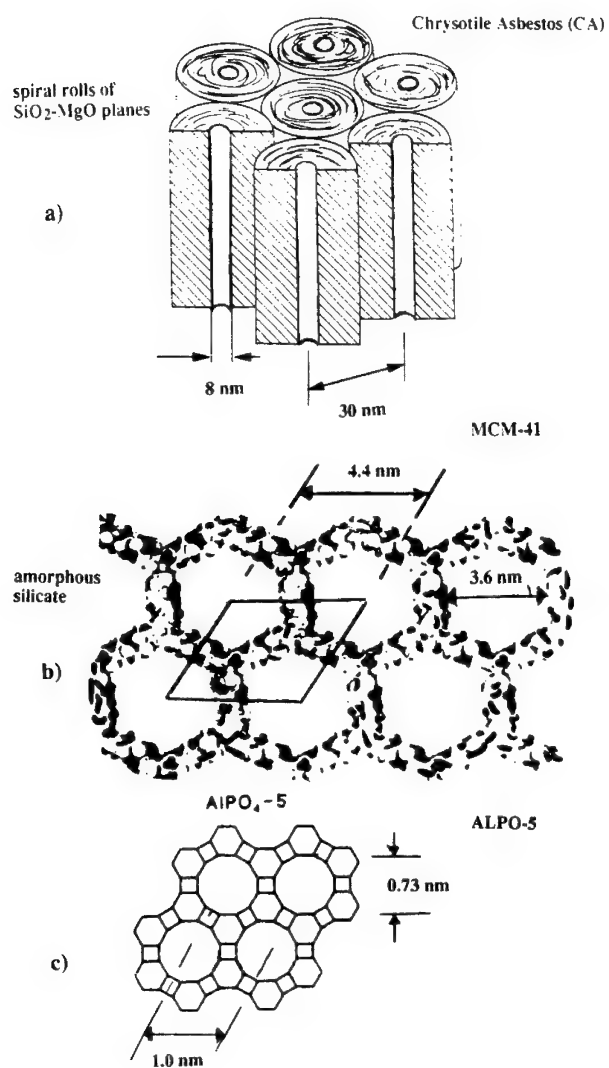
Figure 1 Schematic representations of the dielectric matrices
a) Chrysotile Asbestos b) MCM-41 c) ALPO5
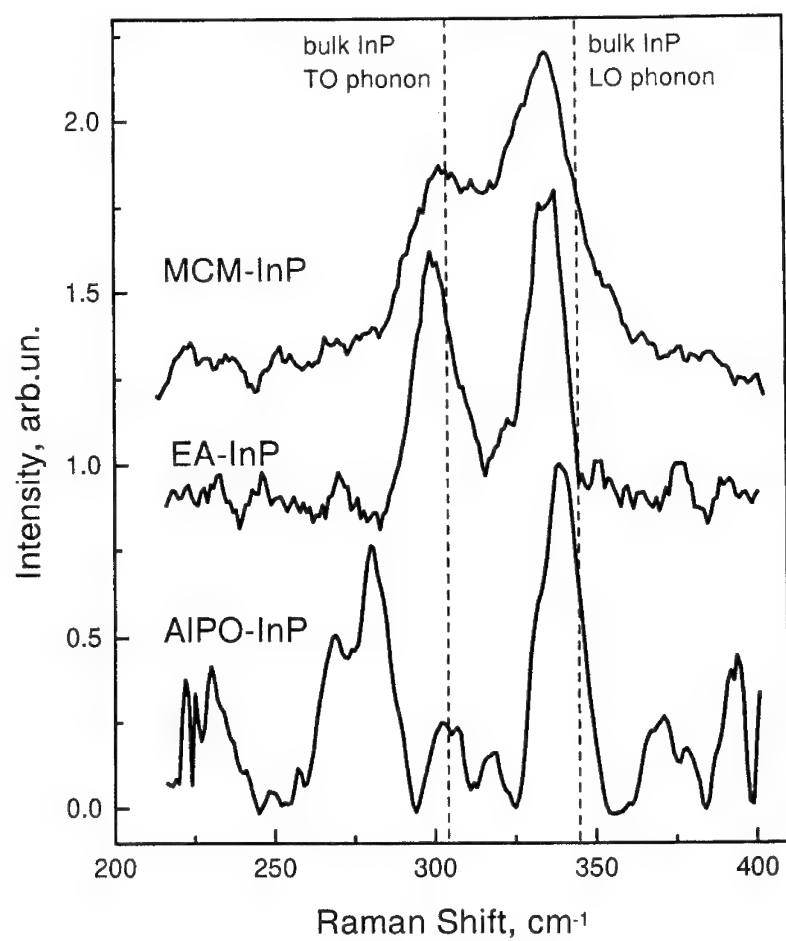
Figure 2 Raman spectra of InP filled dielectric matrices
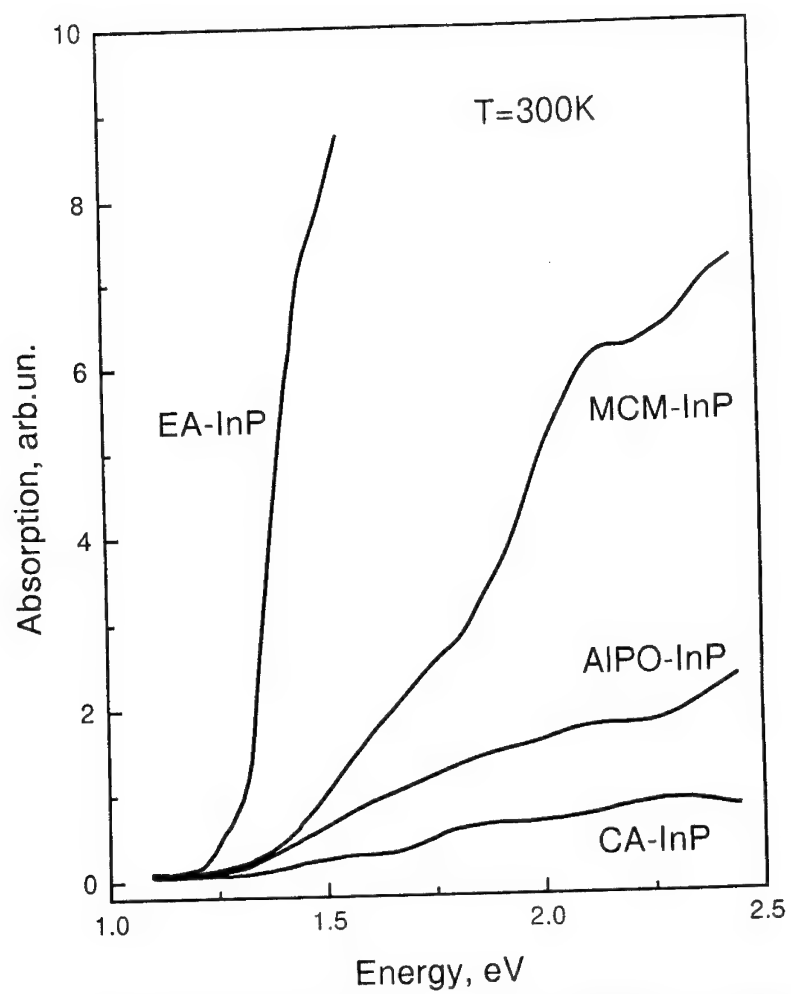
Figure 3 Absorption of InP embedded in different matrices
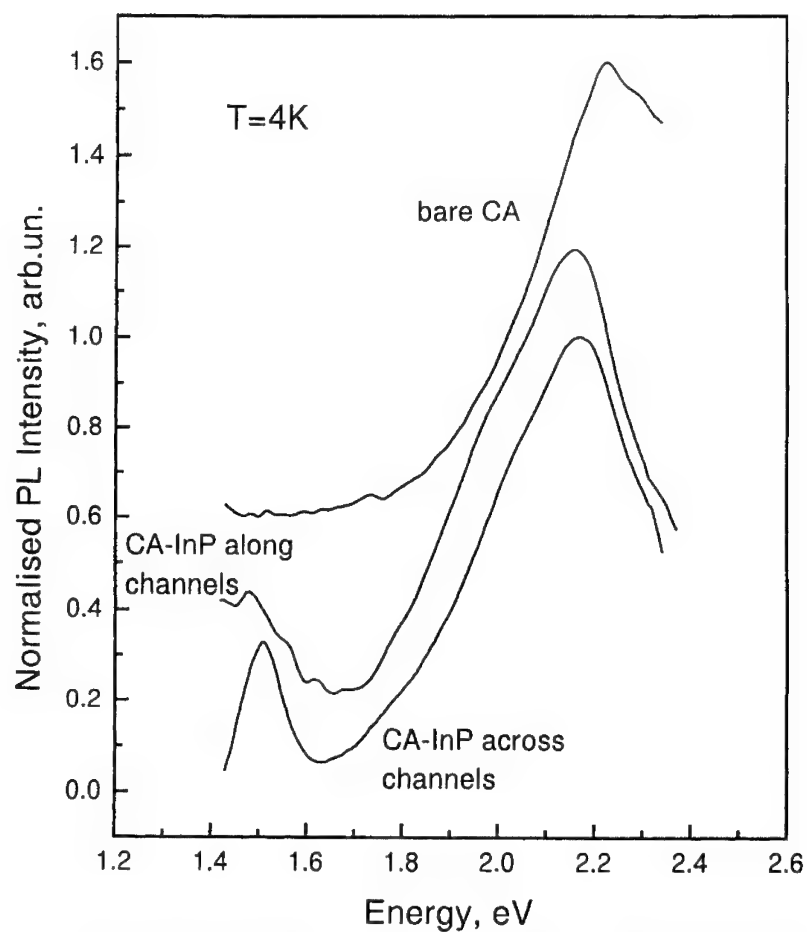
Figure 4 Comparison of PL from empty and InP filled CA
along and across the channels
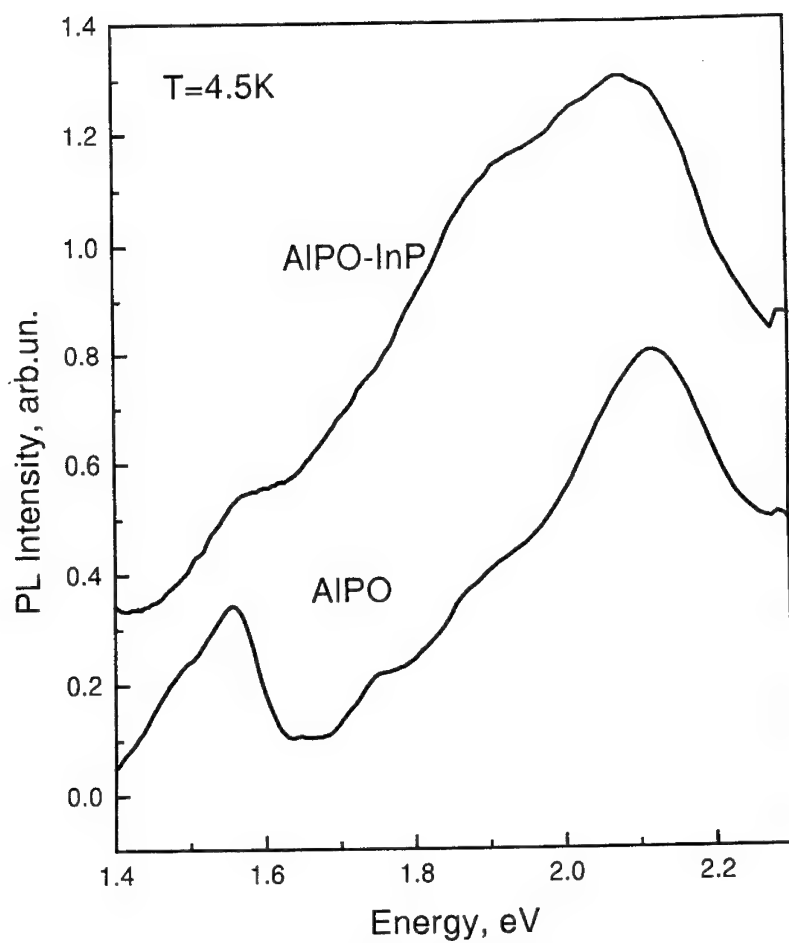
Figure 5 PL of ALPO empty and filled with InP
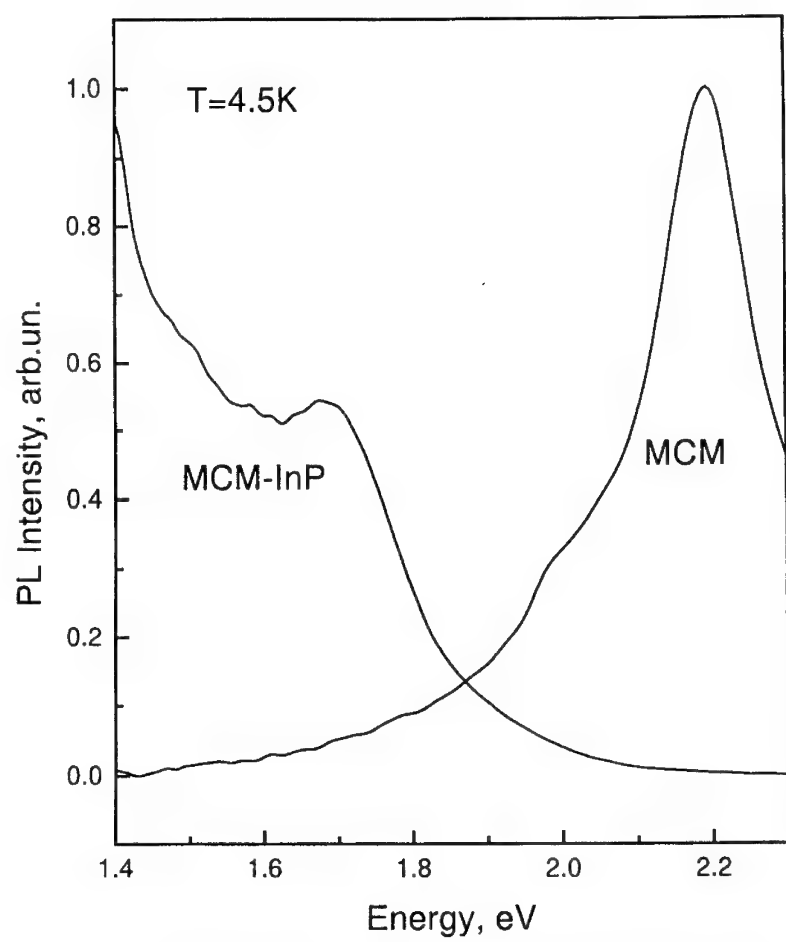
Figure 6 PL of MCM empty and filled with InP
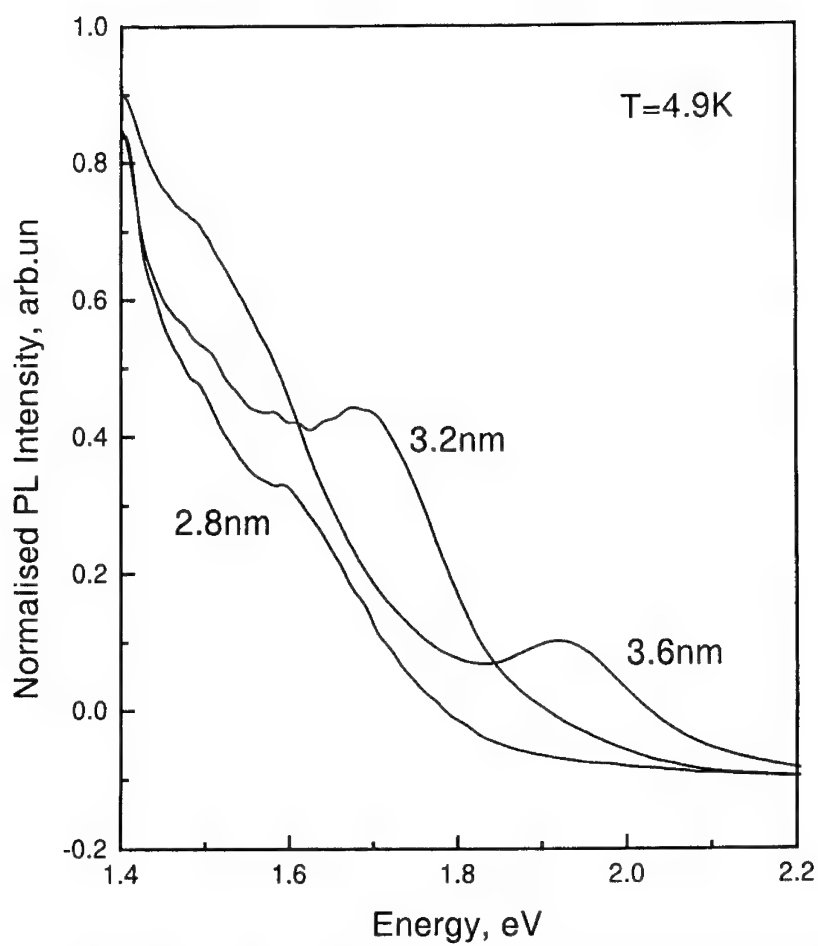
Figure 7 PL of InP in MCM: effect of different channel diameter

Formation of Quantum Wires and Islands in Si/pure-Ge/Si Heterostructure

Y. Shiraki, H. Sunamura, S. Fukatsu*, and N. Usami
Research Center for Advanced Science and Technology, and *Department of
Pure and Applied Sciences, The University of Tokyo
Komaba, Meguro-ku, Tokyo 153, Japan

Formation of quantum wires and islands was successfully observed in gas-source
molecular-beam-epitaxy grown Si/pure-Ge/Si heterostructures. Emergence of a
new photoluminescence peak reflecting island formation was identified when the Ge
layer thickness exceeded 4 monolayers (MLs), while PL peaks characteristic of
quantum wires were seen in the Ge layer with the thickness less than 1 ML. Island
and wire formation was confirmed by cross sectional as well as plan view transmi-
ssion electron microscope measurements. Optical properties characteristic of low
dimensional structures different from quantum wells were identified.

1. Introduction

Quantum structures, not only quantum wells but also quantum wires and
dots, in the system of SiGe/Ge are now attracting much attention. This is
because these quantum structures can modify the band structures and therefore
have a potential to realize optoelectronic devices as well as high speed electron-
ic devices with high performances. However, comprehensive studies on optical
and electrical properties of these structures are still lacking. In this paper, a
promising technique for formation of quantum structures in SiGe/Si system,
that is, gas source molecular beam epitaxy (GSMBE) where hydrogenated gases
are employed as molecular sources, is introduced and characteristics of quan-
tum structures made by this method are discussed. One of the interesting
features of Si/Ge heterostructures is that the band alignment can be modified by
changing the strain distribution in the structure and type-1 and 2 alignments are
realized depending upon which substrates are employed. However, we here
concentrate on the growth of strained SiGe and Ge layers on unstrained Si sub-
strates. One of the important issues of lattice mismatched systems concerning
crystal growth is the so-called critical thickness of coherent epitaxy.
Therefore, we investigate first what happens when Ge content is increased in a
standard Si/SiGe/Si quantum well and the well layer thickness exceeds the criti-
cal thickness. As an extreme case, quantum structures with pure Ge as a well
layer are also intensively investigated here. And interestingly they are shown
to exhibit unique optical properties reflecting the modification in energy band
structures due to low dimensionality of the structures.

2. Formation of quantum wells by gas source MBE

In this study, a gas source dedicated MBE machine, the details of which was
described elsewhere [1], was used for the formation of SiGe/Si quantum struc-

tures and pure Si_2H_6 and GeH_4 were employed as gas sources. Figure 1 shows growth temperature dependence of photoluminescence (PL) spectra as well as PL intensity [1]. It is seen that at temperatures higher than 680 C, the PL intensity is not significantly dependent on the temperature while it exponentially decreases with decreasing temperature. This behavior well corresponds to the temperature dependence of the growth rate and it is known that the lower temperature region is called a reaction-limited regime where the growth is governed by the hydrogen desorption from Si surfaces while the higher temperature region is supply-limited.

It is well known that surface segregation of Ge atoms is the main cause of the interfacial smearing during Si/SiGe heterointerface growth. Luminescence from quantum wells is known to reflect distortion of the potential shape due to the surface segregation and show PL peak shifts to higher energies compared with the theoretical calculation based upon an ideal square potential [2]. QWs grown by the GSMBE were found, however, to show no energy shift and provide precise agreement between experiments and square-well potential calculation [2]. This is probably due to the surfactant effect of a large amount of atomic hydrogen [3] which is constantly supplied to the growth front in this method. Recent experiment of introduction of atomic hydrogen into the solid source MBE chamber has shown that the surface segregation is really suppressed [4].

3. Ge composition dependence of luminescence

Strain accommodation into epitaxial layers increases with increasing Ge content and/or layer thickness. Basically the strain energy is released by introducing misfit dislocations which deteriorate optical as well as electrical properties of heterostructures. However, it has been recognized recently that another pathway to release strain without introducing misfit dislocations is possible.

Figure 2 shows PL spectra of QWs with different Ge composition [5]. It is seen that the peak positions systematically shift to lower energies with increasing Ge content without loosing luminescence intensity even when the well thickness exceeds the equilibrium critical thickness (x > 0.5). Moreover, no luminescence characteristic of misfit dislocations is observed, indicating high quality of these samples. The inset of Fig. 3 is temperature dependence of PL intensity and it gives an activation energy corresponding to the valence band discontinuity, which is also an indication of high quality of samples. However, as shown in Fig. 3, the peak position deviates to higher energies from the theoretically predicted exciton energy (dotted line) when the Ge content exceeds 0.4. Along with this deviation, the composition dependence of the PL activation energy shows significant drop from the value of band discontinuity at the valence band (closed circles). These facts suggest that significant changes occur in properties of epitaxial films and island formation at Si/SiGe interfaces was found to set in at this Ge composition from transmission electron microscope (TEM) measurements [5].
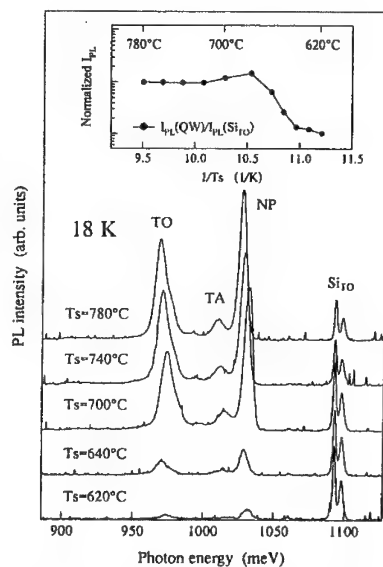
Fig.1 Growth temperature dependence of PL spectra and integrated intensity (inset) of SiGe/Si QWs grown by GSMBE.

Fig.2 PL spectra of SiGe/Si QWs with different Ge composition.

Fig.3 Ge composition dependence of NP peak energy and activation energy. Inset is temperature dependence of PL intensity.
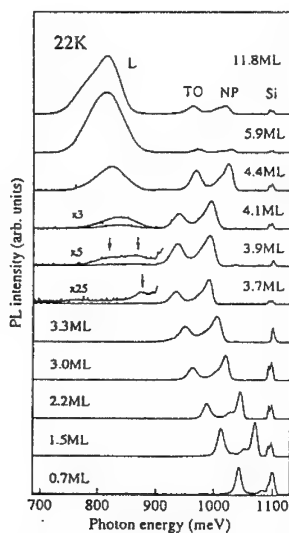
Fig.4 PL spectra of Si/pure-Ge/Si QWs with various Ge widths.

4. Si/pure-Ge/Si quantum wells

In the case of pure Ge wells, the situation is more drastic. Figure 4 shows PL spectra of Si/pure-Ge/Si quantum wells [6]. Well resolved no-phonon (NP) peak and its TO phonon replica are observed when Ge is less than 4 MLs. PL peaks shift toward lower energies with increasing Ge width, showing quantum confinement effect of Si/Ge/Si quantum wells (QWs). This indicates that the two dimensional layer-by-layer growth takes place without generation of misfit dislocations till 4 MLs. When Ge exceeds 4 MLs, a new broad peak is seen to appear in the lower energy region along with NP and TO edge emissions. Emergence of this broad peak was found to well correspond to the formation of islands from TEM measurements and the peak was unambiguously assigned to come from islands with the size where quantum confinement is possible. The broad peak shows energy shift in the early stage of its development, probably showing the quantum confinement effect in islands. The peak was found to be stable against temperature and be observed even at room temperature.

It is noteworthy that the NP and TO peaks of QWs show the blue shift to the energy corresponding to Ge 3 MLs during evolve of islands. This probably indicates that excess Ge atoms more than 3 MLs are consumed to form islands, and Ge wet layers with 3 MLs and islands coexist in this system.

QWs with Ge thickness even less than 1 ML were found to give rise to sufficient intensity of luminescence and the energy monotonically increased with decreasing Ge thickness in the almost same manner as QWs with thicker widths as shown in Fig. 5 [7]. Plan view TEM measurements revealed that Ge wires were formed in this region as seen in Fig. 6 and PL can be attributed to emissions from Ge quantum wires embedded in Si crystals.

Figure 7 shows excitation intensity dependence of PL spectra both of QWs and wires formed here [7]. Band filling effect is well seen in the case of QWs, that is, the peak position shifts to higher energies with increasing excitation intensity. However, there are no shifts in the case of wire structures, probably reflecting the high density of states of the quantum wires. Moreover, in wires formed with Ge less than 0.5 ML, a new peak is observed to develop on the lower energy side of the original peak as the excitation intensity is increased as seen in Fig. 7. The PL intensity increases more rapidly than that of the original peak, by the square of the original peak intensity. This is one of characteristic features of biexcitons and one may consider that high density of excitons cause formation of biexcitons in Ge quantum wires since the life time of excitons in the SiGe systems is quite long. It is also noted that although the peak position of wire structures shows systematic blue shift as the Ge amount is decreased, the energy position is much lower than the results based upon a simple effective mass calculation. This probably suggests the increase in the exciton binding energy in lower dimensional structures.

5. Conclusion
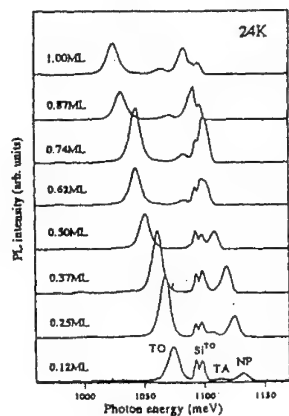
Fig.5 PL spectra of Si/pure-Ge/Si QWs with submonolayer Ge.
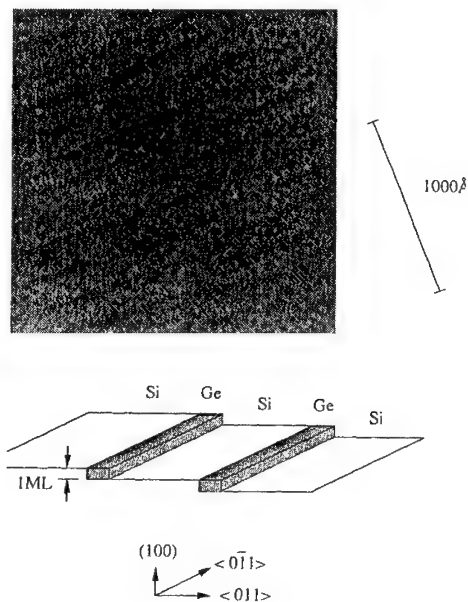
Fig.6 Plan view TEM photograph of Si/pure-Ge/Si QWs with submonolayer Ge and the schematics.
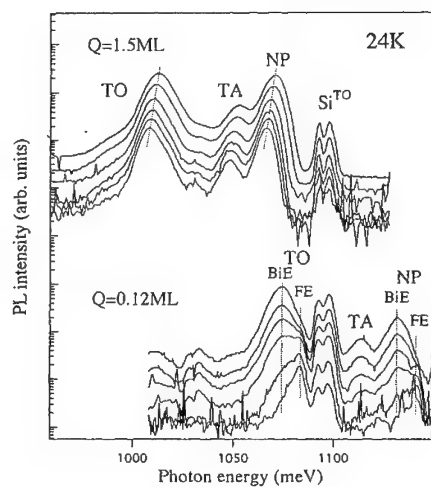
Fig.7 Excitation intensity dependence of PL spectra of QWs (upper) and wires (lower).

Quantum wires and islands as well as quantum wells were successfully formed by GS-MBE in Si/Ge systems. When Ge content in SiGe/Si quantum wells exceeded the amount corresponding to the critical thickness, characteristic changes were observed in PL properties, which was revealed to originate from formation of SiGe islands with high optical properties. When pure Ge layers were employed for the well, PL peaks monotonically shifted toward lower energies with increasing Ge width. When Ge exceeded 4 MLs, however, a new broad peak originating from Ge islands was seen to appear. QWs with Ge thickness less than 1 ML were found to give rise to sufficient intensity of luminescence and the energy monotonically increased with decreasing Ge thickness in the almost same manner as QWs with thicker width. Plan view TEM measurements revealed that Ge wires were formed in this region. Characteristic optical features of the structure, different from those of quantum wells, may lead to a conclusion that quantum wires and islands are self-assembled in Si/pure-Ge/Si heterostructures.

References

[1] S. Fukatsu, N. Usami, Y. Kato, H. Sunamura, Y. Shiraki, H. Oku, T. Ohnishi, Y. Ohmori, and K. Okumura; J. Crystal Growth 136, 315 (1994)

[2] S. Fukatsu, H. Yoshida, N. Usami, A. Fujiwara, Y. Takahashi, and Y. Shiraki; Thin Solid Films 222, 1 (1992)

[3] M. Copel and R. M. Tromp; Appl. Phys. Lett. 58, 2648 (1991)

[4] G. Ota, S. Fukatsu, , Y. Ebuchi, T. Hattori, N. Usami, and Y. Shiraki; Appl. Phys. Lett. 65, 2975 (1994)

[5] H. Sunamura, S. Fukatsu, and Y. Shiraki; Appl. Phys. Lett. 66, 953 (1995)

[6] H. Sunamura, N. Usami, S. Fukatsu, and Y. Shiraki; unpublished

[7] H. Sunamura, S. Fukatsu, and Y. Shiraki; unpublished

CHARACTERISTICS OF THE SELF- ORGANIZED STRAINED InGaAs QUANTUM DISK LASER ON GaAs (311)B SUBSTRATE

Eiichi Kuramochi, Mitsuru Sugo, Masaya Notomi, Hidehiko Kamada, Teruhiko Nishiya, Jiro Temmyo, Richard Nötzel[a], and Toshiaki Tamamura

NTT Opto-electronics Laboratories, 3-1, Morinosato Wakamiya, Atsugi-shi, Kanagawa 243-01 Japan

[a] Present address : Paul-Drude-Institut fur Festkörpelektronik, Berlin, Germany

The disk-shaped nano-scale InGaAs dot arrays self-organized on GaAs (311)B substrate in the growth of strained InGaAs film by MOVPE were applied to the active region of ridge type semiconductor lasers. This quantum disk laser successfully oscillates in continuous wave single-mode at room temperature with a low threshold current of 18 mA, which is lower than that of quantum well laser grown on (100) GaAs simultaneously. The temperature dependence of lasing and PL spectra revealed that the lasing always occurred at the ground level in the quantum disks. The lasing characteristics of the quantum disk laser drastically degraded with lowering temperature below 100K. The origin of this anomaly is discussed from the photo-luminescence and and photo-luminescence excitation analysis.

1. INTRODUCTION

Nano-scale semiconductor heterostructures have been extensively studied for realizing low dimensional quantum confinement effect. In the case of quantum box where the confinement is zero-dimensional, the density-of-states is considered to be delta-function-like (1,2). The theoretical analysis predicts that this feature is suitable for reducing threshold current and enhancing quantum efficiency of semiconductor lasers (3). Although various attempts to fabricate quantum box structure such as the lithographical patterning of quantum film and the growth on patterned substrate have been reported, the previous prediction was not realized so far, mainly due to the difficulty in the fabrication of nano-scale crystals with

device quality.

Recently, the fabrication of quantum boxes using self-organization phenomenon of highly strained film system come into prominence (4). Most of self-organization phenomena reported so far are in the category of coherent islanding that spontaneously occurs in Stranski-Krastanow epitaxial growth mode (5-11). InGaAs or InAs nano-crystals as small as 10nm have been obtained in the MBE growth of strained film on GaAs substrate (9-11). Extremely narrow CL or PL lines are observed from these nano-crystals, indicating the zero-dimensional confinement is actually realized in these systems (10,11).

We have also found a new self-organization phenomenon in a growth of strained-InGaAs/AlGaAs heterostructure on GaAs(311)B surface by MOVPE (4). During the growth-interruption after the growth of strained InGaAs film, the rearrangement of the film into an array of nano-crystals spontaneously occurs. Figure 1 shows SEM images of self-organized nano-crystals on a GaAs (311)B substrate. The interesting feature of this system is the evolution of clear ordering among the dots, which is never observed in the islanding phenomena in MBE growth. As shown in the cross-sectional SEM image, a nano-crystal consists of disk-shaped InGaAs and a barrier layer automatically covering the disk. The lateral size of the disk can be controlled in a range of 30-120 nm by changing In content, and the density can be roughly changed by the nominal thickness of strained InGaAs film. Another important feature of this system is that the resultant structure shows excellent optical properties, that is, strong and narrow PL spectra comparable to quantum well film on conventional (100) substrate at room temperature (12,15). This suggests that the crystal quality of the disk is almost perfect.

From those excellent features, the quantum disk structure could have a high device application capability, thus, we have applied the quantum disk structure to the active region of semiconductor laser diodes. This paper deals with the characteristics of quantum disk lasers.

2. EXPERIMENTALS

The active layer consists of doubly-stacked InGaAs/AlGaAs quantum disk layers (13). Figure 2 shows a cross-sectional view of the laser structure. The composition of strained

InGaAs film is $In_{0.25}Ga_{0.75}As$, and the nominal thickness was 6nm and the lateral disk size was found to be about 60-70 nm from SEM observation. The filling factor which represents the aerial area occupying with quantum disks was about 6%. The doubly stacked quantum disks were buried and separated by $Al_{0.15}Ga_{0.85}As$ barrier. The SCH structure was composed from AlGaAs cladding and guiding layers.

The laser structure was grown on GaAs (311)B and (100) substrates by MOVPE, simultaneously. As the self-organization does not occur on (100) substrate, the conventional double quantum well laser structure was grown on (100) substrate. Hereafter, the quantum disk laser on (311)B is abbreviated as QD-LD, and this quantum well laser on (100) is as QW-LD, respectively.

The transverse-mode stabilized ridge waveguide lasers were fabricated by conventional patterning and dry-etching process with he ridge width of 2.5 μm. The device was cleaved 0.9mm long, and the facets were uncoated. The laser was mounted on heat sink for the evaluation of cw operation.

For the measurement of photoluminescence(PL) and photoluminescence excitation (PLE) of laser structure, a GaAs cap layer was removed by wet-etching. Ti-sapphire wavelength tunable laser was used for pumping samples in a wavelength range of 700-850 nm. Both pumping and observation were performed from the top side of epilayer in these measurements.

3. LASING CHARACTERISTICS AT ROOM TEMPERATURE

Figure 3 shows the typical light output versus current curves of QD-LD and QW-LD under room temperature cw operation. The QD-LD has low threshold current of about 18 mA. This is less than that of the QW-LD in spite of low optical confinement of the QD-LD. The exact reason of such low threshold current of QD-LD with only 6% active region is not clear. However, the excellent optical property, that is, the high crystal quality could be a part of this reason. As increasing the drive current, a marked saturation of optical power was observed in QD-LD. This gain saturation probably due to the small volume of active region occurs in QD-LD.

The characteristic parameter of threshold current on temperature, T_0, of the QD-LDs around room temperature was 140K, which is almost the same as that of QW-LD. Figure 4 shows lasing spectra of a QD-LD in comparison with a QW-LD. Single-mode lasing with side-mode suppression ratio of 23 dB is obtained from both LDs under room-temperature 100 mA cw operation. The lasing wavelength of the QD-LDs is about 940 nm, which is slightly blue-shifted from that of the QW-LD. This blue-shift is consistent with that of PL spectrum, and probably originates not from quantum confinement but from the difference of substrate.

Unfortunately, no clear evidence of 0-dimensional quantum confinement was so far obtained in the lasing characteristics of quantum disk lasers at room temperature. This could be due to a too large disk size for realizing 0-dimensional quantum confinement. We have already confirmed 0-dimensional confinement in the magneto-luminescence measurement of the quantum disk sample with a disk size of about 30 nm (14). The MOVPE growth of such smaller disks for the laser structure using high indium content is not so uniform at present, then the improvement of the uniformity is now under investigated. Nevertheless, the low threshold current of QD-LD at room temperature demonstrates the high application capability of self-organized quantum disk structure to the optical devices, and promises the future possibility of realization of quantum box lasers in this system.

4. LASING CHARACTERISTICS AT LOW TEMPERATURE

The lasing characteristics of QD-LD at low temperature are investigated under cw operation. Figure 5 shows temperature dependence of threshold current and slope efficiency. In the case of QW-LD, both of threshold current and slope efficiency improves monotonously with reducing temperature. These are typical characteristics of conventional quantum well lasers. On the other hand, the threshold current of QD-LD decreases with lowering temperature and reaches to 7 mA at 60 K. However, a further decrease of temperature causes a drastic increase of threshold current which exceeds over 100 mA at 7 K. This anomaly is also observed in the slope efficiency, which deteriorates already from 150 K. This temperature dependence is reproducible and observed in all QD-LDs we measured.

Figure 6 shows the temperature dependence of lasing wavelengths of both LDs. Except slight blue-shift, the lasing wavelength of the QD-LD almost coincides with that of the

QW-LD at all measured temperature, and no anomalous change in the wavelength was observed below 60 K. This result suggests that lasing occurs from the disk structure even at low temperature. These results suggest that this anomaly is intrinsic property of the QD-LDs.

5. OPTICAL PROPERTIES AT LOW TEMPERATURE

In order to elucidate the origin of this anomaly, PL and PLE spectra of the laser structures were measured at low temperature. Figure 7 shows the PL spectra at 112 K, 56 K, and 4 K under two levels of excitation. The high excitation has a pumping power ten times larger than that of low excitation. At 112 K only one definite and relatively narrow peak was observed at 890nm for both excitation levels. At 56 K the spectrum is almost composed of this peak, but another broad peak at 870 nm was grown by increasing the excitation power. At 4 K this broad peak became clearer and one more peak appeared at 825 nm. Figure. 8 shows lasing spectra of the QD-LD. From the comparison of Fig. 8 with Fig. 7, it is found that lasing peak almost coincides with the narrow PL peak, despite a large difference in injection current caused by the anomaly. From these results we assign that the narrow PL peak around 890 nm in Fig. 7 is due to excitonic recombination at the ground state of the quantum disks. The peak at 825 nm at 4 K can be assigned to n-doped GaAs. The origin of the broad peak around 870 nm is not clear. Hereafter this PL peak is labeled as A.

Figure 9 shows the PL spectra of the QW-LD at 8.5 K. The emissions from GaAs substrate and InGaAs quantum wells were observed. It is noteworthy that no emission corresponding to the peak A in the QD-LD was observed even under high excitation. Therefore, it is considered that the origin of the emission A might be provided by the self-organization because the phenomenon does not occur in growth of QW-LD on (100) substrate.

In order to get information about the peak A, we measured photoluminescence excitation spectrum of this peak at 4 K. The excitation wavelength was scanned as long as 857nm limited by wavelength tunable laser we have used. Figure 10 shows that no clear structure is observed in PLE of peak A. For other two peaks a clear structure was observed, indicating that the peak originates not from quantum structure but from some

bulk-like structure. In addition, large absorption onset below 800 nm in the PLE spectrum suggests the possibility that In-rich AlGaInAs contribute to this emission.

As a result, the anomaly in the lasing characteristics of QD-LD at room temperature could be caused by bulk-like structure such as compound (Al)GaInAs. The radiative recombination process in such bulk-like structure is enhanced by reducing temperature. Probably the recombination in bulk-like structure inhibits supply of injected carrier into quantum disks at low temperature. The limited diffusion length at low temperature also accelerates this inhibition of carrier supply. This may cause the anomaly of lasing characteristics of quantum disk lasers.

In order to make this explanation more clearly, the mechanism of self-organization on (311)B substrate is discussed in the next section.

6. SELF-ORGANIZATION MECHANISM

In our previous papers, we explained the AlGaAs barrier layer automatically covers the isolated disks due to mass-transport. However, the detailed structural analysis revealed that the mechanism is more complex. Figure 11 illustrates the possible mechanism of the self-organization on GaAs(311)B substrate. A strained InGaAs film is not stable at a relatively high growth temperature of around 750 °C, and starts to condense forming an undulation in the film during the growth interruption. Afterward, or simultaneously the intermixing of InGaAs with AlGaAs occurs at their interface. This partial intermixing could reduce the strain energy. As the undulation grows, relatively thinner part of InGaAs completely mixes with beneath AlGaAs forming AlGa(In)As compound, then, this ternary compound migrates on top of InGaAs disks. This speculation was proved by EDS analysis of TEM samples, in which considerable amount of In is detected in the barrier layer on top of the disk (16). These reactions may be enhanced by a low surface energy of (311)B substrate and high growth temperature. Consequently buried heterostructures of isolated InGaAs disks and AlGa(In)As barrier layer are spontaneously formed. The ordering could originate in the stage of undulation formation in the film.

From this mechanism, it is clear that this self-organization growth is quite different from the Stranski-Krastanow growth mode which is observed in the coherent islanding of

strained film. Therefore, the thin quantum well film layer, so-called wetting layer, forming inevitably in Stranski-Krastanow growth mode cannot exist in our quantum disk system.

Although the In is contained in the barrier layer, the resultant AlGa(In)As does not seem to correspond to the bulk-like (Al)GaInAs responsible for the lasing anomaly. This is because the wavelength of about 870-nm PL peak indicates the composition of the bulk structure is very close to that of InGaAs quantum disks. This suggests that some portions of disks change into the bulk-like structure caused by the imperfection of self-organization in the growth of the complex laser structure. That is, the intermixing between InGaAs and AlGaAs proceeds seriously, resulting in the disappearance of certain percentages of InGaAs disks even in the thicker parts. The uniformity improvement in the self-organized growth of quantum disks in the laser structure will be an important work in near future.

7. SUMMARY

We have examined the application of new self-organization phenomenon on (311) B substrates to the fabrication of semiconductor laser. Quantum disk laser has shown excellent lasing characteristics at room temperature. This demonstrates high potential of self-organized structure for future optical device application. However, anomalous lasing characteristic was observed at low temperature. This is probably due to bulk-like structure caused by imperfect self-organization in the growth of complex laser structure.

ACKNOWLEDGEMENTS

REFERENCES

1. Y. Arakawa and H. Sakaki, Appl. Phys. Lett. 40, 939 (1982)

2. E.L. Ivchenko, A. V. Kavokin, V. P. Kochreshko, P. S. Kop'ev, and N. N. Ledentsov, Superlattices Microstruct. 12, 317 (1992)

3. M. Asada, Y. Miyamoto, and Y. Suematsu, IEEE J. Quantum Electron., QE-22, 1915

(1986)

4. R. Nötzel, J. Temmyo, and T. Tamamura, Nature, 369, 131 (1994)

5. S. Guha, A. Mudhukar, and K. C. Rajkumar, Appl. Phys. Lett., 64, 2110 (1990)

6. J. M. Moison, F. Houzay, F. Barthe, L. Leprince, E. Andre, and O. Vatel, Appl, Phys. Lett., 64, 196 (1994)

7. D. Leonard, M. Krisnamurthy, C. M. Reaves, S. P. DenBaas, and P. M. Petroff, Appl. Phys. Lett., 63, 3203 (1993)

8. N. N. Ledentsov, A. Yu. Egorov, A. E. Zhukov, M. V. Maksimov, I. G. Tabatadze, and P. S. Kop'ev, Semiconductors 28, 832 (1994)

9. J. Oshinowo, M. Nishioka, S. Ishida, and Y. Arakawa, Appl. Phys. Lett. 65, 1421 (1994)

10. J.-Y. Marzin, J.-M, Gérard, A. Izraël, D. Barrier, and G. Bastard, Phys. Rev. Lett. 73, 716 (1994)

11. M. Grundmann, J. Christen, N. N. Ledentsov, J. Böhrer, D. Bimberg, S. S. Ruvimov, P. Werner, U. Richter, U. Gösele, J. Heydenreich, V. M. Ustinov, A. Yu. Egorov, A. E. Zhukov, P. S. Kop'ev, and Zh, I. Alferov, Phys. Rev. Lett. 74, 4043 (1995)

12. R. Nötzel, J. Temmyo, H. Kamada, T. Furuta, and T. Tamamura, Appl, Phys. Lett. 65, 457 (1884)

13. J. Temmyo, E. Kuramochi, M. Sugo, T. Nishiya, R. Nötzel, and T., Tamamura, Electron, Lett. 31, 209 (1995)

14. H. Weman, H. Kamada, M. Potemski, J, Temmyo, R. Nötzel, and T. Tamamura, to be published in Solid State Electron.

15. J. Temmyo, E. Kuramochi, T. Nishiya, M. Sugo, R. Nötzel, and T. Tamamura, Conference Digest of the 14th IEEE Semiconductor Laser Conference, Hawaii, September 1994, PD4

16. J. Temmyo, R. Nötzel, H. Kamada, T. Furuta, and T. Tamamura, in *22nd International Conference on THE PHYSICS OF SEMICONDUCTORS, Vancouver, Canada,* edited by D. J. Lockwood, Vol. 3, 1851, World Scientific, Singapore (1995)

1 μm

Alignment of disks

Cross-sectional photo
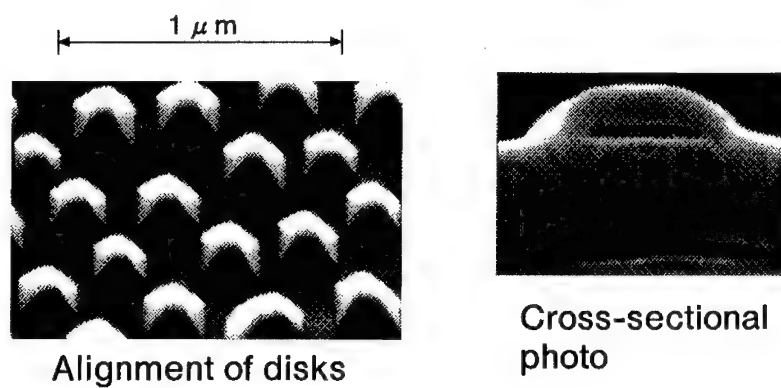
Fig. 1   SEM images of self-organized strained InGaAs quantum disks on a GaAs (311)B substrate

p-AlGaAs cladding layer
Metal electrode
Insulating layer
p-AlyGa1-yAs wave-guide
$In_{0.25}Ga_{0.75}As$ quantum disks
$Al_{0.15}Ga_{0.85}As$ barrier
n-AlyGa1-yAs wave-guide

n-Al_xGa$_{1-x}$As cladding layer

n-GaAs (311)B substrate
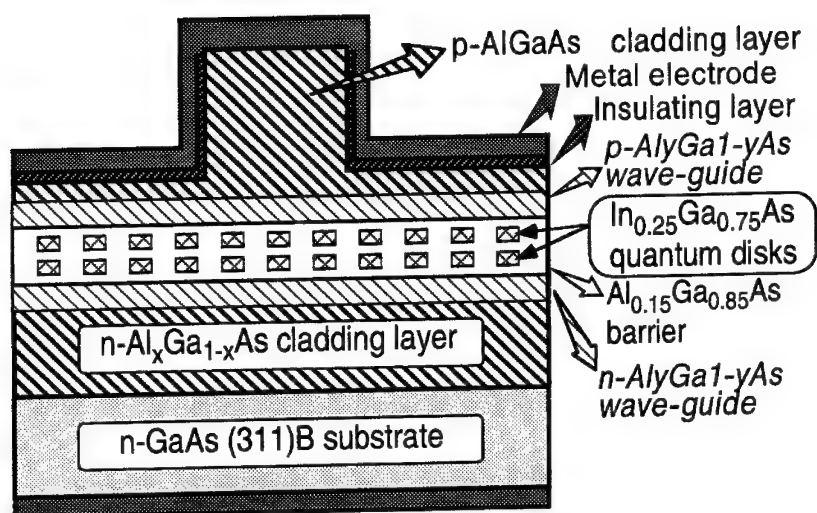
Fig. 2 A cross-sectional view of quantum disk lasers
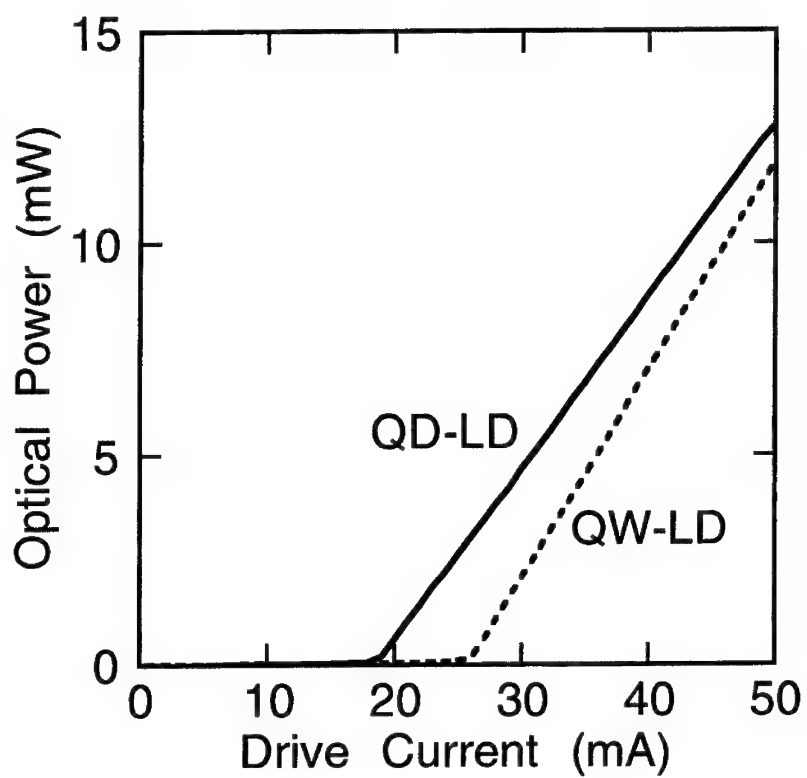
Fig. 3 I-L curves of QD-LD and QW-LD in CW operation at 25 °C
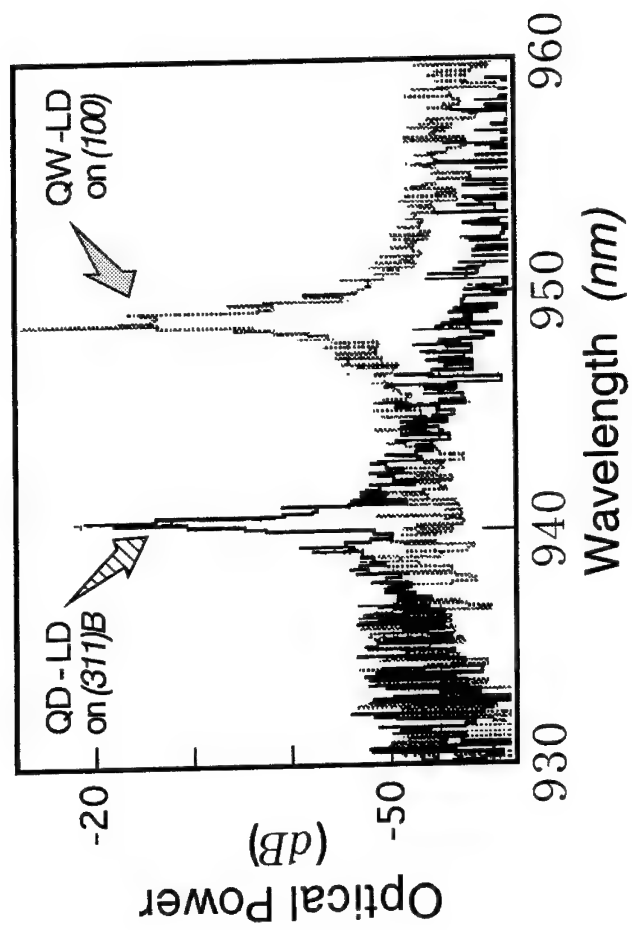
Fig. 4 Lasing spectra of LDs under room-temperature 100-mA cw operation
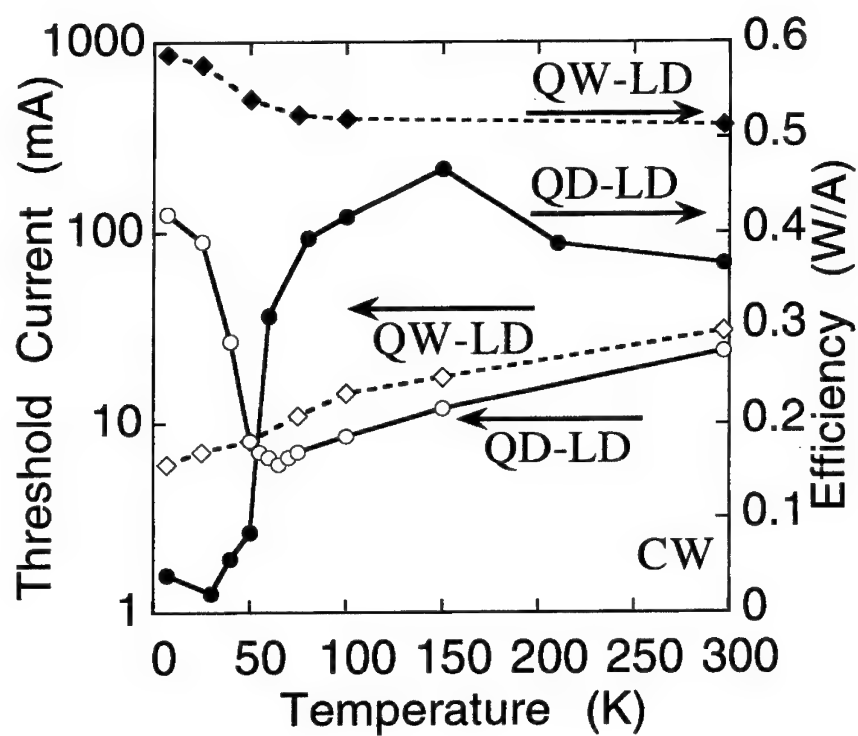
Fig. 5 Temperature dependence of threshold cuı
and slope efficiency of QD-LD and QW-LD

Fig. 6 Temperature Dependence of Lasing wavelength

H : pumped with high excitation power
L : pumped with low excitation power

PL Intensity (arb. units)

pumped by 730-nm laser   11 2 K
H
L

56 K
H
L

n$^{\pm}$GaAs 'broad peak'   4 K
disk
H
L

800   840   880   920
WAVELENGTH (nm)
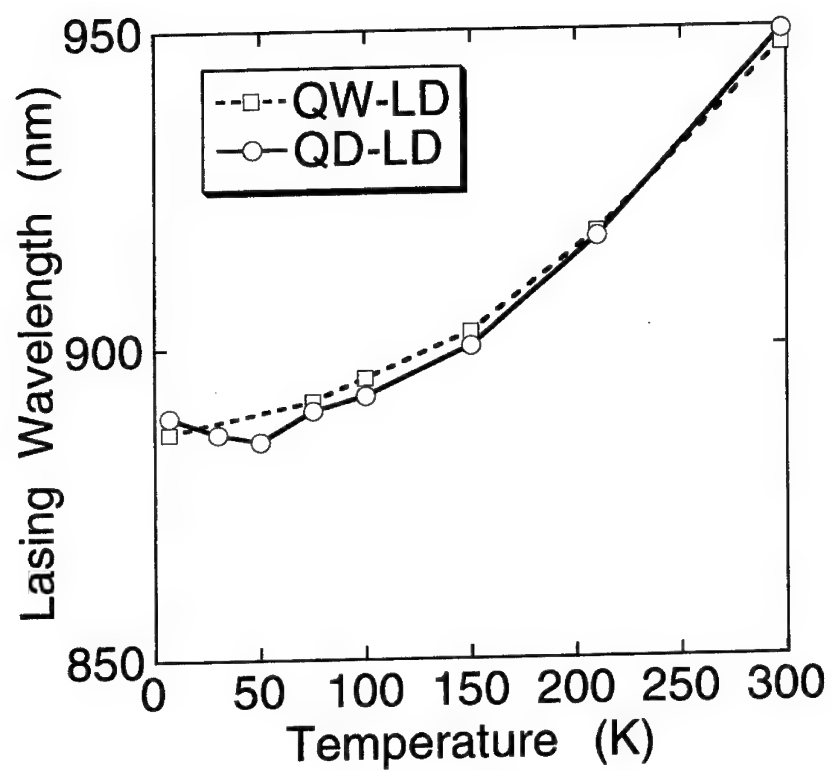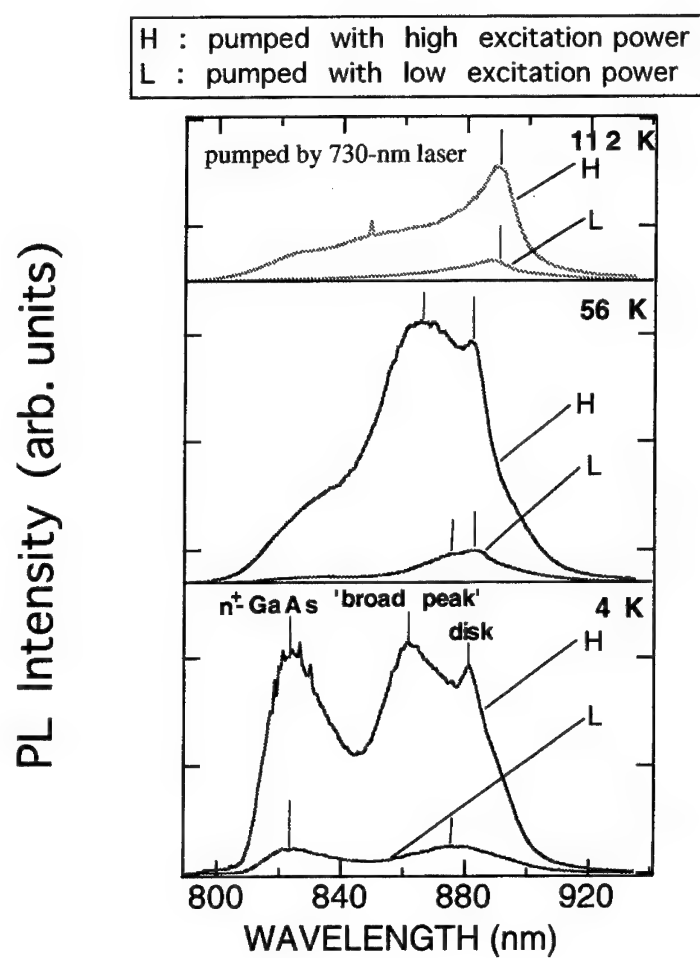
Fig. 7   PL Spectra of QD-LD at Low Temperature
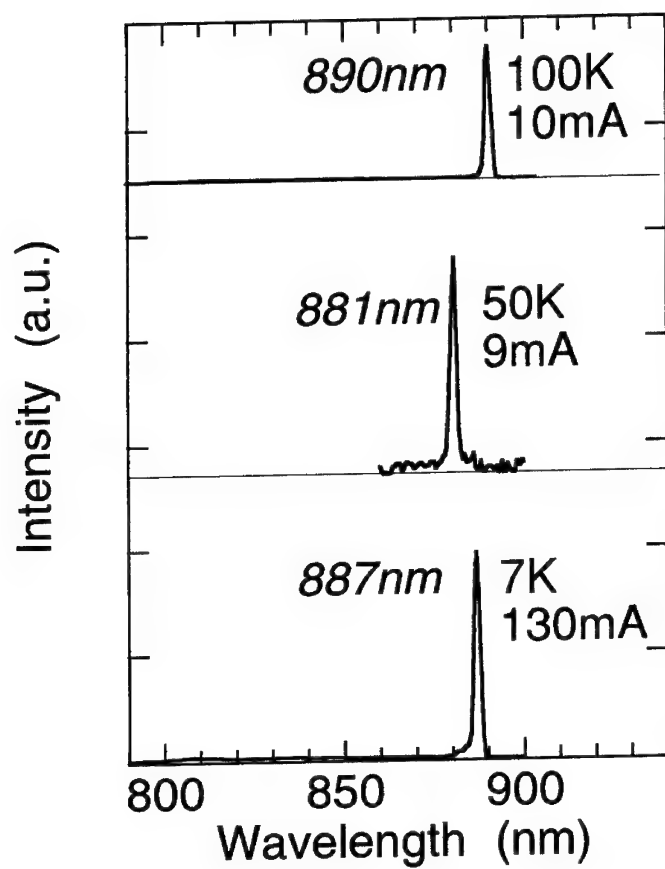
Fig. 8   Lasing spectra of QD-LD at low temperature

H : pumped with high excitation power
L : pumped with low excitation power
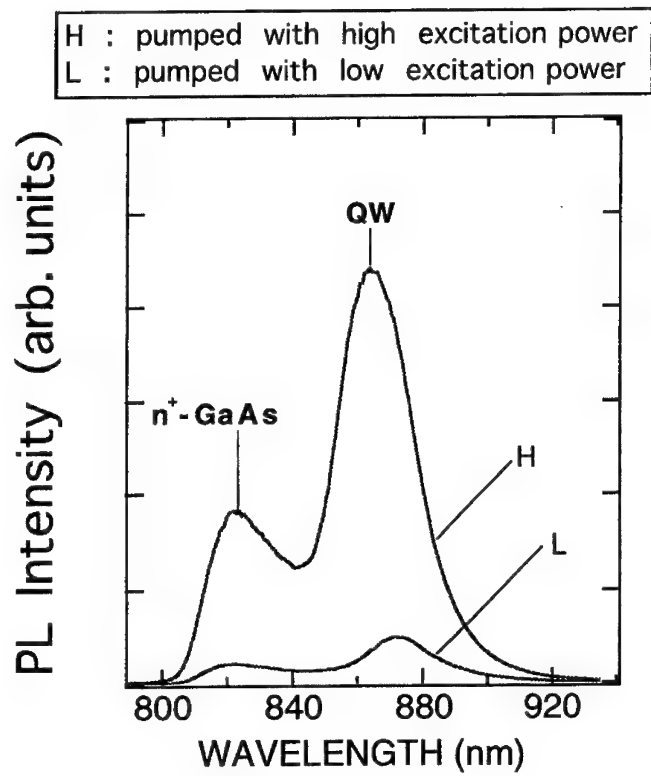
Fig. 9   PL spectra of QW-LD at 8.5K
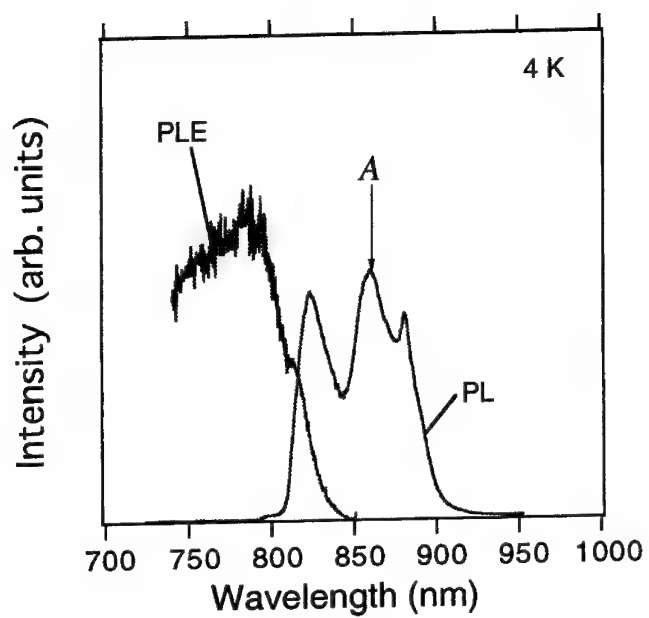
Fig. 10   PLE spectrum of the PL peak *A* of QD-LD

Strained InGaAs film

AlGaAs

GaAs(311)B Substrate

(a) Growth of strained InGaAs film

Intermixing   *Rearrangement*
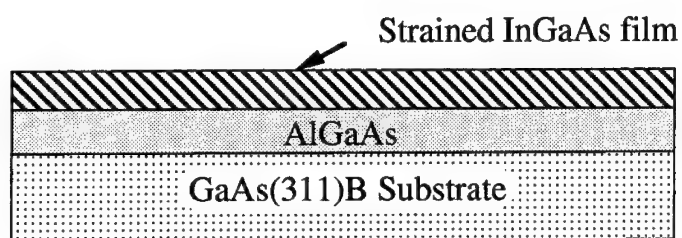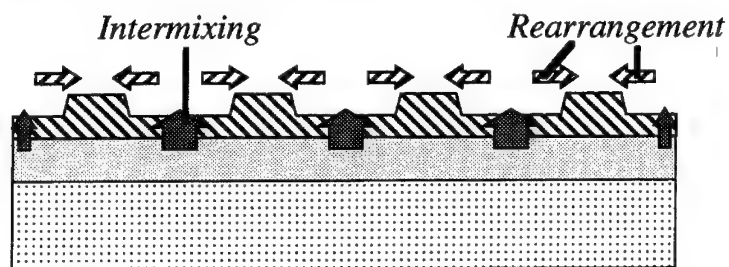
(b) During growth interruption

AlGa(In)As compound   Strained InGaAs disk

AlGaAs

GaAs(311)B Substrate
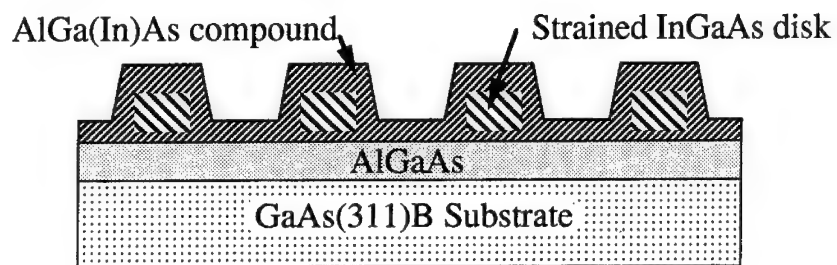
(c) Completion of self-organization

Fig. 11 Mechanism of Self-organization on (311)B
Substrate

TWO-DIMENSIONAL ARRAYS OF ELECTRICALLY COUPLED NANOMETER DIAMETER METALLIC CLUSTERS

V.R. Kolagunta [†], D.B. Janes [†], J.D. Bielefeld [††], R.P.Andres [††],
R.G. Osifchin [††], J.I. Henderson [†††] and C.P. Kubiak [†††]

† School of Electrical and Computer Engineering
†† School of Chemical Engineering
††† Department of Chemistry

Purdue University
West Lafayette, IN47907

Abstract

We report on the synthesis and characterization of close-packed arrays of nanometer-diameter metal clusters electrically coupled by the use of rigid,double-ended organic molecules. These cluster arrays are self-assembled on a flat surface from a colloidal suspension containing the metal clusters encapsulated by a monolayer of dodecanethiol molecules. The array is then exposed to the linking "molecular wire" dissolved in solution wherein the dodecanethiol molecules on the surface of the clusters are displaced by the linking molecule. The formation of these arrays between two metal contact pads that are separated by about 500nm is demonstrated. Electrical characterization at various stages of array formation is be presented along with a discussion of the possible conduction mechanisms.

Introduction

One-dimensional and two-dimensional arrays of quantum dots coupled by tunnel junctions are interesting both for their conduction characteristics and for potential applications in nanometer scale computational or memory devices. Such arrays of metallic islands have generated interest as computational cells which could potentially solve difficult problems like the travelling salesman problem by using the property that the array would settle to a minimum energy state corresponding to the solution of the problem [1]. Conduction in such two-dimensional arrays has been modelled, under various regimes of coupling to an underlying gate plane, including the extremes of strong and weak coupling [2,3] At zero temperature it is predicted that these arrays would show a conduction gap around zero bias. In the case of strong gate coupling, Middleton and Wingreen have predicted a conduction beyond threshold of the type $I = (V/V_T - 1)^{\Gamma}$, with values of Γ ranging between 1/2 and 5/3 depending on whether the array is one- or two-dimensional. Recently, in experiments conducted at temperatures below 0.1 K, such a conduction has been observed through one- and two- dimensional arrays of aluminum dots separated by aluminum oxide layers [4]. The measured values of Γ are consistent with theoretical predictions of Middleton and Wingreen. In the case of weak coupling to a gate, studies using similar Al/AlO_x metal islands have demonstrated the observance of a threshold along with the sub-threshold conductance showing an activation energy dependence at higher temperatures [5]. The observance of the gap in all the above studies is attributed to the Coulomb charging effect, which dominates when the charging energy corresponding to the capacitance of the metal island C_D is such that $e^2/C_D \gg k_B T$. Also the threshold voltage is related to the number of islands in series between the contact pads and coupling between the clusters and the underlying gate plane.

In order to see interesting quantum and Coulomb charging effects in arrays of metallic dots at room temperature, it is necessary to reduce the dot capacitance, C_D, i.e. the total capacitance between a dot and all other dots, to less than 1×10^{-18} Farads. This corresponds to metallic dots with diameters less than 2nm. A promising technique for synthesis of controlled size, nanometer diameter single crystal metal clusters is the gas aggregation source known as the multiple expansion cluster source (MECS) [6]. Room temperature Coulomb charging effects have been observed using a scanning tunneling microscope (STM) and gold clusters with diameters of 1-2 nm, synthesized using the MECS system [7]. In this STM experiment, bare gold clusters were vacuum deposited on a gold substrate coated with a self assembled monolayer (SAM) of a dithiol molecule. The dithiol SAM served as a tunneling barrier from the gold cluster to the gold substrate. The other barrier was between the cluster and the STM tip [7]. It is expected that similar charging effects resulting in a conduction gap can be observed at room temperature in coupled two-dimensional arrays of nanometer diameter metal clusters.

In this paper, we report on the fabrication and electrical characterization of such

coupled two-dimensional arrays using nanometer-size clusters. These arrays are self assembled as a coupled network of single crystal gold clusters (4 nm diameter) bridging the gap between two gold contact pads separated by 400-500nm, resulting in arrays with 70-80 clusters in series between contact pads. The self-assembly procedure of the cluster array involves deposition from a colloidal suspension, followed by reactive addition of a linking molecule (molecular wire) which bridges the gap between nearest-neighbor clusters and also provides electrical coupling between the two clusters to form a Coupled Cluster Network (CCN) [6]. To facilitate non-destructive characterization of the physical structure of the CCN before the electrical characterization, a substrate was developed with Au contact pads patterned on a TEM transparent insulating film. The substrate and array fabrication are described, and the TEM images and conduction properties of sample cluster arrays are discussed.

Sample Preparation

A cross-sectional view of the substrate developed is shown in Fig.1. The substrate consists of two thin metal contacts fabricated on a TEM-transparent, free-standing, SiO_2 film supported on a GaAs wafer. The thin SiO_2 film (40-70nm) is deposited by thermal evaporation on a clean GaAs wafer. To obtain continous close-packed arrays of clusters, the RMS roughness of the surface on which these arrays are formed has to be less than the diameter of the clusters. Atomic force microscope (AFM) studies of these thin SiO_2 films yielded a RMS surface roughness of approximately 1nm, with features that vary slowly on the scale of a cluster diameter. The metal contacts were 30-40 nm thick gold contacts separated by 100-500nm and were patterned by liftoff using a Cambridge EBMF-2 electron beam lithography system [8]. Contacts to exter-nal leads were made by 300-500nm thick gold pads patterned using conventional UV lithography and liftoff. Free-standing SiO_2 windows aligned to the gap between the two metal contacts were formed by backetching the GaAs wafer in a H_2SO_4:H_2O_2 solution, with the top surface protected by photoresist. This solution does not etch SiO_2 and hence the etching self-stops when it reaches the SiO_2 layer. The surface preparation of the SiO_2 layer after the backetching step is critical for successful for-mation of uniform cluster arrays by self-assembly. The photoresist on the top surface is stripped using a Microposit 1165 stripper. This is followed by a brief exposure to an oxygen plasma in a barrel etcher to eliminate possible organic contamination of the SiO_2 surface which can occur during and after the resist stripping process. The GaAs TEM substrates are then mounted on thin PC boards for ease of handling and mounting in the TEM. Since the oxide layer that is used to deposit the cluster array is an evaporated film of thickness about 40-80nm, good quality isolation is difficult to achieve and breakdown of the oxide film can occur at high substrate to contact-pad bias. Only substrates that show isolation between pads greater than 10GΩ are used to study the cluster arrays.

The gold clusters used for this study were synthesized using a MECS, details of

which are presented elsewhere [6]. The clusters had an average diameter of 4nm and a size distribution with a half-width of 0.5 nm, determined using transmission electron microscope (TEM) imaging. The clusters are single fcc crystals whose external shape is best described by a truncated octahedron with eight hexagonal (111) facets and six square (100) facets. For an ideal truncated octahedron of nominal diameter 4.2nm, each cluster contains about 4000 atoms. Each of the (111) facets of these clusters consist of 127 atoms with a facet area of $9.1nm^2$. During synthesis the clusters are encapsulated by a monolayer of dodecanethiol (DDT) molecules to prevent the clusters in the suspension from coalescing. It is believed that on a (111) gold surface, a covalent bond is formed between the sulphur atom in the thiol group at the end of the DDT molecule and four gold surface atoms [9]. The encapsulated clusters are stored as a dilute colloidal suspension in mesitylene. This suspension contains about 25 ppm gold, as determined by atomic adsorption, and is stable at room temperature with no precipitation observed over many months.

The clusters are deposited onto the substrates by placing a drop of the colloidal suspension in the gap between the contact pads using a micropipette. The suspension spreads over both gold and silica surfaces and as the solvent evaporates, the encapsulated clusters start forming islands of closely packed arrays as illustrated in Fig.2. In order to form a relatively continuous monolayer of clusters in the gap, this procedure is repeated several times. The DDT encapsulation prevents the clusters from aggregating to form larger particles and produces a fairly uniform spacing between adjacent clusters. However, it does not provide strong mechanical tethering or reliable electrical coupling between clusters. Most often, the clusters deposit as a single monolayer but occasionally multilayer islands have been observed.

In order to stabilize the cluster network and to control the electron tunneling resistance between adjacent clusters, the clusters are covalently linked using a linking molecule (molecular wire). For the linking process, the sample is exposed to the linking molecule by immersion in a 1 millimolar solution of the molecule dissolved in acetonitrile (CH_3CN) for 12-14 hours followed by a 20 minute rinse in acetonitrile. During this process, it is believed that the sulphur atom of the DDT molecule that is bonded to the gold surface is dislodged by the end group of the linking molecule. Such displacement reactions have been demonstrated on flat gold surfaces wherein the sulphur atom bonded to the gold surface can be displaced by either another thiol molecule or an iso-nitrile group [10]. The molecules that are used for the linking between the clusters have a stiff backbone to rigidly connect the two clusters. In the next section we shall demonstrate the formation of such linked arrays using two different linking molecules, namely the p-xylene-α,α-dithiol ($C_8H_{10}S_2$) with a length of approximately 1nm and 1,4-di(4-isocyanophenylethynyl)-2ethylbenzene with a length of approximately 2.2nm. For easy reference the dithiol molecule is referred to as XYL-Dithiol and the second molecule which has two isonitrile end groups is referred to as 22$\mathring{A}$ Di-isonitrile or 22ADI. Fig. 3 shows the structure of both the XYL-Dithiol and the 22ADI. The XYL-Dithiol molecule was used to form the SAM for the STM-tunneling

experiment wherein room-temperature Coulomb-blockade was observed. The 22ADI molecule was synthesized at Purdue and has been shown to displace DDT from the (111) surface of bulk gold [10]. Structural evidence for cross-linking of a gold cluster array in the case of both the linking molecules has been studied on MoS_2 substrates.

Large close-packed arrays of DDT encapsulated gold clusters spanning a micron or more have been fabricated on MoS_2 substrates and other similarly flat substrates (e.g. HOPG and Mica) [11]. On such atomically-flat substrates, the clusters self-assemble into a two-dimensional, ordered, hexagonal array with relatively few defects. However, such large uniform arrays have been difficult to fabricate on the surfaces commonly used in semiconductor fabrication, mostly because of a lack of surface flatness coupled with the fact that conventional semiconductor processing leads to molecular-level contamination of the surface. The current SiO_2 substrates provide a surface that is suitable for deposition of large area arrays, but the quality of the array is limited by residual contaminants and imperfections on the surface, along with the chemistry of the SiO_2 surface.

TEM Studies and Electrical Measurements

We present DC I-V measurements of four samples at various stages of fabrication. Three of these samples (Samples A-C) were linked with the 22ADI molecule and the fourth with the XYL-Dithiol molecule (Sample D). Table 1 shows the measured values of low-field conductance (resistance) at various stages of fabrication of the CCN. As mentioned earlier the isolation between the contact pads was measured to be greater than 10GΩ before deposition of the array. Clearly the formation of a cluster array between the two contact pads is indicated by the change in conductance between the pads. The conductance of the array 'as deposited' is determined by the structure of the unlinked array which is not mechanically very stable. Upon linking re-ordering of the array is observed. This is seen by comparing the TEM micrographs from each stage. Similar arrays were studied on MoS_2 to confirm the re-ordering and lack of dependence on the type of substrate. In the case of XYL-Dithiol as a linking molecule, significant restructuring including coalescing of clusters was observed. The reduction of the low-field conductance in the case of Sample D could be associated with the destructive nature of the linking process. In the case of the 22ADI molecule no change in the size distribution of the clusters was observed, but the spacing between the clusters was modified from approx 1nm 'as deposited' to about 2nm when 'linked' [8]. Fig. 4 shows the measured I-V of sample A, which is symmetric about zero bias. In the case of Samples A and B, the back of the free-standing SiO_2 surface was metallized to study the effect of a gate on the conduction properties of the CCN. No evident gating effects were observed. Two control samples, consisting of bare contact pad substrates (no clusters), were also characterized. The first control sample was imaged in the TEM system while the second was exposed to the 22ADI molecule, using the procedure described previously. Negligible changes in conduction between

the pads was observed following these exposures, indicating that the processes of imaging and linking the cluster array do not cause molecular contamination of the surface, which would result in formation of parasitic conduction paths between the two contact pads.

Discussion

As is evident from Table 1 the deposition of cluster arrays between contact pads can be monitored by observing changes in the electrical conduction between the contact pads at every stage. The measured conductances indicate that the conduction between clusters is modified due to the addition of a linking molecule. In addition to re-ordering of the array, the linking molecule also modifies the electrical coupling between adjacent clusters in the array. The exact value of the resistance measured between the contact pads is determined by the geometry of the array. In the high temperature limit, where Coulomb charging effects are negligble, it is possible to estimate the resistance between the two contacts pads if one has a handle on; i) the resistance of the linking molecule, ii) the number of linking molecules connecting two adjacent clusters and iii) the geometry of the cluster array.

In the case of Sample A and B the minimum distance between the pads is approximately 450nm and 500nm respectively, thus giving a minimum of 70-80 clusters in series between the pads [12]. The resistance per molecule of the 22ADI molecules between gold surfaces has been calculated using a molecular orbital calculation to be about 43 MΩ [13]. The packing density on a (111) gold surface for single-ended thiol molecules (such as DDT), when chemisorbed from solution is approximately one thiol molecule for every four gold molecules [9]. For the clusters used in this study, this corresponds to approximately 32 molecules chemisorbed on each (111) facet. Since the packing density of 22ADI on gold is not known, this same value (32) is assumed. The simulated resistance between two adjacent clusters (R_D), assuming 32 parallel resistors, each with a resistance of 43 MΩ, is 1.4 MΩ. For calculation of the expected resistance between the pads, we modeled the samples as semi-infinite hexagonal arrays with contact pads having a parabolic shape. For the high temperature limit, for which Coulomb charging effects can be ignored, this model yields an array resistance approximately equal to R_D. The high temperature resistance extrapolated from variable temperature measurements of the linked arrays using the 22ADI molecule is approximately 1MΩ, which is in reasonable agreement with this calculated resistance.

In a study of two-dimensional arrays using the Al/AlO_x system by Tighe et.al. where the metal islands are weakly coupled to the underlying gate plane, a conduction gap has been observed for temperatures where $(e^2/2C_D) \gg 10(k_BT)$ and measurable conductance has been observed within the gap for higher temperatures [5]. Since the capacitance values of the clusters in the CCN is not directly measurable, one can only estimate the charging energy of an individual dot. We estimate that the charging energy ranges between 72meV($\epsilon_r = 2$) and 140 meV($\epsilon_r = 1$) for a hexagonal closed

closed packed array of 4nm clusters separated by 1nm. Since there are about 70-80 clusters in series, the threshold voltage would range between 5 and 12 Volts for the present structure. At room temperature $k_B T \approx 26$meV and is lower than the estimated charging energy of the cluster. Hence the low-field conductance would be affected by this Coulomb charging effect and would result in the observance of a higher measured value of R_D at room temperature than the value obtained from the model. Although for the present CCN structure (4nm clusters) no conduction gap has been observed at room teperature, for the STM experiment, a Coulomb gap has been experimentally observed using 1-2nm diameter clusters [7]. It is therefore expected that a conduction gap around zero-bias at room-temperature can be observed in CCNs if the cluster diameter is reduced to 1-2nm. CCNs with 4nm diameter clusters should show comparable behavior at temperatures below about 100K.

At this preliminary stage, the dimensions of the array are not well controlled. However, the array structure itself seems robust, yielding reliable structures from sample to sample. While conduction through cluster arrays has been demonstrated, the irregularities in the present arrays are believed to play a significant role in the conduction properties. Particular issues that must be addressed include voids and lack of ideal ordering in the arrays. Varying the array composition, including changing the cluster size and the cluster metal would be interesting and possible using current technology. A better understanding of the linking process and the conditions for successful linking is needed to exploit the inherent flexibility of the CCN structure. It is hoped that such studies will lead to fabrication of CCNs whose properties can be tuned between the conducting and the insulating limits.

Conclusion

An experimental study of electronic conduction in CCNs of 4 nm diameter gold clusters linked by rigid organic molecules ('molecular wires') has been carried out. A comparison of the current-voltage relationships at various stages of sample synthesis indicates that the conduction properties of these arrays can be used to character-ize the properties of the array during various stages of the CCN fabrication. It is expected that CCNs can be fabricated which will exhibit interesting conduction be-havior, including room-temperature Coulomb charging effects.

References

1. S. Bandyopadhyay, V. P . Roychowdhury, and X. Wang, Physics of Low-Dimensiona Structures (VSV Co. Ltd.), **8/9**, 29(1995).

2. N.S. Bakhvalov, G.S. Kazacha, K.K. Likharev, S.I. Serdyokova, Physica B, **173**, 319, (1991).

3. A.A.Middleton, N.S.Wingreen, Phys. Rev. Lett., **71**, 3198 (1993).

4. A.J.Rimberg, T.R.Ho, J.Clarke, Phys. Rev. Lett., **74**, 4714 (1995).

5. T.S. Tighe, M.T. Touminen, J.M. Hergenrother, M.Tinkham, Phys. Rev. B., **47**(2), 1145(1993).

6. R. S. Bowles, S. B. Park, N. Otsuka, R. P. Andres, J. of Molecular Catalysis, **20**, 279 (1983).

7. M. Dorogi, J. Gomez, R. Osifchin, R. P. Andres, R. Reifenberger, Phys. Rev. B, **52**(12), 9071(1995).

8. An early version of the substrate was supplied by Professor H. Craighead at the Cornell National Nanofabrication Facility.

9. A.Ulman, An Introduction to Ultrathin Organic Films: from Langmuir-Blodgett to Self-Assembly, (Academic Press, Boston, 1991).

10. J. I. Henderson, G. M. Ferrence, S. Feng, T. Bein and C. P. Kubiak, Inorg. Chim. Acta., (in press)

11. R. G. Osifchin, W. J. Mahoney, J. D. Bielefeld, R. P. Andres, J. I. Henderson and C. P. Kubiak, Superlatt. and Microstruct., (in press)

12. D.B. Janes, V.R. Kolagunta, R.G. Osifchin, J.D. Bielefeld, R.P.Andres, J.I. Henderson, C.P. Kubiak, Superlatt. and Microstruct. (in press)

13. M. Samanta, W. Tian, S. Datta, J. I. Henderson and C. P. Kubiak, submitted to Phys. Rev. B.

Figure Captions

Figure 1:   Substrate developed for the electrical characterization and imaging of cluster arrays (CCN).

Figure 2:   Illustration of the self-assembly of cluster arrays on the free-standing SiO_2 film from a colloidal suspension containing DDT encapsulated clusters

Figure 3:   Structure of the linking molecule; a) XYL-Dithiol molecule and b) 22ADI molecule.

Figure 4:   Measured room temperature current-voltage characteristics of conduction through cluster array for Sample A. Inset shows structure of linking molecule (22ADI).

Table 1:   Measured low-bias conductances of the samples at various stages of the CCN fabrication. Isolation between pads for bare sample (no clusters) exceeded $10G\Omega$.

Sample	Distance between pads	As Deposited	Linked	Linking Molecule
A	450 nm	1.28×10^{-8} S ($78.1 M\Omega$)	1.13×10^{-7} S ($8.84 M\Omega$)	22ADI
B	500 nm	1.32×10^{-7} S ($7.57 M\Omega$)	8.20×10^{-8} S ($12.1 M\Omega$)	22ADI
C	190 nm	1.72×10^{-7} S ($5.81 M\Omega$)	9.6×10^{-8} S ($10.4 M\Omega$)	22ADI
D	—	6.16×10^{-9} S ($162 M\Omega$)	1.7×10^{-10} S ($5.8 G\Omega$)	XYL-Dithiol

300A Gold Pads
(defined by E-beam
lithography)

2500A
thick
Gold Pad

GaAs Substrate

SiO film

CROSS-SECTIONAL VIEW

TEM - transparent
SiO window

2500A
thick
Gold Pad

TOP VIEW

Drop of colloidal solution containing thiol-coated clusters

Thiol-encapsulated cluster

Contact pad

GaAs Substrate

SiO film

Contraction of Drop due to solvent evaporation

Cluster array formation between contacts after complete evaporation of the solvent

(a)

(b)

Resistance of an Organic Molecule

W. Tian, M. P. Samanta, S. Datta

School of Electrical Engineering, Purdue University
West Lafayette, IN   47907

J.I. Henderson, C.P. Kubiak

Department of Chemistry, Purdue University
West Lafayette, IN   47907

Abstract

This paper presents a theoretical calculation predicting the resistance of a class of organic molecules as measured between two semi-infinite gold contact pads. These organic molecules consist of one or more para-substituted benzene rings with different end-groups designed to bond to the gold pads. Such molecules are potentially useful as interconnectors for nanoscale electronic devices. Our calculations are based on the Landauer formula which relates resistance to the transmission function. To evaluate the transmission, we use a Green's function based method which is well-suited to handle the open boundary conditions associated with the gold contacts. Our approach demonstrates (a) that conduction through these molecules is largely by tunneling, with a resistance in the range of megohms; (b) the resistance is lower with thiol (-S-) end-groups compared to isocyanide (-CN-) end groups; (c) the resistance increases exponentially with the number of benzene rings; and (d) the resistance depends sensitively on the internal coupling between benzene rings.

Introduction

In the last few years there has been significant progress in the preparation and characterization of organic molecules attached to metal surfaces [1-5]. Metallic clusters have also been interconnected using organic molecules, opening up new possibilities for nanoelectronic devices [6]. Recent advances have made it possible to probe the resistance of individual molecules using scanning tunneling microscopes [4,7]. However, the factors that control the electronic transport in these molecules is not well understood. The natural questions to ask are (a) what is the magnitude of the resistance that one can expect from this class of molecules, (b) how is the resistance affected by the internal structure of the molecule, and (c) what effect do the end groups have on the resistance? This paper attempts to provide answers to these questions through a systematic theoretical study of the resistance of organic molecules consisting of one or more para-substituted benzene rings attached to gold contact pads through thiol (-S-) or isocyanide (-CN-) end groups (see Fig.1 where thiol end group is shown).

Our calculations are based on the Landauer formula which expresses the conductance G in terms of the transmission function T through the molecule from one contact to another at the Fermi energy:

$$G = (2e^2 / h)T \qquad (1)$$

As long as the voltage drop across the molecule is small compared to the HOMO-LUMO gap, this linear conductance formula (eq.(1)) should be adequate. Also, it is not necessary to consider thermal averaging since $k_B T$ is very small compared to the gap even at room temperature. Inelastic processes are neglected in this approach. Neglecting inelastic processes may not be fully justified since the coupling between electronic motion and vibrational modes of the molecule is often quite strong. We leave it to future work to assess the effect of such coupling on the conductance.

The energy levels of the different molecules all have the same generic structure, consisting of a set of occupied levels separated by a gap of 2-3eV from a set of empty levels. Clearly the resistance can be quite low, if the Fermi energy were aligned with one of the energy levels of the molecule. However, it seems fairly certain that under normal circumstances this will never be the case; the Fermi energy will lie in the gap regardless of the nature of the metal or the molecule. This is exactly what one finds with metal semiconductor contacts due to the formation of Metal Induced Gap States (MIGS) [8]. We find a similar effect in our simulations [9], leading us to believe that the conduction through the molecules at low bias will generally involve tunneling through the HOMO-LUMO gap (rather than free propagation through a molecular energy level) leading to resistances of the order of megohms.

The model

There are various ways to evaluate the transmission function T appearing in eq.(1) [10,11]. We use the Green's function approach described in ref.[12], which provides a powerful and versatile technique for handling the open boundary condition associated with the semi-infinite contacts. The basic input needed in the calculation is the Hamiltonian matrix for the system. If a set of orthogonal atomic wave functions is chosen, it can be written as:

$$\begin{bmatrix} H_l & C_l & 0 \\ C_l^+ & H_m & C_r \\ 0 & C_r^+ & H_r \end{bmatrix} \qquad (2)$$

Here H_m is the Hamiltonian for the molecule and C_l, C_r describe the coupling of the molecule to the left and right contacts respectively, while H_l and H_r are the Hamiltonians for the isolated left and right contacts. The transmission function is given by:

$$T = Tr[A_l M A_r M^+] \qquad (3)$$

which can be viewed as a generalized version of the familiar result (from tunneling Hamiltonian theory) that $T \sim \rho_l \rho_r |M|^2$, where ρ_l and ρ_r are the density of states and M is the matrix element. A_l and A_r are the spectral functions (generalized density of states), while M is an effective matrix element. Unlike the tunneling Hamiltonian result, eq.(3) is valid for arbitrary coupling, since M is evaluated taking the coupling into account.

The different quantities appearing in eq.(3) can be evaluated once we have the Hamiltonian in eq.(2). A_l and A_r are the spectral functions for the isolated left contact and the isolated right contact respectively:

$$A_l = i \cdot [g_l - g_l^+] \qquad\qquad g_l = [E \cdot I - H_l + i0^+]^{-1} \qquad (4a)$$

$$A_r = i \cdot [g_r - g_r^+] \qquad\qquad g_r = [E \cdot I - H_r + i0^+]^{-1} \qquad (4b)$$

Additionally M is the effective matrix element connecting the two contacts via the molecular energy levels:

$$M = C_l G_m^R C_r^+ \qquad\qquad G_m^R = [E \cdot I - H_m - C_l^+ g_l C_l - C_r g_r C_r^+]^{-1} \qquad (5a)$$

We are primarily interested in the matrix element at $E = E_f$, which lies in the HOMO-LUMO gap. Since the energy is well separated from any of the molecular energy levels and the coupling is usually weak, eq.(5a) can be approximated as:

$$M \cong C_l [E \cdot I - H_m]^{-1} C_r^+ \qquad (5b)$$

This is particularly convenient for it allows us to evaluate M without reference to H_l and H_r. To calculate the transmission function T (see eq.(3)) we do need the spectral functions for the left and right contacts (A_l and A_r) but these can be calculated once and for all and then re-used with different molecules (13). Additionally, if we are not interested in the absolute conductance and simply wish to compare different molecules (with the same contact material) we can compare their 'M' values.

The basic input in this calculation (see eq.(2)) can be obtained from different approaches and any inherent approximation will be reflected in the calculated results. For example, we use HyperChem [14] to obtain the geometric structure of the molecule and then use the Extended Huckel model [15] to obtain H_m, C_l and C_r. This method is simple,

intuitive and fast at the expense of accuracy. Better accuracy could be achieved with sophisticated *ab initio* programs and might be desirable for accurate calculations once the basic physics has been clearly identified and understood.

The Hamiltonians H_l and H_r describing the isolated left and right contacts are obtained from standard handbooks describing band structure calculations for bulk metals [16]. These matrices are infinitely large since the contacts are semi-infinite regions, so that technically we need to invert infinite matrices to calculate g_l and g_r. This can be accomplished by making use of the periodicity of the crystal, as one does in band structure calculations. Note that we do not need all the components of the infinite matrices g_l and g_r. We only need $g_l(i,j)$ and $g_r(i,j)$, for orbitals 'i' and 'j' in the metal that are coupled to the molecular levels.

An important point to note is that the Extended Huckel method uses nonorthogonal atomic wave functions. As a result three different kinds of Green's functions can be defined, i.e., contravariant, mixed and covariant [17]. These Green's functions are not independent but related to each other through the representations of unity. We use the covariant representation of the Hamiltonian so that the identity operator appearing in eqs.(4) and (5) should be interpreted as the overlap matrix S, where $S_{ij} = \langle i|j \rangle$. Also the coupling matrices C appearing in eqs.(5a,b) should be replaced by (ES-C).

Xylyl dithiol

We have used the above approach to compute the resistance of xylyl-dithiol connected between the (111) surfaces of two gold pads (Fig.1). This molecule has 8 hydrogen, 8 carbon and 2 sulfur atoms. We use hydrogen 1s, carbon 2s2p and sulfur 3s3p3d (total $8 \times 1 + 8 \times 4 + 2 \times 9 = 58$) nonorthogonal wave functions to describe the molecule, and 5d6s6p nonorthogonal orbitals for each gold atom. We calculate a resistance of about 4.3 MΩ, in reasonable agreement with the reported experimental value of 4 MΩ[4].
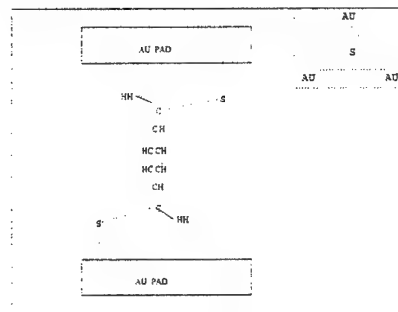
Fig.1: Chemical structure of xylyl-dithiol connecting two gold substrates. Inset shows the position of the sulfur atom with respect to gold atoms at (111) surface.

Factors affecting the resistance

To gain some insight into the different factors affecting the resistance of a molecule, it is convenient to write the matrix element M in eq.(5) as:

$$M = M_l \, g_m^R \, M_r \qquad (6)$$

where g_m^R is Green's function for the molecule *without the end groups*. M_l and M_r are the effective coupling between the molecule and the left and right pads respectively. This coupling is mediated by the end group (-S- or -CN-) and is thus different for different end groups. The advantage of this viewpoint is that it allows us to separate the effect of the end

groups (M_l and M_r) from the effect of the molecule (g_m^R). We will now use this viewpoint to compare different molecules and different end groups.

Role of end groups

One interesting question in molecular conduction is the role of the end groups (like -S- or -CN-). To understand this problem we studied two molecules with exactly same structure but different end groups. To be specific we considered (1) a benzene ring with two sulfur atoms at each end replacing two hydrogen atoms, and, (2) a benzene ring with 'CN' end groups replacing the hydrogen atoms. Which will conduct better ?

One should be able to answer this question simply by looking at the corresponding M (M_l or M_r), since g_m^R is the same for both. However, M is a matrix, and has too much information. It would be convenient to have a single number to quantify the coupling strength of each end group. The problem is simplified by concentrating on the most important terms, namely the gold 6s orbital and the carbon $2p_z$ orbital (in the molecule) which have the biggest contribution at energies around E_f. The effective coupling M between these orbitals is a single number which can be written as:

$$M = \sum_i \frac{C_{gi}C_{im}}{E_f - \varepsilon_i}$$

(7)

where ε_i represents the energy of the ith energy level of the end-group, and C_{gi} and C_{im} represent its coupling to the gold (s orbital) and the molecule (carbon p_x orbital) respectively. Figs.2 a and b show M vs. Fermi energy for the two end
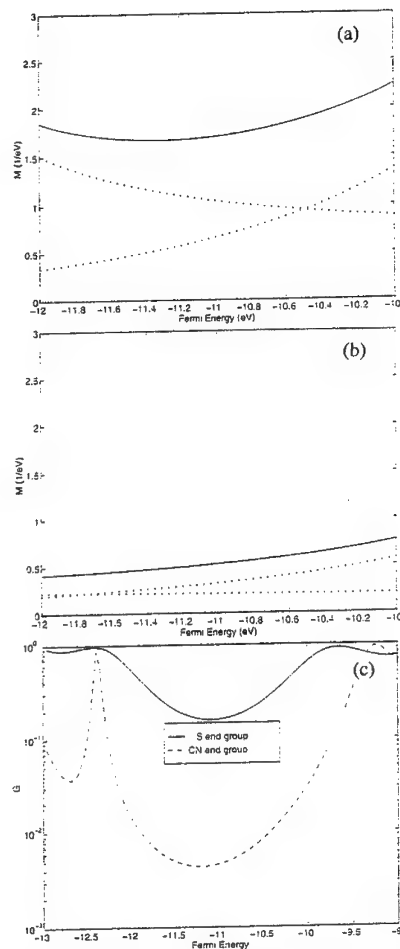
Fig.2: (a). M matrix element for 'S' from gold s orbital though sulfur to carbon p_z orbital. Dotted lines show contributions from the sulfur p_z and d_{z^2} orbitals. Other orbitals have negligible contribution. Solid line shows the total contribution. (b). Same as (a) for 'CN' group where two main contributions come from linear combination of carbon and nitrogen p_z states. (c). Conductance (in units of $2e^2/h$) vs. Fermi energy for two molecules differing only in their end groups.

groups -S- and -CN-. The former clearly provides larger coupling, and should lead to larger conductance. An exact calculation confirms this expectation (Fig.2c).

Eq.(7) also allows us to separate out the contribution of different energy levels to the coupling as shown in Figs.2a and 2b. For the end group, -S-, we find that the main contribution comes from the p_z and d_{z^2} states having energies at -13.3 and -8.0 eV respectively. The contribution from the other levels is negligible. For the end group, -CN-, the main contribution comes from two states at -12.2 and -7.9 eV, which represent linear combinations of p_z states in carbon and nitrogen.

Effect of successive benzene rings in series

Next we compare molecules with identical end-groups, but with differing numbers of benzene rings in between. It is readily shown that the Green's function across two benzene rings in series is given by:

$$g_m^R = g_b^R C_b g_b^R + g_b^R C_b g_b^R C_b^+ g_b^R C_b g_b^R + g_b^R C_b g_b^R C_b^+ g_b^R C_b g_b^R C_b^+ g_b^R C_b g_b^R + \ldots\ldots$$

$$\cong \quad g_b^R C_b g_b^R \tag{8}$$

where g_b^R is the Green's function across a single benzene ring, and C_b is the coupling matrix between the two rings. Since most of the contribution comes from carbon p_z orbital we can treat these quantities as pure numbers instead of matrices, so that the Green's function (and hence the effective matrix element) is proportional to the coupling c_b between the p_z orbitals in successive benzene rings. The conductance being proportional to the square of the matrix element changes as $|c_b|^2$.

Organic molecules are typically not very rigid. The molecule is constantly vibrating and rotating. For the molecule discussed above, the rotation is most likely to occur in the
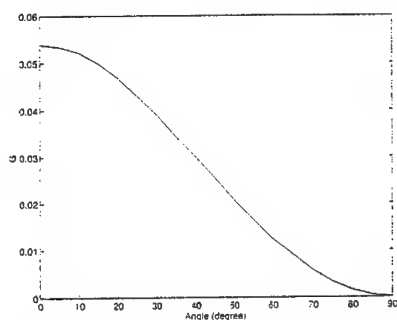
Fig.3: Conductance (in units of $2e^2/h$) of a long molecule as a function of the misalignment angle θ between successive benzene rings.
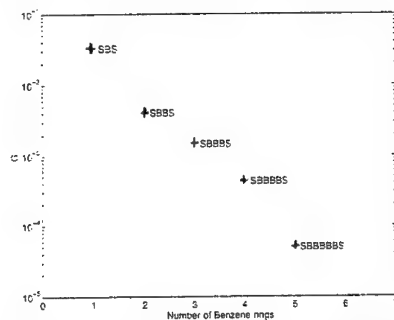
Fig.4: Conductance (in units of $2e^2/h$) of molecules with different number of benzene rings. Conductance goes down exponentially with increasing number of benzene rings.

region between two benzene rings so that successive benzene planes have an angle θ between them. Since c_b is proportional to the overlap integral which changes as $\cos(\theta)$, the conductance will be proportional to $\cos^2(\theta)$. This is confirmed by a direct numerical simulation (see Fig.3). We would expect the measured conductance to represent an appropriate statistical average over configurations with different values of θ. Additional effects could arise due to inelastic scattering by the molecular vibration which we are neglecting.

In general for a chain of weakly coupled rings (whose Green's functions are g_1^R, g_2^R, etc.) we can write approximately:

$$g_b^R \approx g_b^R\, C_b\, g_b^R\, C_b\, \bullet\bullet\bullet\bullet\bullet\bullet\bullet\bullet\, g_b^R\, C_b\, g_b^R$$

For benzene rings we can consider only p_z orbitals and treat the different elements as pure numbers. This means that the conductance should decrease exponentially with the number of rings. Numerical results for 1,2,3,4,5 benzene rings with two sulfur atoms at each end is consistent with this expectation (see Fig.4).

Summary

To summarize, we present theoretical calculations predicting the resistance of a class of organic molecules as measured between two semi-infinite gold contact pads. These molecules are potentially useful as interconnectors for nanoscale electronic devices. Our approach shows: (a) that the conduction through molecules generally involves tunneling and the resistance is of the order of megohms; (b) the resistance is lower when thiols (-S-) are used rather than isocyanides (-CN-) as end groups to attach the molecule to the gold; (c) the resistance increases exponentially with the number of benzene rings; and (d) the resistance depends sensitively on the internal coupling between benzene rings. This theoretical study should aid experimentalists in choosing molecules with appropriate resistance and could stimulate new experimental work in this direction.

References

1. R.F.Service, Science, **265**, 316, (1994).
2. J.Guay, A.Diaz, R.Wu, J.M.Tour, J. Am. Chem. Soc.,**115**, 1869, (1993).
3. J.I.Henderson, S.Feng, G.M.Ferrence, T.Bein, C.P.Kubiak, Inorg. Chem. Acta, submitted for publication.

4. M.Dorogi, J. Gomez, R.G.Osifchin, R.P.Andres, R.Reifenberger, Phys. Rev. B. (1995), in press.
5. R.P. Andres, et al, Science, (1995), submitted for publication.
6. D.B.Janes, V.R. Kolagunta, R.Osifchin, J.D.Bielfeld, R.P.Andres, J.I. Henderson, C.P. Kubiak, Superlattices and Microstructures, accepted for publication.
7. C.Joachim, J.K.Gimzewski, R.R.Schlittler, C.Chavy, Phys. Rev. Lett., **74**, 2102, (1995).
8. W. Monch, Rep. Prog. Phys. **53**, 221, (1990).
9. W. Tian, M.P. Samanta, S. Datta, unpublished.
10. C.Joachim and P.Sautet, in *Scanning Tunneling Microscopy and Related Methods* (Kluwer Academic, Dordrecht, 1990).
11. V.Mujica, M.Kemp, M.A.Ratner, J. Chem. Phys., **101**, 6849, (1994).
12. S.Datta, *Electronic Transport in Mesoscopic Systems* (Cambridge University Press, Cambridge, 1995).
13. M.P. Samanta, MSEE thesis, Purdue University, 1995.
14. HyperChem™ Release 3 for Windows, Molecule Modeling System: Hypercube, Inc. and Autodesk, Inc.
15. R. Hoffman, J. Chem. Phys., **39**,1937,(1963).
16. D.A. Papaconstantopoulos, *Handbook of the Band Structure of Elemental Solids* (Plenum Press, New York, 1986).
17. D. Lohez and M. Lannoo, Phys. Rev., **B27**, 5007, (1983).

Quantum Wires and Dots

InAs/GaAs Quantum Dots:
Single Sheets, Stacked Dots and Vertically Coupled Dots

M. Grundmann*, N.N. Ledentsov§, R. Heitz and D. Bimberg
Institut für Festkörperphysik, Technische Universität Berlin
Hardenbergstraße 36, D-10623 Berlin, Germany

S.S. Ruvimov§, A.O. Kosogov§, P. Werner and U. Gösele
Max-Planck-Institut für Mikrostrukturphysik
Weinberg 2, D-06120 Halle, Germany

V.M. Ustinov, M. Maximov, P.S. Kop'ev and Zh.I. Alferov
A.F. Ioffe Physical-Technical Institute
Politekhnicheskaya 26, 194021 St. Petersburg, Russia

Abstract

InAs/GaAs quantum dots (QD's) have been grown with molecular beam epitaxy in a variety of assemblies. Single sheets of ordered arrays of dots are fabricated with single InAs layers. Vertically stacked dots, forming a tetragonal lattice of InAs islands are created by deposition of multiple InAs layers, separated by thick GaAs layers (typically 10nm). The vertical arrangement of dots is driven by the extended strain field of the underlying dots. Vertically electronically coupled QD's develop when thin (1.5nm) GaAs spacer layers are grown. The electronic structure of the various island geometries is determined with luminescence techniques and found to agree with theoretical calculations.

I. Structural Properties

InAs/GaAs quantum dots (QD's) have been grown using molecular beam epitaxy in the coherent island Stranski-Krastanow growth mode. Under optimized growth conditions, regarding arsenic pressure and substrate temperature, pyramidal quantum dots with square bases along <100> develop on a thin wetting layer [1-4]. Their size (typically 12nm base length and {101} or {203} facets) is independent of the amount of material deposited for 1.6 to 4 mono-layers (ML's) of InAs, if for small deposition thickness growth interruption is employed (Fig.1). High density (10^{11} dots/cm^2) arrays of dots exhibit alignment of dots along the two <100> interface directions [2] due to the repulsive island-island interaction. The anisotropic elastic properties of the III-V compounds involved make the square 2D lattice energetically more favorable than other arrangements, like e.g. hexagonal.

Multiple deposition of InAs layers with relatively thick GaAs spacer layers (typically 10nm) results in vertical alignment of dots in different layers as has been reported already in [5] and more recently in [6,7]. This is due to the extension of the strain field of the underlying dots. A simulation of the strain field at the surface shows an expansion of the surface unit cell above the dot and a contraction in between dots, thus making the nucleation of islands on top of already present ones more favorable [8]. For sufficient separation (10nm or larger) of the sheets of islands the electronic coupling is negligible. The basic properties of the individual dots is thus not altered. We note that for laser application
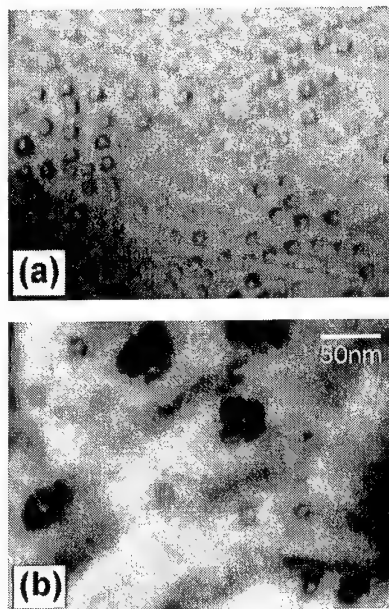
Fig.1: Plan view TEM images of (a) 4ML InAs on GaAs and (b) 2ML InAs on GaAs deposited with 100s growth interruption.

the gain is enhanced due to the increase of the confinement factor. If the threshold is given by the

inversion condition, it is also increased accordingly due to the larger number of states to be filled.
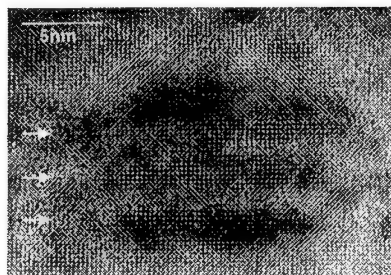
Fig.2: (100) cross section HREM of triple InAs/GaAs stacked dots, resulting from 3x (0.5nm InAs - 1.5nm GaAs) deposition. Markers denote position of InAs parts.
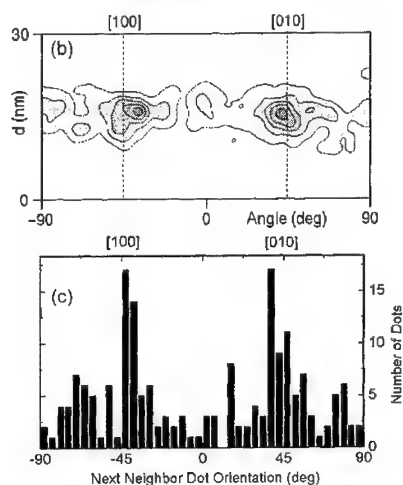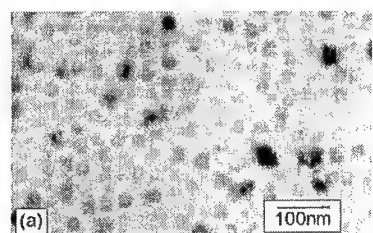
Fig.3: (a) Plan view TEM image of VECOD structure, (b) and (c) histograms of two next neighbor dot distribution.

In order to modify the properties of the QD's themselves (towards larger localization and higher

oscillator strength) we fabricated vertically coupled quantum dots (VECOD's) by alternating *short-period* InAs-GaAs deposition, resulting in vertical splitting of pyramids (Fig.2).

The formation mechanism of such structures [9] results from a gain in strain energy by transfering InAs from the burried part of the pyramid to the uncovered part. This *island shape transformation* effect has to be strictly distinguished from the formation of uncoupled multiple sheet structures. We note that the VECOD's exhibit lateral ordering similar to single sheets of QD's [2]. Fig.3 shows a plan view TEM and $N(d,\theta)$ and $N(\theta)$ histograms of the next neighbor dot arrangement with clear maxima in the <100> interface directions (square 2D Bravais lattice).

II. Electronic Structure

A numerical calculation of the strain distribution within the pyramid, the wetting layer and in the surrounding barrier is performed [10]. The hydrostatic part of the strain is confined to the dot. The anisotropic strain is partly transferred into the barrier, and has a minimum within the dot. The strain induces a strong modification of the confinement potentials. Additionally the piezoelectric charges on the {112}-like edges of the pyramid, resulting in the piezoelectric potential, have to be taken into account. In the realistic three-dimensional potentials we solve the effective mass Schrödinger equation with locally varying anisotropic mass. Level energies and wavefunctions of quantized states are obtained as a function of QD size [10].

The inclusion of the piezoelectric effect leads to an *intrinsic* lifting of the degeneracy of the in-plane excited (p-like) states [10], which could potentially be revealed by polarization dependent measurements of inter-subband transitions. The polarization anisotropy should be in the [110] and [1-10] directions for the piezoelectric effect. The level splitting could be also explained by a non-symmetric in-plane shape of the dots. A distinction between those two effects could be made by measuring the polarization dependence of the level splitting for electron and holes for the same dots. The geometric effect would yield the *same* polarization dependence for electrons and holes, while the piezoelectric effect should be rotated by 90° for electrons and holes (Fig.4).

For single pyramids in the 12nm range we predict that only the electron ground state is confined for the QD sizes present, while several hole states are localized. The separation between hole ground and excited state is quite large (about 80meV). Since we are in the strong confinement regime, the exciton binding energy can be calculated in first order perturbation theory, and is more than one order of magnitude larger than the binding energy in InAs bulk material [10].

Absorption and photoluminescence (PL) of the ground state are in resonance [11]. High and low area density dot samples (Fig.1a and b) exibit dot luminescence at 1.1eV. Higher transitions are revealed in absorption. In PL excited levels appear at higher excitation density (larger than about 100W/cm^2 for the sample of Fig.1a), when the average carrier number per QD is larger than 2 e-h-pairs (i.e. the ground state is filled). The higher transitions are due to transitions of ground state electrons with excited holes of which some states have large overlap with the electrons (contrary to the case of a box-like QD) [12]. On the other hand, the complete lack of other recombination channels than the QD's ground state up to moderately high excitation densities proves very efficient carrier capture into the QD's and energy relaxation there. The wetting layer at typically 1.4eV is found in absorption, PL excitation (PLE) spectra and PL at very high excitation densities.

PL excitation spectra of single sheets of dots are dominated by ~10meV broad resonances, centered at multiples of the InAs QD LO phonon energy. The experimental phonon energy is in agreement with the theoretical value obtained from the strain induced shift [10]. The phonon bottleneck problem is passed by with multi-phonon emission. In selectively excited luminescence QD, GaAs barrier, wetting layer and interface optical phonon modes are identified, together with acoustic phonons [13].

The ground state luminescence of the VECOD's is found at 1.17eV. We predict hole levels with a separation of less than one LO phonon energy (around 30meV) from the hole ground state. Accordingly we observe additional structure at small excess energy (20 meV) in PLE spectra (Fig.5), never seen for single pyramids where the first excited hole level has a much larger separation from the ground state than E_{LO}.

Piezoelectricity

Shape Anisotropy
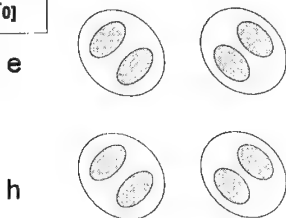
Fig.4: p-like states in a quantum dot (schematic wavefucntions). Lifting of degeneracy due to piezoelectric charges and shape anisotropy. "e" and "h" denote wavefunctions for electrons and holes. "lower" and "upper" denote the levels with the lower and higher energy, respectively.
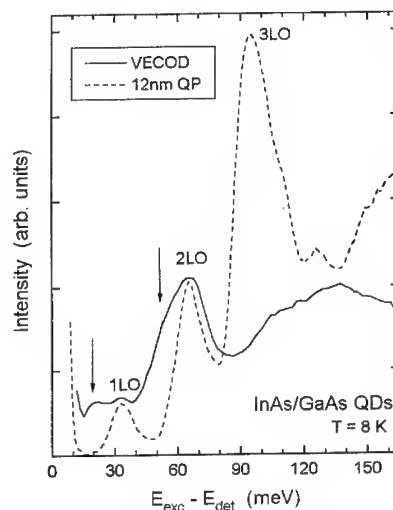
Fig.5: PLE spectra of InAs pyramids (Fig.1a) and VECOD's of Fig.2, detected at PL maximum of 1.1eV and 1.17eV, respectively. Arrows denote response due to low lying hole levels in VECOD's.

Conclusion

Ordered InAs/GaAs quantum dot arrays of different geometry have been fabricated using different deposition schemes in molecular beam epitaxy. Vertical electronic coupling of quantum dots leads to a modification of the basic electronic structure of the QD's in agreement with theoretical simulations.

References

* e-mail: mariusgr@w422zrz.physik.tu-berlin.de
  WWW: http://sol.physik.tu-berlin.de/
§ on leave from A.F. Ioffe Institute, St. Petersburg

[1] N. N. Ledentsov, M. Grundmann, N. Kirstaedter, J. Christen, R. Heitz, J. Böhrer, F. Heinrichsdorff, D. Bimberg, S. S. Ruvimov, P. Werner, U. Richter, U. Gösele, J. Heydenreich, V. M. Ustinov, A. Yu. Egorov, M. V. Maximov, P. S. Kop'ev, Zh. I. Alferov, Proc. 22nd Int. Conf. Phys. Semic. (Vancouver, Canada), D.J. Lockwood, ed., (World Scientific, Singapore, 1995) Vol. 3, 1855

[2] M. Grundmann, N.N. Ledentsov, J.Christen, J. Böhrer, D. Bimberg, S.S. Ruvimov, P. Werner, U. Richter, U. Gösele, J. Heydenreich, V.M. Ustinov, A.Yu. Egorov, A.E. Zhukov, P.S. Kop'ev, Zh.I. Alferov, phys. stat. sol. (b) 188, 249 (1995)

[3] S. Ruvimov, P. Werner, K.Scheerschmidt, J. Heydenreich, U. Richter, N.N. Ledentsov, M. Grundmann, D. Bimberg, V.M. Ustinov, A.Yu. Egorov, P.S. Kop'ev, Zh.I. Alferov, Phys. Rev. B 51, 14766 (1995)

[4] S. Ruvimov, K. Scheerschmidt, phys. stat. sol. (a) 150, 471 (1995)

[5] L. Goldstein, F. Glas, J.Y. Marzin, M.N. Charasse, G. Le Roux, Appl. Phys. Lett. 47, 1099 (1985)

[6] Q. Xie, A. Madhukar, P. Chen, N.P. Kobayashi, Phys. Rev. Lett. 75, 2542 (1995)

[7] Y. Sugiyama, Y. Nakata, K. Imamura, S. Muto, N. Yokoyama, Ext. Abstr. ssdm 1995, Osaka, p. 773

[8] M. Grundmann, R. Heitz, N. Ledentsov, O. Stier, D. Bimberg, V.M. Ustinov, P.S. Kop'ev, Zh.I. Alferov, S.S. Ruvimov, P. Werner, U. Gösele, J. Heydenreich, Superlattices and Microstructures (1995), *in print*

[9] N.N. Ledentsov, V.A. Shchukin, M. Grundmann, N. Kirstaedter, J. Böhrer, O. Schmidt, D. Bimberg, V.M. Ustinov, A.Yu. Egorov, A.E. Zhukov, P.S. Kop'ev, Zh.I. Alferov, A.I. Borovkov, A.O. Kosogov, S.S. Ruvimov, P. Werner, U. Gösele, J. Heydenreich, unpublished

[10] M. Grundmann, O. Stier, D. Bimberg, Phys. Rev. B 52, 11969 (1995)

[11] M. Grundmann, J. Christen, N.N. Ledentsov, J. Böhrer, D. Bimberg, S.S. Ruvimov, P. Werner, U. Richter, U. Gösele, J. Heydenreich, V.M. Ustinov, A.Yu. Egorov, A.E. Zhukov, P.S. Kop'ev, Zh.I. Alferov, Phys. Rev. Lett. 74, 4043 (1995)

[12] M. Grundmann, N.N. Ledentsov, O. Stier, D. Bimberg, V.M. Ustinov, P.S. Kop'ev, Zh.I. Alferov, Appl. Phys. Lett. 68, 979 (1996)

[13] R. Heitz, M. Grundmann, N.N. Ledentsov, L. Eckey, M. Veit, D. Bimberg, V.M. Ustinov, A.Yu. Egorov, A.E. Zhukov, P.S. Kop'ev, Zh.I. Alferov, Appl. Phys. Lett. 68, 361 (1996)

ELECTRON SCATTERING AND EDGE-STATE COUPLING IN MAGNETOTRANSPORT IN TWO-DIMENSIONAL ELECTRON GAS SYSTEMS

Yeong-Ah Soh and Harold G. Craighead
Applied and Engineering Physics
Cornell University, Ithaca, NY 14853
Frank M. Zimmerman and Jeevak M. Parpia
Department of Physics, Cornell University, Ithaca, NY 14853

ABSTRACT

We report on magnetotransport measurements in two-dimensional electron gas (2DEG) systems. By using a tunable 130 nm central gate that acts as an artificial scatterer in a 2DEG channel and measuring the two-terminal conductance through the channel, we studied the evolution of the edge states as a function of the potential strength of the artificial scatterer. The results indicate strong coupling between edge states of different Landau levels. In another set of measurements, we measured the two-terminal conductance of a 2DEG Hall bar. We observed strong Shubnikov-de Hass oscillations, which we attribute to backscattering in the highest occupied Landau level when it is partially filled, combined with strong interlevel coupling.

Adiabatic transport through edge states which form at high magnetic fields has been used to explain the quantum Hall effect [1]. Scattering and coupling of these edge states by random potential fluctuations (due to defects and inhomogeneities) can cause the breakdown of the quantum Hall effect [1]. Studying the influence of scattering and edge-state coupling can shed new light on transport in the quantum Hall regime.

We report on magnetotransport in two-dimensional electron gas (2DEG) systems. We fabricated a submicrometer-wide constriction defined by split gates (0.4 μm apart and $0.6\mu m$ long), with a tunable central gate (130 nm diamter) in the middle of the constriction [2]. The split gates were biased negatively to modulate the density of the underlying electron gas. The central gate acted as an artificial scatterer whose strength was varied independently of the split gate bias. Two-terminal magnetoconductance measurements through the channel were performed at 0.3 Kelvin with a magnetic field of 3 Tesla perpendicualr to the 2 DEG.

Conductance was measured as a function of split gate voltage, with various central gate bias voltages. By sweeping the split gate voltage, we depleted the landau levels one by one. With the central gate voltage held at zero., we observed two plateaus in the conductance, near $2e^2/h$ and $4e^2/h$ (Fig.1). (The spin splitting is not resolved in our system). This behavior changes drastically as the negative bias of the central gate is increased. The two plateaus disappear and a new plateau forms at $G \approx 2.6e^2/h$ (Fig. 1).

We attribute this new step to the formation of an edge state of the first Landau level (LL) which loops around the central gate potential bump. The edge state of the second Landau level couples to this loop state, which in turns couples to the second Landau level on the other side of the central gate (Fig. 2). In this way, the second Landau level contributes to the conductance by a forward scattering mechanism through the loop state. Since both the sample-edge channel (first Landau level) and the forward scattering channel (second LL + first LL loop state) involve conduction through the first Landau level, the conductance goes to zero in a single step as the first Landau level is pinched off with increasing split gate bias.

The above model predicts a plateau at a conductance value

$$G = (1 + \frac{|t|^2}{2 - |t|^2})\frac{2e^2}{h} \qquad (1)$$

where $|t|^2$ is the probability of an electron scattering from the second LL edge state into the loop state and vice versa. From the measured conductance at the plateau $G \approx 2.6e^2/h$, we conclude that $|t|^2 \approx 0.5$. The value $t^2 = 0.5$ corresponds to strong coupling limit, in which an electron makes many transitions back and forth between the two coupled states, and thus emerges from the coupling region with equal probability in either state. This means that the current caryying edge states

equilibrate remarkably efficiently in a very short coupling region (a few hundred nanometers in length).

In another set of measurements, we measured the two-terminal and four-terminal magnetoconductances of a 2DEG Hall bar at 0.3 Kelvin while ramping the magnetic field perpendicular to the 2DEG. We observed strong Shubnikov-de Hass oscillations of the two-terminal measurements coincide with the locations of the quantum Hall plateaus in the four-terminal Hall conductance measurements (Fig.3).

We attribute the strong oscillations to backscattering (edge to edge coupling) in the highest occupied Landau level when it is partially filled, combined with interlevel edge-state coupling. When the magnetic field is at a value where N Landau levels are completely filled, backscattering of the edge states is suppressed and the two-terminal conductance is given by the Landauer formula for N one-dimensional channels (in the absence of backscattering) [1]:

$$G = N\frac{2e^2}{h} \tag{2}$$

As the magnetic field decreases, the degeneracy of the landau levels decreases and a new Landau level stars to be populated. The partially occupied Landau level couples the edge states at opposite edges of the channel through bulk states at the Fermi level. This model predicts a decrease in the two-terminal conductance as a new level starts to be populated, and a recovery to a quantized value (with N replaced by N+1) as the new Landau level is filled. The observed behavior follows this sequence exactly.

In conclusion, we have observed significant coupling between different Landau levels, in both forward and backward scattering mechanisms. In the forward and backward scattering mechanism, we were able to measure the coupling strength between edge states of adjacent Landau levels.

REFERENCES

1. M. Büttiker, Phys. Rev. B 38, 9375 (1988).

2. Y. Soh, G. L. Snider, M. J. Rooks, H. G. Craighead, and J. Parpia, J. Vac. Sci. Technol. B 12, 1372 (1994).
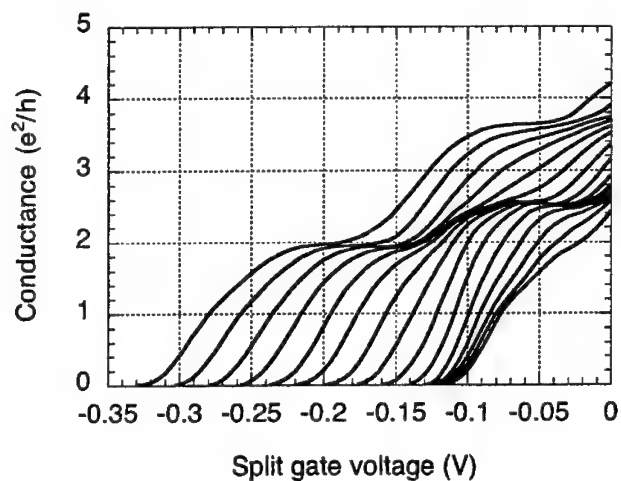
Figure 1: Conductance vs split gate voltage at various central gate biases ranging from)V (lefmost curve) to -0.7V (rightmost curve). The magnetic field was 3 Teslas.
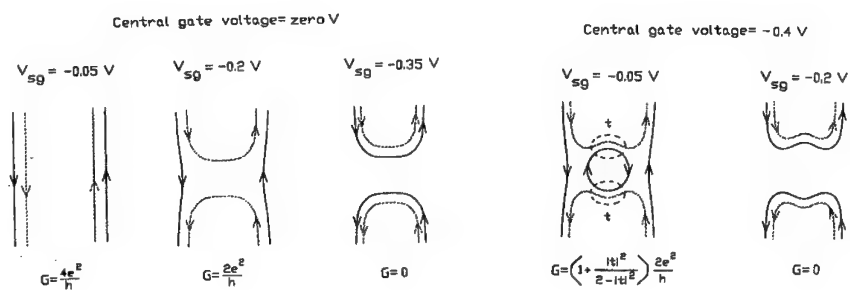
Figure 2: Schematic diagram of the conducting edge-state channels at the indicated split gate (V_{sg}) and central gate biases. The dark and shaded lines represent the edge states of the first and second Landau levels, respectively.
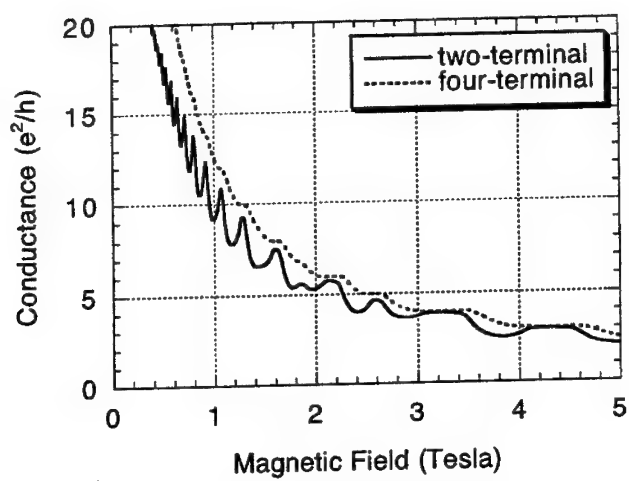
Figure 3: Two-terminal and four-terminal magnetoconductance measurements of a 2 DEG Hall bar.

MAGNETO-RAMAN SCATTERING FROM ELECTRONIC EXCITATIONS IN DEEP-ETCHED QUANTUM DOTS

D.J. Lockwood and P. Hawrylak
National Research Council, Ottawa, Canada
A. Pinczuk and B.S. Dennis
AT&T Bell Laboratories, Murray Hill, NJ, USA
P.D. Wang, C.M. Sotomayor Torres, Y.P. Song and M.C. Holland
Glasgow University, Glasgow, UK

An experimental and theoretical investigation of resonant inelastic light scattering from electronic excitations in quantum dots in an applied magnetic field has been carried out. Experimental results for 100, 150 and 200 nm samples in fields up to 12 T show a complex behavior, with Raman lines exhibiting level splitting, crossing, and anticrossing and even mode softening. Hartree calculations including correlation effects predict such magnetic field induced changes.

INTRODUCTION

Resonant inelastic light scattering has proved to be a valuable characterization technique for studying electronic excitations in semiconductor heterostructures of low dimensionality (1). Such studies can probe the energy and wave vector dispersion of collective and single particle excitations (SPEs) at low energies. A number of investigations of one-dimensional electron systems have been undertaken including measurements of intrasubband and intersubband excitations in GaAs quantum wires where only a few subbands are occupied (2–5) and the anisotropic wave vector dispersion of confined plasmons and SPEs in GaAs wires with many occupied subbands (6,7). Only very recently, has electronic Raman scattering from such excitations in zero-dimensional electron systems been observed (7,8). Nearly all of this inelastic light scattering work has been carried out on shallow etched single-quantum-well GaAs wires and dots. It is now possible to observe these electronic excitations in *deep-etched* GaAs wires and dots (8). Here we report the first Raman measurements of the magnetic field dependence of such excitations in dots.

EXPERIMENT

The modulation-doped MQW heterostructure was grown by solid source molecular beam epitaxy (MBE) on (001) semi-insulating GaAs. The active region was 580 nm thick and consisted of the following layers repeated 10 times: a 30 nm $Al_{0.3}Ga_{0.7}As$ layer, a δ-doped layer, 20 nm of a GaAs(0.85 nm)/AlAs(0.85 nm) superlattice structure, and a 8 nm GaAs quantum well region. Shubnikov-de Haas measurements at 4 K indicated a two-

dimensional electron carrier concentration of 8.5×10^{11} cm^{-2} and a mobility of 2.85×10^4 cm^2/V.s. Patterns were defined by electron beam lithography using a standard double layer PMMA resist. After the development of the resist, a 30 nm layer of NiCr was deposited before the lift-off and subsequently used as an etching mask. For pattern transfer, a low-damage anisotropic reactive-ion-etching process has been developed using SiCl$_4$ (9).

Raman measurements were carried out in a backscattering geometry under excitation at near-resonance conditions.

RESULTS AND DISCUSSION

Raman results for 100 nm dots in zero field are shown in Fig. 1 and they showed no strong polarization properties. Sharp resonance profiles were obtained. For example, for the peak near 8 meV in Fig. 1, the line intensity reached a maximum at an excitation energy of 1.635 eV (compared with the PL maximum of 1.588 eV) and with a symmetric resonance profile full-width at half-maximum of only 17 meV. Similar results were obtained for other dot samples. The intersubband excitations show a systematic shift to higher energy with decreasing dot diameter in the range 100–200 nm consistent with the increasing lateral confinement.

Three dot samples were investigated in magnetic fields up to 12 T. A rich spectrum of excitations was revealed, particularly for a 150 nm sample, as can be seen in Fig. 2. In general, most excitations show a weak field dependence with increasing field until a critical field is reached (e.g., 5 T in the 200 nm dot sample) when a sharp change to a steep linear increase (~ 2 meV/T) regime occurs. Other excitations exhibit level splitting, crossing and anti-crossing and mode softening with increasing magnetic field (see Fig. 3). These phenomena are a consequence of many body effects in the zero-dimensional electron gas.

Calculations for small numbers of correlated electrons in dots (10) predict the appearance of such soft modes as signatures of magnetic field induced phase transitions. The results of similar Hartree calculations for many electron dots (11) are shown in Fig. 2. The theoretical SPE spectrum is quite consistent with the experimental spectrum at low magnetic fields (up to 5 T). The SPE spectrum reflects the formation of electronic shells within the quantum dots and exhibits a complex evolution with magnetic field, including the appearance of a low energy excitation due to a Landau-like band crossing the Fermi level with increasing magnetic field (see the 5 T spectrum in Fig. 2).

CONCLUSION

Raman measurements at large in-plane wave vector transfer have revealed a multicomponent excitation spectrum of many-electron quantum dots. The observed single particle excitations exhibit a shell-like structure. The complex spectral behavior found at low magnetic fields is consistent with that predicted by Hartree model calculations.

REFERENCES

1. A. Pinczuk and G. Abstreiter, in *Light Scattering in Solids V*, edited by M. Cardona and G. Güntherodt (Springer-Verlag, Berlin, 1989), p. 5.
2. J.S. Weiner et al., Phys. Rev. Lett. **63**, 1641 (1989).
3. A.R. Goñi et al., Phys. Rev. Lett. **67**, 3298 (1991).
4. A. Schmeller et al., Sol. State Elec. **37**, 1281 (1994).
5. A. Schmeller et al., Phys. Rev. B **49**, 14778 (1994).
6. T. Egeler et al., Phys. Rev. Lett. **65**, 1804 (1990).
7. R. Strenz et al., Phys. Rev. Lett. **73**, 3022 (1994).
8. P.D. Wang et al., Superlattices & Microstructures **15**, 23 (1994).
9. Y.P. Song et al., J. Vac. Sci. Tech. B **12**, 3388 (1994).
10. P. Hawrylak, Sol. State Comm. **93**, 915 (1995).
11. D.J. Lockwood, P. Hawrylak, P.D. Wang, C.M. Sotomayer Torres, A. Pinczuk, and B.S. Dennis, to be published.
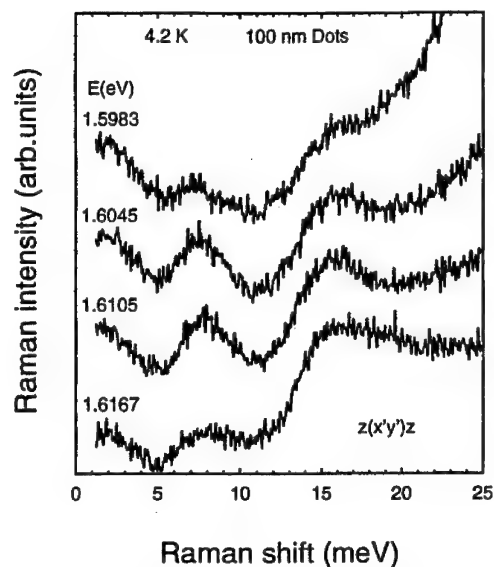
Fig. 1. Depolarized Raman spectrum of 100 nm dots at 4.2 K excited with different energies E.
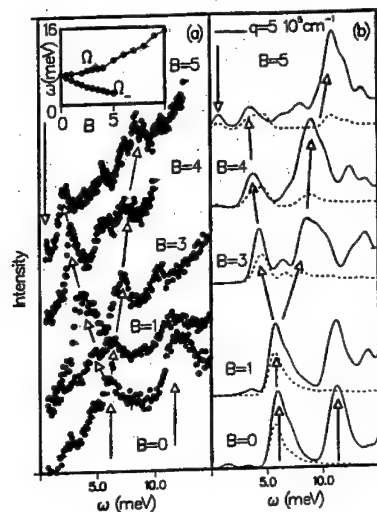
Fig. 2. Magnetic field dependence of the measured (a) and calculated (b) 2 K Raman spectra of 150 nm quantum dots. The inset shows the field dependence of two main transitions and the arrows mark related peaks in experiment and theory for each magnetic field.
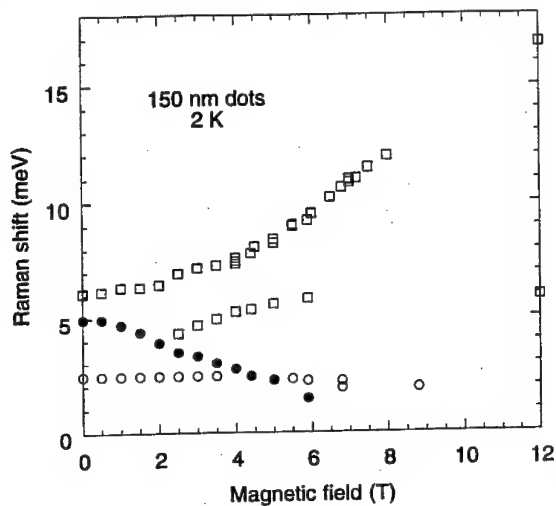
Fig. 3. Magnetic field dependence of lower-energy single particle excitations in 150 nm dots at 2 K.

ELECTRONIC AND NONLINEAR OPTICAL PROPERTIES OF EXCITONIC AND BIEXCITONIC STRUCTURES IN RECTANGULAR GaAa/AlGaAs QUANTUM WELL WIRES

Frank L. Madarasz
Optical Science and Engineering Program
and
Center for Applied Optics
University of Alabama in Huntsville
Huntsville, Alabama 35899

Frank Szmulowicz and F. Kenneth Hopkins
Wright Laboratory, Materials Directorate (WL/MLPO)
Wright-Patterson Air Force Base, Dayton, Ohio 45433-7707

Exciton and biexciton binding energies, and wave functions are calculated with a three parameter variational model in an effective mass approximation for a rectangular GaAs quantum well wire surrounded by an AlGaAs cladding. Moreover, the Al interdiffusion into the wire and the finite band offsets between the wire and the cladding have been included. For the range of dimensions studied, the inclusion of the Al interdiffusion had a pronounced affect on the binding energies when compared to those obtained from the infinite barrier model (Frank L. Madarasz, Frank Szmulowicz, F. Kenneth Hopkins and Donald L. Dorsey, Phys. Rev. B49, 13 528 (1994); J. App;. Phys. 75, 639 (1994); Phys. Rev. B51, 4633 (1995)). In particular, for small (symmetric) wire dimensions the binding energies remain finite. And for asymmetric wires all binding energies were markedly lowered. Using the results of the exciton and biexciton calculation, we calculate the third-order nonlinear optical susceptibility as a function of pump-probe frequencies in a small range about the exciton absorption resonance. We restricted our calculation to the optical nonlinearity via the biexciton state arising from the population saturation of the exciton state. We have found, depending upon wire dimensions, broadening parameter(s) size, and the amount of pump detuning, values of the imaginary parts of the susceptibilities to be on the order of -10^{-2} to -10^{-1} esu and a fairly large off-resonance absorption due to biexciton formation.

I. INTRODUCTION

Excitonic properties have been extensively modeled in quantum wells, wires, and dots[1-19]. For the lowest dimensional confinement of a quantum well, it is possible to analytically construct a model which incorporates accurately the physics and the geometry[11,12]: finite barrier potentials and band offsets, barrier penetration, parabolic shaped wells, etc. Rectangular quantum well wires (QWW's), on the other hand, are more difficult. In general, because of the two-dimensional confinement the Hamiltonian is not precisely separable unless the two orthogonal potentials are infinite[1,2,13,14]. Because of this problem, most exciton structure modeling has been done for the ideal case of cylindrical wires with an infinite potential at the circumference of the wire. And, when considering the biexciton binding energy--which is needed for the calculation of $\chi^{(3)}$--an "effective" one-dimensional Coulomb potential in the radial direction was employed[5]; still, $\chi^{(3)}$ was not explicitly calculated. Although, in a subsequent publication[20] Bányai et al., the authors of Ref. 5, extended that work to the calculation of the total absorption coefficient, and total refractive index (both related to the total χ) for various beam intensities in a two-photon absorption model. On the other hand, Glutsch and Bechstedt[1] have approximated the separation of the two-dimensional potential in orthogonal directions in a square wire with the condition that the potential in one direction is infinite while in the other direction is finite. Their interest though, was only in calculating the spatially nonlocal absorption, $\chi^{(1)}$, by single excitons; no attempt was made to determine $\chi^{(3)}$.

However, Madarasz et al.[14-16] have calculated exciton and biexciton binding energies and wave functions in rectangular GaAs wires and have applied the results to the problem of $\chi^{(3)}$ for a pump-probe experiment. The calculation was done variationally utilizing three variational parameters. The Coulomb interaction terms were treated exactly in their full three-dimensional form throughout the calculation, especially in the case of the biexciton, which is a more physically realistic procedure than employed in previous calculations that relied upon an effective one-dimensional potential(s). As a result, if one dimension of the rectangular wire is nonzero, no matter how small, the other may be collapsed to zero without giving rise to an infinite energy. A unique feature of the calculation was its use of a two-dimensional Fourier expansion of the Coulomb potential(s), which removes the numerical difficulty with the 1/r singularity and considerably reduces the computational effort. The results of the excitonic electronic structure computation were then applied to the problem of the third-order nonlinear optical susceptibility. With the goal of determining peak values of susceptibilities for various cross-sectional wire dimensions, $\chi^{(3)}$ was first expanded in the density matrix formalism, and then evaluated for near-resonant exciton absorption in the rotating-wave approximation (RWA)[21]. Values of $|\text{Im } \chi^{(3)}|$ on the order of 10^{-1} esu were obtained.

High quality rectangular QWW's have been most recently manufactured via Al-Ga interdiffusion from the cladding material due to local heating by means of a focused laser[22]. A similar technique is being pursued using focused ion beam technology[23]. In both cases, the potentials in the lateral directions are graded due to the Al interdiffusion. The previous model by Madarasz et al.[14-16] assumes an abrupt infinite potential in the lateral direction. In the present paper we refine/extend that model to include finite graded barrier potentials for the electrons and holes in the lateral direction. In section 2.1, we review the original exciton/biexciton theory making the necessary changes to included the Al interdiffusion. In section 2.2, we display the expression of the third-order optical susceptibility, now including terms beyond the RWA. Results and discussion are given in section 3. And finally, a summary is given in section 4.

2. THEORY

In the present work we build upon the existing infinite potential barrier model of Madarasz et al.[14-16]. The reader is referred to our original papers for the complete and quantitative details of our basic model. Here we will outline the basic theory including the appropriate modifications needed to incorporate the Al interdiffusion into the wire from the surrounding cladding material.

2.1. Excitonic Properties

The interdiffusion is in the lateral direction, here taken as the z-direction. Since the potential in the orthogonal direction is square and we are interested only in the lowest lying states, we may approximate it, relative to the lateral direction, as infinite. The electron and hole potential energies, V_e and V_h, respectively, are defined via the finite conduction, ΔE_c^0, and valence, ΔE_v^0, band offsets are taken to be in the ratio of 60/40. All quantities are graded with the interdiffusion Al composition distribution $x(z)$. Following the work of Madarasz et al.[24] on Cd interdiffusion across HgCdTe heterojunctions, the Al grading distribution will be taken as

$$x(z) = x_0 + x_c + \left[\frac{x_c - x_0}{2}\right]\left\{\text{erf}\left[\frac{z - z_0^+}{C}\right] - \text{erf}\left[\frac{z - z_0^-}{C}\right]\right\} , \qquad [1]$$

where x_0 (here zero) and x_c are the Al compositions in the wire and cladding material, respectively, $z_0^{\pm} = \pm W/2$, and 2C is the Al grading width in which the Al composition changes by 85%.

The Schrödinger equation for the single particle states, in the lateral direction is:

$$-\frac{\hbar^2}{2}\frac{d}{dz}\left\{\frac{1}{m_i^*[x(z)]}\frac{du_i^{(n)}(z)}{dz}\right\}+V_i[x(z)]\,u_i^{(n)}(z)=E_i^{(n)}\,u_i^{(n)}(z)\ ,\qquad [2]$$

$$i=e,h\qquad n=1,2,3....$$

where $E_i^{(n)}$ is the eigen-energy of the nth subband. Eq.(2) must be solved numerically. This we did with a "modified" fourth-order Runge-Kutta routine which accounts for the values of the variable coefficients, $m_i^*[x(z)]$ and $V_i[x(z)]$, between the node points of the integration mesh. Here m_i^* and V_i are written as functions of $x(z)$ to emphasize their implicit dependence on the Al compositional grading; $x(z)$ should not be confused with the coordinate x.

In the envelope function approximation (EFA), the exciton Hamiltonian is given by

$$\hat{H}_{ex}=\frac{p_{ye}^2}{2m_c^*}+\frac{p_{yh}^2}{2m_\perp^*}+\frac{p_x^2}{2\mu}-\frac{e^2}{\varepsilon\sqrt{x^2+\rho^2}}+E_g^o+V_e(z)+V_h(z)\ ,\qquad [3]$$

where m_c^* is the electron conduction-band effective mass, $m_\perp^*$ is the heavy-hole valence band effective mass perpendicular to the axis of the wire, μ is the heavy-hole exciton reduced mass, e is the charge of an electron, ε is the static dielectric constant, E_g^o is the fundamental band-gap of the wire material, and $\rho^2=(y_e-y_h)^2+(z_e-z_h)^2$ is the exciton cylindrical radius in the confined directions.

Even for this relatively simple Hamiltonian no exact solution is possible. The envelope function is then chosen to be a trial wave function in a variational procedure:

$$\psi=\frac{2}{L}g_t(x;\eta_x)\cos(k_yy_e)\cos(k_yy_h)u_e^{(1)}(z_e)u_h^{(1)}(z_h)\ ,\qquad [4]$$

where $g_t(x;\eta_x)$ is a Gaussian-type "orbital" function,

$$g_t(x;\eta_x) = \frac{1}{\sqrt{\eta_x}} \left[\frac{2}{\pi}\right]^{1/4} \exp\left(-x^2 \Big/ \eta_x^2\right) , \qquad [5]$$

in which η_x is the e-h variational parameter and $k_y = \pi/L$.

The variational parameter η_x is determined by minimizing the expectation value of the exciton Hamiltonian with respect to η_x; its value will reflect the dimensions of the wire and specific values of the material parameters used. The only components of the Hamiltonian which depend on η_x are the kinetic energy of relative motion and the e-h interaction term. Together, they define the exciton binding energy[15]:

$$E_{K_\mu}^x = \langle\psi|\frac{p_x^2}{2\mu}|\psi\rangle = \frac{\hbar^2}{2\mu}\frac{1}{\eta_x^2} \qquad [6]$$

and

$$V_{eh} = V\left(\left|xi + \vec{\rho}_e - \vec{\rho}_h\right|\right) = \langle\psi|\frac{(-)e^2}{e\sqrt{x^2+\rho^2}}|\psi\rangle \qquad [7a]$$

$$= (-)\frac{e^2}{2\pi}\frac{1}{\eta_x}\int_0^{2\pi}d\phi \int_0^{+\infty}dQ_{\eta_x}\ I(Q_{\eta_x})\ H_{LW}(Q_{\eta_x},\phi). \qquad [7b]$$

The integrand is given by

$$I(Q_{\eta_x}) = \exp\left(Q_{\eta_x}/2\sqrt{2}\right)^2 \left[1 - \text{erf}\left(Q_{\eta_x}/2\sqrt{2}\right)\right] , \qquad [8]$$

where erf is an error function. The factor $H_{LW} = H_L H_W$, where

$$H_L(Q_{\eta_x}, \phi) = \frac{\pi^4}{\left[\pi^2 - \left(\frac{L}{2\eta_x}Q_{\eta_x}\sin\phi\right)^2\right]^2} \cdot \frac{\sin^2\left(\frac{L}{2\eta_x}Q_{\eta_x}\sin\phi\right)}{\left(\frac{L}{2\eta_x}Q_{\eta_x}\sin\phi\right)^2} \qquad [9a]$$

and

$$H_W(Q_{\eta_x}, \phi) = \int_{-\infty}^{+\infty} dz_e \exp\left(-i\frac{Q_{\eta_x}}{\eta_x}\cos\phi\, z_e\right)\left|u_e^{(1)}(z_e)\right|^2$$

$$X \int_{-\infty}^{+\infty} dz_h \exp\left(-i\frac{Q_{\eta_x}}{\eta_x}\cos\phi\, z_h\right)\left|u_h^{(1)}(z_h)\right|^2 \qquad [9b]$$

The biexciton Hamiltonian is considerably more complicated since it involves the interaction of four particles. The kinetic energy operator is

$$E_K^{xx} = -\frac{\hbar^2}{2\mu}\left[\frac{\partial^2}{\partial x_{1a}^2} + \frac{\partial^2}{\partial x_{2b}^2}\right] - \frac{\hbar^2}{m_\parallel^*}\left[\frac{\partial}{\partial x_{ba}} + \frac{\partial}{\partial x_{1a}} - \frac{\partial}{\partial x_{2b}}\right]\frac{\partial}{\partial x_{ba}}$$

$$-\frac{\hbar^2}{2m_c^*}\left[\frac{\partial^2}{\partial y_1^2} + \frac{\partial^2}{\partial y_2^2}\right] - \frac{\hbar^2}{2m_\perp^*}\left[\frac{\partial^2}{\partial y_a^2} + \frac{\partial^2}{\partial y_b^2}\right]$$

$$-\frac{\hbar^2}{2}\frac{\partial}{\partial z}\left[\frac{1}{m_c^*(z)}\frac{\partial}{\partial z}\right] - \frac{\hbar^2}{2}\frac{\partial}{\partial z}\left[\frac{1}{m_\perp^*(z)}\frac{\partial}{\partial z}\right] \qquad [10]$$

where $m_\parallel^*$ is the effective mass parallel to the wire axis, and the potential energy is

$$V_{xx} = \frac{e^2}{\varepsilon}\left[\frac{(-)1}{\sqrt{x_{1a}^2 + \rho_{1a}^2}} + \frac{(-)1}{\sqrt{x_{2b}^2 + \rho_{2b}^2}} + \frac{(-)1}{\sqrt{x_{2a}^2 + \rho_{2a}^2}}\right.$$

$$+\frac{(-)1}{\sqrt{x_{1b}^2+\rho_{1b}^2}}+\frac{(+)1}{\sqrt{x_{ba}^2+\rho_{ba}^2}}+\frac{(+)1}{\sqrt{x_{21}^2+\rho_{21}^2}}\Bigg] \qquad [11]$$

where 1 and 2 label the electron coordinates, and a and b label the hole coordinates, $x_{\alpha\beta}=x_\alpha-x_\beta$, $\vec{\rho}_{\alpha\beta}=(y_\alpha-y_\beta)\hat{j}+(z_\alpha-z_\beta)\hat{k}$, and $\alpha,\beta=1, 2, a,$ or b.

Since it is not possible to solve a four-body problem exactly, again a variational approach is employed. The trial wave function includes the Heilter-London approximation for the e-h pair contributions and is of the form[15]

$$\Psi=\frac{1}{S(x_{ba})}\Big[\psi_{1a}\psi_{2b}+\psi_{2a}\psi_{1b}\Big]\psi_{ba} \qquad [12]$$

$\psi_{\alpha\beta}$ is of the general form of Eq.(4) but with $g_t(x;\eta_x)\Rightarrow g_{\alpha\beta}(x_{\alpha\beta};\eta_{xx})$ given by Eq.(5), but not normalized, where η_{xx} is the e-h variational parameter within the excitonic molecule, and $g_{ba}=g_{ba}(x_{ba};\xi)$, which is nornalized, is a function of the hole-hole variational parameter ξ. $S(x_{ba})$ is the normalization factor.

The final expressions for the expectation values of both the kinetic and potential energies are long and complicated. They may be found in their entirety in the paper by Madarasz et al.[15] What is important for the present work is just their functional forms, which are represented by $\mathcal{K}$ and $\mathcal{P}$. The kinetic energy and potential energies are

$$E_K^{xx}=2E_K^x+\mathcal{K}(\eta_{xx};\xi), \qquad [13]$$

where E_K^x is the total kinetic energy of a single exciton, and

$$V_{xx}=\frac{e^2}{2\pi\varepsilon}\frac{1}{\eta_{xx}}\int_0^{+\infty}dQ_{\eta_{xx}}\int_0^{2\pi}d\phi\left\{\ \mathcal{P}\Big[I_1^{(ba)};I_1^{(1a)},I_2^{(1a)},I_3^{(1a)};I_0^{(21)},I_1^{(21)},I_2^{(21)}\Big]\right.$$
$$\left. X\ H_{LW}\big(Q_{\eta_{xx}},\phi\big)\ \right\}, \qquad [14]$$

where the I's are functions of $Q_{\eta_{xx}}$, η_{xx} and ξ, and each is made up of two terms similar in form to Eq.(8). $H_{LW}(Q_{\eta_{xx}},\phi)$ is identical to Eq.(9), but with $\eta_x\Rightarrow\eta_{xx}$. As in the

case of the single exciton, the biexciton Hamiltonian must be minimized with respect to the variational parameters in order to obtain the biexciton binding energy.

Since the biexciton wave function of Eq.(12) is made up of single particle states-- now given by Eq.(4)--the Al-graded potential will also affect the biexciton binding energy.

2.2. Nonlinear Optical Properties

Pump-probe spectroscopy is used experimentally to extract excitonic optical nonlinearities from other nonlinearities in semiconducting materials. We restrict our calculation to the optical nonlinearity via the biexciton state arising from the population saturation of the exciton state. For resonant excitation, the expression for $\chi^{(3)}$ in the RWA[20] is given by Ref.s 14-16. However, here we wish to investigate the frequency dependence of $\chi^{(3)}$ in a narrow range about the resonant exciton absorption line. The general derivation of $\chi^{(3)}$ for low density exciton/biexciton systems is given in the appendix of our previous paper[15]: it is based on the summation over sixteen double Feynman diagrams[21,25]. The spurious size dependence which generally accompanies the derivation of $\chi^{(3)}$ for a local two-level system has been eliminated by taking into account the "Pauli Exclusion Principle", that is one physical site is not allowed to be doubly excited[21,25].

In the frequency range of interest, the lowest lying states are the major contributors to $\chi^{(3)}$. Accordingly, the general expression reduces to

$$\chi^{(3)} = \frac{(-)2}{\pi\sqrt{2\pi}}\left(\frac{n_o}{\eta_x}\right)\left(\frac{\xi}{\eta_x}\right)\frac{e^4}{m_o^2\omega_{go}^4}E_P^2$$

$$\left[\left[\frac{1}{(\omega_1-\omega_{go}+i\Gamma_{go})}-\frac{1}{(\omega_1-\omega_{go}+\omega_{bx}(\eta_{xx},\xi)+i\Gamma_{bg})}\right]\left[\sum_{r=1}^{2}\left\{\frac{1}{\hbar^3(\omega_r-\omega_2+i\gamma)}\right.\right.\right.$$

$$\left[\frac{1}{(\omega_{go}-\omega_2+i\Gamma_{go})}+\frac{1}{(\omega_r-\omega_{go}+i\Gamma_{go})}\right]\right\}+\frac{1}{(\omega_1+\omega_2-2\omega_{go}+\omega_{bx}(\eta_{xx},\xi)+i\Gamma_{bo})}$$

$$\left.\left.\left\{\frac{1}{(\omega_1-\omega_{go}+i\Gamma_{go})}+\frac{1}{(\omega_2-\omega_{go}+i\Gamma_{go})}\right\}\right]\right], \qquad [15]$$

where ω_2 and ω_1 are the pump-probe frequencies, respectively, n_0 is the average areal density of unit cells, m_0 is the rest mass of an electron, e is the charge on an electron, E_P is the Kane matrix element and $\hbar\omega_{bx}$ is the biexciton binding energy. γ and Γ_{ij} are longitudinal and transverse relaxation/broadening parameters, respectively. The ij indices refer to: o-system ground state; g-exciton ground state; and b-biexciton ground state. $1/\gamma = 1/\Gamma_{ii}$ is the population decay time for state i, and $1/\Gamma_{ij}$ is the dephasing or lifetime of the coherent superpositons between states i and j. Note that, if all the transverse relaxation parameters are assumed to be equal, the model reduces to the independent boson model. Then, when the biexciton binding energy approaches zero so does the third-order susceptibility, because of the first bracketed factor in Eq.(15), as it should.

3. RESULTS AND DISCUSSION

In order to calculate the exciton and biexciton binding and ground state energies and optical susceptibilities, we employed the physical parameters summarized in Table I. All parameters needed but not listed in Table I are shown on the figures.

TABLE I. **Physical parameters for $Al_xGa_{1-x}As$**

x=	0.0	0.3
$E_g^o=$	1.512 eV (a)	1.899 eV (a)
$m_\perp^*=$	0.450 m_0	0.576 m_0
$m_c^*=$	0.067 m_0	0.092 m_0
$m_\parallel^*= 0.027 m_0$ (Ref.s 4 and 14)		
$\varepsilon=12.5$		
$n_0=7.89 \times 10^{14}/cm^2$	$E_p=23.0$ eV	

(a) $E_g^o(x)=1.512+1.155x+0.37x^2$

The Al interdiffusion in the lateral direction requires a numerical solution to Eq.(2) for the single particle electron and hole states. As a part of this numerical approach one must search for the integration range, i.e., numerical infinity, in which the wave function appropriately tends to zero and yields the correct corresponding eigenvalue: this must be done for every set of cross sectional dimensions and for each characteristic Al-grading width 2C. In turn, the values of the three variational parameters are changed; one must

further search for an acceptable starting value of the exciton variational parameter in order to start the minimization process. Needless to say, the whole process is time consuming. Thus, we have limited our dimensional parametric study to the smallest grading, C=W/16, corresponding to an almost abrupt junction. And, for illustrative purposes we have limited ourselves to one set of wire dimensions--LxW=125x75 Å^2--and four characteristic diffusion lengths--C=W/16, W/8, W/4, W/2. This particular set of wire dimensions was chosen because it is on the order of the bulk exciton radius and corresponds to a peak third-order optical susceptibility calculated for the infinite barrier model. The results of the electronic part of the calculation are summarized in Fig. 1 and Tables II, III, and IV.

In Fig. 1 we compare the exciton and biexciton binding energies when calculated with finite band offset potentials and with infinite potentials in a square, L=W, wire. The exciton energies are plotted with blackened triangles (▲) and plus signs (+) representing infinite potential barriers and finite band offset potential barriers, respectively. The biexciton energies are plotted with blackened squares (◆) and x's (✗) representing infinite
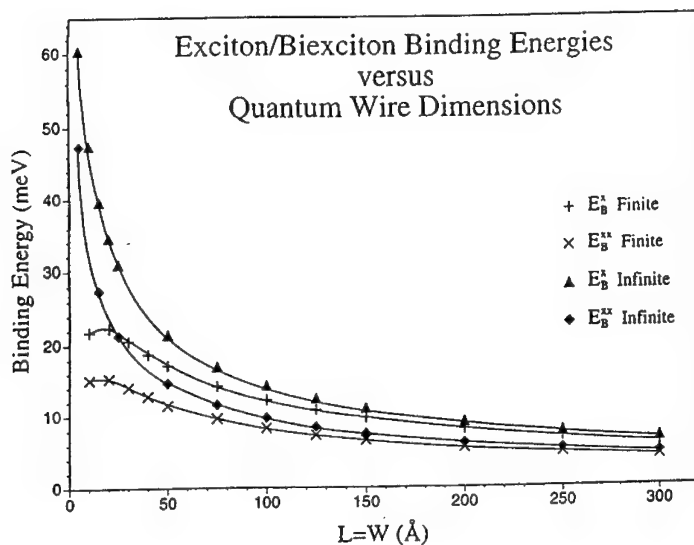
FIG. 1 Exciton/biexciton (E_B^x / E_B^{xx}) binding energies in square GaAs/Al$_{0.3}$Ga$_{0.7}$As quantum wires, with and without finite band offset potentials included.

potential barriers and finite band offset potential barriers, respectively. In the case of the infinite potential barriers, as L=W approaches zero, both exciton and biexciton binding energies tend to infinity as would be expected in analogy to the one-dimensional hydrogen atom[14,15]. However, when finite band offsets and wave function barrier penetration are included, even for just one dimension, dramatic effects are seen, especially at the smaller dimensions. For example, at L=W=25 Å the percent differences before and after the finite band offsets have been included are 44.8% and 45.4% for the exciton and biexciton, respectively.

The roll-over of both curves at the smaller dimensions is reminiscent of a quasi-bidimensional, a quantum well, system with finite band offsets. The binding energy of the exciton first increases with decreasing dimension. However, when either particle possesses a confinement energy which is close to the height of its respective band offset potential barrier the bidimensional character is lost and the binding energy begins to decrease. In the present case it is the unidimensional character which is lost. For the 10x10 Å^2 wire, the single particle electron and hole ground state energies in the direction of the finite band offsets, are 186.9 meV and 91.3 meV, respectively. These are comparable to the respective conduction and valence band offsets of 232 meV and 155 meV.

In Tables II and III we compare the exciton and biexciton binding energies when calculated with finite band offset potentials and with infinite potentials in a rectangular, L≠W, wire. Table Ii features the holding of L, the strong confinement dimension, fixed and the varying of W, the dimension of the finite band offset potentials. On the other hand, Table IIi holds W fixed and varies L. In each table, the varied dimension ≥ the fixed dimension. The binding energy percent difference is simply: % diff.=|finite-infinite|/finite. The general trend in either table is obvious: the larger the dimensions the smaller the percent difference.

Another general observation, between the two tables, is that for any set of dimensions, LxW, larger (one or both) or equal to 50x50 Å^2 the corresponding percent differences are comparable to within a few tenths. The implication is clear--while wave function penetration is important in lowering the binding energy it is not significant enough, at least for ground state energies, to affect the results whether L<W or L>W. Conversely, for any set of dimensions in which one (or both) is smaller than or equal to 25 Å the corresponding percent differences are not comparable. Here, L<W results in a significant difference between the binding energies than when L>W within the set. Finally, it appears that for the larger dimensions, nominally 400 Å and above, wave function penetration is insignificant, at least for the ground state energies, and the infinite potential model may be used in both confinement directions.

TABLE II. Exciton/biexciton binding energies (E_B^x / E_B^{xx}) in GaAs/Al$_{0.3}$Ga$_{0.7}$As quantum wires of various dimension, L≤W, with and without finite band offset potentials included.

Wire Dimensions		Exciton Binding Energy (meV)		% Diff.	Biexciton Binding Energy (meV)		% Diff.
L (Å)	W (Å)	Finite	Infinite		Finite	Infinite	
10	10	21.78	47.56	118.4	15.15	33.32	119.9
10	25	23.58	36.84	56.2	16.36	25.55	56.2
10	50	20.89	28.15	34.8	14.50	19.48	34.3
10	75	18.38	23.40	27.3	12.78	16.22	26.9
10	100	16.51	20.25	22.7	11.51	13.96	21.4
10	125	15.08	18.11	20.1	10.54	12.61	19.7
10	150	13.90	16.43	18.2	9.73	11.46	17.8
25	25	21.38	30.96	44.8	14.64	21.29	45.4
25	50	19.27	25.06	30.1	13.19	17.19	30.3
25	75	17.17	21.42	24.8	11.75	14.66	24.8
25	100	15.55	18.89	21.5	10.64	12.93	21.6
25	125	14.29	17.00	18.9	9.78	11.62	18.9
25	150	13.23	15.52	17.3	9.05	10.61	17.2
50	50	17.10	21.39	25.1	11.45	14.64	27.9
50	75	15.49	18.85	21.7	10.58	12.88	21.8
50	100	14.20	16.95	19.4	9.690	11.58	19.5
50	125	13.16	15.47	17.5	8.984	10.57	17.7
50	150	12.26	14.27	16.4	8.373	9.755	16.5
75	75	14.17	16.93	19.5	9.664	11.57	19.7
75	100	13.10	15.44	17.8	8.935	10.54	18.0
75	125	12.23	14.23	16.4	8.343	9.707	16.4
75	150	11.47	13.24	15.5	7.820	9.030	15.5
100	100	12.20	14.22	16.6	8.313	9.710	16.8
100	125	11.45	13.22	15.4	7.806	9.023	15.6
100	150	10.78	12.37	14.8	7.352	8.447	14.9
125	125	10.78	12.37	14.7	7.348	8.440	14.9
125	150	10.19	11.64	14.2	6.948	7.931	14.1
150	150	9.678	11.00	13.6	6.595	7.506	13.8
200	200	8.091	9.091	12.4	5.516	6.207	12.5
250	250	7.008	7.807	11.4	4.781	5.335	11.6
300	300	6.168	6.874	11.5	4.211	4.702	11.7

TABLE III. Exciton/biexciton binding energies (E_B^x /E_B^{xx}) in GaAs/Al$_{0.3}$Ga$_{0.7}$As quantum wires of various dimension, L≥W, with and without finite band offset potentials included.

Wire Dimensions		Exciton Binding Energy (meV)		% Diff.	Biexciton Binding Energy (meV)		% Diff.
L (Å)	W (Å)	Finite	Infinite		Finite	Infinite	
10	10	21.78	47.56	118.4	15.15	33.32	119.9
25	10	19.87	36.84	85.4	13.61	25.55	87.7
50	10	17.46	28.15	61.2	11.93	19.48	63.2
75	10	15.69	23.40	49.1	10.71	16.22	51.4
100	10	14.32	20.25	41.4	9.775	13.96	42.9
125	10	13.23	18.11	36.9	9.022	12.61	39.7
150	10	12.32	16.43	33.4	8.402	11.46	36.4
25	25	21.38	30.96	44.8	14.64	21.29	45.4
50	25	18.61	25.06	34.7	12.72	17.19	35.1
75	25	16.61	21.42	29.0	11.34	14.66	29.3
100	25	15.08	18.89	25.3	10.29	12.93	25.7
125	25	13.86	17.00	22.7	9.454	11.62	23.0
150	25	12.86	15.52	20.7	8.772	10.61	21.0
50	50	17.10	21.39	25.1	11.45	14.64	27.9
75	50	15.46	18.85	21.9	10.55	12.88	22.2
100	50	14.16	16.95	19.7	9.659	11.58	19.9
125	50	13.11	15.47	18.0	8.937	10.57	18.3
150	50	12.23	14.27	16.7	8.338	9.755	17.0
75	75	14.17	16.93	19.5	9.664	11.57	19.7
100	75	13.10	15.44	17.9	8.928	10.54	18.1
125	75	12.20	14.23	16.6	8.318	9.707	16.7
150	75	11.45	13.24	15.7	7.803	9.030	15.7
100	100	12.20	14.22	16.6	8.313	9.710	16.8
125	100	11.43	13.22	15.7	7.789	9.023	15.8
150	100	10.77	12.37	14.9	7.341	8.447	15.1
125	125	10.78	12.37	14.7	7.348	8.440	14.9
150	125	10.20	11.64	14.1	6.952	7.931	14.1
150	150	9.678	11.00	13.6	6.595	7.506	13.8
200	200	8.091	9.091	12.4	5.516	6.207	12.5
250	250	7.008	7.807	11.4	4.781	5.335	11.6
300	300	6.168	6.874	11.5	4.211	4.702	11.7

With reference to Table IV, we first note that the inclusion of finite band offsets lowers both electron and hole single particle subband energies for the narrowest grading (almost abrupt), W/16, giving approximately 61% difference for the electron and 35%

difference for the hole. And, of course this is precisely what is expected to happen. Fixing our attention on just the electron states for the moment, we see that, by increasing the diffusion length from W/16 to W/8 and then from W/8 to W/4, the subband energies rise. The reason for this trend is clear especially when we consider the graded well structure: as the diffusion width is increased the bottom of the well narrows pushing the states up. However, when increasing the diffusion length from W/4 to W/2

<div align="center">

TABLE IV

Infinite Potential Results

vs.

Finite Graded Potential Results
(GaAs Wire $--$ $Al_{0.3}Ga_{0.7}As$ Cladding)[a]

L x W = 125 x 75 Å

</div>

	Infinite	W/16*	W/8*	W/4*	W/2*
$\mathcal{E}_i^e(meV)$	99.75	38.67	41.69	51.38	47.24
$\mathcal{E}_i^h(meV)$	14.85	9.66	11.11	16.73	16.76
$\eta_x(a_0)$	362.20	395.45	393.58	389.95	395.12
$E_B^X(meV)$	-14.23	-12.27	-12.35	-12.54	-12.29
$V_{eh}(meV)$	-19.69	-16.85	-16.97	-17.25	-16.88
$E_{go}^X(eV)$	1.662	1.597	1.602	1.617	1.668
$\xi(a_0)$	1024.43	1116.79	1111.62	1101.55	1115.88
$\eta_{xx}(a_0)$	293.38	320.36	318.86	313.96	318.09
$E_B^{XX}(meV)$	-9.71	-8.36	-8.42	-8.55	-8.38
$V^{XX}(meV)$	-53.61	-45.88	-46.22	-46.97	-45.97
$E_{go}^{XX}(eV)$	3.31	3.186	3.195	3.225	3.328
$Z(0.01 u_{e\,max}^{(1)})$ (Å)		97.00	99.00	100.00	115.00
$Z(0.01 u_{h\,max}^{(1)})$ (Å)		61.00	62.00	63.00	69.00

a. Band Offsets--0.6 Conduction, 0.4 Valence
* 1/2 Al Grading Width

the trend appears to be reversed. The cause of this reversal is also clear: the well is now "over graded". That is, under this condition, there is enough Al concentration located at the center of the well to change the fundamental gap from that of pure GaAs to some percentage AlGaAs--the gap is increased and the well, as it rises, begins to flatten out. Relative to the bottom of the graded well the subband energy has indeed become smaller, but relative to the bottom of the GaAs well has continued to rise. In fact, as the fraction of Al in the center of the graded well, approaches $x=0.3$ the subband(s) coalesces at the bottom of the well and form the conduction band in bulk AlGaAs; the lowering of subband energies is to be expected.

A similar argument can be made for the hole subband energies. However, it is apparent from Table IV that, when the diffusion length reaches W/4 the subband energy exceeds that of the infinite barrier model. The cause of such a result is not totally unexpected. The barrier height for the holes is two thirds of that for the electrons. This means that the corresponding Al-grading of the valence band produces a well which is narrower for $z<W/2$ and wider for $z>W/2$ than that of the conduction band. One then expects a larger percentage increase in energy for the lower-lying hole subbands bands. For example, changing the diffusion length from W/8 to W/4 produces about a 19% increase in the electron subband energy and about a 34% increase in the hole subband energy.

The exciton and biexciton binding energies are lowered with the inclusion of the finite band offsets by approximately 14% for the smallest diffusion length of W/16. The evolution of their respective values with increasing Al-grading width can easily be explained in terms of the arguments given above for the electron and hole subbands. Similarly, the exciton and biexciton ground state energies are lowered with the inclusion of the finite band offsets. Since each is dominated by the fundamental band gap energy, their change is rather small, both being approximately 4% for the smallest diffusion length of W/16. Because of such a small change in the exciton ground state energy, the effect on the magnitude of optical susceptibility is negligible. However, at higher densities of excitons and biexcitons than considered here, the lower binding energies do affect the stability of the system and will thus limit the operational conditions under which peak $\chi^{(3)}$ values may be obtained and maintained.

The structure in $\chi^{(3)}$ is a strong function of the values of the longitudinal and transverse relaxation parameters. These parameters are quite difficult to obtain accurately by experiment and there are no first principles theoretical models of which we are aware. In addition, they are probably strong functions of the confinement dimensions as well as the population density of the excitons and temperature.[26,27] Consequently, some researchers have chosen them to be equal--for example, Ref.'s. 18 and 19--while some

have used them as fitting parameters--for example, Ref.'s 17 and 19. There is, however, good reason to believe that the longitudinal parameter is perhaps as much as an order of magnitude smaller than the transverse parameters[17,20]. Accordingly, for comparison, we have calculated $\chi^{(3)}$ for values $\gamma=0.1\,\Gamma_0$ and all $\Gamma_{ij}=\Gamma_0$, and for $\gamma=\Gamma_{ij}=\Gamma_0$, where $\sqrt{2}\,\Gamma_0$ corresponds to the full width at half max (FWHM) of the gaussian representing the exciton linear absorption.

In figures 2-7 we have calculated $\mathrm{Im}\chi^{(3)}$ for a two beam experiment in which one beam, the pump, is fixed and the other, the probe, is allowed to vary over a frequency range in which the pump is fixed. Specifically, in figures 2 and 3 the pump is fixed right on the exciton resonance, and in figures 4 and 5, and 6 and 7, the pump is detuned from the exciton resonance by $+\sqrt{2}\,\Gamma_0\,/2$ and $-\sqrt{2}\,\Gamma_0\,/2$, respectively. The abscissas on all plots are in dual energy units: on top are the more conventional meV units, and on the bottom are the FWHM units of $\sqrt{2}\,\Gamma_0$. We have chosen the FWHM units in order to give a measure of the relative strengths of the optical susceptibility and exciton absorption. The peak value of exciton absorption for all plots given here is 1.94×10^4 cm^{-1}. Figures 2, 4 and 6 have values of $\gamma=0.1\,\Gamma_0$, while figures 3, 5 and 7 have values of $\gamma=\Gamma_{ij}=\Gamma_0$. Note that $-\mathrm{Im}\chi^{(3)}$ is proportional to $-\Delta\alpha$ the differential change in optical transmission.

In comparing figures 2 with 3, 4 with 5, and 6 with 7 it is immediately apparent that 2, 4 and 6 all posses a rather abrupt, narrow negative peak for probe energies near or equal to the pump energies. The genesis of these peaks may be directly traced back to the $1/[\omega_r-\omega_2+i\gamma]$ factor in Eq.(15) for the susceptibility. When $\chi^{(3)}$ is separated into real and imaginary parts, this factor leads to a resonance factor in both parts which goes as $1/[(\omega_r-\omega_2)^2+\gamma^2]$. ω_2 corresponds to the pump and the index r on ω_r is summed over values of 1 (probe) and 2. Since ω_1 is the probe, it is varied, and, when in resonance with ω_2, the resonance factor becomes dominant (in the RWA the third line of Eq.(15) is negligible compared to the first two lines). Its strength, however, is extremely sensitive to the magnitude of γ: when $\gamma=0.1\,\Gamma_0$ its strength is 10^2, or two orders of magnitude larger then when $\gamma=\Gamma_0$, as is the case in figures 3, 5 and 7. Physically, γ is related to the population decay rate of the exciton state. A smaller γ, then, means the lifetime of the exciton state is larger and that the exciton system is more stable. In turn, there is a higher probability of forming an excitonic molecule in a two-step photon absorption process. The resonance spiking is only significant if the detuning of the pump lies within one to two FWHM of the exciton absorption peak. Note that in figures 4 and 6 the curves tend to have a relative minimum at peak exciton absorption. Of course, when the pump is in resonance with the peak exciton absorption, the spiking is amplified even further resulting in the curve displayed in figure 2. On the other hand, the curves displayed in figures 3, 5 and 7, those for which $\gamma=\Gamma_0$, show no sign of the abrupt spiking: the resonance factor is now approximately 10 times smaller than before. The larger γ not only smears out the

FIG. 2 The imaginary part of the third-order optical susceptibility as a function of the probe energy for a dual beam pump-probe experiment. The pump is set at exciton resonance and the longitudinal broadening parameter is one-tenth the value of the transverse broadening parameters.
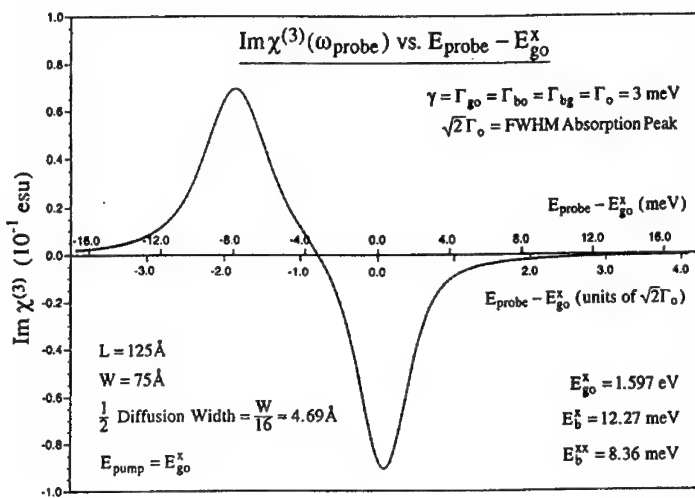
FIG. 3 Same as figure 2 but with the longitudinal broadening parameter equal to the transverse broadening parameters.
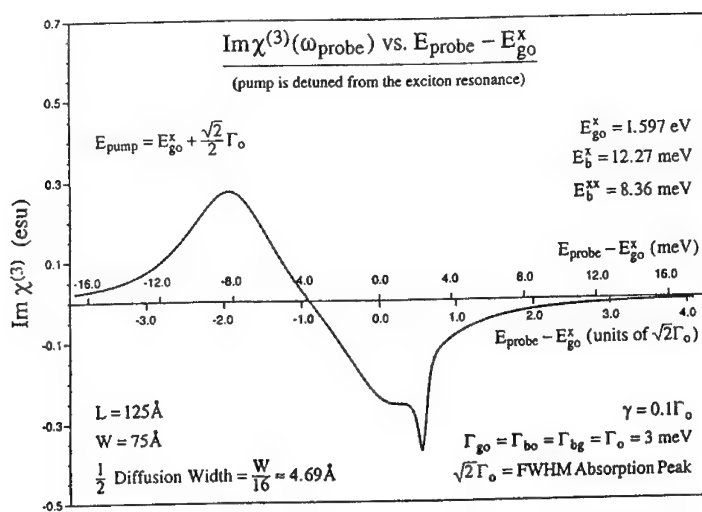
FIG. 4   Same as figure 2 but with the pump detuned slightly above the exciton resonance.

FIG. 5   Same a figure 4 but with the longitudinal broadening parameter equal to the transverse broadening parameters.
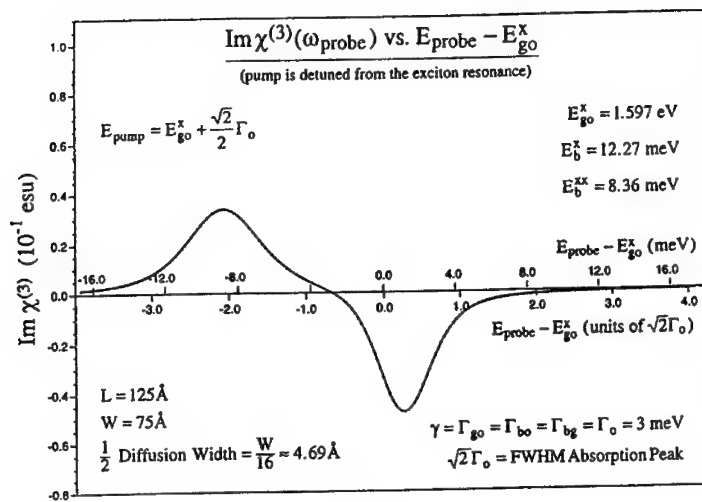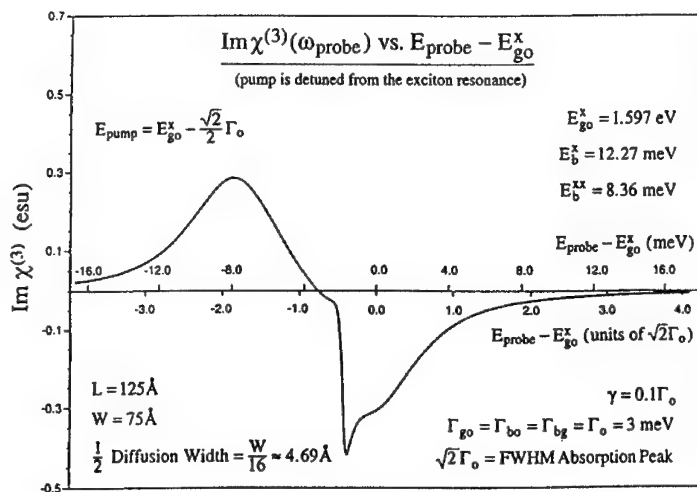
FIG. 6 Same as figure 4 but with the pump detuned slightly below the exciton resonance.
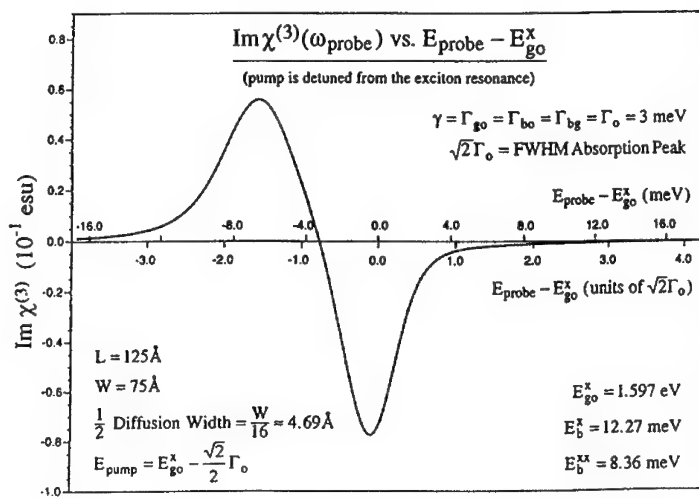
FIG. 7 Same as figure 6 but with the longitudinal broadening parameter equal to the transverse broadening parameters.

resonance spiking but it reduces the overall magnitude of each $\chi^{(3)}$ curve (note the scales of these curves are a factor of 10 times smaller).

The negative peak in all of these spectra, indicating transmission, is due to a bleaching (saturation) of the one-pair exciton transition. Physically, the initial exciton population created by the pump beam tends to amplify the probe beam, by way of stimulated emission, when the probe energy is tuned at or near the exciton linear absorption peak.

Another feature in all of the curves is the optical absorption--the region of positive $\text{Im}\chi^{(3)}$. The absorption may be attributed to the formation of the excitonic molecule[17-19]. The initial exciton population enables the probe to be more strongly absorbed when its energy matchs the exciton-biexciton transition energy, $\hbar\omega_{go} - \hbar\omega_{bx}$. In the present case, the biexciton binding energy is 8.36 meV. The maximum of each curve occurs at energies slightly greater than $-2.0 \times \sqrt{2}\,\Gamma_o = -9.3$ meV, in other words, very near the biexciton binding energy. Calculations for a wire of dimensions $LxW=225x175$ Å^2 substantiate this interpretation. In that calculation, the biexciton binding energy was -5.55 meV, and the maxima of the $\text{Im}\chi^{(3)}$ curves occurred at energies slightly less than $-1.3 \times \sqrt{2}\,\Gamma_o = -6.61$ meV.

In the last two plots, figures 8 and 9, we show typical curves for a single beam pump-probe experiment, where $\gamma=0.1\,\Gamma_o$ and $\gamma=\Gamma_o$, respectively. Since the pump and probe beams are always in resonance, the factor $1/[(\omega_r-\omega_2)^2+\gamma^2]$ becomes just $1/\gamma^2$, which is constant, and it now acts to modulate the magnitude of $\text{Im}\chi^{(3)}$. Both curves exhibit similar structure but, as expected, the curve for which $\gamma=0.1\,\Gamma_o$ is approximately an order of magnitude larger.

4. SUMMARY

We have solved the exciton/biexciton binding energy problem in a three parameter variational calculation in the effective mass approximation for a rectangular GaAs quantum wire surrounded by Al$_{0.3}$Ga$_{0.7}$As cladding material with finite Al graded band offsets included. For the biexciton part of the problem, we employed a Heitler-London-type wave function.

Because of the inclusion of the graded finite band offsets, the single particle states which make up the exciton/biexciton envelope functions had to be obtained numerically. For illustrative purposes we limited ourselves to one set of wire dimensions--$LxW=125x75$ Å^2--and four characteristic diffusion lengths--$C=W/16$, $W/8$, $W/4$, $W/2$. We then compared the single particle and exciton/biexciton binding energies results with those of the
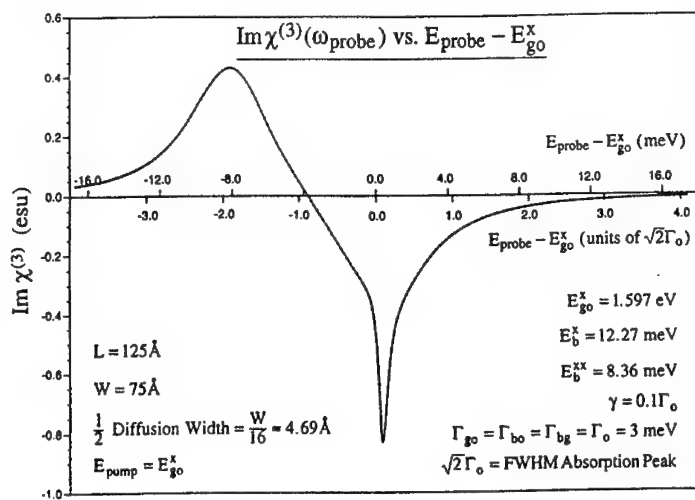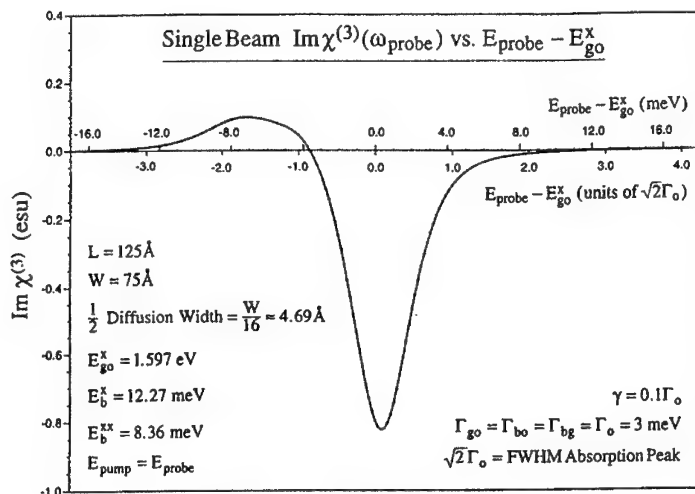
FIG. 8 The imaginary part of the third-order optical susceptibility as a function of the energy for a single beam pump-probe experiment. The longitudinal broadening parameter is one-tenth the value of the transverse broadening
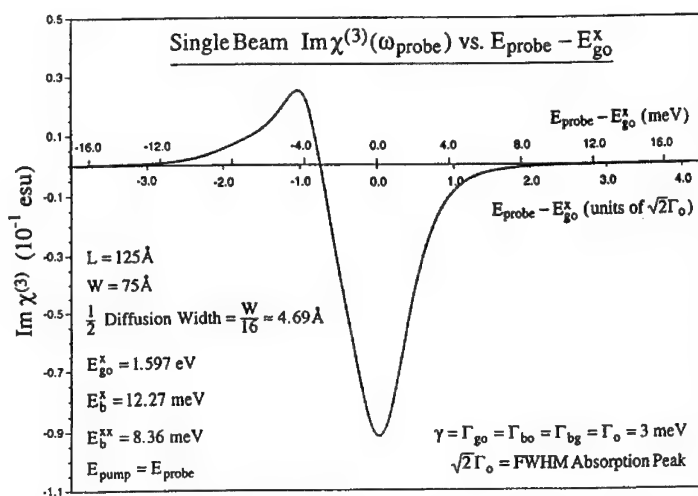
FIG. 9   Same as figure 8 but with the longitudinal broadening parameter equal to the transverse broadening parameters.

previous calculation with infinite potential barriers by Madarasz et al.[14-16] All energies were lowered with the inclusion of the finite band offsets. For the narrowest grading, we found a percent difference of approximately 61% for the electron ground state subband energy, while for the hole it was approximately 35%. The exciton and biexciton binding energies were both reduced by approximately 14%. As the grading widths increased, so did all energies; because as the diffusion width is increased the bottom of the well narrows pushing the states up.

Next, we applied the results of the exciton/biexciton calculation to obtain the nonlinear optical susceptibility $\chi^{(3)}$. Unlike our previous work[14-16], in which we calculated only peak values of $|\text{Im } \chi^{(3)}|$ for resonant exciton absorption using the RWA, here we studied $\text{Im}\chi^{(3)}$ as a function of pump-probe frequencies in a narrow range about the exciton resonant absorption. To do so, we used the general expression derived in the appendix of our previous paper via a double Feynman diagram method[14]: sixteen diagrams all total. We then reasoned that near resonance the ground states of the exciton and biexciton would be the major contributors to $\chi^{(3)}$. Accordingly, we simplified the general expression, retaining only ground state terms.

With the resulting expression, we calculated values for $\text{Im}\chi^{(3)}$ as a function of the pump and probe frequencies for dual and single beam experiments. In each case, we repeated the calculation using two different sets of relaxation parameters: $\gamma = 0.1\,\Gamma_0$ and all $\Gamma_{ij} = \Gamma_0$; and for $\gamma = \Gamma_{ij} = \Gamma_0$. We found, in general, the structure of the $\text{Im}\chi^{(3)}$ curves to be strongly dependent on the values of relaxation parameters used. Specifically, in the present calculation, we found the overall magnitude and structure of the curves to be a strong function of the longitudinal relaxation parameter, γ. The smaller value of γ, i.e., the longer mean lifetime of the exciton, gave results which were systematically about an order of magnitude larger than when the larger value of γ was used, and considerably enhanced the resonance when the probe equaled the pump in the dual beam case, which was especially dramatic when the pump was slightly detuned from the exciton resonance. The maximum values of the resulting $|\text{Im}\chi^{(3)}|$'s were on the order of 10^{-2}-10^{-1} esu.

A feature of all the curves was a region of positive $\text{Im}\chi^{(3)}$ for energies below the exciton saturation. The optical absorption was attributed to the biexciton formation. This absorption region was also of considerable magnitude but was displaced within one to two FWHM below the exciton resonance absorption peaking at approximately the exciton-biexciton transition energy.

ACKNOWLEDGMENTS

REFERENCES

1. S. Glutsch and f. Bechstedt, Phys. Rev. B47, 4315 (1993); Phys. Rev. B47, 6385 (1993); Superlattices and Mircrstructures 12, 459 (1992).
2. U. Bockelmann and G. Bastard, Europhys. Lett. 15, 215 (1991).
3. Mark Sweeny, Jingming Xu, Michael Shur, Superlattices and Mircrstructures 4, 443 (1988).
4. Ikuo Suemune and Larry A. Coldren, IEEE J. Quant. Electron. QE-25, 1778 (1988).
5. Ladislaus Bányai, Ian Galbraith, Claudia Ell, and Hartmut Haug, Phys. Rev. B36, 6099 (1987).
6. K. Ishda and H. Aoki, 21st International Conference on the Physics of Semiconductors, Beijing, China, August 10-14, 1992.
7. Hiroaki Ando, Hironu Oohashi, and Hiroshi Kanbe, J. Appl. Phys. 70, 7024 (1991).
8. A. D'Andrea and R. Del Sole, Phys. Rev B46, 2363 (1992).
9. Eiichi Hanamura, Phys. Rev. B37, 1273 (1988); Phys. Rev. B38, 1228 (1988); Solid State Comm. 73, 551(1990).
10. R. Chen, D. L. Lin, and B. Mendoza, Phys. Rev. B48, 11873 (1993). The results of this paper appear unphysical; the third-order susceptibility depends on the length of the wire.
11. D. A. B. Miller, D. S. Chemla, T.C. Damen, A. C. Gossard, E. Wiegmann, T. H. Wood, and C. A. Burrus, Phys. Rev B32, 1043 (1985).
12. D. S. Chemla, D. A. B. Miller, and S. Schmitt-Rink, in Optical Nonlinearities and Instabilities in Semiconductors, ed. Hartmut Haug (Academic Press, New York, 1988), pp 38-120; and pp. 325-359 and the refrences therein.
13. D. Gershoni, H. Temkin, G.J. Dolan, J.Dunsmuir, S.N.G. Chu, andM.B. Panish, Appl. Phys. Lett. 53, 955 (1988).
14. Frank L. Madarasz, Frank Szmulowicz, F. Kenneth Hopkins and Donald L. Dorsey, Phys. Rev. B49, 13 528 (1994).
15. Frank L. Madarasz, Frank Szmulowicz, F. Kenneth Hopkins and Donald L. Dorsey, J. App;. Phys. 75, 639 (1994).

16. Robert O. Klepfer, Frank L. Madarasz and Frank Szmulowicz, Phys. Rev. B$\underline{51}$, 4633 (1995).
17. T. Takagahara, Phys. Rev. B$\underline{39}$, 10 206 (1989).
18. Y.Z. Hu, M. Lindberg and S.W. Koch, Phys. Rev. B$\underline{42}$,1713 (1990).
19. L. Belleguie and L. Bányai, Phys. Rev. B$\underline{47}$, 4498 (1993).
20. L. Bányai, I. Galbraith, and H. Haug, Phys. Rev. B$\underline{38}$, 3931 (1988).
21. T. Ishihara, Phys. Stat. Sol. $\underline{159}$, 371 (1990).
22. K. Brunner, G. Abstrieter, M. Walter, G. Böhm and G. Tränkle, Surface. Sci. $\underline{267}$, 218 (1992).
23. J. Boyd, H. Jackson, and A. Steckl, University of Cincinnati, private communications.
24. Frank L. Madarasz and Frank Szmulowicz, J. Appl. Phys. $\underline{62}$, 3267 (1987).
25. Hajime Ishihara and Kikuo Cho, Phys. Rev. B$\underline{42}$, 1724 (1990).
26. T. Takagahara, Solid State Commun. $\underline{28}$, 279 (1991).
27 H. Qiang, Fred. H. Pollack, C. M. Sotomayor Torres, W. Leitch, A. H. Kean, Michael A. Stroscio, Gerald Iafrate, and K. W. Kim, Appl. Phys. Lett. $\underline{61}$, 1411, (1992).

Biexcitons in Quantum Wires Subjected to a Magnetic Field

A. Balandin and S. Bandyopadhyay
Department of Electrical Engineering
University of Notre Dame
Notre Dame, Indiana 46556

Abstract

In this paper, we have calculated the binding energies of biexcitons (excitonic molecules) in a semiconductor quantum wire subjected to a magnetic field. A magnetic field squeezes the individual electron and hole wave functions thereby increasing the biexciton binding energy. The increase in the binding energy can lead to enhanced third order non-linear susceptibilities and therefore improved non-linear optical properties.

I. Introduction

The physics of biexcitons in quantum wires is an important topic of research since these entities contribute directly to the giant third-order non-linear susceptibility in quasi one-dimensional systems.[1,2] The large non-linear susceptibility arises from a constriction of phase space (one dimensional confinement) in quantum wires. A magnetic field causes further confinement of the biexciton thereby leading possibly to enhanced non-linear susceptibility.

In this paper, we present variational calculation of the biexciton binding energies in a rectangular quantum wire subjected to a magnetic field. First, we present the theory, then the results, and finally, the conclusions.

II. Theory

Our prototypical system consists of a quantum wire of rectangular cross-section where x is the free (unconfined) direction and y and z are confined directions (see the inset of Fig. 1). We assume infinite potential barriers

located along the confinement directions at $y = \pm L/2$ and $z = \pm L/2$. A magnetic field is applied along the z direction.

We choose the Landau gauge

$$\vec{A} = (-By, 0, 0),$$

where B is the z directed magnetic flux density. For nondegenerate and isotropic bands, the Hamiltonian of the biexciton subjected to a magnetic field is given in the envelope-function approximation by

$$
\begin{aligned}
H^{\hat{X}X} = & \frac{1}{2m_e}(p_{x_1}^{\hat{2}} + p_{x_2}^{\hat{2}}) + \frac{1}{2m_h}(p_{x_a}^{\hat{2}} + p_{x_b}^{\hat{2}}) + \frac{1}{2m_e}(p_{y_1}^{\hat{2}} + p_{y_2}^{\hat{2}}) + \frac{1}{2m_h}(p_{y_a}^{\hat{2}} + p_{y_b}^{\hat{2}}) \\
& + \frac{1}{2m_e}(p_{z_1}^{\hat{2}} + p_{z_2}^{\hat{2}}) + \frac{1}{2m_h} p_{z_a}^{\hat{2}} + p_{z_b}^{\hat{2}}) \\
& + \frac{1}{2m_e}\left[e^2 B^2(y_1^2 + y_2^2) - 2eB(y_1 p_{x_1}^{\hat{}} + y_2 p_{x_2}^{\hat{}}) \right] \\
& + \frac{1}{2m_h}\left[e^2 B^2(y_a^2 + y_b^2) + 2eB(y_a p_{x_a}^{\hat{}} + y_b p_{x_b}^{\hat{}}) \right] + V_{Coulomb} + V_{conf}, \quad (1)
\end{aligned}
$$

where V_{conf} is the confinement potential along the y- and z-direction, and $V_{Coulomb}$ is the Coulomb interaction between various charged entities. The electron coordinates are labeled by the numerics 1 and 2 while hole coordinates are labeled by the letters a and b. In Equation (1) we neglected the Zeeman splitting since the effective Lande factor in most semiconductors is quite small (g=-0.445 in GaAs so that the Zeeman splitting is only 0.26 meV at 10 tesla). Additionally, we neglect polariton effects.

Because the trial wave function for the biexciton will be written in terms of the electron-hole and hole-hole separations, it is convenient to use the following relative and center-of-mass coordinates:

$$
\begin{cases}
x_{1a} = x_1 - x_a \\
x_{2b} = x_2 - x_b \\
x_{ab} = x_a - x_b \\
X = [m_e(x_1 + x_2) + m_h(x_a + x_b)]/2(m_e + m_h)
\end{cases}
$$

To re-write the biexciton Hamiltonian in the new coordinate system, we utilize the usual canonical transformations for the momentum operators. We also drop the kinetic energy operators associated with the center-of-mass motion since the Hamiltonian is invariant in X so that P_X is a good quantum number. We are only interested in solving for the biexcitonic states which can be accessed optically and under optical excitation the center-of-mass motion can be neglected since the photon momentum is too small to create states of significant center-of-mass kinetic energy. Consequently, the transformed

Hamiltonian becomes

$$H^{\hat{X}X} = -\frac{\hbar^2}{2\mu}\left(\frac{\partial^2}{\partial x_{1a}^2} + \frac{\partial^2}{\partial x_{2b}^2}\right) - \frac{\hbar^2}{m_h}\left(\frac{\partial^2}{\partial x_{ab}^2} - \frac{\partial^2}{\partial x_{1a}\partial x_{ab}} + \frac{\partial^2}{\partial x_{2b}\partial x_{ab}}\right)$$

$$-\frac{\hbar^2}{2m_e}\left(\frac{\partial^2}{\partial y_1{}^2} + \frac{\partial^2}{\partial y_2{}^2} + \frac{\partial^2}{\partial z_1{}^2} + \frac{\partial^2}{\partial z_2{}^2}\right)$$

$$-\frac{\hbar^2}{2m_h}\left(\frac{\partial^2}{\partial y_a{}^2} + \frac{\partial^2}{\partial y_b{}^2} + \frac{\partial^2}{\partial z_a{}^2} + \frac{\partial^2}{\partial z_b{}^2}\right)$$

$$+\frac{e^2 B^2}{2}\left(\frac{y_1^2 + y_2^2}{m_e} + \frac{y_a^2 + y_b^2}{m_h}\right) + \frac{eBi\hbar}{m_e}\left(y_1\frac{\partial^2}{\partial x_{1a}} + y_2\frac{\partial^2}{\partial x_{2b}}\right)$$

$$+\frac{eBi\hbar}{m_h}\left(y_a\frac{\partial^2}{\partial x_{1a}} + (y_b - y_a)\frac{\partial^2}{\partial x_{ab}} + y_b\frac{\partial^2}{\partial x_{2b}}\right) + V_{Coulomb} + V_{conf} \quad (2)$$

The Coulomb interaction term in Eq. (2) is given by

$$V_{Coulomb} = \frac{e^2}{4\pi\epsilon}\Big\{\frac{(-1)}{\sqrt{x_{1a}^2 + r_{1a}^2}} + \frac{(-1)}{\sqrt{x_{1b}^2 + r_{1b}^2}} + \frac{(-1)}{\sqrt{x_{2b}^2 + r_{2b}^2}} +$$

$$\frac{(-1)}{\sqrt{x_{2a}^2 + r_{2a}^2}} + \frac{1}{\sqrt{x_{ab}^2 + r_{ab}^2}} + \frac{1}{\sqrt{x_{12}^2 + r_{12}^2}}\Big\}, \quad (3)$$

where

$$r_{\alpha\gamma}^2 = (y_\alpha - y_\gamma)^2 + (z_\alpha - z_\gamma)^2,$$

$$x_{\alpha,\gamma} = x_\alpha - x_\gamma,$$

with $\alpha, \gamma = 1, 2, a, b$, and $\alpha \neq \gamma$.

Direct numerical evaluation of the eignefunctions of the Hamiltonian operator in Equation (2) is computationally burdensome. Therefore, we employ a variational approach as in Ref. [2-5]. The choice of the variational wavefunction is dictated by many considerations. For instance, in the regime of weak quantum confinement, where the lateral dimensions $L_{y,z}$ of the wire are much larger than the effective Bohr radius a_B^* of a free exciton, one may apply the "free boson" model to determine the different electron-hole-pair states. The "free boson" model is based on the Heitler-London approximation in which the biexciton wave function is written as a linear combination of atomic orbitals in analogy with the hydrogen molecule. The linear combination is chosen to be symmetric in space so that it corresponds to the singlet state which is known to be lower in energy than the triplet state.

In the regime of strong quantum confinement, $L_{y,z}$ are much smaller that the effective Bohr raduis a_B^*. In this case, the confinement energy is the dominant energy contribution. Electrons and holes are confined separately, and the Coulomb potential may be neglected in comparison with the large kinetic energy caused by the strong confinement.[6] However, we are primarily

interested in the regime of moderate quantum confinement (in our case $L_y = 50 - 700\text{Å}$ and $L_z = 100 - 300\text{Å}$). Therefore, we have to come up with some physically realistic trial wave function which would allow us to use the Heitler-London approach, and at the same time take into account the difference in the motion along confined and "free" directions. We achieve this by considering the electrons and holes to be independently quantized along y and z directions, while applying the Heitler-London approximation along x direction. Following the approach in Ref.[2,7] we choose a trial wave function as a singlet state with the electron-hole pair contributions given by the Gaussian-type "orbital" functions:

$$\Psi = \frac{1}{S}\{\psi_{1a}\psi_{2b} + \psi_{2a}\psi_{1b}\}G_{ab}(x_{ab}), \tag{4}$$

where

$$\psi_{\alpha\gamma} = g_{\alpha\gamma}\phi_\alpha(y_\alpha)\chi_\alpha(z_\alpha)\phi_\gamma(y_\gamma)\chi_\gamma(z_\gamma), \tag{5}$$

with

$$g_{1a} = e^{-x_{1a}^2/\eta^2}, \tag{6}$$

$$g_{2b} = e^{-x_{2b}^2/\eta^2}, \tag{7}$$

$$g_{2a} = e^{-(x_{2b}-x_{ab})^2/\eta^2}, \tag{8}$$

$$g_{1b} = e^{-(x_{1a}+x_{ab})^2/\eta^2}, \tag{9}$$

and

$$G_{ab}(x_{ab}) = e^{-x_{ab}^2/\tau^2}, \tag{10}$$

in which η and τ are variational parameters and S is a normalization constant. The functions $\chi_{e,h}(z_{e,h})$ are the z-components of the biexciton wave function which are not affected by the magnetic field (the magnetic field is oriented along the z-direction). They are given by particle-in-a-box states

$$\chi_{e,h}(z_{e,h}) = \sqrt{\frac{2}{L_z}}cos(\pi\frac{z_{e,h}}{L_z}). \tag{11}$$

The electron and hole wave functions along the y direction, $\phi_{e,h}(y_{e,h})$, are to be calculated numerically when a magnetic field is present. This is done by solving the Schrödinger equation directly following the prescription given in Ref. [8].

The trial wave function in (4) really implies that the "true" wave function is more sensitive to the separation between the holes than between the

electrons. Since holes have higher effective masses, this assumption is physically realistic.[9] The trial wave function (4) is probably the simplest that can be chosen while still preserving the principal features of the actual wave function. The results obtained with this trial function can be checked "a posteriori" by evaluating the zero- magnetic field binding energy and comparing it with binding energy calculated by other methods or extracted from experimental data.
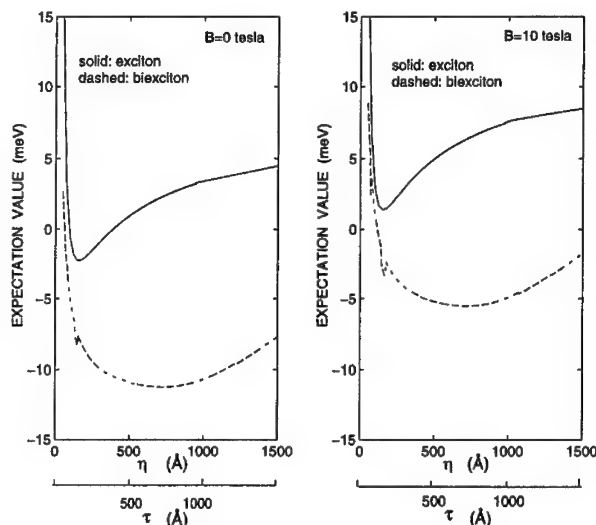
Figure 1: Expectation value of the exciton (biexciton) Hamiltonian as a function of the electron-hole (hole-hole) variational parameter η (τ). The abscissa is dual: the lower part represents hole-hole separation τ and corresponds to the expectation value of the biexciton functional; the upper part represents electron-hole separation η and corresponds to the expectation value of the exciton functional. Thickness of the wire along the z-direction is 200Å.

The biexciton binding energy E_B^{XX} is given by the relationship

$$E_B^{XX} = min < \Psi|H^{XX}|\Psi > -2min < \psi|H^X|\psi >, \qquad (12)$$

where $min < \Psi|H^{XX}|\Psi >$ is found by minimizing the expectation value of the Hamiltonian H^{XX} with respect to the hole-hole variational parameter τ, $min < \psi|H^X|\psi >$ is found by minimizing the expectation value of the exciton Hamiltonian with respect to the electron-hole variational parameter

η. The latter quantity was calculated by us previously over a range of wire widths and magnetic fields.[10,11] As it was pointed out by Klepfer *et al.*,[12] introduction of a third variational parameter, which allows for relaxation of the electron-hole pair within the biexciton, would not seriously change the biexciton binding energy when there is no magnetic field present. We tacitly assume that the same is true when a magnetic field is present.
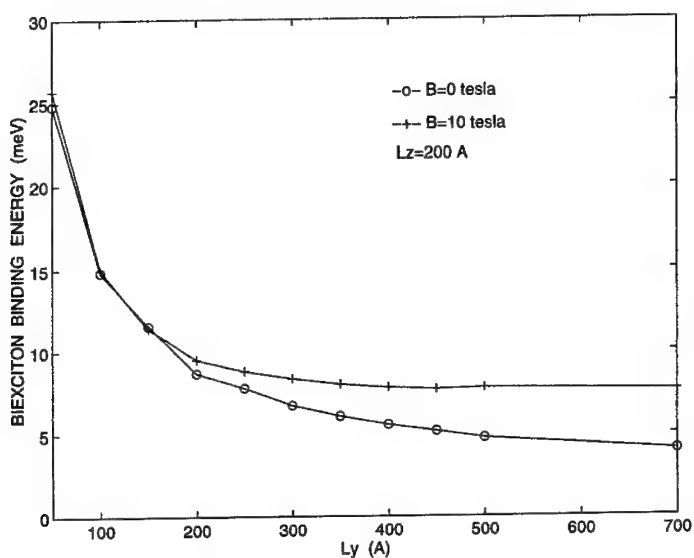
Figure 2: Biexciton binding energy as a function of wire width L_y with and without magnetic field. The thickness along the z-direction is 200 Å.

In order to calculate $< \Psi | H^{XX} | \Psi >$, we have calculated all required spatial derivatives of the trial wave function analytically and evaluated the integrals over all spatial coordinates relevant to the problem numerically. The Coulomb term was treated exactly in its full three-dimensional form throughout the calculation. The evaluation of the integrals in the Coulomb term is not straightforward due to the $1/r$ sinqularity. Moreover, since some components of the biexciton wave function ($\phi_{e,h}(y_{e,h})$) are being calculated numerically, we cannot apply Fourier expansion in a manner similar to that in Ref. [2] which would avoid dealing with the singularity. Fortunately, un-like in the case of the strictly one-dimensional case considered by Banyai *et al.*,[13] the Coulomb term treated in its full three-dimensional form is not problematic, and can be integrated in real space using the extended (multi-dimensional) definition of the improper integral that actually exists in this

case. The integration procedure involved evaluation of 5D and 7D integrals in real space. We checked for the convergence of the integrals by setting all but the free coordinates equal to zero and letting relative coordinates along x direction gradually approach zero over a hyper-sphere in order to ensure that the volume element goes to zero faster than the Coulomb term singularity. Details will be reported in a forthcoming publication. Note that the expectation value of every imaginary term in the Hamiltonian vanishes exactly, which makes the expectation value of the Hamiltonian strictly real and shows that the trial wave function space is admissible.

III. Results

The physical parameters used for the calculations correspond to a *GaAs* quantum wire with $\epsilon = 12.9\epsilon_o, m_e = 0.067m_o, m_h = 0.5m_o$, where m_o is free electron mass and ϵ_o is electrical permitivitty of free space.

We first numerically evaluated $< \Psi|H^{XX}|\Psi >$ and plotted it as a function of the variational parameter τ (hole-hole separation) in Fig. 1. The minimum of $< \Psi|H^{XX}|\Psi >$ gives us the value of $\tau_{critical}$ to be used in the biexciton wave function and in the calculation of the biexciton binding energy. For comparison we also plotted the expectation value of the exciton Hamiltonian as a function of the variational parameter η (electron-hole separation). The exciton Hamiltonian used for this plot can be found in Refs. 10 and 11. Each expectation value has a single well-resolved minimum. The minimum is narrower for the exciton Hamiltonian than for the biexciton Hamiltonian because the electron and hole are more tightly bound within the exciton than in the biexciton. The biexciton therefore always exists as a much broader resonance than the exciton. Although not easily evident from Fig. 1, $\tau_{critical}$ is less sensitive to the magnetic field than $\eta_{critical}$. This is because in a relatively narrow wire of 200 Å (used in the calculation of Fig. 1), the size of the biexcitonic complex is not significantly affected by a magnetic field.

In Fig. 2, we present the biexciton binding energy as a function of L_y (wire width along y direction) with and without a magnetic field. The binding energy initially decreases rapidly with increasing values of L_y because of decreasing quantum confinement of electrons and holes. The magnetic field has two distinct effects. First, it raises the binding energy slightly because of the additional confinement introduced by the field, and second, it causes the binding energy to saturate beyond a wire width of ~ 400 Å. For narrow wires ($L_y < 150$ Å), the magnetic field does not have any significant effect.

These features can be explained by invoking the complementary roles of the electrostatic and magnetostatic confinements of the electrons and holes. For narrow wires, the electrostatic confinement of the boundaries predominates and the additional confinement caused by the magnetic field has little
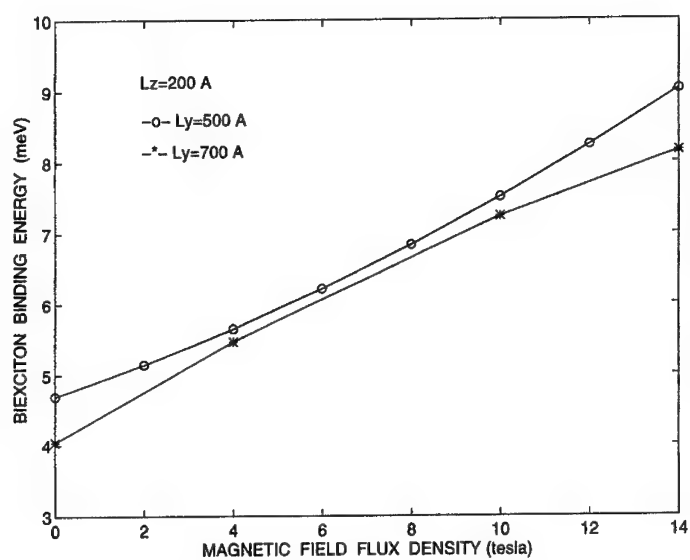
Figure 3: Biexciton binding energy as a function of magnetic flux density for two values of the wire width: $L_y = 500\mathring{A}$ and $L_y = 700\mathring{A}$. The thickness along the z axis for both cases is $L_z = 200\mathring{A}$.

effect. Once the wire width significantly exceeds the magnetic length $l = \sqrt{\hbar/eB}$, the magnetostatic confinement becomes predominant and increasing the wire width has no further effect. This explains why the biexciton binding energy saturates beyond a wire width of 400 Å (the magnetic length for B=10 tesla is 80 Å).

Unfortunately, we cannot examine the behavior of the biexciton binding in the limit when L_y goes to infinity because our model does not contain any provision to make the transverse components of the wave function to deform into atomic Slater orbitals. However, a direct comparison of our results for zero magnetic field with those in Ref.[2] shows excellent agreement.

Figure 3 shows the biexciton binding energy as a function of the magnetic field for different values of L_y. For realtively wide wires ($L_y = 700$ Å), the binding energy increases sub-linearly with the magnetic field, whereas for narrower wires ($L_y = 500$ Å), the increase is super-linear.

(a)
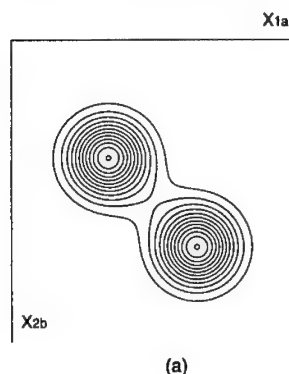
Figure 4: Contour plot of the biexciton probability density as a function of relative coordinates x_{1a}, x_{2b} for a quantum wire with no magnetic field. The wire dimensions are: $L_z = 200Å, L_y = 700Å$.

Figures 4 and 5 show the contour plot of the probability density distribution of the biexciton as a function of relative coordinates x_{1a} and x_{2b} with and without magnetic field. These two relative coordinates are the separations between one electron and one hole, and between the other electron and the other hole. The lateral dimensions of the wire are chosen to be

X1a

X2b

(b)
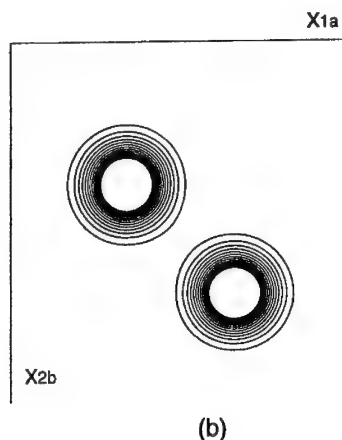
Figure 5: Contour plot of the biexciton probability density as a function of relative coordinates x_{1a}, x_{2b} for a quantum wire subjected to a magnetic field of 10 tesla. The wire dimensions are: $L_z = 200\text{Å}, L_y = 700\text{Å}$.

$L_z = 200\text{Å}, L_y = 700\text{Å}$, i.e. much larger than the magnetic length at 10 tesla so that the effect of magnetic field is well observed. We can see that the magnetic field squeezes the biexciton wave function along the free (x-axis) direction for both relative coordinates.

IV. Conclusions

In this paper, we have calculated the magnetic field dependence of the ground state biexciton (excitonic molecule) binding energy in a $GaAs$ quantum wire. Two important observations are that: (i) the binding energy increases with increasing magnetic field, and (ii) binding energy saturates beyond a wire width of 400Å when a magnetic field of 10 tesla is present. For wide wires the magnetostatic confinement becomes predominant and increasing the wire width has no further effect on the biexciton binding energy. The increase in the binding energy can lead to enhanced third order non-linear susceptibilities and therefore improved non-linear optical properties.

Finally, a few words about polariton effects are in order. It was claimed in Ref. [14] that the biexciton bound state may not exist in quantum wires because of polariton effects. We are presently investigating this possibility. Additionally, neglect of spin effects[15] may not be entirely permissible if in-

teractions with polarized light is considered. These topics are reserved for future research.

REFERENCES

[1]. T. Ishihara, *Phys. Status. Solidi.*, **159**, 371 (1990).

[2]. F.L. Madarasz, F. Szmulowicz, F.K. Hopkins, and D.L. Dorsey, *Phys. Rev. B*, **49**, 13528 (1994).

[3]. R.C. Miller, D.A. Kleinman, W.T. Tsang, and A.C. Gossard *Phys. Rev. B*, **24**, 1134 (1981).

[4]. G. Bastard, E.E. Mendez, L.L. Chang, and L. Esaki, *Phys. Rev. B*, **26**, 1974 (1982).

[5]. D. A. B. Miller, D. S. Chemla, T. C. Damen, A. C. Gossard, W. Weigmann, T. H. Wood and C. A. Burrus, *Phys. Rev. Lett.*, **53**, 2173 (1984) and *Phys. Rev. B*, **32**, 1043 (1985).

[6]. L. Banyai, Y.Z. Hu, M. Lindberg, S.W. Koch, *Phys. Rev. B*, **38**, 8142 (1988).

[7]. F.L. Madarasz, F. Szmulowicz, F.K. Hopkins, and D.L. Dorsey, *J. Appl. Phys.*, **75**, 639 (1994).

[8]. S. Chaudhuri and S. Bandyopadhyay, *J. Appl. Phys.*, **71**, 3027 (1992).

[9]. W.F. Brinkman, T.M. Rice, and Brian Bell, *Phys. Rev. B*, **8**, 1570 (1973).

[10]. A. Balandin and S. Bandyopadhyay, *Phys. Rev. B*, **52**, 8312 (1995).

[11]. A. Balandin and S. Bandyopadhyay, *Superlattices and Microstructures*, in press.

[12]. R. O. Klepfer, F. L. Madarasz and F. Szmulowicz, *Phys. Rev. B*, **51**, 4633 (1995).

[13]. L. Banyai, I. Galbraith, C. Ell, H. Haug, *Phys. Rev. B*, **36**, 6099 (1987).

[14]. A. L. Ivanov and H. Haug, *Phys. Stat. Sol. (b)*, **188**, 61 (1995).

[15]. S. Zivanovich, V. Milanovic, Z. Ikonic, *Phys. Rev. B*, **52**, 8305 (1995).

Strain and Lateral Quantum Confinement Effects in
n-type Modulation Doped Lattice-Mismatched Quantum Wires

J. Hammersberg, M. Notomi*, H. Weman,

M. Potemski+, H. Sugiura*, M. Okamoto*,

and T. Tamamura*

Dep. of Physics and Measurements Technology,

Linköping University, S-581 83 Linköping, Sweden

* NTT Opto-electronics Lab., 3-1 Morinosato-Wakamiya, Atsugi, Kanagawa 243-01, Japan

+ High Magnetic Field Laboratory,

MPI-FKF and CNRS, F-38042 Grenoble, France

We have investigated lateral size effects on luminescence spectra of n-type modulation doped lattice mismatched $InAs_xP_{1-x}$/InP quantum wires. Several subbands in the conduction band are populated, while only the lowest level in the valence band it populated. A clear blue shift is observed for narrow wires in the zero magnetic field luminescence spectra. The striking result is that the blue shift partly remains as a rigid shift of the quantum wires Landau fan chart at high magnetic fields. We have calculated the strain energy in lattice mismatched quantum wires and found that it explains well the rigid energy shift. The wire width dependent rigid energy shift indicates a non-uniform strain distribution in the wires.

INTRODUCTION

Recently there have been an increasing interest in the fabrication of strained quantum well wires. This is encouraged by the great success in the fabrication of low threshold strained quantum well (QW) lasers. An introduction of (ideal) biaxial strain in QW's or QWW's will in addition to the quantum confinement reduce the asymmetry between the conduction and valence band density of states (reduce the non-parabolicity in the valence band).[1] This reduction will lead to a reduced threshold current,[2] improved differential gain, and an enhancement of modulation dynamics (bandwidth) and spectral properties of lasers.[1] Strong improvements have been assigned to biaxial strained wires, i.e. in wires where the lattice constant of the wire region parallel to the substrate interface (lateral direction) has adapted the lattice constant of the substrate, whereas the lattice constant perpendicular to the substrate interface, has changed according to the Poisson ratio.[1]

To accomplish coherent growth at all interfaces using overgrowth (lattice constant $a_{barrier}=a_{substrate}$), a three directional hydrostatic compression of the wire region (relaxed lattice constant $a_0>a_{substrate}$) by the barrier is necessary. This will lead to a uniform hydrostatically strained wire region. It has been considered that a completely embedded wire region leads to a critical thickness smaller than the quantum well due to the strong three-dimensional compression, thus making dislocation free fabrication difficult.[1] However, it is questionable if uniform hydrostatic compression can be considered to be valid for large cross-sectional aspect ratio. In a more realistic model the strain tensor element in the central part of the wire region should for increasing wire width asymptotically approach the model of a biaxial strained quantum well.[3] Hence, the QWW strain distribution is intrinsically non-uniform.[3,4,5]

Here we report on a high field (max. 28T) magneto-luminescence study of strain- and confinement effects of the energy blue shift in n-type modulation doped strained $InAs_xP_{1-x}/InP$ QWW's. The QWW's were fabricated with a combination of electron beam lithography, selective wet etching and overgrowth. This fabrication technique provides the ability to vary the lateral width of the wire and study the dimensional effects on the strain distribution without affecting the composition in the wire region. We use n-type modulation doped structures in this investigation. Several subbands (Landau levels) are populated in the conduction band. In the valence band, only the lowest subband (Landau level) is populated due to low photo-excited carrier density.[6]

To probe the electronic structure in these strained QWW's we apply a magnetic field parallel to the growth direction (perpendicular to the lateral wire potential). The magnetic field generates a lateral harmonic potential, where the confinement strength can be varied by the field strength. In QW's (with the field applied in the growth direction) the magnetic potential generates Landau levels with a linear shift with the magnetic field. This is essentially different from QWW's where the lateral wire confinement potential is coupled to the magnetic potential. The magnetic potential has to dominate the total lateral potential to be able to generate quasi 2D Landau-level states in the centre of the wire.

The principal idea using high magnetic fields is that the energy blue shift due to lateral confinement in QWW's is suppressed when Landau level states are formed at high magnetic fields. The strength of the lateral confinement in different QWW's and a QW-reference is essentially equal in high magnetic fields, dominated by the magnetic field. Observation of a remaining energy blue shift at high magnetic fields can only be due to effects other than lateral quantum confinement.

EXPERIMENTAL DETAILS

We have fabricated n-type (Sn) modulation doped strained QWW's (down to 100 Å width) from a 50 Å thick and 1.5% compressively strained $InAs_{0.48}P_{0.52}/InP$ quantum well (QW) by electron beam lithography, selective wet etching and MOVPE-overgrowth (see the schematic diagram in Fig. 1). The original quantum well structure was grown by chemical beam epitaxy. Several wire patterns including a unetched quantum well reference were fabricated on the same wafer. The well width inhomogeneity within the original quantum well was negligible. The lateral QWW width was determined by SEM measurements. The fabrication technique is similar to that used for undoped lattice matched InGaAs/InP QWW's.[7] The high magnetic field (28T) measurements were performed in the Faraday configuration using a 10 MW hybrid magnet at the High Magnetic Field Laboratory, Grenoble. We used a bath cryostat, which was pumped down to 2K. The field was applied in the z-direction, perpendicular to the original QW. The samples were excited using the 514.5 nm line from an Ar+ -ion laser, with the laser light coupled to the sample using a optical fiber (600 μm core diameter). The luminescence was collected with the same optical fiber and detected with a cooled Ge-detector using a conventional lock-in technique. The excitation density

was approximately 0.1 W/cm^2 for the 100 Å wide wire and 0.025 W/cm^2 for the wider QWW's and the reference QW. Undoped lattice mismatched InAsP/InP and lattice matched InGaAs/InP quantum wires have previously been measured under similar conditions.

EXPERIMENTAL RESULTS

Fig. 2. shows low-excitation magneto-luminescence spectra of the doped strained InAs$_x$P$_{1-x}$/InP QWW's and QW-reference. There are clear blue shifts in the zero field spectra for narrow QWW's. At high magnetic field the spectra of the QW-reference and the 480 Å wide QWW's split into Landau levels with a linear shift with the magnetic field. The splitting occurs when the cyclotron energy is larger than the line broadening. The splitting point is somewhat higher for the 480 Å wide QWW's than for the QW-reference. This is due to the lateral confinement potential which reduces the magnetic field effect on the electronic structure at low field strength and also to an additional broadening in QWW's. There is Gaussian line broadening of the Landau levels in both the QW and the QWW's. Additional line broadening occurs in the QWW's due to wire width fluctuations, interface defects and impurities introduced by the lithographic technique.[8] The wire width fluctuations occur both within wires and between wires. The intrawire fluctuation for this fabrication technique is approximately 7 Å, while the interwire fluctuation is approximately 20 Å.[8]

We can resolve the subband (Landau level) shifts in the 250 Å sample with deconvolution using an admixture of Gaussian and Lorentzian line shape. The transition energies of the 250 Å wide QWW's and the QW-reference are displayed in Fig. 3. One can easily see that the two lowest subband transitions, e11-h11 and e12-h11, have merged into Landau level transitions 0→0 and 1→0 at high magnetic field in the 250 Å wide QWW's (n_e→n_h, where n_i is the Landau level quantum number in the conduction and valence band, respectively). Note, that the third subband transition, e13-h11, still has a strong quantum wire subband character up to 20 T. This is a clear effect of the lateral confinement potential. The magnetic field effect can be treated as a perturbation if the energy separation between a higher and lower subband is much larger than the 2D-Landau level splitting.

The effect of the lateral potential is even more apparent in the 100 Å wide QWW's. No splitting can occur in the 100 Å wide wire due to the strong lateral confinement. The total shift of the main peak up to 28 T is only around 5 meV.

Furthermore, the QWW's spectra show a clear increasing blue shift relative the QW-reference. This is well documented in the literature and is partly induced by the lateral confinement. Note in Fig. 3 the striking result that a rigid energy shift between the Landau fan charts in the QWW's and the QW-reference still remains even at very high magnetic fields (28 T). This is in sharp contrast to lattice matched QWW's where the energy shift between differently wide QWW's disappears at high magnetic fields. This can be seen in the inset to Fig. 3, where the transition energy for the two lowest subbands in the 200 Å and 350 Å wide undoped lattice-matched InGaAs/InP QWW's are plotted. The excitation density was in this case 5 W/cm², high enough to create a carrier density with the ability to populate several subbands.

We interpret the rigid energy shift between the Landau levels fan charts for the QWW's and the QW-reference, to be due to an additional strain energy shift of the InAsP band gap in the QWW's. The rigid energy shifts, ΔE_z, are around 24 and 10 meV for the 250 Å and the 480 Å wide lattice mismatched InAsP/InP QWW's, respectively. A uniform biaxially or three-directional compresively strained QWW should not be sensitive to the wire width. Our results therefore indicate a wire width dependent non-uniform strain distribution. These observations are consistent with experimental results we previously reported for undoped strained QWW's, see Fig. 4.[9,3]

DISCUSSION AND CALCULATIONS

I. Strain distribution calculations

We calculate the strain distribution of the lattice mismatched (110)-oriented quantum wires by the finite element method (FEM). The x, y and z-axis are oriented in the lateral direction, in the wire direction and in the growth direction, respectively. Fig. 5 shows a three dimensional plot of the strain distribution ε'_{zz} and ε'_{xx} on the cross section of a 400 Å wide QWW. The origin is in the centre of the QWW. ε'_{yy} is -1.5%, i.e lattice coherence between the QWW and the InP substrate in the wire direction. The off-diagonal terms are zero due to the symmetry in this case. One can clearly see that the strain distribution is non-uniform in the QWW. The coherence restriction at the interfaces induces a strain gradient which penetrates toward the centre of the wire. The gradient has a relatively larger impact on the central region for narrow wires. As a result the strain tensor element in the centre of a 400 Å wide QWW ε'_{zz} decreases to 1.43% expansion, and ε'_{xx} decreases to -1.31% compression. This should be compared with $\varepsilon'_{zz} = 1.67\%$ and $\varepsilon'_{xx} = -1.5\%$ for the

biaxially strained QW-reference. The calculations show that the deformation near the origin of the wire approach biaxial strain distribution when the QWW width is increased, i.e. asymptotically approaching the QW-reference. The calculations show also that non-uniform strain is present in the barrier, see Fig 5. Highly non-uniform strain distribution in both the QWW and the barrier is energetically favourable. This is dependent on the stiffness constants of the materials, which in this case are very close. This privets a uniform hydrostatic compression even for a symmetrical cross section. The coupling and non-parabolicity in the valence band is thereby in reality reduced in comparison to the rigid barrier model where the InAsP wire region is uniformly hydrostaticly compressed by InP barrier.

II. Strain effects

For strained quantum wells, the strain effect on the electronic structure can be divided into hydrostatic strain energy $a(\varepsilon'_{xx}+\varepsilon'_{yy}+\varepsilon'_{zz})$ and shear strain energy $b(-2\varepsilon'_{zz}+\varepsilon'_{xx}+\varepsilon'_{yy})$, where a and b are the corresponding deformation potentials. For QWW's, the hydrostatic strain energy is increased, while the shear strain energy is decreased. The increased hydrostatic energy enlarges the gap between the conduction band and the average valence band. The decrease in shear strain will reduce the splitting between the light and the heavy-hole band in the valence band. Both effects result in an increased band gap. The shear strain decrease is however the dominant part for the bandgap increase. The main effect of the non-uniform strain distribution is on the valence band.

To estimate the strain effect on the electronic states in the QWW's we solved the 2D Schrödinger equation with a Fourier expansion method. For the valence band we use a strain incorporated 6x6 $k\bullet p$ Hamiltonian matrix. First we calculated the transition energies for a QWW with the fully non-uniform strain distribution displayed above. Secondly, we calculated the transition energies for a uniform biaxial strained QWW, i.e. the same strain distribution as for the QW-reference. In the latter calculation, we obtain only the quantum confinement shift. The difference in energy between the two calculations gives the strain energy shift. The result of these calculations is displayed as the solid line in Fig. 4.

The good fit to the experimental data shows that we have accurately measured the increased strain energy in both undoped and doped lattice mismatched QWW's. The fact that the strain shifts

in the doped QWW's are close to the undoped QWW's and to the calculated strain shift, shows that we in this case do not need to consider relative shifts due to the electrostatic potential created by the charge transfer in the doped structures. The strain energy shift is a major component of the blue shift in undoped and modulation doped lattice mismatched InAsP QWW's.

III. SPECTRAL PROFILE

The strain energy gives an almost rigid energy blue shift of all 1D-subbands observed in the luminescence spectra. The conduction band offsets are relatively little affected by the strain shift of the band gap (only a few meV). Thus the subband quantum confinement energies in the conduction band can, with a good approximation, be estimated using a uniform strain model. The observed blue shift in the luminescence spectra is therefore mainly due to an increased band gap, not an increased quantum confinement. This can be seen in Fig. 6 where we display the calculated subband energy position for a 250 Å wide -uniformly biaxially strained- QWW. The energy positions were calculated solving 2D Schrödinger equations incorporating both a uniform biaxial strain distribution and the magnetic field. The calculated transition energies are given relative to the zero field transition energy of a biaxial strained QW, whereas the experimental values are given relative to the zero field intersection energy of the high magnetic field Landau fan chart (E_z in Fig. 3). In the calculation we have used the effective masses of the QW-reference. The QW-reference effective masses can, due to off-diagonal transitions, directly be determined in the Landau level fan chart to $m_e^* \approx 0.088 m_0$ and $m_h^* \approx 0.130 m_0$.[6]

We have now gained valuable information, such as the effective electron mass and the subband energy levels, to be able to estimate the Fermi level and explain the zero field luminescence spectra. The carrier concentration in the QW can be determined from the number of filled Landau levels and their linear magnetic field dependent degeneracy. The magnetic field oscillations occurring in the lowest Landau level in the QW are due to oscillations of the particle self energy.[10] The lowest Landau level luminescence peak position is slightly increasing for integer filling factor (see arrows pointing at the lowest Landau level in the QW in Fig. 3). These oscillations are weaker and/or smoother in the QWW's making them less clear. We find that the carrier concentration, N_{QW}, in the QW is approximately equal to 2×10^{12} cm^{-2}. There is only one confined subband in

the conduction band and we can ignore the valence band Fermi level due to the low photo-excited carrier density. Hence the quasi Fermi-level in the luminescence spectra is given by: $E_F^{PL}=E_z+E_F{}^c=E_z+\pi\hbar^2N_{QW}/m_e^*$. E_z is the 2D band gap energy determined by extrapolating the Landau-fan to zero field and $E_F{}^c$ is the conduction band Fermi level. The calculated quasi Fermi level is approximately 54 meV above E_z. This corresponds very well to the observed threshold in the high energy slope of the zero field photoluminescence spectra, as seen in Fig. 7. The threshold is a direct indication of the Fermi-level.[11] The Fermi level position can directly be determined in the luminescence spectra as there exist intensity contributions from impurity assisted indirect processes with high energy electrons. These indirect transition processes contributes with intensity up to the conduction band Fermi-level, where upon the intensity rapidly drops (in a scale of k_BT). The existence of such transitions also explains the offset between E_z and the main intensity peak in the spectra. The transitions will broaden and shift the spectral profile to the high energy side, by subtracting the intensity from low energy side and adding it to the high energy side.[11] The tail on the low energy side of E_z is due to the usual band tailing effect induced by the impurity disorder of the host lattice.

We now continue to estimate the Fermi-level in the QWW's assuming that the depletion width, l_X, is close to the wire width, L_x .[12] Thus, we assume that the depletion depth, l_z, is constant and only the depletion width, l_X, is dependent of and equal to the wire width, see inset to Fig. 7. The carrier concentrations in the wires are thereby 5×10^6 cm^{-1} and 9.6×10^6 cm^{-1} for the 250 Å and 480 Å wide wire, respectively. The Fermi-level position in the photoluminescence spectra is, $E_F^{PL}=E_z+E_{hh}+E_F{}^c$. E_z is the experimental zero field intersection energy of the high magnetic field Landau fan chart. $E_F{}^c$ is given by: $N_{QWW}=\Sigma(2/\pi\hbar)(2m_e^*(E_F{}^c-E_{nznx}(L_Z,L_X))^{1/2}\Theta(E_F{}^c-E_{nznx}(L_Z,L_X))$, where $m_e^*=0.088m_0$ is the in-wire effective electron mass and Θ is the Heaviside's step function. The zero-field lateral quantum confinement induced energies in the conduction band, $E_{nznx}(L_Z,L_X)$, and valence band, E_{hh}, are estimated solving 2D Schrödinger equations, assuming a uniform biaxial strain distribution (pure quantum confinement shift). The calculated Fermi-level thresholds in the zero field spectra are 63 and 59 meV above E_z for the 250 Å and 480 Å wide QWW's, respectively. The calculated quasi Fermi level positions corresponds very well with the threshold observed at the high energy slope of the zero field PL-spectra, see Fig.

7. Thus we can, with a good approximation, use a uniform strain distribution in the calculation of the conduction band Fermi-level in the QWW's.

The strong similarity between the zero field spectral profile of the QW-reference and the QWW's, is due to line width broadening and the reduced transition matrix elements for the off-diagonal transitions between higher levels in the conduction band and the lowest level in the valence band. An increased broadening will reduce the strong singularities which are significant for the 1D-density of state. The 1D-density of state will be smeared out and only show oscillation around the 2D-density of state.[12] The broadening of the 1D-subbands has a minor effect on the absolute position of the Fermi level. It is important to note that the resemblance between the QW and QWW's spectral profile only exist near zero field. The strong lateral confinement has a large impact on the development of the density of states in the magnetic field, as seen in the magneto-luminescence spectra in Fig. 2.

CONCLUSIONS

We have found that the wire energy blue shift in lattice mismatched quantum wires, relative the quantum well reference, partly remains at high magnetic fields. Our calculations shows that the remaining energy blue shift at high magnetic field is due to the strain energy increase of the QWW bandgap. The strain distribution is intrinsically non-uniform and wire width dependent despite the uniform composition of the wire region. For QWW's, the hydrostatic energy is increased, while the shear strain is decreased. Both components enlarge the band gap. The main strain effects are on the valence band. A non-uniform strain distribution is also present in the barrier, which prevents a uniformly hydrostatically compression of the wire region even for small cross sectional aspects ratios and despite the fact that the wire region is completely embedded in InP. Furthermore, the conduction band offsets are relatively little affected by the non-uniform strain shift of the band gap. The subband energies in the conduction band can thereby be estimated using a uniform strain model. The zero field luminescence line widths of the QWW's are in range of the conduction band Fermi level, i.e. high energy electrons up to the Fermi-level contributes to the intensity. The quantum wire conduction band Fermi level can, as a good approximation, be calculated assuming a uniform biaxial strain distribution and a depletion width in the modulation doped area in the range of the wire width.

T. Yamauchi, T. Takahashi, J. N. Schulman, and Y. Arakawa, IEEE J. Quantum Electron. vol. 29, 2109, 1993 and references therein

E. Yablonovitch and E. O. Kane, IEEE Lightwave Technol. vol LT-4, 04-506, 1986

M. Notomi, J. Hammersberg, H. Weman, S. Nojima, H. Sugiura, M. Okamoto, T. Tamamura, and M. Potemski, unpuplished

Y.-P. Chen, J. D. Reed, W. J. Schaff, and L. F. Eastman, Appl. Phys. Lett. 65, 2202 (1994)

L. De Caro, L. Tapfer, Phys. Rev. B. 49, 11 127 (1994)

S. K. Lyo, E. D. Jones and J. F. Klem, Phys. Rev. Lett. 61, 2265, 1988

M. Notomi et al Appl. Phys Lett., 58, 720 (1991)

M. Notomi, M. Okamoto, and T. Tamamura, J. Appl. Phys. 75, 4161, 1994

J. Hammersberg, M. Notomi, H. Weman, M. Potemski, H. Sugiura, M. Okamoto, and T. Tamamura, Seventh Int. Conf. InP and Rel. Mat., Sapporo, Japan, May 9-13, 1995, page 315

0 S. Katayama and T. Ando, Solid State Commun.70, 97 (1989)

1 S. K. Lyo and E. D. Jones, Phys. Rev. B 38, 4113 (1988)

2 G. Bastard, J. A. Brum, R. Ferreira, Solid State Phys. vol. 44, page 388,1991
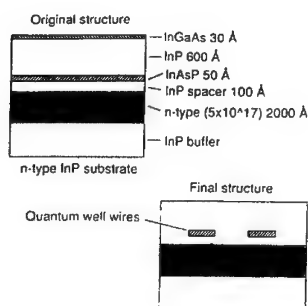
FIG. 1. A schematic diagram outlining the original single quantum well structure and the final quantum well wire structure. The original structure contains a 1.5% compressively strained quantum well.
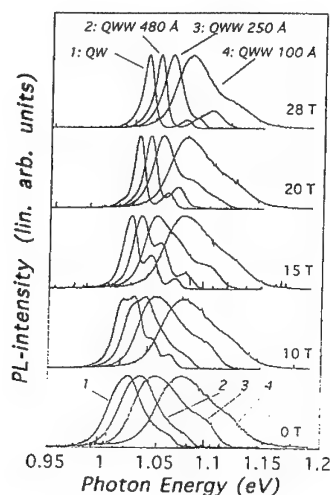
FIG. 2. Magneto-luminescence spectra of n-type modulation doped and lattice mismatched $InAs_xP_{1-x}/InP$ quantum well wires (480, 250 and 100 Å wide) and the quantum well reference.
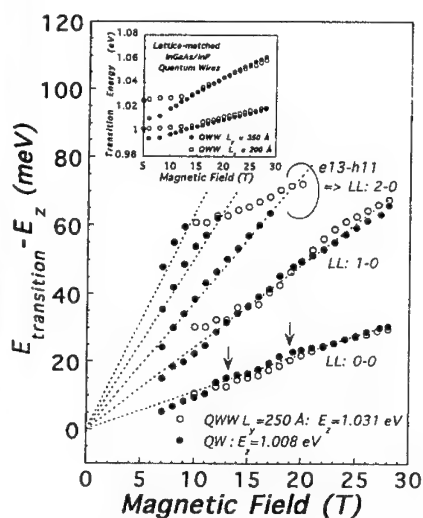
FIG. 3. The transition energy position as a function of magnetic field for n-type modulation doped lattice mismatched quantum well wires (250 Å wide) and the quantum well reference. The transition energy is given relative to the zero field intersection energy of the high magnetic field Landau fan chart. The inset shows the transition energies as a function of magnetic field for lattice matched $In_{0.53}Ga_{0.47}As/InP$ quantum well wires
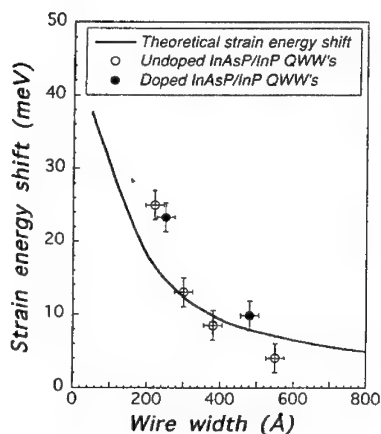
FIG. 4. Wire width dependent strain energy shift. The solid line shows the calculated enhancement of strain energy due to a non-uniform strain distribution (FEM) present in the wires. The experimental values are given by the rigid energy shift of the Landau level fan chart.
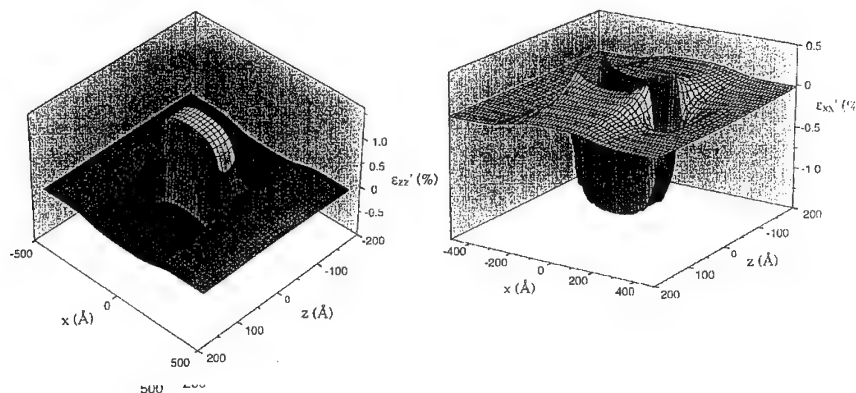
FIG. 5. Strain distribution for a $L_x = 400$ Å wide wire ($L_z=50$ Å). The vertical axis is (a) ε_{zz}' (b)ε_{xx}'. The wire region is ranging from -25 to 25 Å and -200 to 200 Å.
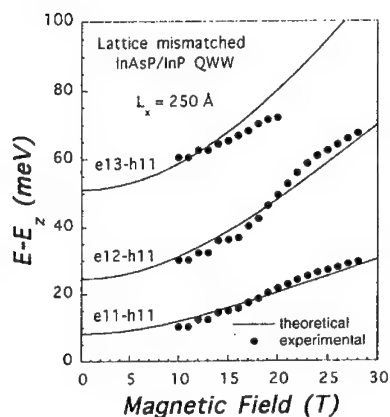
FIG. 6. The subband transition energy position as function of magnetic field. The theoretical calculations show how the 1D subbands merge into Landau levels for a *uniform biaxial strained* quantum well wire (250 Å wide). For the calculated transition energies, the reference energy Ez is the transition energy of a biaxially strained quantum well. The reference energy, E_z, for the experimental values is the zero field intersection point of the high magnetic field Landau level fan chart, see Fig. 2. The ΔE_z values are displayed in Fig. 4.
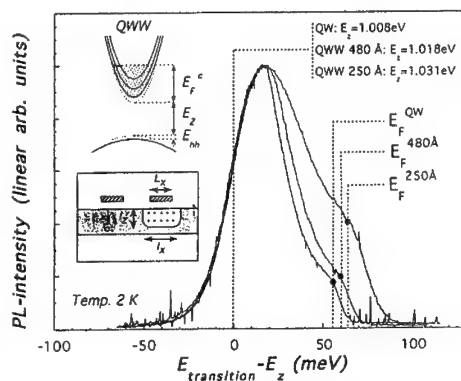
FIG. 7. Zero field photoluminescence spectra of the n-type modulation doped lattice mismatched quantum well wires (480 and 250 Å wide) and the quantum well reference. The inset contains information about the parameter notation used in the text.

Optical studies of $Ga_xIn_{1-x}P$ multiple quantum wires grown by a strain induced lateral ordering process

P. Dua, S. L. Cooper

Department of Physics and Frederick Seitz Materials Research Lab,oratory
University of Illinois at Urbana-Champaign, Urbana, IL 61801, USA

A. C. Chen, K. Y. Cheng

Department of Electrical and Computer Enginering and Microelectronics Laboratory,
University of Illinois at Urbana-Champaign, Urbana, IL 61801, USA

Abstract: We report Raman scattering, continuous-wave PL and time-resolved PL measurements of $Ga_xIn_{1-x}P$ / GaAs multiple quantum wire arrays grown via a novel strain induced lateral ordering process. Optical polarization studies and resonance Raman measurements indicate that the carriers in these structures are confined to 1-dimension by a strong composition modulation in the growth plane. Luminescence arising from both free and localized excitons is observed and a preliminary analysis of lifetime measurements is presented. These SILO grown systems appear to be strong candidates for true quantum wires.

Increasing use of opto-electronic devices in telecommunications, publishing, scanning and display technologies, has caused a drive to increase device efficiency by reducing threshold power requirements, attaining higher differential gain and modulation bandwidth, and improving device stability and lifetime. To these ends, band-gap engineered lower dimensional heterostructures have significant performance advantages compared with conventional double-heterostructure counterparts.[1,2] These improved device characteristics are due primarily to the modification of the band structure and density-of-states (DOS) in low dimensional systems.

Very early on it was realised that the 1D DOS of quantum wires (QWR) would afford improvements over quantum well (QW) devices.[3-5] But despite the obvious advantages, researchers have been unable to fabricate QWR structures in a controlled, repeatable manner, with quality close to present day QW devices. Almost all the conventional techniques for QWR fabrication create wires with certain inherent shortcomings, such as surface and interface defects, insufficient confinement, or low areal wire density.

Recently, Cheng et al. showed[6] that quantum wires with a periodicity as small as ~200Å can be achieved in GaInP and GaInAs alloys through strain induced lateral composition modulation within the growth plane. The growth method involves growing a short period superlattice (SPS) of incommensurate bilayers of $(GaP)_{2-\delta}/(InP)_{2+\delta}$ on a [001]-oriented on axis GaAs substrate. The resulting elastic stress and strain fields generated by the global average strain have been shown[7] to render an alloy with lateral composition modulation more thermodynamically stable than a random homogeneous alloy for certain III-V alloy systems. Composition modulation in these systems is known to occur preferentially in the [110] direction in the growth plane, resulting in alternating In- or Ga-rich regions extending along [$\bar{1}$10] direction. The band edge modulation accompanying the composition modulation, together with a quantum well confinement in the [001] growth direction, confines the carriers in the lower band gap In-rich "wire" regions along the [$\bar{1}$10] direction.[8]

Figure 1 shows a schematic diagram of a typical multiple QWR structure. As the composition varies about the average SPS value of x = 0.525 in the [110] direction, so does the bandgap of the material. The In-rich wire regions are compressively strained while Ga-rich barrier regions are under tensile strain. These structures have been examined by cross-sectional TEM. The plan-view TEM photo shown in Figure 2 reveals that the QWRs are characterized by an average length on the order of 3000Å and an average width of ~200Å in the growth plane. That the contrast modulation in the TEM image is indeed due to lateral composition variation is confirmed by energy dispersive X-ray spectroscopy (EDS).[8] A lower limit for the amplitude of the composition modulation in the $Ga_xIn_{1-x}P$ alloy was determined, using a 10Å probe electron beam, to be $x_{max} - x_{min} > 0.2$.
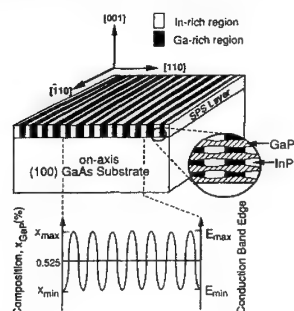
FIG. 1. Diagram illustrating the lateral superlattice structure resulting from the SILO process. Also shown is the composition and band-gap modulation along [110] direction.
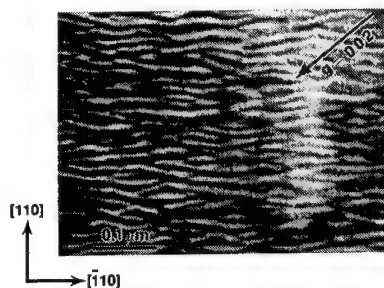
FIG. 2. Plan-view TEM photo of the $Ga_xIn_{1-x}P$ superlattice structure. The image was taken with the g-vector at 45° from the [110] and [-1 1 0] directions to eliminate the effects of strain from the image.

Photoluminescence from these wires is observed at 1.72 eV (see figure 3). By comparison, the bandgap for a random x = 0.525 $Ga_xIn_{1-x}P$ alloy is known to be 1.94 eV. The 200 meV red shift of QWR PL compared with the homogeneous bulk alloy is thought to be due to the large composition modulation. Shown in figure 3 are polarized PL measurements at liquid helium temperatures. These measurements reflect the polarization dependence of optical transitions for carriers in the wire regions only, as care was taken to excite the luminescence with an excitation energy of 1.78 eV to avoid generating carriers in the well-barriers or Ga-rich barrier regions.

We find that the PL intensity is strongly anisotropic with respect to both the incident laser polarization and the collected luminescence polarization. This would be expected for free exciton luminescence, but we believe that the luminescence in these wires is associated with localised excitons based on our time-resolved studies. Optical anisotropy in quantum wires has been experimentally[9,10] and theoretically shown to arise due to the effects of the two-dimensional confinement potential on the interband matrix element. Bockelmann and Bastard[11] have demonstrated that confinement-induced mixing between light- and heavy-hole states is crucial for anisotropy of interband transitions. An ~80% polarized luminescence from our samples therefore indicates narrow wires with a large confinement potential.
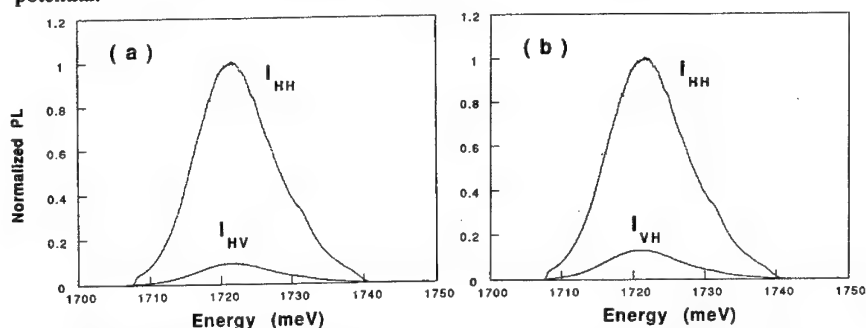
FIG. 3. Quantum wire PL intensity dependence upon a) luminescence polarization and b) incident laser polarization.

One needs to be cautious in assigning all the luminescence polarization to carrier confinement, because other mechanisms, such as residual strain and Cu-Pt type ordering, have also been known to result in optical anisotropy. For example, in many III-V ternary alloys, inhomogeneities have been found in the layers, not because of poor growth, but rather due to the thermodynamic properties of the alloys themselves. Under certain growth conditions, Cu-Pt type long range ordering is known to occur when Ga and In atoms reside

preferentially in alternate [111] planes.[12] This type of ordering lowers the band gap (by as much as 90 meV)[13] and leads to anisotropic luminescence.[14]

To estimate the degree of Cu-Pt ordering in these SILO grown wires, we studied both the PL power dependence and the PL excitation (PLE) spectra of wires and reference quantum wells with the same thicknesses. According to a recent model,[15] in the presence of Cu-Pt ordering there is expected to be a distribution $F(\eta)$ of ordered domains identified by a parameter η which characterizes the degree of ordering in that domain. Both a substantial shift between the PL and PLE peak energies, and a shift in the PL peak with increasing power, is expected in such systems due to the width of $F(\eta)$. However, we did not observe any noticeable power dependence of PL energy in our SILO grown QWR samples (see figure 4). Also, the PL Stokes shift from the PLE was less than ~15 meV. This suggests that there is not too much Cu-Pt type ordering in these materials.
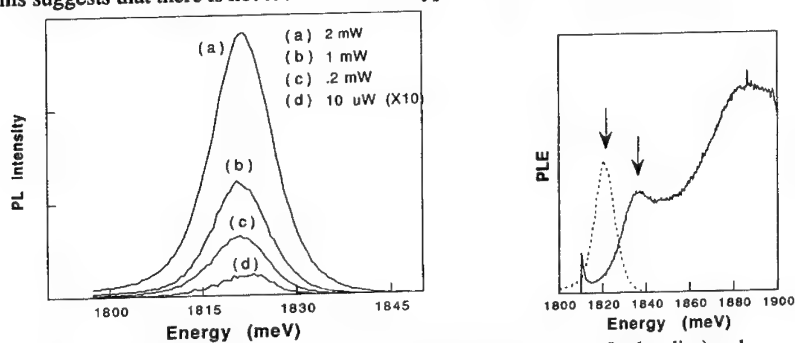
FIG. 4. Reference quantum well: a) PL power dependence and b) PL (broken line) and PLE (solid line).

We have also studied the carrier kinetics in these systems using time-resolved photoluminescence. The kinetics of photoexcited free excitons in heterostructures have been extensively studied by a number of authors,[16] with a special focus on the role of interface roughness. Interface roughness has been recognized[17] to affect the exciton kinetics in two ways depending on whether the size of the regions with constant width is larger or smaller than the exciton Bohr radius. In regions larger than the Bohr radius, the excitons behave as free particles and are ballistically scattered at the boundaries. Interregion exciton diffusion will occur, however, and influence the decay kinetics of the excitons.[18-20]

In regions having sizes comparable to or smaller than the Bohr radius, the mobility of the exciton is limited and the exciton can be localised by potential fluctuations associated with interface roughness.[21,22] There exists a dynamic equilibrium between free and localised excitons that adds to the richness of the recombination kinetics in heterostructures.

It is commonly believed that the main part of the observed luminescence originates from the recombination of FE's trapped at these interface defects.

The SILO grown quantum wires are spontaneously ordered structures and hence, they are expected to have associated size fluctuations. This fact is borne out both by the TEM pictures and by the PL peak width of ~38 meV, which is substantially larger than PL widths in high quality quantum wells of comparable size. Figure 5 shows the PL specta from these wires for different delays after excitation with 4 picosecond laser pulses. We observe that the luminescence peak is at 1750 meV immediately after excitation, but shifts to 1728 meV at longer times. This behavior reflects the trapping of free excitons after excitation. These bound excitons then slowly migrate to sites with the lowest energies via thermally activated hopping, whereupon the PL peak position moves to 1722 meV.
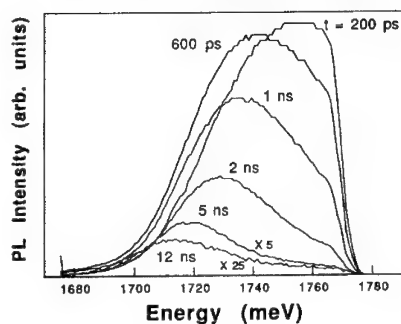
FIG 5. QWR PL spectra for different delay times after excitation with 4 ps laser pulse.
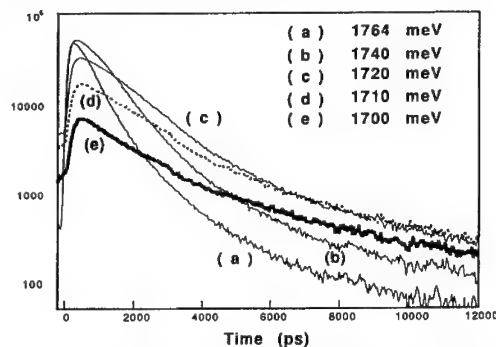
FIG 6. Quantum wire PL decay measurements for a range of energies near the PL peak (1720 meV) for T=4.2K.

The luminescence decay at different energies (see figure 6) around the PL peak is also interesting. At energies higher than 1750 meV, the decay is nonexponential and free-exciton-like, in agreement with recently proposed models that predict a non-exponential decay for free excitons in thermal equilibrium with free carriers.[23,24] Around 1720 meV, the decay can be fit with two exponentials, with the longer lifetime process corresponding to bound exciton recombination dominates recombination near the peak PL energy, but fades out at the lower energy tail of the luminescence. At lower energies, the decay is nearly exponential, which suggests it might be controlled by nonradiative channels.[24]

These wires have large exciton binding energies, as evidenced by the PL peak shift, that makes them stable even at relatively high temperatures. The activation energy associated with thermally activated hopping of the bound excitons appears to be quite large

as well. This explains the increasing importance of the long lifetime processes in the PL peak with increasing temperature (shown in figure 7). The bound excitons are rendered almost immobile at very low temperatures. As the temperature is increased, bound excitons are able to relax down to sites with lower bound-exciton-energies. In other words, there is a larger number of bound excitons contributing at the PL peak energy at elevated temperatures.

FIG.7. Temperature dependence of luminescence decay from QWR's.
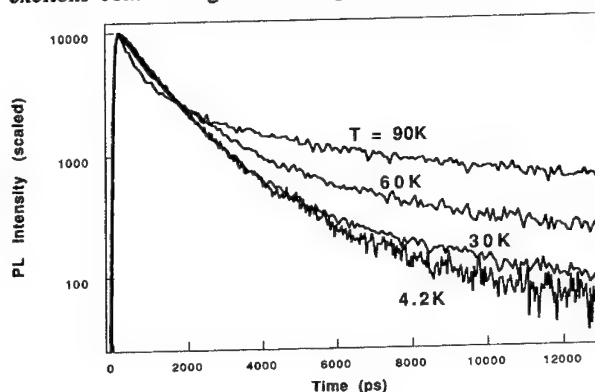
To better understand and model the SILO grown composition modulated quantum wires, we need a tangible estimate of certain parameters such as a) the extent of composition modulaton and b) the modulation profile (see figure 8). We have done some preliminary measurements towards this end using resonance Raman spectroscopy.
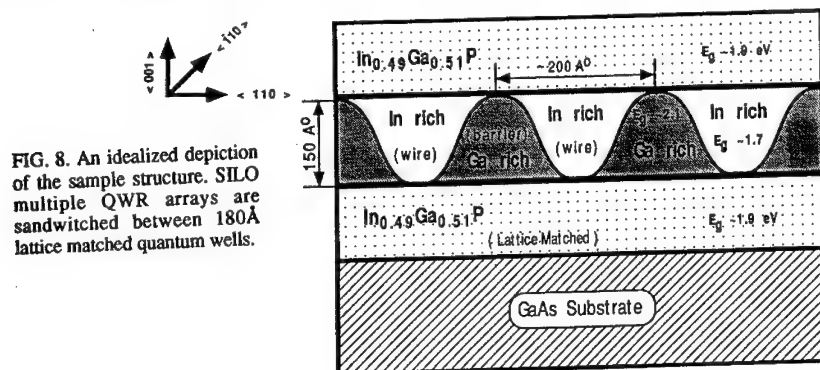
FIG. 8. An idealized depiction of the sample structure. SILO multiple QWR arrays are sandwitched between 180Å lattice matched quantum wells.

Figure 8 portrays an idealized depiction of the sample structure. By selectively tuning the laser to band gaps of different parts of the composition modulation, we can effectively

study excitations associated with different parts of the physical structure. In particular, the energy of the GaP like LO phonon in $Ga_{1-x}In_xP$ alloys has been observed to depend upon the In fraction 'x' as[25]

$$\omega_{LO}(GaP) = 404.99 - 38.97x - 18.18x^2 \ (cm^{-1}) \qquad ...(1)$$

Thus, by studying the frequency of the GaP-like phonon as we tune the excitation frequency, we can estimate the composition profile of the structure. From the results shown in figure 9, we observe that the GaP like LO phonon peaks originating from the Ga-rich barriers and In-rich wires exhibit a 7 cm^{-1} energy difference. Therefore, from eqn.(1), we estimate approximately 38% Ga in the wire regions, 60% Ga in the barrier regions and a squarish, rather than sinusoidal, composition modulation.
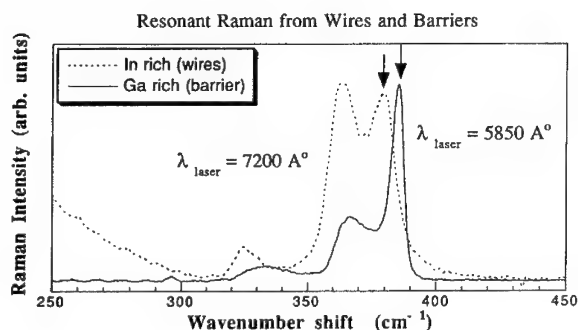
FIG. 9. Resonant Raman spectra corresponding to two extreme compositions. Arrows indicate the GaP like LO phonons. Also note the stronger InP like LO phonon from the In rich wires.

In conclusion, we have studied narrow quantum wires grown by a novel SILO process with PL and time-resolved measurements. We observe luminescence from excitons localized due to wire-width fluctuations, but the wires seem very promising due to their large radiative efficiencies and high wire density (50% surface coverage). A strongly polarized luminescence indicates srong carrier confinement.

References:

[1] J. N. Holonyak, R. M. Kolbas, R. D. Dupuis, and P. D. Dapkus, IEEE J. Quantum Electronics **QE-16**, 170 (1980).

[2] Y. Arakawa and A. Yariv, IEEE J. Quantum Electronics **QE-22**, 1887 (1986).

[3] H. Sakaki, Jpn. J. Appl. Phys. **19**, 95 (1980).

[4] Y. Arakawa and H. Sakaki, Appl. Phys. Lett. **40**, 939 (1982).

[5] M. Asada, Y. Miyamoto, and Y. Suemetsu, IEEE J. Quantum Electronics **22**, 1915 (1986).

[6] K. Y. Cheng, K. C. Hsieh, and J. N. Baillargeon, Appl. Phys. Lett. **60**, 2892 (1992).

[7] F. Glas, J. Appl. Phys. **62**, 3201 (1987).

[8] P. J. Pearah, A. C. Chen, A. M. Moy, K. C. Hsieh, and K. Y. Cheng, IEEE J. Quantum Electronics **30**, 608 (1994).

[9] M. Tsuchiya, J. M. Gaines, R. H. Yan, R. J. Simes, P. O. Holtz, L. A. Coldren, and P. M. Petroff, Phys. Rev. Lett. **62**, 466 (1989).

[10] P. Ils, C. Greus, A. Forchel, V. D. Kulakovskii, N. A. Gippius, and S. G. Tikhodeev, Phys. Rev. B **51**, 4272 (1995).

[11] U. Bockelmann and G. Bastard, Europhysics Letters **15**, 215 (1991).

[12] S. H. Wei and A. Zunger, Phys. Rev. B **39**, 3279 (1989).

[13] R. G. Alonso, A. Mascarenhas, G. S. Horner, K. A. Bertness, S. R. Kurtz, and J. M. Olson, Phys. Rev. B **48**, 11833 (1993).

[14] T. Kanata, M. Nishimoto, H. Nakayama, and T. Nishino, Phys. Rev. B **45**, 6637 (1992).

[15] G. S. Horner, A. Mascarenhas, S. Froyen, R. G. Alonso, K. Bertness, and J. M. Olson, Phys. Rev. B **47**, 4041 (1993).

[16] J. P. Bergman, P. O. Holtz, B. Monemar, M. Sundaram, J. L. Merz, and A. C. Gossard, Phys. Rev. B **43**, 4765 and references therein (1991).

[17] B. Deveaud, J. Y. Emery, A. Chomette, B. Lambert, and M. Baudet, Superlattices and Microstructures **1**, 205 (1985).

[18] H. Stolz, D. Schwarze, W. v. d. Osten, and G. Weimann, Superlattices and Microstructures **6**, 271 (1989).

[19] B. Deveaud, T. C. damen, J. Shah, and C. W. Tu, Appl. Phys. Lett. **51**, 828 (1987).

[20]M. Kohl, D. heitmann, S. Tarucha, K. Leo, and K. Ploog, Phys. Rev. B **39**, 7736 (1989).

[21]G. Bastard, C. Delalande, M. H. Meynadier, P. M. Frijlink, and M. Voos, Phys. Rev. B **29**, 7042 (1984).

[22]J. Hegarty, L. Goldner, and M. D. Sturge, Phys. Rev. B **30**, 7346 (1984).

[23]B. K. Ridley, Phys. Rev. B **41**, 12190 (1990).

[24]W. Pickin and J. P. R. David, Appl. Phys. Lett. **56**, 268 (1990).

[25]H. Lee, D. Biswas, M. V. Klein, and H. Morkoç, J. Appl. Phys. **75**, 5040 (1994).

INTERSUBBAND CARRIER RELAXATION IN GaAs/AlAs 20 NM WIDE QUANTUM WIRES

T. Sogawa, S. Ando, H. Ando, and H. Kanbe

NTT Basic Research Laboratories

3-1 Morinosato-Wakamiya, Atsugi-Shi, Kanagawa 243-01, Japan

Effects of intersubband carrier relaxation on photoluminescence (PL) rise time are investigated in GaAs/AlAs 20-nm-wide quantum wires. The time evolution of the PL intensity is found to vary significantly, depending on the excited conduction subbands. The experiments demonstrate that intersubband carrier relaxation from the second conduction subband to the first subband causes a delay time of 30-40 psec between excitation and the peak of the PL intensity, while intrasubband carrier relaxation causes no significant delay.

INTRODUCTION

Low-dimensional quantum structures such as quantum wires (QWRs) and quantum dots have attracted a lot of attention in view of their physics and potential device applications. It has been predicted that semiconductor lasers including QWRs or dots in the active regions will greatly improve device performance due to the sharp density of states (1). On the other hand, it has been pointed out that phonon bottleneck effects may degrade luminescence efficiency as well as time response (2). However, this bottleneck phenomenon has not been clearly observed up to now probably because of poor sample quality and weak lateral quantum confinement. It has been theoretically predicted that the carrier relaxation process due to phonon scattering and carrier-carrier scattering significantly depends on the confinement dimension of the structures (3-6).

We have reported the fabrication of GaAs/AlAs trench-buried QWRs with a lateral size of about 20 nm (7-9), which is small enough to cause wide energy separation between the first and second conduction subbands as large as the LO phonon energy of 36 meV. We have observed clear one-dimensional (1-D) subband structures in photoluminescence excitation (PLE) spectra of the QWRs. Here, to investigate the intersubband carrier relaxation in the GaAs/AlAs 20-nm-wide rectangular QWRs, we measure the dependence of PL rise time on the excited 1-D conduction subband.

EXPERIMENTAL

Fabrication of Rectangular QWRs

Trench-buried QWRs were grown on V-grooved (001) GaAs substrates by low-pressure (76 torr) metalorganic chemical vapor deposition. 150-nm-pitch gratings composed of 600 grooves were patterned along the $\langle \bar{1}10 \rangle$ direction by using electron-beam lithography (JEOL: JBX-6000FE) and wet chemical etching. The growth temperature was 620 °C and the group V/III ratios were 120 for GaAs growth and 220 for AlAs-trench growth. The detailed growth procedure is described in Ref. 7-9. Figure 1 shows a typical cross-sectional shape of the trench-buried QWR. The dark layer grown on the corrugated GaAs substrate corresponds to the AlAs layer that forms a trench structure having (110) vertical sidewalls. In this case, a nearly square 20-nm-wide and 20-nm-thick GaAs wire (bright area) covered by an upper AlAs layer is formed at the bottom of the trench. The thickness of the GaAs wires can be precisely controlled by changing the growth time (7). In this experiment, we prepared approximately 20-nm-wide and 10-nm-thick QWRs, with the emission line separated far from the emission line of the GaAs substrate.

PLE Spectra of QWRs

Figure 2 shows the low-temperature (15 K) PLE spectra together with the PL spectrum for the QWRs. A few mW Ti-sapphire laser light with a focused spot size of 100 μm was used for excitation. The dotted line corresponds to the PL spectrum. The solid and dashed lines are the PLE spectra obtained with incident light polarized parallel and perpendicular to the wires, respectively. In the figure, $(ci\text{-}vj)_{m,n}$ denotes the transition levels between the quantized ith conduction subband ci and the jth valence subband vj, where m and n refer to the indices of quantum confinement in the lateral and vertical directions, respectively. It is observed that the PL peak is Stokes-shifted by about 25 meV, which is comparable with the PL line width. We ascertained that the PLE peak energies slightly decreased (by less than a few meV) when the PLE detection energy was widely shifted to the lower energy side of the PL peak. Thus, the Stokes-shift is attributed to the structural nonuniformities along the wires.

Figure 3 schematically shows the 1-D conduction and valence subband structures. The conduction band can be described by the conventional one-band model, thus, the $c1$, $c2$, and $c3$ subbands are formed by the electron states with indices of $(m, n) = (1, 1)$, $(2, 1)$, and $(1, 2)$, respectively, in the elongated QWRs. On the other hand, valence subbands exhibit complicated characteristics resulting from the heavy-hole (hh) – light-hole (lh) band mixing caused by lateral and vertical quantum confinement (10-12). Since the $v1$ and $v3$ subbands are mixtures of the hh and lh states with indices of $(m, n) = (1, 1)$, these subbands can optically couple with the $c1$ subband (10). As shown in Fig. 2, the $(c1\text{-}v1)_{1,1}$ and $(c1\text{-}v3)_{1,1}$ transitions exhibit strong polarization anisotropy because of the difference in the hh and lh components forming each valence subband. The $v2$ subband is composed of the hh and lh states

with indices of $(m, n) =$ both $(2, 1)$ and $(1, 2)$, thus it couples with the $c2$ and $c3$ subbands. In Fig. 2, the $(c1\text{-}v1)_{1,1}$ and $(c2\text{-}v2)_{2,1}$ transitions are clearly resolved for excitation light polarized parallel to the wires.

Subband Dependence of PL Rise Time

Mode-locked Ti-sapphire laser pulses (time duration of 1 psec) and a streak camera with a monochromator were used to measure the PL dynamics of the QWRs at 15 K. As a few mW laser light (repetition rate of 82 MHz) with a spot size of about 100 μm was used, the excited carrier density was estimated to be about 5×10^{16} cm^3, which is probably smaller than the residual hole density due to the carbon impurities incorporated during growth. Therefore, we expect the PL rise time to be dominantly determined by the electron relaxation process in the conduction band. In the experiment, as indicated in Fig. 3, the wavelengths of the excitation laser light with parallel polarization were tuned at 770 nm for the excitation of only the $c1$ subband (dashed arrow) and at 750 nm for the excitation of both the $c1$ and $c2$ subbands (solid arrows).

Figures 4 (a) and (b) show the time evolution of the PL intensity for the excitation wavelengths (a) 770 nm, and (b) 750 nm. Here, the time traces of the PL intensity at four emission wavelengths (782, 787, 792, and 797 nm) are plotted. The excitation time ($t = 0$) was calibrated based on the simultaneously observed PL peaks of the extremely short emission from GaAs hot carriers around 800 nm. When only the $c1$ subband is excited, in Fig. 4 (a), the delay time between excitation and the PL peak is not clearly observed. On the other hand, the excitation of both the $c1$ and $c2$ subbands significantly causes the delay time, as shown in Fig. 4 (b). The time traces at the wavelengths of 782 nm and 787 nm show delay times of 5-10 psec. Moreover, the time trace at 792 nm, which corresponds to the lower energy side of the PL peak, exhibits a large delay of 30-40 psec.

Figure 2 exhibits that the energy separation between the $(c1\text{-}v1)_{1,1}$ and $(c2\text{-}v2)_{2,1}$ transitions is about 45 meV. Since the energy separation between the $v1$ and $v2$ subbands at the zone center is calculated to be about 10 meV in the 20 nm $\times$ 10 nm QWRs (10), the energy separation between the $c1$ and $c2$ subbands is about 35 meV, which is almost resonant with the LO phonon energy of 36 meV. However, it should be noted that the emission dominantly occurs in the local minima due to the carrier diffusion along wires because the sample has the considerable nonuniformity as wide as 25 meV and the experiment was done under the very weak excitation condition at low temperature. In the local minima, where the lateral width is larger than 20 nm, the energy separation between the $c1$ and $c2$ subbands is smaller than the LO phonon energy, resulting in the off-resonant condition. The effect of the off-resonant condition on the intersubband relaxation should be more significant in the regions with larger lateral width. In Fig. 4 (a), the time trace at the wavelength of 792 nm (the lower energy side of the PL peak) exhibits no delay time, suggesting that intrasubband relaxation for the $c1$ subband electrons is faster than the time resolution of 10 psec. On the other hand, the time trace at 792 nm in Fig. 4 (b) shows the slow

component with the delay time of 30-40 psec. Therefore, this delay time is considered to be caused by the intersubband carrier relaxation process from the $c2$ to $c1$ conduction subbands at the off-resonant wire regions.

CONCLUSION

In conclusion, we investigated the effects of intersubband carrier relaxation on PL rise time in GaAs/AlAs 20-nm-wide QWRs. It has been demonstrated that the PL delay time due to the intersubband carrier relaxation from the second conduction subband to the first subband is 30-40 psec, which is much longer than the intrasubband carrier relaxation time of less than 10 psec. This result shows that the intersubband carrier relaxation process cannot be neglected in the carrier dynamics of QWRs and suggests the significance of bottleneck effects in the 1-D systems.

ACKNOWLEDGMENTS

REFERENCES

1. Y. Arakawa and H. Sakaki, Appl. Phys. Lett., 40, 939 (1982).
2. H. Benisty, C. M. Sotomayor-Torres, and C. Weisbuch, Phys. Rev., B 44, 10945 (1991).
3. U. Bockelmann and G. Bastard, Phys. Rev., B 42, 8947.(1990).
4. L. Rota, F. Rossi, S. M. Goodnick, P. Lugli, E. Molinari, and W. Porod, Phys. Rev., B 47, 1632.(1993).
5. I. Vurgaftman and J. Singh, Appl. Phys. Lett., 62, 2251 (1993).
6. R. Mickevicius, R. Gaska, V. Mitin, M. A Stroscio, and G. J. Iafrate, Semicond. Sci. Technol., 9 (1994).
7. T. Sogawa, S. Ando, and H. Kanbe, Appl. Phys. Lett., 64, 472 (1994).
8. T. Sogawa, S. Ando, and H. Kanbe, Appl. Phys. Lett., 64, 3299 (1994).
9. T. Sogawa, S. Ando, and H. Kanbe, Appl. Phys. Lett., 67, 1087 (1995).
10. H. Ando, S. Nojima, and H. Kanbe, J. Appl. Phys., 74, 6383 (1993).
11. U. Bockelmann and G. Bastard, Phys. Rev., B 45, 1688.(1992).
12. Peter C. Sercel and Kerry J. Vahala, Phys. Rev., B 44, 5681.(1991).
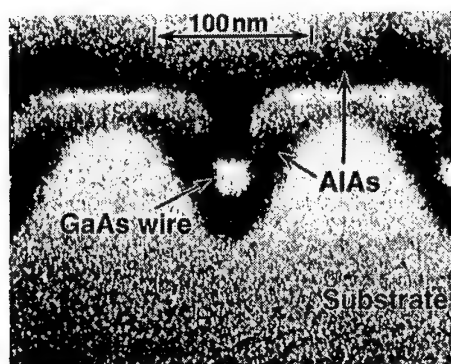
Figure 1. Cross-sectional view of trench-buried QWR observed by high-resolution scanning electron microscopy.
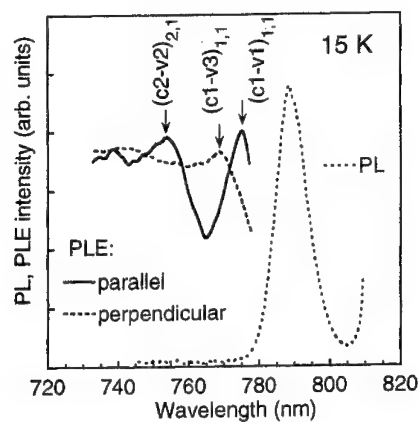
Figure 2. Low-temperature (15 K) polarization-dependent PLE spectra and PL spectra for 20-nm-wide and 10-nm-thick QWRs. Dotted line indicates the PL spectrum. Solid line and dashed line were obtained with incident polarization parallel and perpendicular to the wires, respectively. $(ci\text{-}vj)_{m,n}$ denotes transition levels between the quantized ith conduction subband and jth valence subband, where m and n are indices of lateral and vertical quantum confinement, respectively.
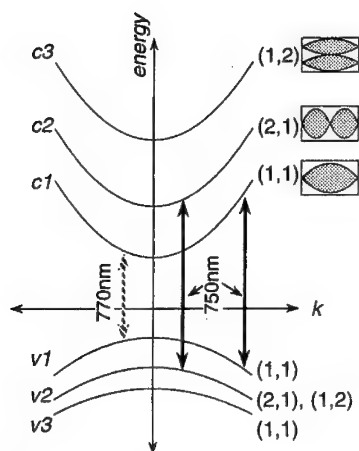
Figure 3. Schematic illustration of one-dimensional conduction and valence subband structures.
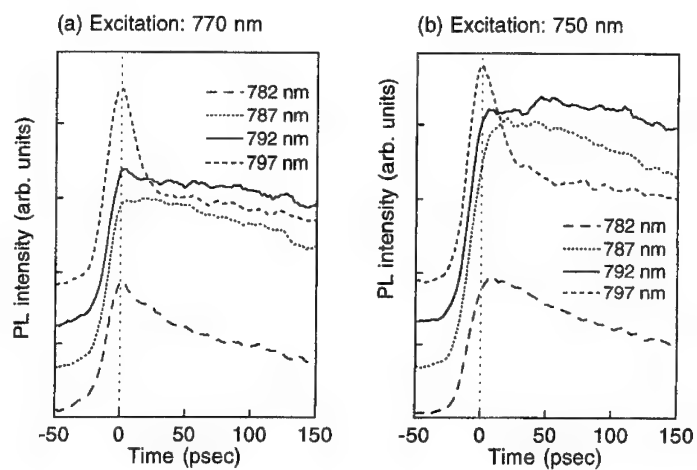
Figure 4. Time traces of PL intensity at various wavelengths for the excitation wavelengths of (a) 770 nm, and (b) 750 nm.

HOPPING TRANSPORT IN TUNNELING STRUCTURES

Yu.B.Lyanda-Geller and J.P.Leburton
Beckman Institute
University of Illinois at Urbana-Champaign, Urbana, IL 61801

ABSTRACT

We study hopping transport in quantum structures with localized electron (hole) states. Two systems are investigated: quantum box superlattice and the interband resonant tunneling structure with confined electron and hole states in electrodes. We show that electric current in a one dimensional (1D) chain of quantum boxes is characterised by a set of zero minima (antiresonances) due to the momentum selection rule for the interaction of acoustic phonons with Wannier-Stark localized electrons or due to the folded phonon gaps. We calculate current-voltage characteristics for resonant interband tunneling structure and demonstrate that phonon-assisted transmission may play considereably lower role in interband structures than in intraband based devices as a result of the symmetry difference between electron and hole states.

INTRODUCTION

Quantum microstructures can be designed to achieve arbitrary spectra of electrons and phonons and are flexible to geometrical confinement providing new windows for technological innovation. In the present paper we address transport phenomena in nanostructures with confined electron states where multiply Negative Differential Resistance occur with high peak to valley ratio. In such systems with localized states electrons move in the direction of the electric field by hopping from one state to another due to scattering.

We discuss two types of structures. One of them is the quantum box superlattice (QBSL) recently proposed to control phonon scattering [1, 2]. We investigate the conductance mechanisms in QBSL and predict a set of minima (antiresonances) in the current-voltage characteristics due to the momentum selection rule for the interaction of acoustic phonons with the Wannier-Stark (WS) localized electrons. We also discuss the onset of antiresonances due to the gaps in folded phonon spectrum and analize resonant hopping of electrons between localized states due to elastic and optical phonon scattering. We find that not only electron but also phonon confinement can be observed in conductance experiments.

Another system we consider is the resonant interband tunneling structure with confined electron and hole states. With improved resolution in crystal growth and delta-doping techniques such structures attracted renewed attention. For example, Negative differential resistance (NDR) due to resonant interband tunneling (RIT) with large peak-to-valley current ratios has been demonstrated in two-terminal devices [3]. Several proposals for RIT-based transistors with important applications in digital and microwave systems have been reported[4]. One of the essential issues for implementing RIT device into practical applications is the ability to control the level of dissipation during the device operation. Specifically, the limit of the valley current in resonant tunneling electronic devices, and, correspondingly, the lowest achievable power dissipation is determined by phonon-assisted transitions. We demonstrate that electron transport in devices with confined electron and hole states may be considered as hopping conductance. We show that the electric current in RIT structures induced by interband phonon transitions may play considerably lower role in device operation than the phonon induced current in structures based on intraband tunneling. We find that the phonon contribution could be substansially reduced by the appropriate choice of the compound semiconductor materials forming the confining channel for electrons in the active region of the device.

HOPPING CONDUCTANCE

Scattering-assisted transport between localized electron and hole states may

be considered as an electron hopping process: carriers interact, for instance, with phonons to hop from one localized state to another. The presence of the electric field creates an imbalance between the net transition of carriers from the left to the right and from the right to the left which results in the charge tranfer. We describe the hopping conductance by the following formula

$$j_z = e \sum_{\alpha,\alpha',N,N'} (z_{\alpha,N} - z_{\alpha',N'}) W_{N,N'}^{\alpha,\alpha'}, \tag{1}$$

where $z_{\alpha,N} - z_{\alpha',N'}$ is the electron displacement (the hopping length) upon the scattering $(\alpha, N \to \alpha', N')$, N stands for the set of indices describing the transverse states, α, α' are indices describing logitudinal states. $W_{N,N'}^{\alpha,\alpha'}$ is the scattering probability. The transverse states are size quantization levels for spatial confinement in QBSL and Landau levels for magnetic confinement of conventional superlattices. Longitudinal states are the Stark ladder levels if the superlattice is in the regime of the Wannie-Stark localization. In resonant tunneling interband devices, the transverse states are 2D components of the electron wavevector, and the longitudinal states are size quantization levels for electrons and holes, respectively. Eq.1 was applied in the past for hopping conductance in disordered doped semiconductors [5] and for conventional superlattices in strong electric field [6].

For elastic processes (due to impurities, surface or interface roughness) the scattering probability is

$$W_{N,N'}^{\alpha,\alpha'} = |V_{N,N'}^{\alpha,\alpha'}|^2 \delta(E_{\alpha N} - E_{\alpha'N'})(f_{\alpha N} - f_{\alpha'N'}), \tag{2}$$

where $E_{\alpha N}$ is the electron energy, $V_{NN'}^{\alpha\alpha'}$ is the scattering matrix element ($|V|^2$ accounts for the number of defects and their correlation), $f_{\alpha N}$ is the nonequilibrium electron distribution function. For phonon-assisted hopping

$$W_{NN'}^{\alpha\alpha'} = \sum_{\mathbf{q}\perp q_z} |C_{N,N'}^{\alpha,\alpha'}|^2 \delta(E_{\alpha N} - E_{\alpha'N'} + \hbar\omega_q)[(f_{\alpha N} - f_{\alpha'N'})N_q - f_{\alpha'N'}(1 - f_{\alpha N})], \tag{3}$$

$C_{N,N'}^{\alpha,\alpha'}$ is the electron-phonon scattering amplitude, ω_q and N_q are the phonon frequency and the occupation number. Eq.(3) accounts for spontaneous emission, emission and absorption of phonons.

Evaluating the current as due to hopping processes, we explicitly take into account the perfect structure of a system, include direct tunneling between wells in a spectrum and wavefunctions of localized states and consider impurities, fluctuations and inelastic scattering as a perturbation. This procedure in many cases may be more adequate for the description of microstructures than the calculation of the current due to direct tunneling. It is especially important when the electric field in a device cannot be considered as a perturbation, for instance, in the regime of the negative differential conductance. Electric-field–independent part of tunneling between electron states also may be conveniently considered as perturbation within hopping conductance formalism.

QUANTUM BOX SUPERLATTICES

In one-dimensional array of quantum boxes (QB) conductance at strong electric fields, in the Wannier-Stark (WS) localization regime, only exists if the transverse energy spacing is equal to the separation of WS levels or differs from it by the phonon energy (Fig.1). As we demonstrate [7], in addition to such resonances due to elastic and optical phonon scattering, acoustic phonon-assisted-hopping leads to zero conductance minima.

One reason for these minima is gaps in the folded phonon spectrum. The dispersion relation for phonons in periodic potential is of the same form as Kronig-Penney dispersion relation for electrons. The phonon spectrum can be considered as linear only at small wavevectors q, while at the Bragg plane the wave velocity is zero and a gap arises. This phenomenon is called the phonon folding. If by energy conservation (Eq.3) the phonon energy $\hbar\omega_q$ falls into the gap, the current vanishes and plateaux with zero conductance are observed in current-voltage characteristics.

Another reason for conductance minima is that amplitudes $C_{N,N'}^{\alpha,\alpha'}$ of transitions between QB vanish at certain values of the phonon longitudinal momentum. The probability of the transition between QB numbered α and α' is proportional to

$$J_{\alpha-\alpha'}^2 \left(\frac{\Delta}{eFd} \sin \frac{q_z d}{2} \right), \tag{4}$$

where J_k is the Bessel function of order k, F is the electric field, Δ is the bandwidth at $F = 0$, d is the period of QB array and q_z is the longitudinal component of the phonon wavevector. If to describe the dispersion of acoustical phonons is by a constant speed of sound s and to assume that phonons propagate in the $z-$direction, then the energy conservation law given by δ-function in Eq.(3) determines q_z. At electric fields $F = nF_0$, n is the integer number,

$$F_0 = 2\pi\hbar s/ed^2, \tag{5}$$

phonons are ineffective and the scattering probability (3) and the hopping current (1) vanish. We have a specific momentum selection rule (having its origin in the electron Bragg reflection) for the scattering of the WS localized electrons. The difference between SL with the continuous transverse spectrum and QBSL with the discrete one is very important here, and only the discrete spectrum results in a single value of q_z. If there are no other acoustic phonons in the structure this means the absence of the background current and the appearance of zero minima in the conductance (Fig.2). These minima will be observable experimentally if either the density of states of 1D phonons is essential or the transverse scattering formfactor given by

$$F(\mathbf{q}_\perp) = | \left\langle N | e^{iq_\perp r_\perp} | N' \right\rangle |^2 \tag{6}$$

has a sharp maximum at $\mathbf{q}_\perp = 0$. Such a maximum is realized in SL in magnetic field, when the transverse modes are Landau levels. At the moment this experimental geometry is the best way to simulate a Quantum Box Superlattice. In strong electric field, when the Wannier-Stark quantization is present, the 1D array of quantum boxes with magnetic- and electric-field-controlled discrete spectrum is realized. If the energy difference between the initial and final WS levels satisfies the antiresonant condition, electron hopping occurs between partially filled Landau levels with the same quantum number and the formfactor is

$$F(\mathbf{q}_\perp) \propto e^{-l_B^2 q_\perp^2}, \tag{7}$$

where l_B is the magnetic length. Consequently, the energy conservation law takes the form $eFd \simeq \hbar s q_z$, if the inequality

$$eFd/\hbar s \gg q_\perp \sim l_B^{-1} \tag{8}$$

or

$$(eFd)^2/ms^2 \gg \hbar\omega_c, \tag{9}$$

where ω_c is the cyclotron frequency, is satisfied. One sees that in high electric fields only the q_z component of the phonon momentum is relevant and therefore hopping current reaches a minimum.

We note that in the case of the folded phonon spectrum Eqs (3,4) give the condition for current vanishing in the vicinity of gaps. Interestingly, current peaks may arise due to the phonon "defects", which levels fall inside the folded phonon gap. These phonon modes come from the potential fluctuations.

RESONANT TUNNELING DEVICES

We have also applied [8] the hopping conductance model to a RIT structure which consists of a heavily-doped p-n junction of a low-gap material (GaAs) sandwiched between a high-gap material (AlGaAs) (Fig.3). The homojunction creates a narrow tunneling barrier (similar to a tunnel diode) between the conduction and valence bands. Charge on both sides of the tunnel junction is confined with a 2D density of states at the heterojunction between the wide gap material and the depleted p-n junction. This structure is similar to a BiTFET (bipolar tunneling field-effect transistor) where tunneling is transverse and controlled by an external gate bias [9]. Heterojunctions form a barrier which efficiently reduces thermionic emission current of minority carriers. In these conditions NDR which occurs when two quantized electron and hole states cease to overlap, is expected to be abrupt with a large peak to valley ratio [10].

Although, as a result of several overlapping electron and hole channels, multiple negative NDRs with large peak-to-valley ratios have been predicted for this

structure [9, 10], we only consider one overlapping electron and (light) hole channel in the present analysis. Moreover, since elastic resonant tunneling between electron and heavy hole channel is negligible compared to the light hole process [10], we only examine in phonon-assisted tunneling between an electron and a light hole state, which is expected to be the main contribution to phonon-assisted current. Owing to the high 2D channel conductance, carriers are assumed to be immediately collected in the terminal current flowing parallel to the interface, once they have tunneled.

For the sake of simplicity we also assume the longitudinal confinement for both carriers is taken half parabolic: with one infinite wall representing the heterojunction and an infinite parabola branch modeling the modulation doping potential although our results are more general than this type of confinement. The parabolic shape is in contrast with quasitriangular potentials in FET channels [9], and is justified by small interface fields resulting from the low level of modulation doping in AlGaAs.

We calculate LO phonon-assisted hopping between electron and hole states and compare the hopping current (curve 2) with the coherent RT contribution (curve 1) (Fig.4). The coherent contribution have been also calculated in hopping conductance formalism with matrix elements of interband transitions determined by the Kane Hamiltonian [11]. Such hopping formalism is equivalent to the transfer Hamiltonian method for the calculation of coherent elastic tunneling [10, 12].

For phonon assisted tunneling transitions, the electric current may result from two processes. One is due to transitions through an intermediate state in the same band with subsequent direct interband tunneling. The other process is a one-step phonon-assisted tunneling across the homojunction. In our analysis we consider only the second situation since the first case is more unlikely and, be specifically forbidden for optical phonons due to energy conservation.

The interband scattering matrix element in Eq.(3) is taken between the electron $< \alpha, N | = < e, \mathbf{k}_\perp |$ and hole $< \alpha', N' | = < h\mathbf{k'}_\perp |$ states. These states are of different, $|s>$ and $|p>$ symmetry, in contrast to the intraband phonon-assisted tunneling case. We consider scattering by optical phonons which is usually the dominant scattering mechanism at room temperatures in semiconductor structures. The corresponding matrix elements read

$$|C_{e\mathbf{k}_\perp, h\mathbf{k'}_\perp}|^2 = \frac{2\pi\hbar\Omega e^2}{V_0 q^2} \left(\frac{1}{\epsilon_\infty} - \frac{1}{\epsilon_0} \right) I_{e,h}^2(q_z) \frac{P^2}{3} \left(q^2 + 3q_z^2 \right) \frac{1}{E_g^2}, \qquad (10)$$

where Ω is the phonon frequency, $I_{e,h}$ is the overlap integral between electron and hole states evaluated at the wavevector q_z, P is the constant of the Kane Hamiltonian [11], V_0 is the normalization volume, ϵ_0 and ϵ_∞ are the static and dynamical dielectric constants of a crystal respectively and E_g is the semiconductor bandgap.

The last factor in Eq.(10) accounts for two contributions: one results from the nonconservation of the longitudinal component of carrier wavevector (the part proportional to $q^2 - q_z^2$) while the other one results from the evaluation of the Bloch functions at finite 2D transverse wavevectors (the part proportional to $4q_z^2$).

It appears that the same (Kane) matrix element characterizes the strength of direct tunneling and the interband phonon tunneling. The latter is forbidden for symmetry reason at the band edge, and as a result, the large denominator E_g^2 considerably reduces the phonon-assisted current. The ratio between direct tunneling and phonon-assisted contributions is given by

$$\frac{j_{ph}}{j_D} \sim \frac{\hbar\Omega e^2 (m\omega/\hbar)^{1/2} kT \left(\frac{1}{\epsilon_\infty} - \frac{1}{\epsilon_0}\right)}{E_g^2 \hbar\omega}, \tag{11}$$

where $\hbar\omega$ is the level spacing between size-quantized electron (hole) states, and m is the electron mass which, for simplicity, we have chosen equal to the light hole mass. This ratio is usually small because of the large value of E_g. Fig. 4a displays the phonon-assisted current and Fig. 4b shows the direct and the phonon contributions to the current. We have chosen the following parameter values: $m = 0.08m_0$, $a = 200A$, $\hbar\omega = 50$meV. When electron and hole states cease to overlap (the applied voltage $eV = 50$meV) direct tunneling drops to zero (Fig.3 inset), while phonon-assisted transmission still occurs, until the energy separation between electron and hole levels is exceeds the phonon energy ($eV < 86$meV, $\hbar\Omega = 36$mev). It is seen that the phonon-assisted tunneling is three orders of magnitude lower than coherent tunneling. It is important to notice, that in our type of RIT structures electrons are confined in direct semiconductors with the conduction band located at the Γ symmetry point. By contrast, in indirect semiconductors the overlap between the Bloch amplitudes characterized by the X symmetry in the conduction band and Bloch amplitudes of the valence band does not vanish and would lead to significant contribution of phonon-assisted tunneling because these transitions are no longer forbidden at the band edge. Finally, let us point out that estimates of acoustic phonon assisted tunneling indicate that their contribution is smaller than that of optical phonons.

CONCLUSIONS

We have shown that the influence of quantum confinement on the electron and phonon states results in antiresonances in the hopping conductance of quantum box superlattices. The momentum selection rule for the interaction of phonons with Wannier-Stark localised electrons as well as the folded phonon gaps are to be observed in the magnetoconductance.

In RIT structures, Our analysis demonstrates the suppression of the phonon current between Γ-electron and hole states of different symmetry. In conjunction with

the 2D character of the electron and hole states this effect is predicted to be responsible for the very low valley current observed recently in RIT structures [3], which is mostly determined by direct tunneling channel between confined electron and heavy hole states. We show also that phonon-assisted current plays a much more important role in RIT devices made of type II heterostructures with vectorial symmetry of electron states, which characterizes some of the X or L subbands.

ACKNOWLEDGEMENT

References

[1] H.Sakaki, Jpn.J.Appl.Phys. **28**, L314 (1989).

[2] H.Noguchi, J.P.Leburton and H.Sakaki, Phys.Rev.B., **47**,15593 (1993).

[3] D.J.Day, R.Q.Yang, J.Lu and J.M.Xu, Appl. Phys.Lett., **73**, 1542 (1993).

[4] F.Capasso, S.Sen and F.Beltram, "Quantum Electron Devices", in *High Speed Semiconductor Devices*, S.M.Sze, Ed NY: Wiley, 1990, p.465.

[5] Miller A., Abrahams E. Phys.Rev. **120**, 745 (1960).

[6] R.Tsu and G.Dohler, Phys.Rev.B **12**, 680 (1975).

[7] Yu.B.Lyanda-Geller and J.P.Leburton. Phys.rev.B. **52** 2779, (1995).

[8] Yu.B.Lyanda-Geller and J.P.Leburton. Appl.Phys.Lett., **67**, 1423 (1995)

[9] J.P.Leburton, J. Kolodzey, and S.Briggs, Appl.Phys.Lett., **52**, 1608 (1988)

[10] J.M.Bigelow and J.P.Leburton,IEEE Trans.Electron Devices, **41**, 125 (1994)

[11] E.O.Kane, J.Phys.Chem.Sol,**1**, 82 (1957); **1**, 249 (1957).

[12] C.Duke, *Tunneling in Solids, in Solid State Physics, ed. by F.Seits, D.Turnbull and H.Ehrenreich*, Academic Press, NY (1969).
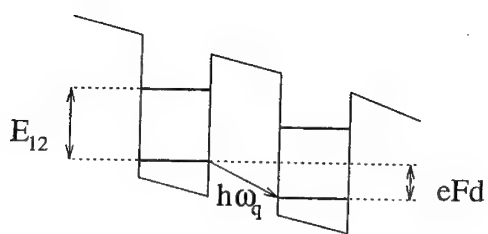
Figure 1: Schematic representation of a superlattice with transverse confinement in Wannier-Stark regime.
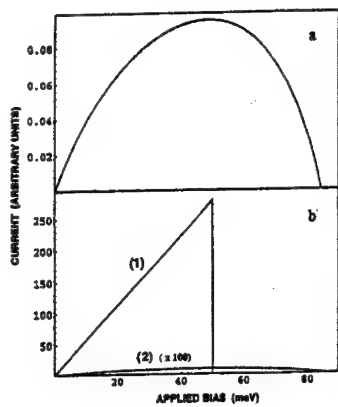
Figure 2: Hopping current for magnetically confined superlattice in the conditions of partial occupation of the zeroth Landau level. $F_0 = 2.17 kV/cm$. Curve 1: B = 6T; Curve 2: B= 12T.
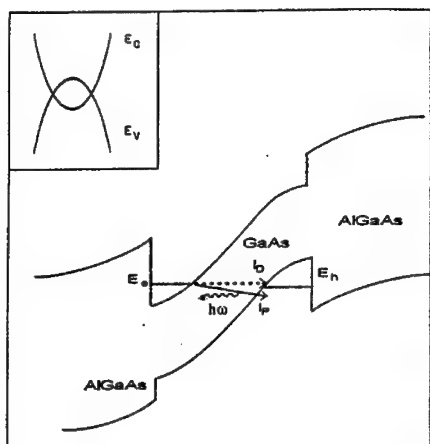
Figure 3: Schematic representation of the Resonant Interband Tunneling (RIT) structure with confined electrons and hole states.
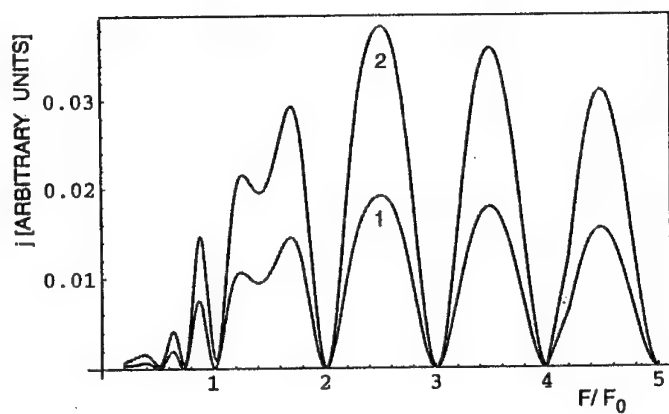
Figure 4: (a) Phonon-assisted tunneling current in RIT device; (b) The comparison of direct (1) and phonon-assisted (2) tunneling currents in RIT device.

Nonlinear Optical Properties of Semiconductor Quantum Wires and Dots

V.Dneprovskii, N.Gushina, E. Zhukov
Moscow State University, Physical Faculty, 119899 Moscow,Russia

V.Karavanskii
General Physics Institute, 117942 Moscow, Russia

V.Poborchii, I.Salamatina
Ioffe Physiko-Technical Institute, 194021 St. Petersburg, Russia

Picosecond laser saturation spectroscopy method has been applied to investig nonlinear optical properties of semiconductor nanocrystals. Discrete bleaching bands h been observed in the time-resolved nonlinear transmission spectra of GaAs wires crysotile asbestos nanotubes with average diameter 6 nm, in porous silicon and nanostructures of CdS crystallized in mica molecular filters. The increase of transmissior discrete frequencies has been attributed to the saturation of optical transitions between energy levels of electrons and holes spatially confined within quasi-zero-dimensio (quantum dots) and quasi-one-dimensional (quantum wires) nanostructures.

I. Introduction.

In recent years semiconductor nanostructures in which the movement of carriers restricted to two or three dimensions - quantum wires (QWRs) and quantum dots (QDs) - attracting much interest not only from the viewpoint of fundamental physics, but also fi their potential application in electronics and optoelectronics. As the dimensionality is redu to one or zero dimension, giving QWRs or QDs , the density of states becomes sharper narrower. Carrier confinement should lead to a narrower gain spectrum, higher differential ç [1], to an increased exciton binding energy and lasing from excitons [2], to enhanced opt nonlinearities [3]. So application of QWRs and QDs promises the improvements in performa of lasers (lower threshold, increased modulation bandwidth, reduced threshold temperal

sensitivity), of transistors (application of extremely high electron mobility channels), and optical switching devices (low switching energy, fast switching). This letter reports observation of nonlinear optical absorption of GaAs QWRs, porous silicon QWRs and QDs ; nanocrystals of CdS in transparent mica matrix. It may be attributed to the saturation optical transitions in 1D- and 0D-structures exited by powerful picosecond laser pulses.

II. Experiment.

For the nonlinear absorption measurements the samples of QWRs and QDs were excited ultrashort pulses at the second harmonic of a mode-locked Nd:YAG laser, with a pho energy 2.33 eV. The duration of an individual pump pulse was about 20 ps, and its inten reached 100 MW/cm^2. The exciting light was directed along the normal to the surface of sample and was focused into a spot $\approx 200\mu m$ in diameter. The central part of the excital region was probed by an oppositely directed focused beam of "white" light. An ultrashort pu of "white" light was produced by sending a part of the laser beam at the fundamer frequency into a cell filled with heavy water. An optical delay line made it possible to de the probing pulse with respect to the exciting pulse and to measure the kinetics of the indu absorption. The probing light was detected in front and behind the sample by multichar optical analyzer, with accumulation of 50 pulses and with energy selection of the ultrasl excitation pulses within an error ±10%. In these experiments we measured the differer transmission spectra

$$DT(\lambda) = \frac{T(\lambda) - T_0(\lambda)}{T_0(\lambda)},$$

where $T(\lambda)$ and $T_0(\lambda)$ are the transmission spectra of the excited and unexcited sam respectively. So it was possible to eliminate the effect of the spectral characteristics of photodetectors on the final results and to reduce the role played by an instability of spectral composition of the probing light. Transmission spectra normalized to the refere spectra of the probing pulse were used in (1).

III. Results and discussion.

a). Nonlinear absorption of GaAs quantum wires.

Several methods of GaAs QWRs preparation exist [4]. Most of them utilize complicated and expensive MBE or MOCVD technique together with etching, application of prepattern substrates, cleaving of a conventional 2D-structure perpendicular or at slight angle to surface. In the latter case epitaxy is used for a second time to create new layers semiconductor on the cleaved surface (smooth or atomically stepped). These methods do allow to create samples containing QWRs whose dimensions are suitable for linear and nonlinear optical absorption measurements.

Recently a new method of GaAs QWRs production in a transparent dielectric matrix been realized [5]. Following [6] the molten material was injected into the empty nanometer radius channels (nanotubes) of chrysotile asbestos. The dimensions of the obtained samp allowed to measure the linear absorption. Optical transitions between the energy levels of quantization in GaAs QWRs and essential anisotropy of the absorption of light polari parallel and perpendicular to QWRs have been observed [5]

The samples containing ultrathin wires of GaAs in transparent matrix represent a regular of closely packed parallel dielectric chrysotile asbestos nanotubes (Insert in Fig.2). measured external diameter of these nanotubes is about 30 nm, and the diameter of internal channels - 6 nm. A regular set of ultrathin wires has been prepared by filling up internal channels with molten GaAs that is a wetting material for asbestos. The main par GaAs is consentrated in cylinders with a characteristic size of about 30 nm along the wire which exceeds its diameter. The size of the samples is $\approx 300\,\mu m$ along the channels, the wi $\approx 200\,\mu m$, the thickens $\approx 10\,\mu m$. To avoid light scattering the samples have been inserted i transparent glue with a refractive index close to that of crysotile asbestos.

Fig.1, a and b, shows the linear absorption (LA) and DT(λ) spectra of GaAs wires in crysc asbestos matrix. Two bleaching bands with maximum at about 1.8 eV and 2.2 eV are v
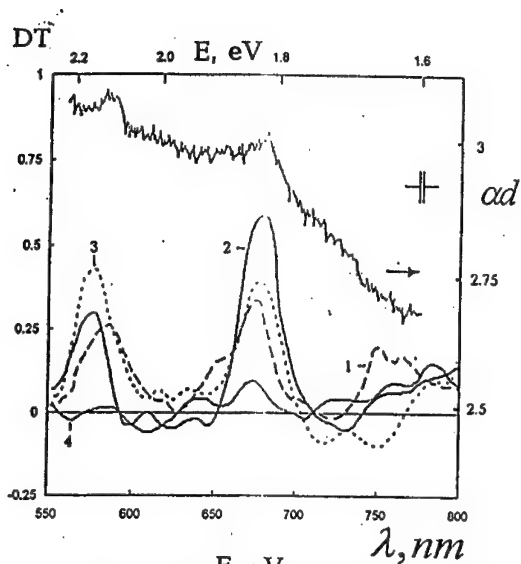
Fig.1

Linear absorption and differential transmission spectra of GaAs quantum wires obtained at different delays between the pumping and probing pulses: 1-(-15) ps, 2-0 ps, 3-20 ps, 4-50 ps.
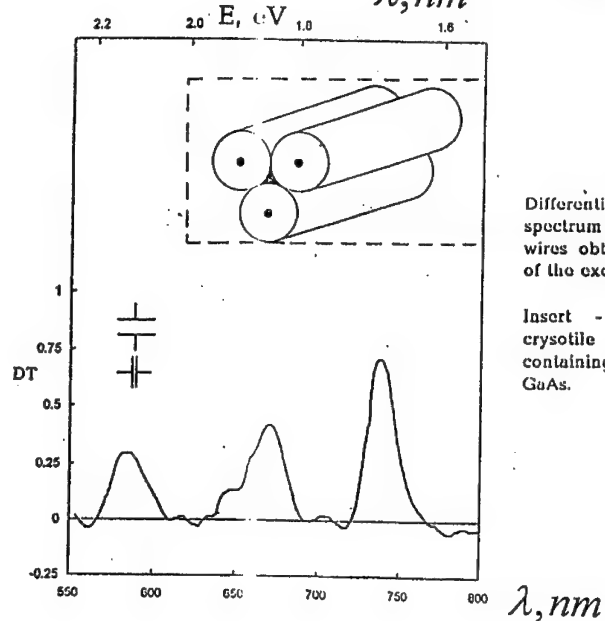
Fig.2

Differential transmission spectrum of GaAs quantum wires obtained for some parts of the excited sample.

Insert - the structure of crysotile asbestos nanotubes containing ultrathin wires of GaAs.

pronounced in DT(λ) spectrum (Fig.1, b). Their energy positions coincide with the position absorption bands of LA (Fig.1, a) spectrum. The induced bleaching disappears over 50 ps. additional bleaching band 1.7 eV in DT(λ) spectrum have been observed (Fig.2) only for sc parts of the excited sample (the spot sizes of the focused pump and probing beams were] than the sample's size). A corresponding shoulder may be seen in LA spectrum. The 1.7 bleaching band relaxed faster than the 1.8 eV and 2.2 eV bands. The time resolution of pump and probe system was not enough to measure its relaxation time.

In bulk semiconductors different nonlinear processes compete and coexist: the Burst Moss saturation effect, renormalization of the energy gap at a high density of carri bleaching or broadening of the exciton absorption line, etc. The increase or decrease absorption dominates in the vicinity of the energy gap at different temperatures of the sam In semiconductor QDs and QWRs the only surviving mechanism for nonlinear absorption n the lowest resonance is state filling [3].

The bleaching bands 1.8 eV and 2.2 eV may be explained [8] by the saturation of opt transitions between the lowest energy levels of size quantized electrons and holes of differ valence bands in GaAs QWRs. The corresponding absorption bands exist both in LA spec registered in [5] and in LA spectra obtained in this work (Fig.1, a).

Within effective mass approximation combined with assumption of infinitely deep cylindr potential well and negligible role of Coulomb interaction between carriers, the energies transitions between space quantization levels in corresponding valence bands and conduct band are given by [7] :

$$E_i = E_g^i + \frac{X_{01}^2 h^2}{2\mu_i \rho^2},\tag{2}$$

where E_g^i is an energy gap (index "i" defines the corresponding valence band); $X_{01} \cong$?

$\mu_i = \dfrac{m_e m_h^i}{m_e + m_h^i}$; $m_{e,} m_h^i$ -the effective masses of electrons and holes; ρ is the radius of QWR.

Using (2) it is easy to show that for QWRs of 6 nm diameter the 1.8 eV band corresponds

the transition between the highest valence subband and the lowest conduction subband, wl

2.2 eV band - to the split off by spin orbit coupling valence subband and the lowest conduct

subband. So the 1.8 eV and 2.2 eV bleaching bands may be attributed to the saturation of th

transitions. The observed only at the moment of excitation 1.7 eV bleaching band may

attributed to the saturation of the lowest transition in QWRs of greater cross section that r

be formed   in the space between the crysotile asbestos nanotubes. The decrease of

relaxation time of this band as compared with other bleaching bands may be explained by

stronger influence of nonradiative surface recombination in QWRs with greater specific surf ϵ

The observed induced bleaching of GaAs QWRs in crysotile asbestos nanotubes allows

determine the third order nonlinear susceptibility [8]: $\chi^{(3)} \cong -4.10^{-8}$ e.s.u.

b). Strong optical nonlinearities of porous silicon.

Silicon which is widely used in microelectronics attracts researcher's attention because of

possible application in optoelectronics. One possibility is the prospect for obtaining effici

visible luminescence in porous silicon (PS) formed by electrochemical etching of the origi

bulk material [9]. Till now there is no evidence of a discrete energy spectrum of PS determin

by quantum confinement in QDs or QWRs. The linear absorption spectrum of PS is shiftec

the high energy side compared with the original bulk material. Unfortunately there are

peculiarities determined by discrete optical transitions. This may be explained by signific

inhomogeneous broadening of optical transitions due to the size dispersion and different sh

of nanostructures.

In the present paper the method of picosecond laser saturation spectroscopy is appliec

measure the time-resolved nonlinear absorption and to define the energy spectrum of PS. '

nonlinear absorption is less dependent on surface properties than the luminescence. '

observed increase of transmission (bleaching) at discrete frequencies [10] allows us to supp

that the investigated samples of PS contain nanostructures of two types: quantum wires ⋅

quantum dots. Additional independent measurements with an electron microscope conf

this supposition.

The transparent plane-parallel platelets 10-30 μm thick of PS were detached from the n-t;

(111) oriented silicon substrate by briefly raising the current density to 100 mA/cm^2 a

customary anodic etching of the substrate in 50% solution of HF in ethanol. Their Ran

spectra reveal a narrow peak at about $517\ cm^{-1}$, which is characteristic of crystalline silic

There were no bands that would indicate the presence of an amorphous phase.

The linear transmission spectra of PS platelets at 300 K and 80K do not contain any featu

even at 80K that would indicate a discrete nature of the optical transitions in this mater

They are shifted to the higher frequency region compared with bulk silicon .Fig. 3, 4 sh

differential transmission spectra of PS sample for various values of the delay Δt between

ultrashort pumping and probing pulses. These spectra correspond to the positive values

differential transmission, indicating an effect of excitation- induced bleaching. This bleach

exhibits a sharp discrete structure which is not pronounced in the linear transmission. Th

relatively narrow bands are well resolved at room temperature of PS at zero delay with spec

position $\lambda_1 = 760nm, \lambda_2 = 680nm$ and $\lambda_3 = 570nm$. As the delay Δt is increased to 30

the λ_3 band disappears from the DT spectra and the amplitudes of λ_1 and λ_2 ba:

essentially decrease. The DT spectra of the cooled (80K) platelets of PS are more complical

They contain at least five disci

bands: $\lambda_1' = 730nm, \lambda_2' = 670nm, \lambda_3' = 640nm, \lambda_4' = 590nm$ and $\lambda_5' = 565nm$. Wl

the delay was increased the amplitudes of λ_2', λ_3' and λ_5' bands gradually diminished wl

the amplitudes of λ_1' and λ_4' bands were increasing at $\Delta t \leq 10$ ps and then decreased. A

30 ps all bands diminished.

The above data may be explained by the saturation of discrete optical transitions betw‹

the energy levels of space quantization in silicon nanostructures: nanocrystals (QDs) and v

thin wires (QWRs) [10]. The density of states in a zero or one-dimensional system is peal
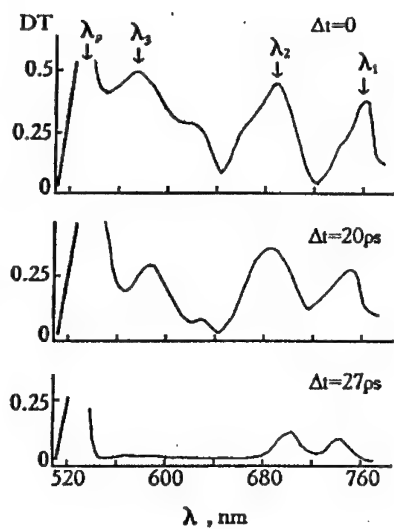
Fig.3 The differential transmission spectra of a porous silicon platelet (300K) at different delays of the probing pulse.
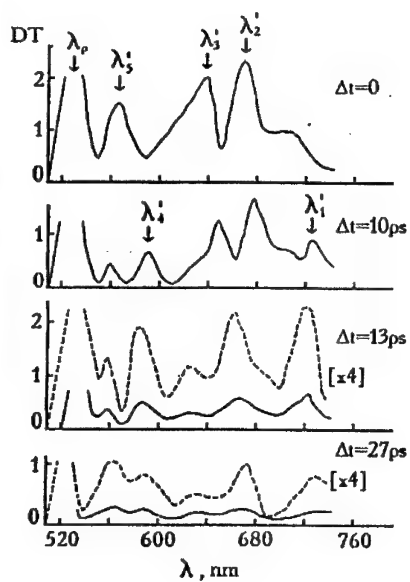
Fig.4 The differential transmission spectra of a porous silicon platelet (80K) at different delays of the probing pulse.

and in an ideal case it tends to infinity. The absence of a corresponding structure in the lin

transmission spectra is obviously caused by inhomogeneous broadening of the quantum-

energy levels due to the size dispersion of nanocrystals and wires and variation in the shape

these structures. This broadening can be substantially suppressed in the nonlinear transmiss

spectra because of a selective effect of the narrow-band laser pumping light - by select

excitation of nanostructures of a certain size. This effect was previously observed for C

nanocrystals dispersed in a glass matrix [11].

In evaluating of the energies of optical transitions in PS we considered both types

nanostructures: 1. wires which are long parallelepipeds oriented along the [001] axis with fac

perpendicular to the [110] and [110] directions and 2. nanocrystals (quantum dots) of spher

shape. To get an idea of the nature of optical transitions in wires of PS one can examin

projection of the band structure of the bulk material onto the one-dimensional Brillouin z

of a quantum wire [13]. Two electron valleys lying in the [001] direction form an indi

minimum with $k \cong_-^+ 0.4\pi/a$. The four electron valleys lying in the perpendicular directions

projected onto the center of the Brillouin zone and form an absolute minimum [14]. One

obtain the energies of optical transitions in quantum wires of PS using (1).

The λ_1 and λ_2 bands in the $DT(\lambda)$ spectra (Fig.3) and λ_1' and λ_2' bands (Fig.4) can

attributed to a saturation of the two lowest direct optical transitions E_{h11} and E_{l11} in

quantum wires of PS. The high energy shift of these bands relative to E_g allows us to estim

the lateral dimensions of the wires : L = 2.6-2.9 nm. The high efficiency of the excitation

these wires' dimensions may arise because the energy of a laser photon is close to the ene

of the third transition $E_{h12}(E_{h21})$. Probably the λ_3' bleaching band corresponds to

saturation of the E_{h11} transition for thinner wires with $L \cong 2.3$ nm because the energy of

E_{l11} transition is in resonance with the pumping photon energy. The energy positions of

λ_4' and λ_5' bleaching bands don't allow us to explain them by saturation of the hig

$E_{h(l)12}(E_{h(l)21})$ optical transitions in quantum wires of 2.3-2.9 nm lateral dimensions.

have supposed that in our PS samples nanocrystals (QDs) may exist side by side with t
wires and that these bleaching bands arise due to the saturation of the lowest transitions
quantum dots. In this case it is possible to estimate the average radius of nanocrystals: R
nm. The existence of nanostructures of both types is confirmed by the results of independ
measurements using a transmission electron microscope [10] The PS sample contains t
wires oriented in all directions with 2-10 nm lateral dimensions. The size dispersion of
nanocrystals is almost the same.

c). Optical and nonlinear optical properties of CdS nanostructures.

A new method allows to create nanostructures of different size by crystalliz
semiconductor inside empty channels of the transparent matrix. CdS was crystallized in
channels of mica (in molecular filters) made by preliminary ion's bombardment us
accelerator. The size of the channels and consequently of the nanostructures depends upon
type of the ions and their energy.

The linear absorption spectrum of mica matrix whose empty channels have been filled v
crystallized CdS is presented in Fig.5. The observed two "hills" in the vicinity of 2,6 and ʻ
eV may be explained by optical transitions in QWRs with 7 nm average diameter or QDs v
9 nm diameter: quantum confined holes of the A and C valence bands - quantum confi
electrons of the conduction band. The measured size of the holes in mica does not exceed
nm. The bleaching band with relaxation time about 100 ps (Fig.6) has been registered
differential transmission spectra pointing at strong nonlinearity of CdS nanostructures.

IV. Conclusions.

Strong and fast nonlinearity have been observed in quantum wires of GaAs, quantum w
and dots of porous silicon and in nanocrystals of CdS in transparent matrix (molecular fi
from mica with crystallized semiconductor inside the empty channels). The saturation of opt
transitions between the energy levels of size quantization in quantum wires and dots at I
density of photoexcited carriers is the physical process leading to this nonlinearity.
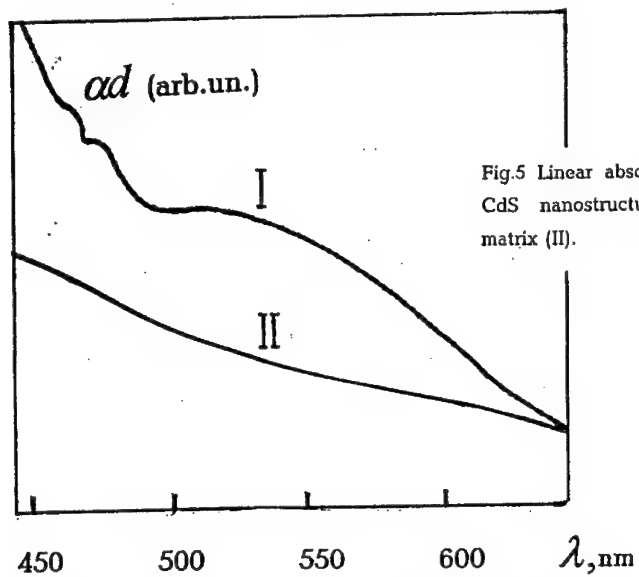
Fig.5 Linear absorption of mica with CdS nanostructures (I) and mica matrix (II).
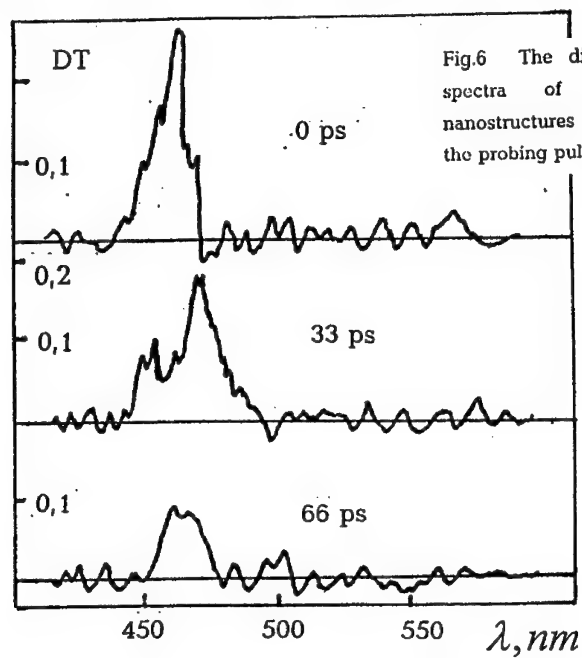
Fig.6 The differential transmission spectra of mica with CdS nanostructures at different delays of the probing pulse

References.

[1] Y. Arakawa and A. Yariv, IEEE J. Quantum Electron. 22 (1986) 1887.

[2] W.Weigscheider, L.N. Pfeiffer, M.M. Dignam, A. Pinczuk,K.W. West, S.L.McCall, and Hull, Phys. Rev. Lett. 71 (1993) 4071.

[3] S Schmitt-Rink, D.A.B. Miller, and D.S. Chemla, Phys.Rev.B 35 (1987) 8113.

[4] M.S. Sundaram, S.A. Chalmers, P.F. Hopkins, A.C. Gossard, Science 254 (1991) 1326.

[5] V.V. Poborchii, M.S. Ivanova, I.A. Salamatina, Superlattices and Microstr. 16 (1994) 133.

[6] V.N. Bogomolov, Usp.Fiz. Nauk 124 (1978) 171.

[7] H. Zarem, K. Vahala, and A. Yariv, IEEE J. Quantum Electron. 25 (1989) 705.

[8] V.Dneprovskii, N.Gushina, O.Pavlov, V.Poborchii, I.Salamatina, E.Zhikov, Phys. Lett. A (1995) 59

[9] L. T. Canham, Appl. Phys. Lett. 57 (1990) 1046

[10] V.Dneprovskii, N.Gushina, D.Okorokov, V.Karavanskii, E.Dovidenko, Superlattices Microstructures,17 (1995) 41; V.Dneprovskii, A.Ejov, N. Gushina, D.Okorok V.Panov,V.Karavanskii,A.Maslov,V.Sokolov, E.Dovidenko, phys.stat.sol.(b) 188 (1995) 297

[11] V.S. Dneprovskii, V.I. Klimov, D.K. Okorokov, Yu.V. Vandyshev, Solid State Commun. (1992) 227 .

[12] G. D. Sanders and Y.-C. Chang, Phys. Rev. B45 (1992) 9202

[15] F. Buda, J. Kohanoff and M. Parrinello, Phys.Rev. Lett. 69 (1992) 1272

THE BLUE AND UV PHOTOLUMINESCENCE OF SI AND C NANOCLUSTERS EMBEDDED IN SIO$_2$ MATRICES

Qi Zhang, S. C. Bayliss and R.G. Pritchard

Department of Applied Physics, School of Applied Sciences, De Montfort University, Leicester. LE1 9BH. UK

Abstract

Silicon and carbon nanoclusters embedded in SiO$_2$ were deposited by rf-sputtering followed by N$_2$ annealing at 800°C. Si K-edge and C K-edge EXAFS suggest that the two types of clusters present are respectively Si and C related materials. Stable blue photoluminescence (PL) from both types of cluster samples were recorded, and observed by naked eye, under excitation power on a scale of μW. UV PL from C clustered films was also recorded, but this was not stable - the intensity decayed with time. The size distributions (from 1 to 4.5nm) of the nanoclusters in the clustered films suggest that a quantum-confined size effect can also apply to the blue PL range.

INTRODUCTION

Visible light emission from elemental semiconductor nanostructures has attracted significant attention in the past few years because the photoluminescence (PL) is strong and lies in the visible region, and could be useful for optoelectronics applications. Apart from the intensively studied porous silicon[1,2] and Si nanopowder[3], work on nanoclusters of group IV elements embedded in SiO$_2$ is one important area of study. Previous reports on Si[4,5], C[6], and Ge[7,8] clusters embedded in SiO$_2$ matrices suggested that optical transitions associated with the fundamental absorption edge of the nanostructured material had direct rather than indirect character, and there was evidence for the presence of nanocrystals in high-resolution TEM real-space images. Recently, a study on Ge doped SiO$_2$ films showed a large visible range of PL, with PL peaks in the 500 to 800nm range observed from annealed

Ge nanocrystallites (with mean sizes from 2-6nm), and weak UV and blue PL from as-deposited samples.[9] From all of the nanocluster studies, it has been concluded that quantum-confinement is a suitable mechanism for the strong blue shift.

We present a study of the blue emission from annealed Si and C clusters embedded in SiO_2, and of unstable UV emission from annealed C clustered films, which follows on from our previous work[10-11]. With information from TEM and both Si and C K-edge EXAFS, the origin of the blue photoluminescence is regarded as due to a quantum size effect, while the origin of the UV emission is unknown at this stage.

EXPERIMENTAL

The semiconductor-doped glasses were deposited in one process by rf co-sputtering in a system with base pressure of 3×10^{-6} mbar. On the pure SiO_2 8" target, between 3 and 20 pieces of Si wafer ($10 \times 10 \times 0.3$ mm³) were placed in an area of ~4" in diameter to produce Si-cluster samples and, between 5 and 16 pieces of pure graphite rod of 6mm diameter were used to produce C clustered films, to give films with a range of PL responses. The deposition conditions were: (1) for Si clustered films - 3×10^{-4} - 6×10^{-3} mbar Ar, 400W rf power; (2) for C clustered films - 6×10^{-4} - 1×10^{-2} mbar Ar, 500 - 1250W rf power. The films were deposited on Si wafer substrates with a film thickness of >1 μm. The samples were subsequently annealed at 800°C for 20 min in a N_2 atmosphere flowing at a rate of 3 l min⁻¹. The PL and Si K-edge and near edge x-ray absorption fine structure (EXAFS and NEXAFS) measurements were performed at DRAL Daresbury Laboratory using stations 12.1 and 3.4 respectively. The EXAFS data were determined by the total-yield technique[12]. Furthermore, C K-edge EXAFS were obtained in fluorescence mode, on the HE - PGM2 station at BESSY Laboratory. The EXAFS data from the clustered films do not contain any contribution from the Si substrate as the film thickness is much greater than the EXAFS sampling depth. For PL the tuneable UV source provided excitation at 260nm, 300nm and 370nm, using a bandwidth of 10nm and a power of 0.12 -2.7 μW on the samples. For all of the samples, PL was only observed from annealed films. The PL data has been normalised to take into account the spectral sensitivity of the system and variations due to beam decay. Cluster size distributions were obtained from TEM real-space images from the edges of tilted samples using a Jeol JEM 100CX. The resolution of this instrument is ~0.5 nm.

RESULTS AND DISCUSSION
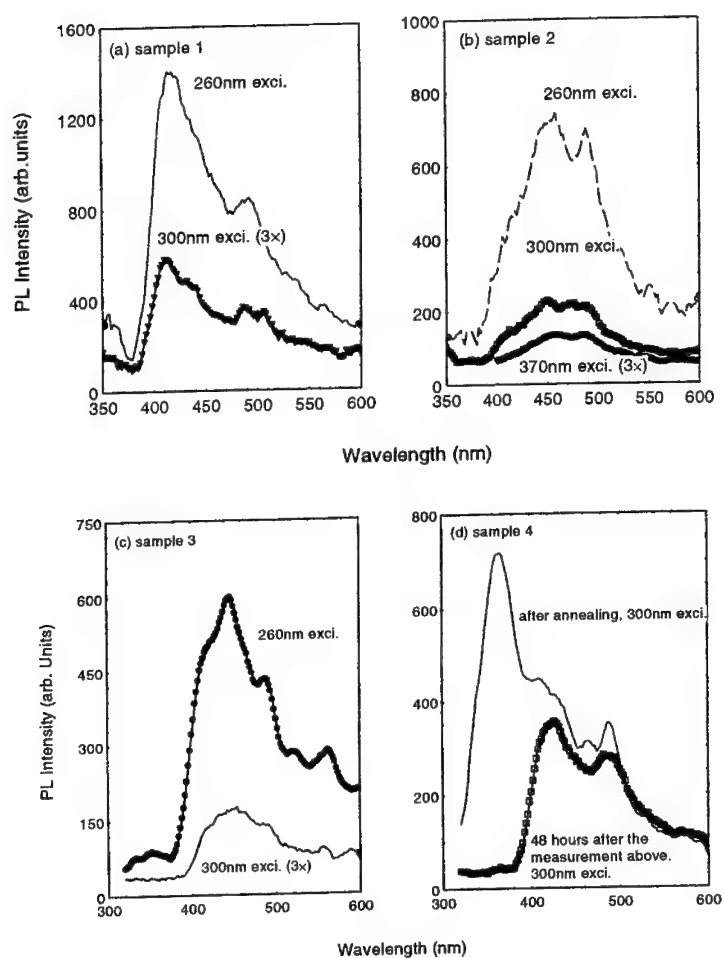
Figure 1. PL from Si ((a) and (b)) and C ((c) and (d)) clustered SiO_2 films.

Figures 1(a) and (b), show the PL of two Si-cluster samples *1* and *2*. Peaks are located from ~420 to 495nm, and from ~450 to 490nm, depending on the sample preparation conditions. No emission was detected for as-deposited samples. Although many samples have been made in very different conditions, data from only two samples, those with highest PL intensities, are shown here. In Figures 1 (c) and (d), the PL from C clustered films (samples 3 and 4) are given. As shown in (d), both UV and blue PL were recorded from this sample when it was measured a few hours after annealing. However, two days after the first measurement, the UV emission disappeared, and only blue emission remained. About half of the carbon clustered films made exhibit this characteristic of unstable UV PL, although, the UV PL intensities varied compared with the blue peaks. The blue emission remained almost constant over a period of 6 months. In general the PL spectra of all our samples consisted of one, two or three strong peaks, plus some smaller peaks which varied with deposition conditions.

The Fourier transform of the EXAFS data shows details of the local structure of the nanosized Si clusters. In Figure 2(a), both experimental and theoretically-fitted Fourier transforms of as-deposited and annealed Si/SiO_2 (sample *1* in Figure 1(a)) are shown. In the unannealed material the Fourier transforms are very similar to those of SiO_2[12], with a Si-O bond-length at 1.58Å, and a second shell corresponding to Si-O-Si at ~3.2Å. After annealing, the nearest neighbour partial coordination number of Si-Si bonds increases from zero, for the as-deposited material, to 0.6 for the sample with the highest contribution from Si-Si bonds. On the contrary, the Si-O bond peak in the Fourier transform decreases significantly. The second shell corresponding to Si-O-Si is still present on annealing, and a third shell corresponding to Si-O-Si-O at ~4Å emerges. As with most EXAFS data fits, however, the 4σ error in the partial coordination numbers obtained by statistical analysis of the fit is rather high : $\pm$ 0.5, but still clearly shows the existence of Si-Si bonds. Since the total coordination number is 4, and silicon oxide is chemically ordered both throughout understoichiometry and at stoichiometry[12], more than one eighth of the Si atoms are potentially bonded in elemental Si regions. The Si-Si bond length in the annealed sample is 2.35 $\pm$ 0.02Å, as expected, and the Si-O distance at 1.58 $\pm$ 0.02Å is within experimental error of the expected 1.62Å. Although crystalline lattice regions have been observed by others in high resolution TEM images[7,9] in similarly-prepared materials, our EXAFS data do not show direct evidence for crystallinity : the fitted Debye-Waller factors of the first shell Si-Si bonds at about 0.006±0.003 $Å^2$ suggest a structure which within experimental error could be anywhere between amorphous and crystalline for which the factors are 0.007 and 0.004 $Å^2$ respectively. One interpretation of the large error in the Debye-Waller factor is that the clusters

are composed of crystalline cores surrounded by disordered bonds, alternatively it could be a result of a range of amorphous-to-crystalline clusters. Either way the absence of any features corresponding to second shell Si-Si-Si is not surprising considering the small first shell Si-Si contribution and the rapid fall off of EXAFS with distance.
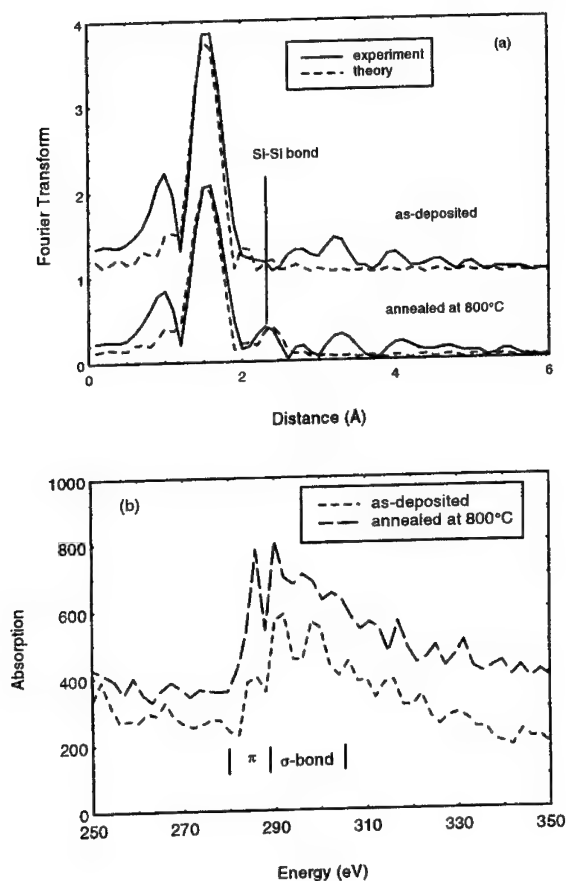
Figure 2. (a) Fourier transformed EXAFS of Si clustered film - sample *1* in Figure 1. (b) NEXAFS of C clustered film - sample *3* in Figure 1.

For the carbon clustered SiO_2 films, the C K-edge near edge EXAFS is shown in Figure 2(b) for one of the carbon cluster films. Because the quantities of carbon atoms are quite small compared to those of Si and O atoms in the films, and because of lower system sensitivity to carbon, the NEXAFS of the C K-edge is fairly noisy. However, the near edge absorption still presents certain important information about the states of carbon bonding in the clustered films. The clear increase of the absorption peak below 290 eV in the annealed films indicative of the presence of π bonds, compared with the as-deposited films, indicates that graphitic carbon clusters have formed from oxygen rich-carbon clusters : the strong σ bond absorption observed above 290eV could be a result of C-O reaction/bonding[13], and furthermore only the annealed clustered films give off strong luminescence. This discussion agrees with the implications from O K-edge EXAFS of the carbon clustered films[14].
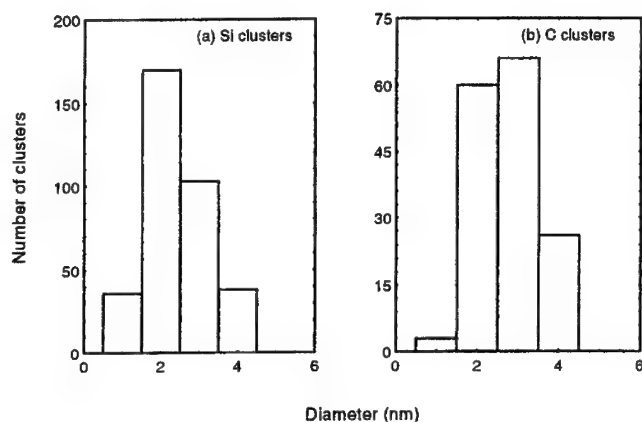
Figure 3. The size distribution of (a) Si and (b) C clusters in SiO_2 matrices.

Having determined the material species involved in the clusters, we can discuss the origin of the blue emission, although the origin of the unstable UV emission is still not clear at this stage. The size distributions of the Si clusters observed by TEM are shown in Figure 3(a) for the Si clusters of sample *1* and (b) for the C clusters of the sample *3* in Figure 1, respectively. Note that the resolution of the TEM makes estimation of cluster densities more difficult for

diameters < 1nm. As expected, based on a quantum confinement model for blue emission, the cluster size is very small and there are no clusters of size > 4.5nm. Crystalline regions have been observed in the diffraction patterns from samples composed of large clusters (about 15-20 nm diameter) which show emission at longer wavelengths. Since the blue-emitting material contained very small clusters and the resolution of the instrument was not very high, we could not obtain evidence for crystallinity in these samples by TEM. However, the order parameters from the EXAFS FTs of Si clusters are not inconsistent with a structure composed of clusters which have some crystalline character. Furthermore, the bonding states assigned to the C NEXAFS suggest that the C clusters have crystalline-like graphite structure. According to the theoretical calculation of the electronic structure of silicon nanocrystallites by an effective-mass approximation[15] and from quantum confinement[16], nanoclusters ~2.5nm in diameter are expected to have a bandgap of 2.25-3 eV. The PL peak energies of clustered films in this work, ~ 2.5 eV (495 nm) and ~ 2.95 eV (420 nm) from Si clusters, ~2.88 eV (430nm), ~2.73 eV (455nm) and ~2.53 eV (490nm) from C clusters, fall in this region.

A further relationships exist between the density of clusters observed by TEM and the intensity of PL, in that stronger PL only comes from films with a higher density of clusters, rather than less clusters. Thus we have an indication that the existence of small elemental Si clusters provides one correct environment for greater PL efficiency in the blue.

SUMMARY

We present a study of stable blue and unstable UV photoluminescence from N_2-annealed Si and C nanoclusters embedded in SiO_2 matrices. The clusters are likely to have a crystalline core, however there is evidence for some disorder surrounding the cores. The intensity of blue PL is directly related to the density of clusters. The size distributions suggest that the quantum size effect can apply to blue emission, however, the origin of the UV emission is unknown at this stage. The local structure of the clusters, e.g. π bonded carbon, and crystallisation is important to emission efficiency based on the size effect.

References

[1] L. T. Canham, Appl. Phys. Lett. 57, 1046(1990).

[2] S. C. Bayliss, D. A. Hutt, Q. Zhang, N. Danson, J. Bates, and A. Waddilove, J. Appl. Phys. 76, 9 (1994).

[3] T. Kawaguchi and S. Miyszima, Jpn. J. Appl. Pyhs. 32, L215(1993).

[4] D. J. Dimaria, J. R. Kirtley, E. J. Parkulis, D. W. Dong, T. S. Kuan, F. L. Pesavento, T. N. Theis and J. A. Cutro, J. Appl. Phys. 56, 401(1984).

[5] T. Ito, T. Ohta and A. Hiraki, Jpn. J. Appl. Phys. 31, L1(1992).

[6] S. Hayashi, M. Kataoka and K. Yamamoto, Jpn. J. Appl. Phys. 32, 1274(1993).

[7] Y. Maeda, N. Tsukamot, Y. Yazawa, Y. Kanemitsu and Y. Masumoto. Appl. Phys. Lett. 59, 3168(1991).

[8] Y. Kanemitsu, H. Uto, Y. Masumoto and Y. Maeda. Appl. Phys. Lett. 61, 2187(1992).

[9] Y. Maeda, Phys. Rev. B 51, 1658(1995).

[10] Q. Zhang, S. C. Bayliss, and D. A. Hutt, Appl. Phys. Lett. 66, 1977(1995).

[11] Q. Zhang, S. C. Bayliss, A. Al-Ajili, D. A. Hutt, Nucl. Instr. and Meth. in Phys. Res. B 97, 329(1994).

[12] S. C. Bayliss and S. J. Gurman, J. Non-Cryst. Sol. 127, 174(1991).

[13] Th. Schedel-Niedrig, H. Werner, M. Wohlers, D. Herein, J. Blöcker, R. Schlögl, M. Keil, A. M. Bradshaw, BESSY-Jahresberidht 1993, 196.

[14] Q. Zhang, S. C. Bayliss, W. Frentrup and R. Raggate, BESSY-Jahresberidht 1995.

[15] T. Tahagahara and K. Takeda, Phys. Rev. B 46, 15578(1992).

[16] C. Delerue, M. Lannoo and G. Allan, J. of Luminescence 57, 247(1993).

OPTICAL AND ATOMIC FORCE MICROSCOPY CHARACTERIZATION OF PbI₂ QUANTUM DOTS

R. Mu, Y. Xue, Y.S. Tung, and D. O. Henderson

Chemical Physocs Laboratory
Department of Physics
Fisk University, Nashville, TN 37208

ABSTRACT

Lead iodide (PbI₂) clusters were synthesized from the chemical reaction of NaI (or KI) with $Pb(NO_3)_2$ in H_2O, D_2O, CH_3OH, and C_3H_7OH media. The observation of the absorption features above 350 nm with the help of integrating sphere accessary strongly suggests the quantum dot formation of PbI₂ in solution. Spectral comparison between the synthesized PbI₂ clusters in solution and PbI₂ nanophase by impregnation of PbI₂ in four different pore-sized porous silica indicates that the PbI₂ cluster size in solution is less than 2.5 nm in lateral dimension. Atomic force microscopy (AFM) measurements show that the PbI₂ clusters deposited on to three different molecularly flat surfaces are single-layered. The measured height is 1.0 ± 0.1 nm. The swollen layer thickness can be attributed to the intralayer contraction from the strong lateral interaction among PbI₂ molecules, which is supported by *ab initio* calculation.[1] Raman scattering measurement of LO and TO modes of PbI₂ in bulk and in the confined state were also conducted in 50 - 150 cm^{-1} region. The observed three bands ar 74, 96, 106 cm^{-1} are assigned to TO_2, LO_2, and LO_1 mode, respectively. The relatively small red-shift in LO modes may be caused by the surface phonon polaritons of PbI₂ nanophase in the porous silica.

INTRODUCTION

The study of nanophase materials physically confined in various hosts has attracted much attention in recent years. Depending upon the physical properties of the confining hosts and the nature of the confined materials, many unique mechanical, thermal, and optical properties have been observed and are related to the different types of confinement effects. The physical confinement, interfacial energy at the guest-host boundaries, and the reduction of the confined particle size can lead to, for example, modification of materials' hardness and depression of the melting and freezing transition temperatures. The quantum confinement of the free electrons in metals and the excitons in semiconductors can result in the observation of the colorful surface plasma resounance and the shifts of the band gap.

Dielectric confinement due to the confining hosts provides the means to tune the surface plasma resourmance frequencies and to enhance the nonlinear optical effects at interface by changing the dielectric constant of the confining hosts. In addition, the observation of the surface phonon polaritons is also due to the dielectric confinement effects. However, it is unfortunate that these forementioned confinement effects are in effect at same time so that a clear fundamental understanding of what exact role of each confinement play is hard to be realized. Further, the often asked question of how these confinement effects modify the physical and chemical properties of the confined materials is not at all conclusive. A clear demonstration of the cross-over effects from bulk state to cluster form has not yet been illustrated.

Heavy metal halides, such as PbI_2, form a unique series of layered semiconductor compounds. Besides having potential applications for γ-ray detection, the strong intralayer chemical bonding and the weak interlayer van de Waals interaction have made these materials to be good candidates for understanding the cluster formation and growth in confining media and for the study of different types of confinement effects along different crystallographic axes.

Sandroff et al.[3] first investigated layered semiconductor clusters in various solvents. Based upon the optical absorption of a solution containing PbI_2 and BiI_3 clusters and the cluster size distribution from TEM measurements, a single layer platelet-like cluster model was proposed. The *disrupt* blue-shifted absorption bands below 350 nm for PbI_2 in different solvents were explained by charge carrier confinement in different-sized crystallites with a single layer thickness. Other research groups[2,3] have re-examined similar systems. Disagreements have been raised in terms of the bands assignments in UV-Vis spectra which may result from the possible I^- or I_3^- presence in solution. However, no efforts have been made to understand how the band gap is truly modified when PbI_2 semiconductor changes its physical dimension from small clusters to its bulk. No solid explanation has been put forward to account for the discontinuous blue-shift of the PbI_2 clusters in solution. In addition, there has been no direct experimental evidence reported in literature to support the proposed disk-like single-layered semiconductor clusters being formed in the solution phase.

Therefore, the motivation of the present research is: i) to study cluster formation and growth mechanisms in the solution phase, which can provide information on crystal growth on earth and in microgravity;[5] ii) to understand how the confining geometry modifies the physical and chemical properties of the restricted clusters in terms of shape, lattice parameters, as well as the thermal and optical properties; iii) to provide direct experimental evidence of the size and morphology of these layered semiconductor clusters formed in solutions; iv) to study quantum confinement effect when PbI_2 is physically confined in four different pore-sized porous glass, which serves as the feed-back to estimate the PbI_2 clusters fromed in solution.

EXPERIMENTAL

Synthesis of PbI₂ Clusters in Solutions

As reported by others,[1,2] The starting materials are $Pb(NO_3)_2$ and NaI or KI which were purchased from Aldrich with purity of 99^+%. No effort was made to further purify the materials. Two reasons why we chose NaI instead of KI in most of our experiments were the following: 1) synthesized PbI_2 clusters are insoluble in pure alchol but $NaNO_3$ is. Therefore, the dilution of the colloidal suspended solution will not result in much of the alteration of the formed cluster size; 2) in order to unembiguously identify PbI_2 cluster formation and cluster sizes with AFM, the complete removal of $NaNO_3$ from the surfaces and maintaining the minimal perturbation to the PbI_2 clusters are critical so that SPM images can directly reflect the structural and frictional information on PbI_2 clusters themselves. Both $Pb(NO_3)_2$ and NaI (or KI) were prepared in same solvent with known amount of molar concentration. Lead iodide clusters were synthesized by simply mixing the two solutions in the optical cell before subject to various measurements.

Impregnation of PbI₂ in Well-Defined Porous Glasses

In order to understand quantum confinement effect on PbI_2 particles, an alternative experiment was planned. That is, to impregnated PbI_2 in well-characterized porous glass. The detailed impregnation procedure has been reported elsewhere.[9] Only a brief outline is given in this paper.

Gelsil porous substrates with 2.5, 5, 10, and 20 nm pore diameters were used for PbI_2 impregnation. The PbI_2 was purchased fron Aldrich with 99^+% purity. The porous glass was first cleaned and then was placed into 10 mm inner diameter and one-end sealed quartz tube. The tube was placed into a vertical furnace. The glass was slowly heated to 450C in 6 hrs and then was cooled down to 110C. A sufficient amount of PbI_2 powder was loaded into a smaller glass tube with open ends. Then the tude containing PbI_2 was transported into the bigger tude where the porous glass was dried. The system was heated again very slowly to 450C. The melted PbI_2 flew out the inner tube and emersed the porous substrates. Upon the 1 hr soaking in the molten state of the PbI_2, the impregnated porous substrate was slowly cooled back to room tempeature. The sample tube was properly sealed for characterization.

Optical Characterization

In order to understand the solution structure and cluster formation kinetics, time resolved and static UV-Vis spectrophotometric measurements were carried out on a Rapid Scan OLIS RSM Spectrophotometer and a Hitichi 3501 spectrophotometer. With OLIS RSM, a series of spectra with time interval of 1- 10 ms was collected in the spectral range of 300 - 550 nm. The spectral intensity and frequencies were analyzed as the function of time. The static electronic absorption and extinction spectra were made possible with or without an integrating sphere accessory on a Hitachi 3501 spectrophotometer. All the

spectra were measured in 1000 - 185 nm region with 1 nm resolution.

Atomic Force Microscopy (AFM)

AFM images in TappingMode,constant force, and laterial force modes were obtained with a Nanoscope III atomic force microscope from Digital Instruments. All measurements were performed under ambient conditions with typical relative humidities ranging from 50 - 60%. Well-calibrated E- and A-scanners were used in the present experiments. With A scanner, atomic scale topography images of the hexagonal sheet of SiO_4 in cleavage basal plane of Muscovite mica can be readily obtained on a freshly cleaved mica surface. By comparing the measured value of the nearest neighbor distance of the SiO_4 tetrahedral with the literature value, the lateral resolution of the A-scanner on the atomically flat surface is less than 0.02 nm. Vertical resolution of both A and E scanners in both tapping and constant force modes is less than 0.1 nm. In order to further ensure the consistency in vertical resolution, as we reported eslewhere,[6] a freshly cleaved PbI_2 single crystal surface was imaged which resulted in the observation of half the unit cell distance on c-axis, i.e. a single molecular layer step of PbI_2 along c-axis. The step height was used as an internal height calibration. The measured single layer step height was 0.7 ± 0.2 nm which is in good agreement with 0.698 nm in literature.[4]

Raman Measurement

Raman scattering measurements of PbI_2 in its bulk and confined phase in porous silica were conducted with a Spex Raman spectrometer, which is equipped with a double-grating monochrometer and Ti:Saphire laser pumped with Ar^+ laser. The scattered light was collected at 90° to the excitation laser beam. Each spectrum was obtained with 2 cm^{-1} resolution and 1 second integration time. A water cooled photomultiplier tube was used as the detector. The typical excitation energy of the laser was ~100 mW at 770 nm.

RESULTS AND DISCUSSION

Optical Characterization of Solution Structure

In order to understand solution structure and to identify of possible species present in solution, effords were made to systematically study i) solvent effect on reactants, i.e., NaI and $Pb(NO_3)_2$; ii) solvent effects on the reaction products, i.e., PbI_2 clusters and $NaNO_3$; iii) Pb:I molar ratio effect on reaction products; and iv) concentration effect on the cluster size formation. In the following section, each individual effect will be discussed sequentially.

Fig. 1 illustrates optical absorption spectra of reactants NaI and $Pb(NO_3)_2$ in methnaol solution. Both solvent and $Pb(NO_3)_2$ did not show any absorption band above 250 nm. However, KI solution did show two absorption bands at 270 and 320 nm, respectively. As pointed out by Wang and Herron[3], the observed two peaks at ~ 325 and 270 nm are primarily due to the absorption of I_3^- species in methanol solution. Similar spectra were

also observed for NaI or KI disolved in H_2O, D_2O, propanol methanol solution under ordinary light irradiation. Fig. 2 demonstrates the optical spectra of reaction products by mixing of NaI and $Pb(NO_3)_2$ with different molar concentration ratio. Three different Pb:I ratios were plotted out in this figure. They were Pb:I = 1:2, 1:3, and 1:4, respectively. As the number of iodine ions increases, the peaks at 270 nm and 320 nm increase accordingly, while a weak peak at 420 nm remained stationary. This observation further suggests that the bands at 270 nm and 320 nm were due to I_3^- complex formed in solution rather than what was believed to be the signature of PbI_2 cluster formation in solution.

In order to unembiguously identify PbI_2 cluster formation and to clearify true electronic absorption band(s) due to PbI_2 clusters in solution, we have collected both extinction and absorption spectra of PbI_2 colloidal solution at four different concentrations. The extinction spectra were obtained via simple transimission spectra, while the true absorption spectra were collected with the help of integrating sphere accessary. The extinction spectra, consistent with the work reported in the past,[1-3] showed two bands at 270nm and 320 nm. However, the absorption spectra clearly showed additional bands above 350 nm, which were not observable in extinction spectra, as shown in fig. 3. In addition, the band position shifts to the red and absorption intensity is enhanced as the PbI_2 concentration increases. When the concentration changed from 5.0 to 1.0 mM/l, the electronic absorption band due to PbI_2 clusters blueshifted from 505 nm to 420 nm. At 0.5 mM concentration, the electronic absorption due to the PbI_2 clusters was expected to overlap with the band at 320 nm.

It is known that when the physical dimension of semiconductors is comparable or smaller than their exciton Bohr radii, the manifestation of the quantum confinement on the excitons will result in the blueshift of the bulk band gap. For PbI_2 semiconductor, the room tempeature band gap was measured at ~ 515 nm (2.4 eV) and the exciton Bohr radius a_B is estimated to be 1.9 nm. Therefore, the cluster size of PbI_2 formed in methanol solution is expected to be comparable or smaller than exciton Bohr radius a_B = 1.9 nm. It needs to point out that the quantum confinement is predominently in lateral direction since the weak interlayer interaction, Van de Waals forces, results in the exciton confinement along c-axis even in its bulk crystal. Therefore, the cluster size of PbI_2 in solution refers to the lateral dimension or diameter of the disk-like quantum dots of PbI_2

Confirmation of the Existence of Single-layered PbI_2 Clusters Formed in Solution

Fig. 4 shows one of the typical TappingMode AFM images of the PbI_2 colloidal solution deposited on mica surface. It is clear that all PbI_2 clusters have the same height of 1.0 ± 0.1 nm. In order to eliminate any possible structure alteration due to the mica surface, which can lead to false height information, the same PbI_2 colloidal solution was used to deposit on graphite and SAM derivatized mica surfaces. The same height information was also obtained. Therefore, the 1.0 nm height of the image is considered to be the true height of the PbI_2 clusters. It is also concievable that the PbI_2 clusters must

be disk-like as discussed in previous section and proposed by others.[2,7] Then, the PbI_2 culsters on mica surface are orientated with their c-axis perpendicular to the mica surface. Therefore, the measured image height should reflect the layer thickness of the PbI_2 clusters. Due to the tip convolution problem, no attempt has been made to resolve the lateral dimension of the PbI_2 clusters. As pointed out earlier, the measured single layer thickness of the bulk lead iodide is 0.7 nm, while the height of the PbI_2 clusters was 1.0 nm. The 1.4 times layer thickness expension seems to be surprising. *Ab Initio* calculation calculation of PbI_2 and BiI_3 clusters, on the other hand, has shown that energy-optimized interlayer and intralayer distances of Pb_6I_{12} were 11% expanded and 1% contracted, respectively, with respect that of the bulk. A geometry optimization calculation suggests that the equilibrium interlayer thickness expanded 40% while the intralayer distance was contracted by 3%. Therefore, the observed 1.4 times of the swollen interlayer is expected. As it was argued by Marino *et al.*[1] In the case of Pb_6I_{12} clusters with D_{3h} point group symmetry, the electron-rich I atoms of the top layer are arranged in head-on configuration with respect to I atoms at the bottom layer. For the bulk PbI_2, however, each I atom in the top layer is located directly above the midpoint between two iodine atoms positioned in the bottom layer. Therefore, it was expected that PbI_2 clusters tend to laterally contract and to vertically expand.

Optical and AFM characterizations have provided sufficient evidence that the PbI_2 clusters formed in methanol solution is single-layered. The lateral size of the disk-like clusters, based on the quantum confinement of the excitons, is comparable or smaller than that of the exciton Bhor radius $a_B = 1.9$ nm.

Optical Characterization of PbI₂ Impregnated in Porous Glass

Fig. 5 showed the electronic absorption spectra of bulk PbI_2 and the PbI_2 physically confined in 2.5,5, 10, and 20 nm pores of silica substrates. As expected, the PbI_2 confined in large pores, the absorption spectrum showed a little blueshift in band gap. However, a noticable blueshift was observed at ~ 505 nm when the PbI_2 was confined in 2.5 nm pore, which is consistent with the quantum confinement theory proposed by Brus.[10] By comparing the optical spectrum of PbI_2 impregnated in 2.5 nm in fig. 5 with the spectrum of PbI_2clusters synthesized in methanol solution at 5 mM concetration in fig. 3, a same absorption band edge was observed. This observation provided strong indication that the PbI_2 clusters synthesized in the methanol solution was less than 2.5 nm in size. As the concentration decreases, the cluster size gets smaller so that the absorption band of the PbI_2 clusters was further blueshifted.

Fig. 6 illustrated Raman spectra of PbI_2 bulk and confined in four different pore-sized silica host. There were three bands observed in 60 - 150 cm^{-1} region. They are at 75, 96, and 106 cm^{-1}, respectively, which had been assigned to TO_2, LO_2, and LO_1 optical phonon modes of PbI_2 crystals. As the pore size decreases, LO modes are broadened and the center frequencies seem to be red-shifted. The red-shift of the band at 106 cm^{-2} is more

pronounced. It is speculated that the red-shifts in LO modes may be due to the enhancement of the surface phonon modes resulting from the local electric field at guest-host interface for small particles. However, the experimental results are further from conclusive to make a claim of surface phonon observation in this system. More experiments are current underway to study surface phonon polartons in layered semiconductor quantum dots.

CONCLUSION

Optical characterization of PbI_2 clusters synthesized in methanol solution with integrating sphere has unemibiguously confirmed the PbI_2 cluster formation. A spectral comparison of the electronic transitions between the PbI_2 clusters synthesized in solution and physically confined in porous glass suggests that the cluster size in solution is less than 2.5 nm in lateral dimension. This observation is consistent with the concept of strong quantum confinement sets in when the particle size is comparable or smaller than the exciton redius ($a_B = 1.9$ nm).

AFM measurements of PbI_2 clusters on mica, graphite, and CH_3 surfaces suggest that the clusters formed from solution synthesis are disk-like. A thickness of 1.0 ± 0.1 nm observed at 0.5 mM concentration confirms, for the first time, that these clusters are single-layered. The 40% expansion of the interlayer distance can be attributed to the finite size effect of the clusters. At small sizes, a strong intralayer chemical bonding can result in the lateral contraction with respect to the bulk value and can lead to the expansion in layer thickness.

LO and TO modes of bulk and the confined PbI_2 were also characterized via Raman scattering measurements. The observed red-shifts and spectral band boradening of LO modes (LO_1 and LO_2) may be attributed to surface phonon polartons of PbI_2 nanophase in the porous host. However, the experimental results are not yet conclusive.

ACKNOLDGEMENT

REFERENCES

1. M. M. Marino, M. Sawamura, W. C. Ermler, and C. J. Sandroff, Phys. Rev. B 41, 1270 (1990); J. Phys. Chem. 94, 7805 (1990); Phys. Rev. B 33, 5953 (1986); J. Chem. Phys. 85, 5337 (1986);
2. A. Roy, D. D. Sarma, and A. K. Sood, Spectrochimica Acta 48A, 1779 (1992);O. I. Mimic, Z. Li, G. Mills, J. C. Sullivan, and D. Meisel, J. Phys. Chem. 91, 6221 (1987).

3. Y. Wang and N. Herron, J. Phys. Chem. 91, 5005 (1987).

4. V. Grasso and G. Mondio "Electronic Structure and Electronic Transitions in Layered Materials", Ed. V. Grasso, pp - 191 (D. Reidel Publishing Comp. 1986).

5. For example R. S. Feigelson, J. Crystal Growth 90 1 (1988); F. Rosenberger, J. Crystal Growth 76, 618 (1993).

6. R. Mu, Y.-S. Tung, and D. O. Henderson, Phys. Rev. B [Rapid Comm.] (submitted 1995).

7. Z. K. Tang, Y. Nozue, and T. Goto, J. Phys. Soc. Japan 61, 2943 (1992); J. Luminescence 58, 127 (1994); Solid State Commu. 80, 331 (1991).

8. E. Lifshitz, M. Yassen, L. Bykov, and I. Dag, J. Phys. Chem. 98, 1459 (1994).

9. D. O. Henderson, R. Mu, A. Ueda, A. Burger, K. T. Chen, and D. O. Frazier, Mat. Res. Soc. Proc. Vol. 366, 283 (1995).

10. L. Brus, J. Chem. Phys. 80, 4403 (1984).
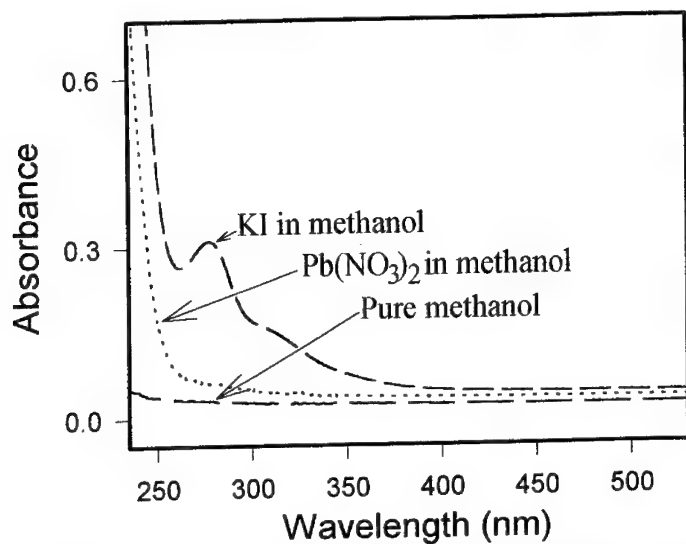
Fig. 1 Optical spectra of NaI and $Pb(NO_3)_2$ in methanol solution, and methanol itself.
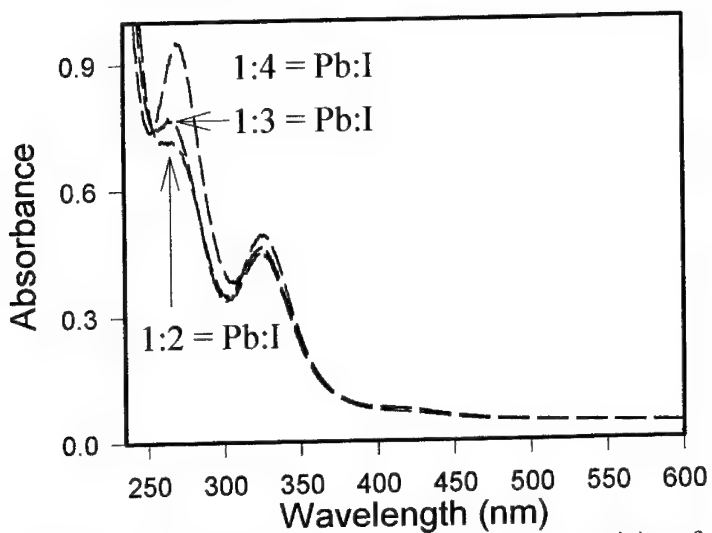
Fig. 2 Optical spectra of the reaction products from mixing of NaI and $Pb(NO_3)_2$ with different molar concentration ratio.
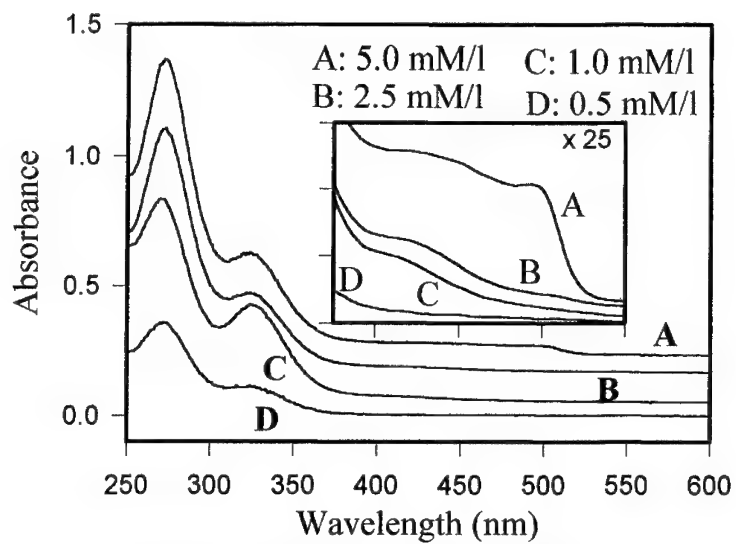
Fig. 3 Absorbance spectra of concentration dependence of PbI_2 in methanol solution.
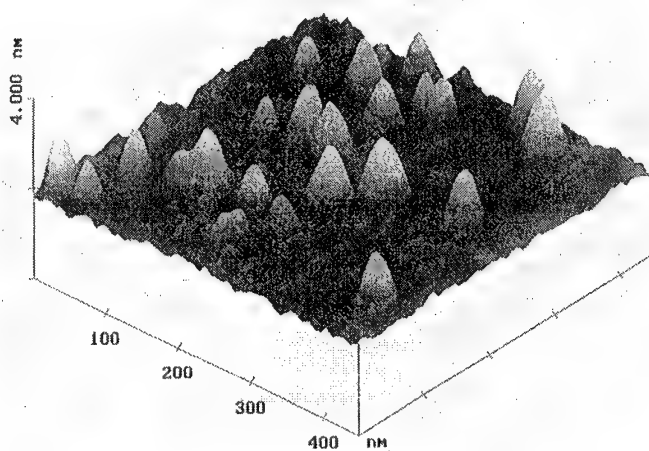
Fig. 4 Tapping mode AFM imageof lead iodide clusters deposited on mica surface.
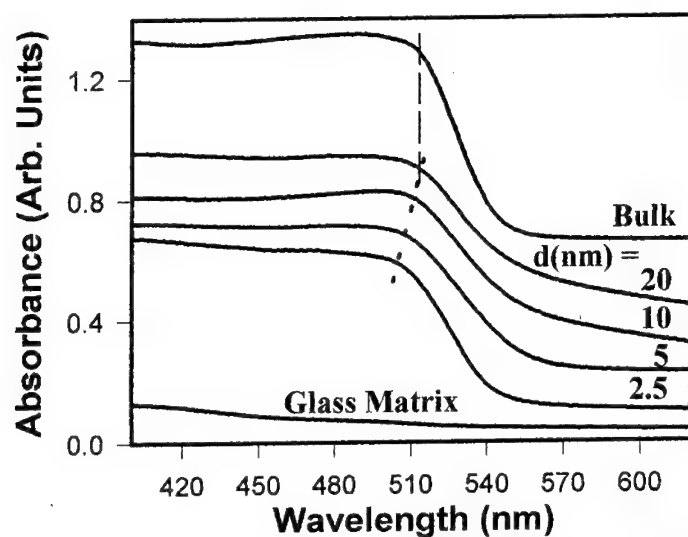
Fig. 5 Electronic spectra of bulk and the confined lead iodide in four different pore-sized silica substrates.
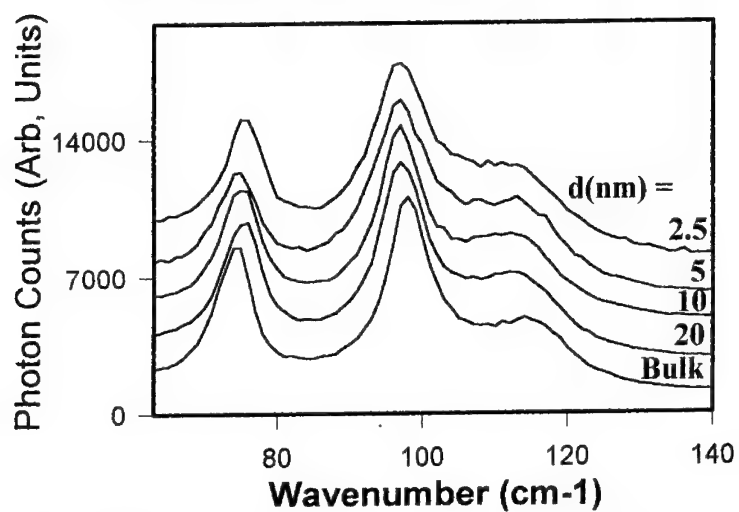
Fig. 6 Raman spectra of the bulk and the confined lead iodide in four different pore-sized silica.

EFFECT OF HETEROINTERFACE VIBRATIONS
ON ELECTRON MOBILITY IN QUANTUM WIRES

V. V. Mitin and F. T. Vasko[†]

Department of Electrical and Computer Engineering
Wayne State University, Detroit, Michigan 48202

Abstract

A contribution of heterointerface acoustic vibrations to electron mobility have been calculated for quantum wires. Such "macroscopic deformation" mechanism may be of the same order of magnitude as the conventional deformation potential contribution to mobility but it shows different dependencies on the carrier concentration and the on wire sizes. Moreover, the interference between these two mechanisms found to be important.

1. Introduction

It is well known and generally accepted in the literature that threre are two complimentary mechanisms of electron interaction with acoustic vibration in a bulk isotropic materials: 1) deformation potential (*da*) interaction with the longitudinal phonons, 2) piezoelectric (*pa*) interaction with the transverse acoustic phonons. There is no interference between *da* and *pa* mechanisms due to a $\pi/2$ phase shift between corresponding contributions to the Hamiltonian of interaction [1]. In the previous publication [2] we have introduce new "macroscopic deformation" mechanism (which we will refer to as *mda*) of an 2D-electron interaction with acoustic vibrations. Such contributions originates from the fact that acoustic-phonon-induced vibrations of heterointerface boundaries modulate electron quantization energies. The *mda*-mechanism become important in narrow heterostructures where the ratio of quantization energy, $\varepsilon_0 = (\pi\hbar/d)^2/2m$ (here d is characteristic thickness of heterostructure and m is effective mass), to deformation potential, D, may be of the order of 0.1. This mechanism may be dominant over the piezoelectric electron-phonon interaction for transverse acoustic phonon emission by hot 2D-electron in quantum wells. For *mda*-mechanism the interaction with transverse acoustic modes is not forbidden and the emission rate of transverse acoustic phonons is of the same order of piezoelectric interaction. The separation of *mda*- and *pa*-contributions is possible due to the difference in the energy and the angle distributions of emitted phonons. In recent report [3] analogous mechanism (called here as "ripple") has been applied to study the interlevel transitions of electrons in small (less then $35nm$ diameter) quantum dots; *mda*-contributions was found the same order of magnitude as the *da*-mechanism and size dependence of the relaxation rates versus a dot diameter is different for these mechanisms.

Because the contribution of the heterointerface vibrations to electron-phonon interaction is more pronounced for low-dimensional cases, it is interesting to introduce and consider this mechanism for quantum wires (QWIs). The electron phonon-interaction

due to the heterointerface vibrations of a QWI is a new and the complementary mechanism to the conventional low-temperature electron-scattering processes by acoustic phonons in selectively doped QWIs considered in [4,5]. Here we presented the results for conductivity in selectively doped rectangular QWIs. The modulation of ground state energy level due to both opposite pairs of heterointerface vibration was taken into account. Both this $(mda-)$ and usual $(da-)$ contributions are under consideration. In contrast with the conventional situation [6] the *interference* between these two mechanisms is essential. As a result, the contribution to the probability of an electron scattering from $mda-$interaction is of order of ε_0/D of the conventional $da-$contribution.

The paper is organized as follows. In Sec. II we introduce the $mda-$interaction of $1D-$electrons with bulk acoustic phonons and analize the transition probabilities taking into account the interference effect mentioned above. In Sec. III the linerized kinetic equation is transformed to the one-dimensional integral equation and it's solution for elastic scattering limit is presented. For this case we calculated the conductivity and analize the electron mobility in Sec. IV. Concluding remarks are in the last section.

II. The "macroscopic deformation" contributions to electron-phonon interaction.

We will consider a thin and narrow rectangular QWI with $(d_x \times d_y)$ cross section (OZ is the direction along QWI) where electron occupy only the lowest subband with parabolic dispersion law,

$$\varepsilon_{0x} + \varepsilon_{0y} + \varepsilon_p, \quad \varepsilon_{0j} = (\pi\hbar/d_j)^2/2m, \tag{1}$$

where $\varepsilon_p = p^2/2m$ is a 1D-kinetic energy. We will consider QWI embodied into a matrix with close elastic parameters (like $GaAs$ wire in $AlAs$ matrix) so that phonons are bulk-like and we will use standard expressions for the displacement operator in $(\mathbf{x}, q)-$representation

$$\mathbf{u}_{\mathbf{Q}k}(\mathbf{x}) = \sqrt{\frac{\hbar}{2\rho\omega_{Qk}}}\mathbf{e}_{\mathbf{Q}k}(b_{\mathbf{Q}k}e^{i\mathbf{q}_\perp \mathbf{x}} + h.c.) \tag{2}$$

Here $\mathbf{Q} = (\mathbf{q}_\perp, q)$ is phonon wave vector ($\mathbf{q}_\perp$ and q are its 2D-transversal and 1D-longitudinal components, $\mathbf{x}$ is a 2D-coordinate in a transverse direction), ω_{Qk} is phonon frequency for the kth-mode (below we will use the linear dispersion relations, $\omega_{Qk} = c_k Q$, with sound velosities c_k, $k = l$ for longitudinal and $k = t_{1,2}$ for transverse modes), ρ is the material density. The anihilation (or criation) operators for kth mode are $b_{\mathbf{Q}k}$(or $b_{\mathbf{Q}k}^+$) and the polarization orts $\mathbf{e}_{\mathbf{Q}k}$ are chosen in the form:

$$\mathbf{e}_{\mathbf{q}l} = \mathbf{q}/q, \quad \mathbf{e}_{\mathbf{q}t_1} = (-q_y/q_\|, q_x/q_\|, 0), \quad \mathbf{e}_{\mathbf{q}t_2} = (-q_x q_z/q q_\|, -q_y q_z/q q_\|, q_\|/q). \tag{3}$$

In 1D-approximation the energy of macroscopic deformation interaction is determined by the shift of ground state energy level $\varepsilon_{0x} + \varepsilon_{0y}$ due to vibration of $x-$ and $y-$

heterointerfaces. Under these approaches mda- and da-contributions to interaction energy take forms:

$$\mathcal{H}_{md}(\mathbf{Q}k) = -\frac{2\varepsilon_{0x}}{d_x}\mathbf{e}_x \cdot \mathbf{u}_{\mathbf{Q}k}(\mathbf{r})\Bigg|\begin{array}{l} x = d_x/2 \\ x = -d_x/2 \end{array} - \frac{2\varepsilon_{0y}}{d_y}\mathbf{e}_y \cdot \mathbf{u}_{\mathbf{Q}k}(\mathbf{r})\Bigg|\begin{array}{l} y = d_y/2 \\ y = -d_y/2 \end{array}$$

$$\mathcal{H}_d(\mathbf{Q}k) = iD\mathbf{Q}\cdot\mathbf{u}_{\mathbf{Q}k}(\mathbf{x}) \tag{4}$$

The meaning of the vertical lines is the same as for the limits of ingration: the value of the function taken at the lower limit should be subtracted from the value of the function taken at the upper limit.

The transition probability between electron states with longitudinal momentums p and p' due to above contributions may be written as

$$W(p, p') = \frac{2\pi}{\hbar}\sum_{\mathbf{Q}k}|< 0p|\mathcal{H}_{md}(\mathbf{Q}k) + \mathcal{H}_d(\mathbf{Q}k)|0p' >|^2 \times$$

$$[(N_{\mathbf{Q}k} + 1)\delta(\varepsilon_p - \varepsilon_{p'} + \hbar\omega_{\mathbf{Q}k}) + N_{\mathbf{Q}k}\delta(\varepsilon_p - \varepsilon_{p'} - \hbar\omega_{\mathbf{Q}k})]. \tag{5}$$

We will use simple ground state electron wave functions for $x-$ and $y-$directions in the form $\sqrt{2/d_j}\cos(\pi x_j/d_j)$ and deformation contribution express through the functions [6]

$$< 0|e^{i\mathbf{q}_\perp \mathbf{x}}|0 >= g(\frac{q_x d_x}{2})g(\frac{q_y d_y}{2}), \quad g(y) = \frac{\sin y/y}{1 - (y/\pi)^2}. \tag{6}$$

For $mda-$contribution such model give

$$e^{iq_j x_j}\Bigg|\begin{array}{l} x_j = d_j/2 \\ x_j = -d_j/2 \end{array} = i2\sin\frac{q_j d_j}{2}. \tag{7}$$

so that interference of $da-$ and $mda-$contributions take place because these addenda are in the same phase (usually [1] deformation and piezoelectric mechanisms are shifted in phase by $\pi/2$ and they give two independent contributions). As a result the transition probability due to $l-$mode $W_l(p, p')$ include $da-$ and $mda-$mechanisms and the contributions from t_1- and t_2-modes to $W_t(p, p')$ caused by the $mda-$mechanism only. After substitution (4),(6) and (7) into (5) the expressions for $W_k(p, p')$ take the form:

$$W_k(p, p') = \int \frac{d\mathbf{q}_\perp}{4\pi\rho\omega_{\mathbf{Q}k}}|C_k(Q)|^2 [(N_{\mathbf{Q}k} + 1)\delta(\varepsilon_p - \varepsilon_{p'} + \hbar\omega_{\mathbf{Q}k})+$$

$$N_{\mathbf{Q}k}\delta(\varepsilon_p - \varepsilon_{p'} - \hbar\omega_{\mathbf{Q}k})]_{|\hbar q=p-p'}. \tag{8}$$

where effective matrix elements $|C_k(Q)|^2$ may be written for $l-$, t_1- and t_2-modes as

$$|C_l(Q)|^2 = \left|QDf(\frac{q_x d_x}{2})f(\frac{q_y d_y}{2}) - \frac{4\varepsilon_{0x}}{d_x}\frac{q_x}{Q}\sin\frac{q_x d_x}{2}f(\frac{q_y d_y}{2}) - \frac{4\varepsilon_{0y}}{d_y}\frac{q_y}{Q}\sin\frac{q_y d_y}{2}f(\frac{q_x d_x}{2})\right|^2 \tag{9}$$

$$|C_{t_1}(Q)|^2 = \left| \frac{4\varepsilon_{0x}}{d_x} \frac{q_y}{q_\perp} f(\frac{q_y d_y}{2}) - \frac{4\varepsilon_{0y}}{d_y} \frac{q_x}{q_\perp} f(\frac{q_x d_x}{2}) \right|^2 \tag{10}$$

$$|C_{t_2}(Q)|^2 = \left| \frac{4\varepsilon_{0x}}{d_x} \frac{q_x q}{q_\perp Q} f(\frac{q_y d_y}{2}) + \frac{4\varepsilon_{0y}}{d_y} \frac{q_y q}{q_\perp Q} f(\frac{q_x d_x}{2}) \right|^2 \tag{11}$$

and longitudinal momentum transfer is determined as $q = (p - p')/\hbar$, like to Eq.(8).

Therefore, we have introduced a new scattering channel due to heterointerface vibration. It allows the electron-phonon interaction with t-modes and introduce *interference* between $da-$ and $mda-$contributions in Eq.(9). This interference term is of order of $(Qd_{x,y})D/\varepsilon_{0x,y}$ to the conventional da-interaction. This correction increases with the decrease of a wire cross section and it become essential for narrow QWIs.

III. Expression for conductivity.

Using evaluated above transition probabilities we can find electron distribution function over 1D-momentum f_p from linearized kinetic equation with the electron-phonon collision integral in the form

$$J_{e-ph}(f|p) = \sum_{k=l,t} \int_{-\infty}^{\infty} \frac{dp'}{2\pi\hbar} [W_k(p,p')f_{p'}(1-f_p) - W_k(p',p)f_p(1-f_{p'})]. \tag{12}$$

Under a weak electric field F along a QWI the distribution function f_p take form $f_F + f_1$ where an additional to the Fermi-distribution, f_F, perturbation f_1 may be introduced according to relation

$$f_1 = \frac{e}{m} F p \chi_p, \quad \chi_{-p} = \chi_p. \tag{13}$$

The even function χ_p needs be determined from the integral equation

$$\int_{-\infty}^{\infty} \frac{dp'}{2\pi\hbar} \sum_k W_k(p,p')(\chi_p - \frac{p'}{p}\chi_{p'}) = -\frac{df_F}{d\varepsilon}. \tag{14}$$

The conductivity σ has the following expression through function χ_p

$$\sigma = 2\frac{e^2}{m} \int_{-\infty}^{\infty} \frac{dp}{\pi\hbar} p^2 \chi_p, \tag{15}$$

and the solution of integral equation (14) with complicate kernels (9)-(11) need for general case.

For the case of strong degenerate electrons when scattering is practically elastic (because $\varepsilon_F \gg c_j p_F$, p_F and ε_F are Fermi momentum and Fermi energy; p_F connected with 1D-concentration n_{1D} through the relation $n_{1D} = 2p_F/\pi\hbar$), so that χ_p is a function of energy only. The solution of (14) may be written as

$$\chi_p = \tau_F \delta(\varepsilon_F - \varepsilon) \tag{16}$$

To obtain the momentum relaxation time τ_F we take into account the strong inequality $T_{ph} \gg c_j p_F$ (T_{ph} is the phonon temperature), so that we can use in (8) the factor

$$\left[(N_{Qk}+1)\delta(\varepsilon_p - \varepsilon_p' + \hbar\omega_{Qk}) + N_{Qk}\delta(\varepsilon_p - \varepsilon_p' - \hbar\omega_{Qk})\right] \simeq \frac{2T_{ph}}{\hbar\omega_{Qk}}\delta(\varepsilon_p - \varepsilon_p'). \quad (17)$$

As a result

$$\tau_F = \int_{-\infty}^{\infty} \frac{dp'}{2\pi\hbar} \sum_k W_k(p_F, p')(1 - \frac{p'}{p_F}). \quad (18)$$

so that the contribution from $p' = -p_F$ is essential in (18) only and l, t—contributions to the transition probabilities $W_{l,p}(p_F, p)$ transform to

$$W_{l,t}(p, p') = \int \frac{d\mathbf{q}_\perp}{4\pi\rho\omega_{Ql,t}}|C_{l,t}(Q)|^2 \frac{2T}{\hbar\omega_{Ql,t}}\Big|_{q=(p_F-p)/\hbar} \delta(\varepsilon_F - \varepsilon_p) \quad (19)$$

here we introduce $|C_t(Q)|^2 = |C_{t_1}(Q)|^2 + |C_{t_2}(Q)|^2$.

After substitution of (16) into (15) we can express mobility $\mu = \sigma/(n_{1D}|e|)$. through the relaxation time at Fermi energy

$$\mu = \frac{|e|}{m}\tau_F \quad (20)$$

where the momentum relaxation rate can be written as

$$\tau_F^{-1} = \frac{m}{p_F} \sum_{k=l,t} \int \frac{d\mathbf{q}_\perp}{\pi^2\rho} \frac{T_{ph}}{(\hbar\omega_{Qk})^2}|C_k(Q)|_{|q=2p_F/\hbar}^2. \quad (21)$$

Thus, the integration over transverse wave vector of phonons is necessary for the calculations of the degenerate electrons mobility only.

IV. Mobility.

The contribution to μ from the da—mechanism of scattering (which is denoted below as μ_d) can be calculated in analytical form (see Ref. [4]). Taking into the account first order interference corrections from mda—scattering we obtain the expression for mobility in form

$$\mu = \mu_d \left\{ 1 + \frac{4}{\pi^2} \int \frac{d\mathbf{l}}{l^2+1} g(l_x\eta_x)g(l_y\eta_y) \times \right.$$

$$\left. \left[\frac{\varepsilon_{0x}}{D}\eta_y l_x \sin(l_x\eta_x)g(l_y\eta_y) + \frac{\varepsilon_{0y}}{D}\eta_x l_y \sin(l_y\eta_y)g(l_x\eta_x)\right] \right\}. \quad (22)$$

Here we introduce $\eta_{x,y} = p_F d_{x,y}/\hbar$ and $\mathbf{l} = (l_x, l_y) = \hbar\mathbf{q}_\perp/p_F$ is dimentionless phonon wave vector. The mda—contribution under consideration in (22) express through the integral

$$I(\eta_y, \eta_x) = -\int \frac{d\mathbf{l}}{l^2+1} l_x \sin l_x\eta_x g(l_x\eta_x)g(l_y\eta_y)^2 \quad (23)$$

according to relation

$$\mu = \mu_d \left[1 + \frac{\varepsilon_{0x}}{D} \eta_y I(\eta_x, \eta_y) + \frac{\varepsilon_{0y}}{D} \eta_x I(\eta_y, \eta_x) \right]. \tag{24}$$

It is convenient to introduce dimensionless concentration η, anisotropy factor ξ and characteristic energy ε_0 according to relation

$$\eta = \sqrt{\eta_x \eta_y}, \qquad \xi = \frac{d_x}{d_y}, \qquad \varepsilon_0 = \frac{(\pi\hbar)^2 / d_x d_y}{2m} \tag{25}$$

and rewrite (24) as

$$\mu = \mu_d \left[1 + \frac{\varepsilon_0}{D} J(\eta, \xi) \right]. \tag{26}$$

The function $J(\eta, \xi)$ in (26) take following form

$$J(\eta, \xi) = 2\pi \int_{-\infty}^{\infty} dz g(z)^2 \times$$

$$\left[\frac{1 - e^{-2\sqrt{(\xi z)^2 + \eta^2 \xi}}}{\xi^2 \sqrt{z^2 + \eta^2/\xi}[(\xi z)^2 + \xi \eta^2 + \pi^2]} + \frac{\xi^2 (1 - e^{-2\sqrt{(z/\xi)^2 + \eta^2/\xi}})}{\sqrt{z^2 + \eta^2 \xi}[(z/\xi)^2 + \eta^2/\xi + \pi^2]} \right]. \tag{27}$$

This function determins the dependencies of μ on electron concentration (through η) and on the form of a QWIs (moreover $\xi = 1$ correspond to squre QWI while $\xi \gg 1$ and $\xi \ll 1$ describe the case of "slab-like" QWI). Note, that $J(\eta, \xi) = J(\eta, 1/\xi)$ and (26) do not depend from QWI orientations.

Fig. 1 demonstrates calculated dependencies of mda−correction to mobility on electron concentration for different form-factors ξ. One can see a visible changing of the mda-contribution to mobility both under variation of concentration (function (27) decreases when η increases) and for different form factors. Concentration dependencies of mobility for different cross sections shown on Fig.2. Dashed lines here correspond the result without mda-corrections, thus we have 10slightly different dependencies from n_{1D}. For QWIs with 30A characteristic size such corrections will be in order of 30-50

V. Concluding remarks.

We considered new channel of scattering for 1D-electrons in QWIs due to acoustic-phonon-induced heterointerface vibration. In order to demonstrate the visible effect of this mechanism we have been analyzed the interference contribution (from da- and mda-scattering) to mobility. As far as we know the direct measurement of mobility [7] carried out for QWIs with relatively big sizes (and scattering due to static inhomogeneous was a main contribution). In, principle, da- and mda- contributions may be selected from total mobility due to their temperature dependence. Optical methods of investigations of QWIs give a new possibilities measurement of mobility (see [8]
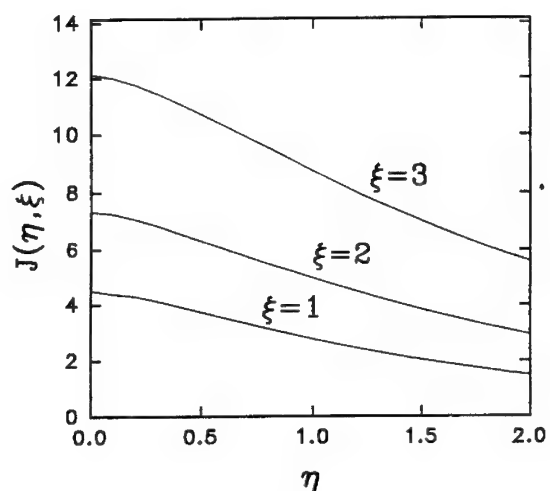
Figure 1: Function (27), which determined mda-contribution to mobility, versus dimensionless concentration η for different form-factors.

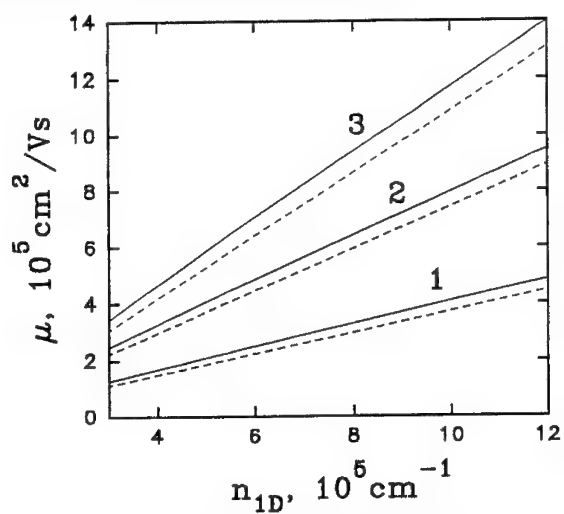Figure 2: Mobility versus concentration for $GaAs$-QWIs with sizes: $50 \times 50A$ (1), $50 \times 100A$ (2), $50 \times 150A(3)$.

and Refs, therein). Acoustic-phonon-scattering determine energy relaxation and *mda*-contributions may be essential too (such relaxation studied both for QWIs and for thin metallic films [9] where mechanism under consideration may be important).

Note, that in this paper we do not take into account some peculiarities of QWIs. Both simple parabolic dispersion law for ground electron state and linear energy spectrum for bulk-like phonons are generally accepted (but for wide QWIs some subband should be taken into account and modifications of phonon spectra may be important for structures with different elastic parameters [10]). Quasielastic approximation will be broken for low temperatures when integral equation (14) should be solved; in this case piezoacoustic scattering may be important too (analogous to 2D-case, which has been studied in [11]). The influence of Coulomb interaction on 1D-conductivity discussed in several papers (see [12]) but this reason do not change the ratio between *da*- and *mda*-contributions to momentum and energy relaxation processes. The influence of the heterointerface roughness has also been discussed before in a number of papers; its significance depends on technology used for fabrication of QWIs. However, it does not change the ratio of the rates of *da*- and *mda*- mechanisms of scattering.

Acknowledgement: The work was supported by ARO.

†Permanent address: Institute of Semiconductor Physics, Kiev-252650, Ukraine

References

[1] V.F.Gantmakher, Y.B.Levinson, *Carrier scattering in metals and semiconductors* (Norht-Holland, Amsterdam, 1987)

[2] F.T.Vasko, and V.V.Mitin, Phys.Rev.B **52**, 1500, (1995).

[3] P.A. Knipp, and T.L.Reinecke in *22nd Int. Conf. on the Physics of Semiconductors*,v.3, 1927, edited by D.J. Lockwood (World Scientific,Singapore, 1995).

[4] F.Comas, C.Trallero-Giner, and J.Tutor, Phys. Status Solidi (b) **139**, 433 (1987)

[5] R.Mickevicius and V.Mitin, Phys. Rev. **B 48** 17194 (1993)

[6] P.J.Price Ann. of Phys. **133**, 217 (1981).

[7] J.H.Burroughes, M.L.Lerdbeater, M.P.Grimshaw, R.J.Evans, D.A.Ritchie, G.A.C.Jon and M.Pepper, Appl. Phys. Lett. **63**, 2219 (1993)

[8] G.Mayer, F.E.Prins, G.Lehr, H.Schweizer, H.Leier, B.E.Maile, J.Straka, A.Forchel, and G.Weimann, Phys. Rev. **B 47**,4060 (1993).

[9] M.Kanskar and M.N.Wybourne, Phys. Rev. Lett. **73**, 2123 (1994)

[10] N.Bannov, V.Aristov, V.Mitin, and M.A.Stroscio, Phys. Rev. B **51**, 9930 (1995)

[11] H.L.Stormer, L.N.Pfeiffer, K.W.Baldwin, and K.K.West, Phys. Rev. B **41**,1278 (1990)

[12] H. Maurey and T.Giamarchi, Phys. Rev. B **51** 10833 (1995)

Study of Thermoelectric Power of One-Dimensional

Hole-Gas in Quantum-Well Wire

Sudakshina Kundu and Sumita Raychaudhuri

Department of Electronic Science,University of Calcutta,

92 Acharya Prafulla Chandra Road, Calcutta 700 009., India.

Abstract : Temperature variation of thermoelectric power for one-dimensional hole-gas (1DHG) present in a quantum-well wire (QWW) has been derived by assuming constant density-of-states (DOS) function and the validity of Boltzmann equation. Effect of different scattering mechanisms with temperature has been considered. Screening has also been included.

Introduction : Semiconductor heterostructures supporting two-dimensional electron-gas (2DEG) find extensive use in high-mobility transistors (HEMT) [1], optical and highspeed logic devices. The need for efficienct p-type HEMT is felt for designing complementary logic gates in supercomputes. Properties of two-dimensional hole-gas (2DHG) are inferior to those of 2DEG because of the higher effective mass of holes and lower mobility. Recent epitaxial growth processes [2] have led to the growth of quantum-well wires (QWW) sup porting one-dimensional hole-gas (1DHG) where the effective-mass of hole in the axial direction is reduced due to valence band anistoropy if proper growth direction is chosen [3].To understand the electronic properties of these devices, a study of thermoelectric power of the low-dimensional carrier system becomes important because it gives informa-

tion regarding the band-structure, density-of-states distribution and the various scattering mechanisms operative.

In this paper the thermoelectric-power of 1DHG has been calculated and its variation with temperature has been studied. The relative contributions of different scattering processes have been calculated.

Theory : The structure considered here is a rectangular quantum-well wire where the hole-gas is quantised in both the y-and z- directions and has real propagation vector along the x-direction only that concides with the axial direction of the QWW . The wave-function of the 1DHG trapped inside a two-dimensional rectangular quantum-well of dimensions $L_z \times L_y = 100 \; \mathring{A} \times 100 \; \mathring{A}$ is given by [4]

$$\Psi_i(x,y,z) = \sqrt{2/L_y} \; \sin(m \pi y/L_y) \sqrt{2/L_y} \; \sin(n \pi z/L_z) \sqrt{1/L} \; \exp(jk.x) \; .... \; (1)$$

Where m and n are integers, k is the wave vector along x-axis, and L is the length of the QWW. The integer i = 1 stands for heavy - holes and i = 2 stands for light holes. The quantum - well is formed by sandwiching a nearly undoped GaAs of low band-gap between highly doped p-type AlGaAs samples of larger band-gap. Lack of inversion symmetry and strong spin-orbit coupling of the valence-band structure split the otherwise degenerate valence-band. The position of the Fermi level with respect to the energy eigen values in the QWW is such that the majority of the one-dimensional holes are present in the spin degenerate highest heavy hole subband for m=n=1, i=1 and are characterised by average effective mass 0.027 m_o [4] The temperature dependent ideal DOS function for the 1DHG is $g_i(E) \; dE = 1/2 \; (2 \; m_i^*/\hbar^2)^{1/2} \; (E_{vi} - E)^{-1/2} \; dE.....(2)$

Where E_{vi} is the valence-band maximum for the i th band. This DOS function is highly peaked and has a singularity near the top of the subband. This singularity is removed if the DOS function is evaluated at absolute zero of temperature [5]. Here the calculations are done at low temperatures so that the departures of the two values are insignificant. The effect of various scattering mechanisms on the hole-mobility is different at different temperatures. The deformation potential and piezoelectric acoustic phonon sacttering together with impurity scattering dominate at low temperatures. At higher temperatures the polar optic-phonon sacttering becomes significant. The effect of remote impurities may be reduced by interposing undoped AlGaAs buffer layer in the barrier region. The effect of background impurities cannot be reduced. Here, a buffer layer has been included to eliminate the effect of remote-impurity scattering. These assumptions have proved to be true for 2DHG [6] . So we have taken these assumptions as valid in case of 1DHG as well. Boltzmann transport equation is assumed to hold for the scattering processes. While evaluating the integrals over the y and z axes, the Momentum Conservation Approximation (MCA) method of Ridley [7] has been considered. The approximation gives negligible errors (< 10%) for not too thin wells. The effectiveness of the MCA method lies in its simplicity. The sacttering angle θ for 1DHG is 180°. Considering all these factors, the relaxation times for individual scattering mechanisms are given below :

$$\tau (k)^{-1}{}_{ac} = (E_1{}^2 C_2 / 32 C_L L_z L_y \hbar) \, [(E_v - E)/K_B T]^{-1/2} \ldots (3)$$

C_L is the elastic constant, E_1 is the deformation potential constant and

$C_2 = (2 m_i K_B T / \hbar^2)^{1/2}$, for acoustic phonon scattering .

For piezoelectric scattering,

$$\tau(k)^{-1}_{pi} = [K^2 e^2 C_2 x^{-1/2}/128\pi\; \varepsilon_o \varepsilon_s L_y L_z \hbar]\; [4/xC_2^2 + \pi^2/4L_z^2)$$

$$+2/(xC_2^2 + \pi^2/4I_{,y}) + 1/xC_2^2 + \pi^2/L_y^2 + \pi^2/L_z^2)\ldots\ldots(4)$$

Where $x = (E_v - E) / k_B T$ and K is the piezoelectric constant.

For impurity scattering we have

$$\tau(k)^{-1}_{im} = [\pi\; m^*_{,i}\; N_B/2\hbar^3\; k^3]\; [2\; Ze^2/4\pi\; \varepsilon_o \varepsilon_s]^2\; [1+(ka)^2\; (K_o^2(ka) - K_1^2(ka))]\; \ldots(5)$$

where K_o, K_1 are Bessel functions, Z is the valency of the ion, $L_y = L_z = a$ and N_B is background impurity concentration. Polar optic phonon scattering is not an elastic process. The average relaxtion time for this scattering is calculated from power loss equations. However, this process is not important at the low temperatures for which thermo-electric power is calculated following the expression for thermopower derived by assuming Boltzmann equation [7]

$$S = (eT)^{-1}\; [<E\tau> / <\tau> - E_F]\; \ldots(6)$$

The hole distribution obeys Fermi-Dirac statistics.

The expressions for relaxation time given by equations 3-5 are unscreened. For low-dimensional carriers the effect of screening becomes very important. Inorder to include screening the dielectric constant present in the expression for probability of scattering is modified to

$$\varepsilon(q.T) = \varepsilon_o(q, E_F)\; (4k_B T\; Cosh^2\; (u))\;]\; dE\ldots(7)$$

Where $u = (E_F - E) / k_B T$,

$$\varepsilon_o(q, E_F) = \varepsilon_{BG} + [4e2m^*_{,i}/\pi\; \hbar^2].\; [F(q)/q].\; [\ln\; |\; (q+2k_F)/(q-2k_F)\; |\;]$$

and $F(q) = 2/(qa)^2]/[1-2K_1(qa) \cdot J_1(qa)]$

ε_{BG} is background dielectric constant and K_1 and J_1 are Bessel functions.

Results and Discussions: The parameters used in the calculation are :

$L_y = L_z = 100\text{Å}$. $E_1 = 9$ eV. $C_L = 139.7$ CN^{-3}. $K = 0.064$; $N_B = 10^{20} m^{-3}$; $\varepsilon_s = 12.9$.

One-dimensional hole concentration $\approx 10^8 m^{-1}$.

The variation of thermopower (S) with temperature (T) is shown in figure 1. The calculations are restricted to below 50 $\overset{\circ}{K}$ otherwise the assumptions on DOS and holes present in first heavy hole subband are no longer valid.
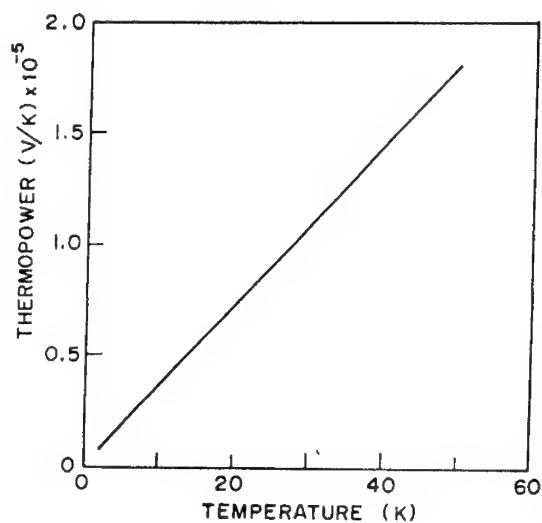
Fig. 1. The variation of themoelectric power of one-dimensional

hole-gas in a quantum-wire with temperature.
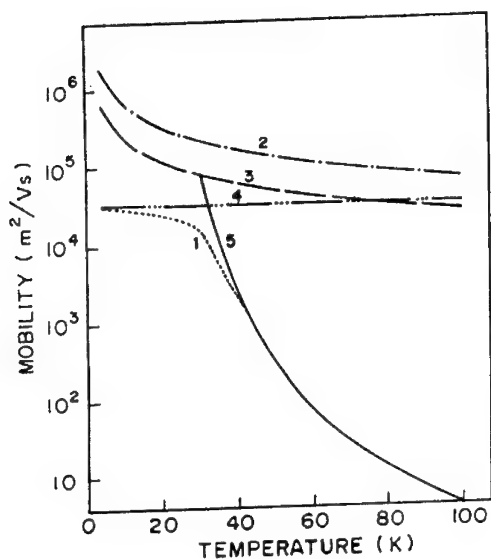
Fig 2: Mobility variation of 1DHG with temperature.

1. Total mobility. 2. Deformation Potential Acoustic Phonon. 3. Piezoelectric.

4. Back ground Impurity . 5. Polar Optic Phonon

Figure 2 is a plot of the relative contribution of the different scattering mechanisms at differnt temperatures. The hole distribution follows Fermi-Dirac statistics. It is amply clear that impurity sacttering is the dominant mechanism below 50°K and deformation potential acoustic-phonon and piezoelectric scatterings also have considerable effect below 20°K. . A similar trend is seen in the case of 2DHG system where it is supported by experimental results as well. So the three scattering mechanism, viz. impurity, deformation potential and

piezoelectric scatterings are consdiered for calculating the thermoelectric power.

It is found from figure 1, that the thermopower increases with temperatures. The variation is almost linear at low temperatures as expected. However, the values are expected to saturate at higher temperatures if polar - optic scattering is included . But at elevated temperatures the constant DOS function and other simplifying assumptions that are valid at lower temperatures , no longer hold . The formula has to be suitably modified at higher temperatures.

References

1:    Solomon, P.M.; Hadis, M.; IEEE Tran, 1984, **ED-31(B)**, 1015

2.   Sakaki, H., 22nd Int. Sym. Compund Semiconductors, 1995, to be published by IOP.

3.   Seumune, I.; Coldern, L.A.; IEEE Jr. Q.E. 1988, **24**, 1778

4.   Leburton, J.P.; J.Appl. Phys, 1983, **56**, 2850

5.   Weisbuch, C.; Vinter, B.; Quantum Semiconductors; Academic Press, Inc.;
      Harcourt Brace Jovanovich Publishers, 1991

6.   Datta, S.; Raychaudhuri, S.; Kundu, S.; Phys. Stat. Sol. 1993, **179**,77

7.   Nag, B.R.; Electron Transport in Compound Semiconductors, Springer Verlag; Berlin;
      1980, 217

MONTE CARLO SIMULATION OF THE GROWTH OF ONE-DIMENSIONAL SEMICONDUCTOR STRUCTURES

S. Keršulis and V. Mitin

Department of Electrical and Computer Engineering
Wayne State University, Detroit, USA

The formation of one-dimensional semiconductor structures on the top of ridges and by deposition through shadowing mask has been simulated by Monte Carlo technique. The simulation model includes tetrahedral lattice coordination of semiconductor material, atom-atom interactions out to second-nearest neighbors, and surface reconstruction effects. The growth of quantum wires with the top (001) or (411) surfaces, and (111) sidewalls is demonstrated. The formation of (111) sidewalls of higher quality than that of top (001) or (411) surface has been obtained due to larger diffusion coefficient of adatoms on (111) plane. The (001) and (411) surfaces on the top of the ridges have been obtained of nearly the same quality, and the only difference has been noticed in their shape being symmetric in (001), and not symmetric in (411) case.

INTRODUCTION

The growth of low-dimensional semiconductor structures by Molecular Beam Epitaxy (MBE) has been a subject of an increasing interest during the recent years. The understanding of atomic processes involved in the growth is crucial for the fabrication and control of high quality semiconductor structures. Many investigations in this area, both experimental and theoretical, have been made trying to elucidate their growth.

The possibility to obtain low-dimensional semiconductor structures by local epitaxy through shadowing masks has been investigated intensively during past years [1-4]. This method, already successfully applied to homoepitaxial Si epilayers [1] is now being adopted to narrow SiGe quantum wells. It has been demonstrated that by this growth technique epitaxial mesa islands of high crystalline quality with sidewalls solely determined by the growth conditions can be achieved [2-3].

The other technique for the formation of semiconductor quantum wires is patterning of the (100) oriented substrates with grooves and ridges. MBE growth of GaAs, AlAs, and AlGaAs on V-grooved GaAs substrates by this technique has been investigated in [5-13]. V-grooves were aligned along the [110] direction on (001) GaAs substrates and had V-shaped profiles with (111)A sidewalls due to the anisotropic etchings. By using the effect of different growth behavior of GaAs, AlAs, and AlGaAs, the multiple crescent-shaped GaAs quantum wires with a size of about (140-160 A) x (400-500 A) have been successfully grown at the bottom of the V-grooves [9-10]. Facetted growth of GaAs/AlGaAs epilayers on ridges has been studied in [12-13]. Rectangular ridges aligned along [011] direction on (001) surface were formed through a photoresist mask by reactive ion etching, and (GaAl)As layers were regrown on them by MBE. (111)B planes on both sides of the ridge as well as the (100) facets in the center of the ridge were formed. With decreasing ridge width, the (111)B planes restrict the formation of (100) facets on top of the ridges resulting in triangular shaped structures. In this way, the quantum wires were grown in [13].

There is however a small number of publications on the Monte Carlo (MC) simulation of the growth of such semiconductor structures. In [14-15], the growth kinetics on an (100) surface with a facetted V groove was studied by MC technique. Their model of facet growth

during MBE included growth of a simple cubic lattice structure in which vacancies and overhangs are forbidden, the so-called solid-on-solid (SOS) approximation [16]. Second-nearest-neighbor interaction was taken into account to incorporate facetting behavior. The effective growth rates on (100), (111)A, and (111)B of surfaces were calculated and good qualitative agreement with experimental data of [9] was obtained.

The growth of GaAs quantum-well wires on vicinal surfaces was studied by Monte Carlo simulation in [17-18]. An optimum regime within which the quality of quantum-well wire is maximum was obtained. The dependence of the quality of quantum-well wires on the direction of misorientation from the (100) plane was considered.

THE MODEL

The tetrahedral lattice structure of semiconductor material with both the nearest-neighbors and the second nearest neighbors taken into account is incorporated into our simulation model. Incorporation of this structure in our simulations of the growth on (100) plane is very similar to that proposed in [19]. A set of two two-dimensional arrays $L(x,y)$ and $R(x,y)$ is used. $L(x,y)$ array indicates the lateral position on the surface and the height of surface atoms relative to an arbitrary substrate reference plane. $R(x,y)$ array is used to describe the effect of surface reconstruction. We also use this technique in our simulations of the growth on (111) and (411) plane.

Four kinetic processes (the deposition of the atom on the surface, the migration of this atom on the surface, the evaporation of deposited atoms from the surface, and the surface relaxation) are taken into account. The complexity of these kinetic processes is simulated using the Arrhenius rate equation for each of these processes: $R = R_0 \, exp \, [-(n_1 \, E_1 + n_2 \, E_2) \, / \, kT \,]$, where n_1 and n_2 are the number of first- and second-nearest neighbors, and E_1 and E_2 are the first- and second-nearest-neighbors interaction energies, respectively. First- and second-nearest-neighbor interaction energies are among the most important parameters in the simulations. Our choice of them was based on the experimental data on the growth of Si(001) indicating the growth of high quality Si(001) surface at substrate temperatures above 650 C [20-23]. According to that, numerical values used in the simulation of the hopping kinetic process were chosen to be $E_1 = 0.6 \, eV$, $E_2 = 0.1 \, eV$. Energy terms for the evaporation event were taken to be $E_1 = 1.1 \, eV$, $E_2 = 0.2 \, eV$. The pre-exponential hopping rate or hopping attempt frequency R_0 was assumed to be $R_0 = 10^{13} \, 1/s$.

The Monte Carlo algorithm used is similar to the fast MBE growth algorithm of Maksym [24]. According to this algorithm, the time, type, and site of each of the four events mentioned above are chosen randomly with a probability of occurrence that depends on the kinetic rates for the individual events at each lattice site.

RESULTS AND DISCUSSION

The simulation of the growth of one-dimensional semiconductor structures on the top of ridges formed on (001) or (411) plane with (111) sidewalls requires the simulation of the growth on all these planes.

In Fig. 1 we present the simulation results of the (001) and (111) growth. For quantitative characterization of the quality of the growing material, we have introduced interface width (roughness) Δ [25]:

$$\Delta = < (h_i - < h >)^2 >^{1/2},$$

where h_i is the height of i-th column of the structure. The angle brackets denote an average over all surface sites. Δ is expressed in units of monolayers (ML).

The temporal evolutions of Δ at different substrate temperatures for (001) and (111) growth are shown in Fig. 1a and 1b, respectively. It can be seen that at $T = 700$ K the (001) growth is clearly rough three-dimensional with Δ increasing over the time (Fig. 1a). Temperature range $T = 750...800$ K can be called intermediate between the rough and smooth growth modes. In this temperature regime the interface width tends to saturate in time (especially at $T = 800$ K), and its value is much lower that in the case of $T = 700$ K. At $T = 900$ K, we observe smooth two-dimensional growth with Δ saturated in time, what is in good agreement with experimental data on the growth of Si(001) [23,25]. Moreover, the temporal oscillations of Δ can be seen in the beginning of the growth at $T = 900$ K, indicating layer-by-layer growth mode.

The temporal evolutions of interface width (roughness) Δ of (111) surface at the same deposition rate ($R_d = 1.0$ ML/s) and using the same activation energies as for (001) surface are depicted in Fig. 1b. We can see from this figure that temperature range $T = 450...475$ K
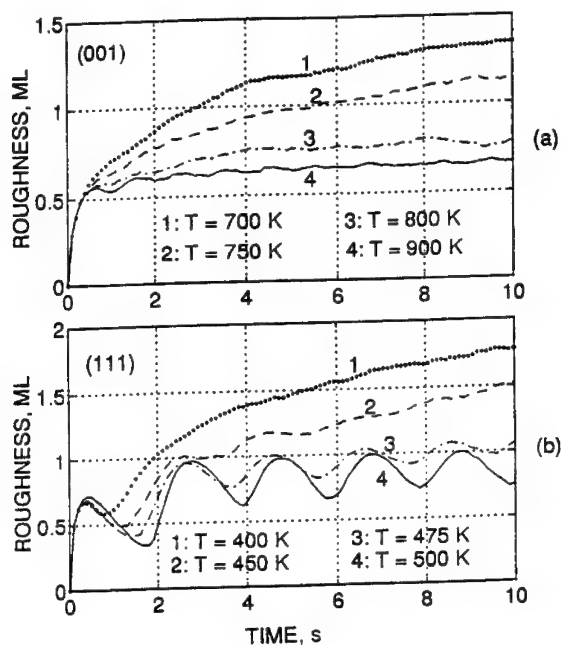

Fig. 1. Temporal evolution of the surface roughness during deposition of ten monolayers of Si on (001) (a) and (111) (b) surfaces at different substrate temperatures (deposition rate $R_d = 1$ monolayer/second).

is intermediate between the rough and smooth growth modes. Temporal oscillations of Δ at temperatures T = 475 K and 500 K can be clearly seen in this graph. The interesting feature of these oscillations is that the period of oscillations is about 2 sec, which corresponds to the time of deposition of one complete bilayer at a deposition rate of 1 monolayer per second. So, in this temperature range we observe not monolayer-by-monolayer (as it was in (001) case) but bilayer-by-bilayer growth mode, what corresponds to the experimental observations [26-28].

Comparison of temporal evolution of surface roughness Δ presented in Fig. 1a and 1b shows that the transition from rough to smooth growth mode for (111) surface occurs at lower temperatures than in the growth on (001) surface. At T = 500 K we observe intensive adatom motion on the (111) surface what causes the growth of high quality material. On the (001) plane the adatoms are almost immobile at T = 500 K (they have very low diffusion up to T = 700 K), and the growth here is rough and three dimensional. This difference in the growth on (111) and (001) surface corresponds to the experimental data of [7-11] where the different migration length of Ga atoms on (100) and (111) surface was observed. This result implies that V-grooved structures or structures with ridges similar to those of [7-11] can be obtained in the growth of silicon-like semiconductor materials.

The main difference between (111) and (001) surfaces of tetrahedral lattice structure is that in the [111] direction there are two types of layers while in the [001] direction all layers are equivalent. Atoms on one type of layer of surface (111) have three nearest-neighbors underneath while atoms on the other type of layer have only one nearest-neighbor underneath them. Therefore, the hopping rates on these two types of surfaces are different. For illustration in Fig. 2 we show the hopping rates for atom on three ideal flat surfaces: (001) plane for atom having two first-nearest and four second-nearest neighbors (dashed curve), (111) surface with one first-nearest neighbor and three second-nearest neighbors (upper solid curve), and (111) surface with three first-nearest neighbor and three second-nearest neighbors (lower solid curve). Large difference in the hopping rates on two types of (111) surface (of the order of 10^8 - 10^{13} s^{-1}) is clearly seen from this figure.
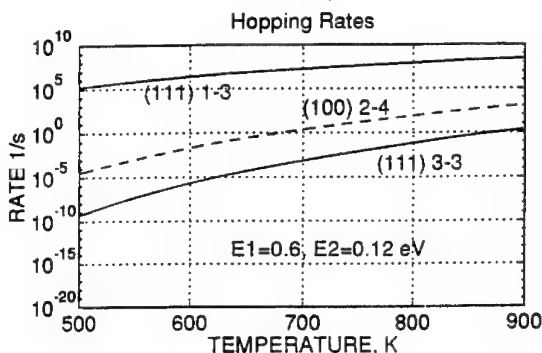
Fig. 2. Rates of hopping of an atom residing on flat (001) surface with two first-nearest and four second-nearest neighbors (dashed curve), residing on (111) surface with one first-nearest and three second-nearest neighbors (upper solid curve), and residing on (111) plane with three first-nearest and three second-nearest neighbors (lower solid curve).

The necessity of the fabrication of semiconductor interfaces with higher quality than in (001) or (111) surfaces has lead to attempts to grow semiconductor materials on (110), (311), (411) and other surfaces. In particular, the growth of GaAs/AlGaAs quantum wells on GaAs (411)A facet was performed in [3]. The possibility to achieve the formation of extremely flat and uniform GaAs/Al$_{0.3}$Ga$_{0.7}$As interfaces using (411)A GaAs substrate was reported in [29].

We have simulated the growth of silicon-like semiconductor on the (411) surface. In Fig. 3 we present the simulation results of the (411) growth at substrate temperature T = 600 K for the deposition rate R$_d$ = 1.0 ML/s. The temporal evolution of interface width (roughness) Δ and filling of layers during the deposition of ten monolayers are shown in Fig. 3a and Fig. 3b, respectively. It can be seen from this figure that at T = 600 K the growth is three-dimensional with many (five, six or seven) monolayers growing together at the same time moment (Fig. 3b), and surface roughness Δ increasing over time (Fig. 3a).
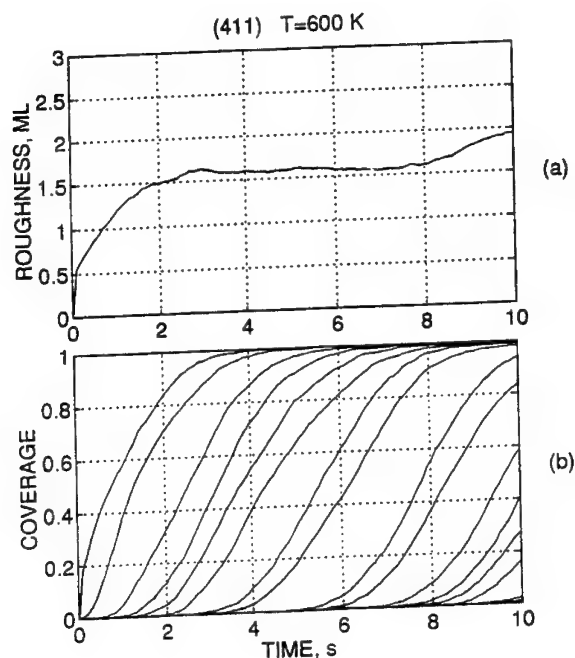
Fig. 3. Temporal evolution of the surface roughness (a), and filling of layers (b) during deposition of ten monolayers of silicon on (411) plane at T = 600 K.

The next set of our simulations was devoted to the investigation of the formation of one-dimensional semiconductor structures.

The results of the simulation of the growth of the structures with ridges on the top of (001) plane with the (111) side walls at two different temperatures (T = 700 K and T = 800 K) are shown in Fig. 4. The dimensions of lattice simulated were 40 x 20, and the deposition rate was 1 ML/s. Hopping rates on the (001) surface are lower than those on the one of the (111) surfaces (Fig. 2). That is why on the first stage of our simulations of the growth of

Fig. 4. The schematic representation of the structure with ridge formed on the top of (001) surface with the (111) side walls grown at substrate temperature T = 700 K (a) and T = 800 K (b).

quantum wires we have assumed infinitely large difference of these rates. Due to this assumption we obtained flat (111) side walls at both temperatures. As we can see from Fig. 4a and Fig. 4b, the only difference between the results is the quality of the top (001) surface which is better at T = 800 K than that of T = 700 K. The reason of this difference follows from Fig. 1a where the time dependence of roughness of (001) surface on substrate temperature is shown. It can be seen from Fig. 1a that the temperature T = 700 K corresponds to the conditions of rough three dimensional growth of (001) surface, while at T = 800 K the roughness is smaller and the quality of a growing surface is higher. The major result of our simulations is the formation of facets with (111) side walls with clear narrowing of the quantum wire during the growth.

We have also studied the growth of silicon-like semiconductor structures with ridges formed on the top of (411) surface with the 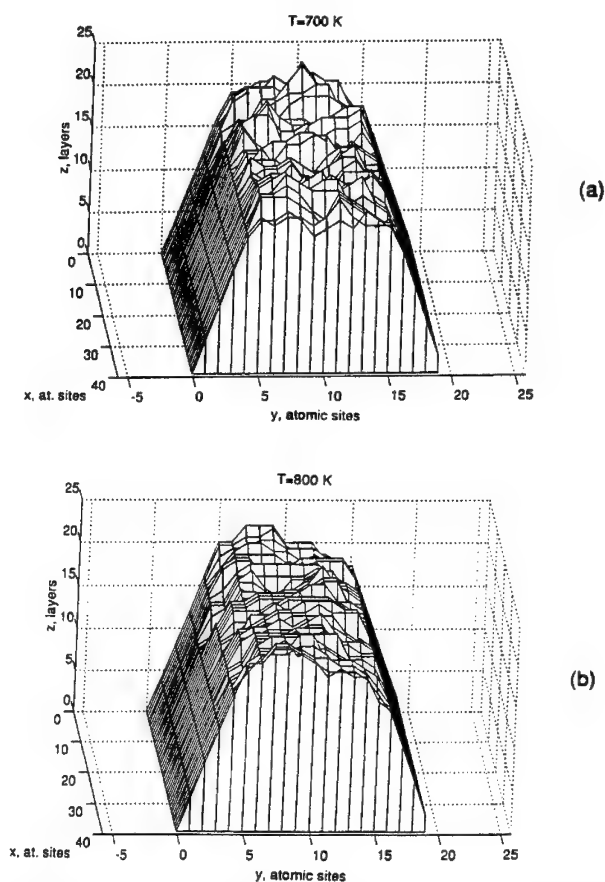(111) side walls. The schematic representation of the structure grown at substrate temperature T = 700 K is shown in Fig. 5. The deposition rate was 1 ML/s, the dimensions of substrate lattice were 20 x 40 with x axis along [122], and y axis along [011] direction, respectively. The result of this simulation is similar to that depicted in Fig. 4. The width of quantum wires formed on the (001) and (411) ridges is approximately the same. The difference is in the shape of these structures. While the quantum wire grown on the ridge on (001) plane is symmetrical, the corresponding one on (411) ridge forms two different angles between (111) side walls and (411) substrate. The (111) side walls are flat (due to enhanced adatom migration on this surface at T = 700 K), and (411) surface has the roughness which is comparable though to Δ at T = 700 K of (001). Therefore, we do not observe the decrease of surface roughness in the growth on (411) plane.
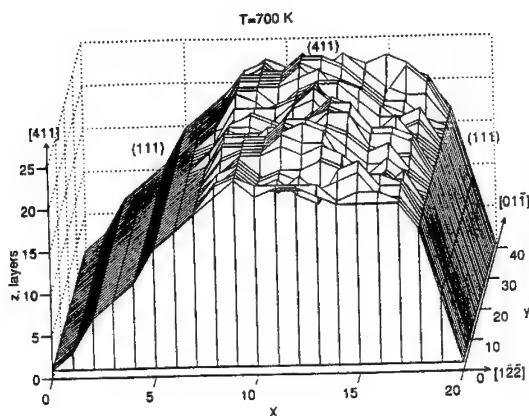
Fig. 5. The schematic representation of the structure with ridge formed on the top of (411) surface with the (111) side walls grown at substrate temperature T = 700 K .

The formation of facets with (111) side walls and (001) surface on the top of structure is clearly pronounced also in the growth of quantum wires by deposition through shadowing mask. In these simulations we went beyond the assumption of infinitely large difference in the hopping rates on different planes and simulated the actual hopping processes everywhere according to Arrhenius expression. First we deposited five monolayers of Si on Si(001) surface with the dimension of 60 x 80 lattice sites. After that we started the deposition of Si atoms on one region (30 x 80 lattice sites) of already formed 60 x 80 sites (001) surface at T = 800 K. Fig. 6 shows the surface configuration of quantum wire after the deposition
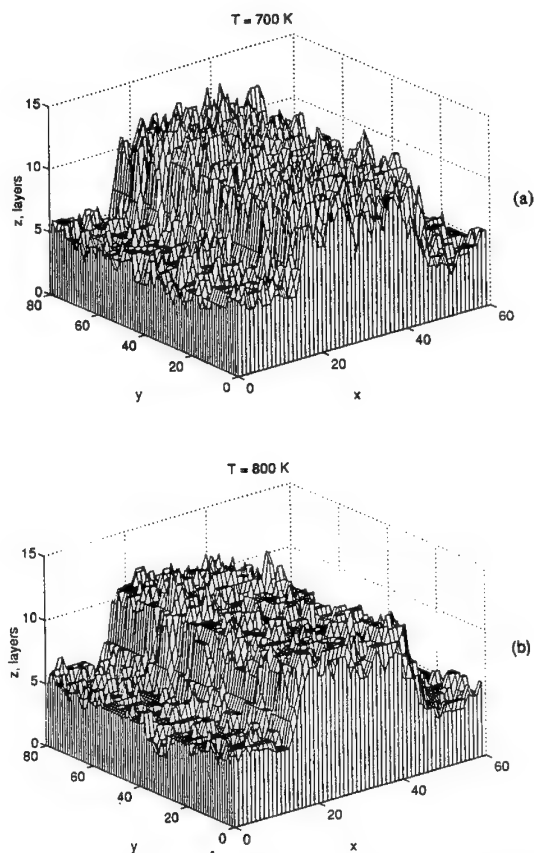
Fig. 6. The surface configuration of quantum wire after the deposition of six additional monolayers of Si on (30 x 80) lattice sites area on five-monolayer-thick (60 x 80) Si(001) "buffer layer" at substrate temperature T = 700 K (a) and T = 800 K (b).

of six additional monolayers on five-monolayer-thick Si(001) "buffer layer" at two different temperatures T = 700 K and T = 800 K. The formation of (111) side walls of higher quality than that of the top (001) surface can be seen in both these pictures. As in the case of the growth of semiconductor quantum wires on the top of ridges, the only difference between the results shown in Fig. 6a and 6b is the quality of the top (001) surface which is better at T = 800 K than that of T = 700 K. After the deposition of "buffer layer" of Si(001) we can start the deposition of Ge atoms. In this way the growth of SiGe/Si can be investigated. Thus, our results demonstrate the possibility of the growth of SiGe/Si quantum wires on the ridge structures as well as by the deposition through shadowing mask.

CONCLUSIONS

Our Monte Carlo simulations of the (001) and (111) growth show that the transition from rough to smooth growth mode for (111) surface occurs at lower temperatures than in the growth on (001) surface indicating higher diffusion coefficient of adatoms on (111) surface in comparison with (001).

The results of the simulation of the growth on (411) surface combine the features of the growth on (001) and (111) planes.

The simulation of the formation of structures on the top of ridges formed on (001) and (411) planes show that (111) side walls are flat in both cases due to the substrate temperature high enough to ensure high mobility of adatoms on (111) surface. The (001) and (411) surfaces on the top of the ridges is of approximately the same quality, and the only difference was obtained in their shape being symmetric in (001), and not symmetric in (411) case.

Our simulation also show the possibility of the growth of SiGe/Si quantum wires by the deposition through shadowing mask.

ACKNOWLEDGEMENTS

REFERENCES

[1] E. Hammerl, J. Messarosch, I. Eisele, V. Huber and H. Oppolzer, Mat. Res. Soc. Symp. Proc., 220 (1991) 27.
[2] E. Hammerl and I. Eisele, Appl. Phys. Lett., 62 (1993) 2221.
[3] J. Brunner, T.S. Rupp, H. Gossner, R. Ritter, I. Eisele and G. Abstreiter, Appl. Phys. Lett., 64 (1994) 994.
[4] J. Brunner, P. Schittenhelm, J. Gondermann, B. Spangenberg, B. Hadam, T. Koster, H.G. Roskos, H. Kurz, H. Gossner, I. Eisele and G. Abstreiter, J. Cryst. Growth, 150 (1995) 1060.
[5] X.Q. Shen, M. Tanaka and T. Nishinaga, J. Cryst. Growth, 127 (1993) 932.
[6] X.Q. Shen, M. Tanaka, K. Wada and T. Nishinaga, J. Cryst. Growth, 135 (1994) 85.
[7] M.E. Hoenk, H.Z. Chen, A. Yariv, H. Morkoc and K.J. Vahala, Appl. Phys. Lett., 54 (1989) 1347.
[8] M.E. Hoenk, C.V. Nieh, H.Z. Chen and K.J. Vahala, Appl. Phys. Lett., 55 (1989) 53.
[9] M. Hata, T. Isu, A. Watanabe and Y. Katayama, J. Vac. Sci. Technol., B 8 (1990) 692.
[10] M. Hata, T. Isu, A. Watanabe and Y. Katayama, Appl. Phys. Lett., 56 (1990) 2542.
[11] F.S. Turco, S. Simhony, D.M. Hwang, T.S. Ravi, E. Kapon and M.C. Tamargo, J. Cryst. Growth, 104 (1990) 766.
[12] T. Rohr, M. Walther, S. Rochus, G. Bohm, W. Klein, G. Trankle and G. Weimann, Mater. Sci. Eng., B 21 (1993) 153.

[13] M. Walther, T. Rohr, G. Bohm, G. Trankle and G. Weimann, J. Cryst. Growth, *127* (1993) 1045.

[14] N. Haider, M.R. Wilby and D.D. Vvedensky, Appl. Phys. Lett., *62* (1993) 3108.

[15] D.D. Vvedensky, N. Haider, T. Shitara and P. Smilauer, Phil. Trans. R. Soc. Lond., *A 344* (1993) 493.

[16] J.D. Weeks et al, Adv. Chem. Phys., *40* (1979) 157.

[17] K.J. Hugill, S. Clarke, D.D. Vvedensky and B.A. Joyce, J. Appl. Phys., *66* (1989) 3415.

[18] K.J. Hugill, T. Shitara, S. Clarke, D.D. Vvedensky and B.A. Joyce, Mat. Res. Soc. Symp. Proc., *v.160* (1990) 405.

[19] S.A. Barnett and A. Rockett, Surf. Sci., *198* (1988) 133.

[20] M. Ichikawa and T. Doi, Appl. Phys. Lett., *50* (1987) 1141.

[21] E. Kasper, Appl. Phys., *A 28* (1982) 129.

[22] E. Kasper and J.C. Bean, *Silicon Molecular Beam Epitaxy*, CRC Press, Boca Raton, FL, 1988.

[23] T. Sakamoto, K. Sakamoto, K. Miki, H. Okumura, S. Yoshida and H. Tokumoto, in M.G. Lagally (ed.), *Kinetics of Ordering and Growth*, Plenum, New York, 1991, p. 263.

[24] P.A. Maksym, Semicond. Sci. Technol., *3* (1988) 594.

[25] J.M. McCoy, P.A. Maksym and T. Kawamura, Surf. Sci., *257* (1991) 353.

[26] T. Sakamoto, N.J. Kawai, T. Nakagawa, K. Ohta and T. Kojima, Appl. Phys. Lett., *47* (1985) 617.

[27] J. Aarts and P.K. Larsen, Surf. Sci., *188* (1987) 391.

[28] T. Yokotsuka, M.R. Wilby, D.D. Vvedensky, T. Kawamura, K. Fukutani and S. Ino, Appl. Phys. Lett., *62* (1993) 1673.

[29] S. Shimomura, S. Ohkubo, Y. Yuba, S. Namba, S. Hiyamizu, M. Shigeta, T, Yamamoto and K. Kobayashi, Surf. Sci., *267* (1992) 13.

222

Nanostructures

Fabrication of InP/InGaAs-based Nanostructures

I. Adesida, R. Panepucci, S. Gu, D. A. Turnbull, and S. G. Bishop
*Center for Compound Semiconductor Microelectronics, Material Research Laboratory,
Coordinated Research Laboratory, and Department of Electrical and Computer
Engineering, University of Illinois, Urbana, IL 61801*

Abstract

The fabrication of nanostructures in InP/InGaAs heterostructures using electron beam lithography followed by a variety of etching methods is reviewed. The specific etching methods utilized here are reactive ion etching, wet etching, and thermal free chlorine etching. Photoluminescence spectroscopy was utilized to assess the optical quality of the nanostructures (quantum wires). Wires fabricated using reactive ion etching exhibited optically inactive dead sidewall layers with high surface recombination velocities. Wet-etched and free-chlorine-etched wires show no evidence of inactive layers for wires down to 15 nm in size. The free chlorine etching is suitable as a technique for transferring ex-situ defined geometries into substrates for subsequent in-situ selective epitaxial overgrowth.

Introduction

Semiconductor structures with nanometer-scale dimensions have received significant attention over the last decade due to their potential for exhibiting new physical phenomena. Some intriguing phenomena such as quantized conductance and Coulomb-blockade effects have been observed in quantum wires and dots, respectively [1]. A strong attraction in this field is that these phenomena could be the basis of future high performance devices. For example, Arakawa et al. [2] have obtained promising results in the fabrication of quantum wire lasers. Success in the utilization of nanostructures fabricated in various material systems for device applications depends on material growth and processing issues. Interface disorder and surface roughness resulting from these issues are known to strongly influence the reliability of quantum-confined structures [3]. High resolution electron beam lithography (EBL) followed by some form of etching have been the conventional means of fabricating nanostructures. The type of etching used has strong impact on the surface roughness and etched-sidewall properties of nanostructures [4].

Over the last several years, various sophisticated approaches have emerged for the realization of low dimensional quantum-confined structures in addition to the conventional techniques mentioned above. These latest techniques rely more on direct growth of quantum wires and dots by epitaxial methods [5, 6] and the growth on patterned substrates [7], including the selective area epitaxy of nanostructures onto masked substrates [8].

As mentioned above, for conventional fabrication of quantum structures involving etching, the quality of the etched surfaces depends largely on the etching method. Techniques making use of low energy ions [9] or exclusively chemical mechanisms produce surfaces with low damage. Epitaxial regrowth provides an avenue for eliminating surface effects on etched structures. However, regrowth on these structures is not effective unless steps are taken to remove damage involving crystallographic defects and impurities. Therefore, *in-situ* etching techniques compatible with overgrowth are highly desirable. Free Cl_2 etching [10] which is based on exclusively chemical mechanisms is a candidate for this application.

In this paper, we present our work on the fabrication and characterization of nanostructures in InP/InGaAs material system. Quantum wires are fabricated using EBL followed by various etching techniques ranging from reactive ion etching to wet etching and free chlorine etching. Optical measurements on InP/InGaAs quantum wires fabricated by these various techniques have been performed and are presented.

Processing: Lithography and Etching

The wires were fabricated from lattice-matched InP/InGaAs quantum well heterostructures grown by metal-organic vapor-phase epitaxy (MOVPE). A 200-nm InP buffer layer was grown on semi-insulating InP substrate followed by a 6-nm $In_{0.53}Ga_{0.47}As$ quantum-well layer and a 40-nm InP cap layer.

Patterning for quantum wire fabrication was carried out in a Cambridge EBMF-10 electron beam lithography system at 40 kV with a probe current of 500 pA, and a beam diameter of approximately 65 nm. A bilayer resist of 950 K / 200 K (45 nm / 60 nm thickness) PMMA was used for lift-off and the developer used was 1:7 MIBK/IPA. The mask material was chosen according to the requirements of the etching technique.

The etching techniques investigated here in the fabrication of quantum structures include reactive ion etching (RIE), free Cl_2 etching (FCE) and wet etching (WE). For the RIE of quantum wires (QWRs), samples were first coated by plasma-enhanced chemical

vapor deposition (PECVD) with a 40 nm layer of SiO_2, and then patterned by high resolution electron beam lithography, followed by a 30 nm Ti evaporation and lift-off. The Ti mask pattern was transferred into SiO_2 using CHF_3-RIE at a pressure of 40 mTorr, a flow rate of 10 sccm and a self-bias voltage (V_{dc}) of -270 V. Finally, quantum wires were etched by CH_4/H_2 (1:3) RIE at a pressure of 30 mTorr, a total flow rate of 40 sccm and a self-bias voltage of -380 V, to a depth of 50 nm through the InP/InGaAs quantum well. The masking materials were removed by wet etching using buffered hydrofluoric acid (HF). The use of this double mask is required due to the polymer formation which occurs in the CH_4/H_2 RIE of InP/InGaAs. Fig. 1 shows a scanning electron micrograph (SEM) of a 40 nm QWR fabricated using this technique.
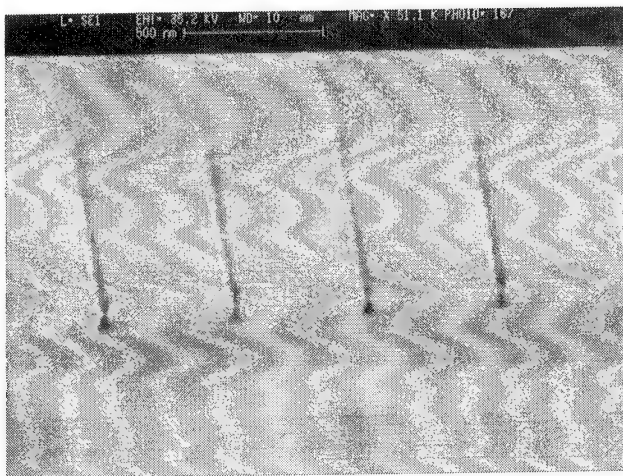
Fig 1 - SEM of a 40 nm $In_{0.53}Ga_{0.47}As$ QWR fabricated using CH_4/H_2 RIE.

For the wet etching of QWRs, the epitaxial structure used included an additional 2-nm $In_{0.53}Ga_{0.47}As$ cap layer. A 30-nm layer of Ti deposited as above was used as a mask for the H_3PO_4:H_2O_2:H_2O (1:1:40) etch of the InGaAs cap layer. This InGaAs layer acts as an ideal mask (there is negligible undercut of the mask) in the selective crystallographic etch of InP by HCl:H_2O (1:1). The reverse-mesa etch profile defines the final width of the quantum wires. In addition, the use of crystallographic etchants was shown to reduce the
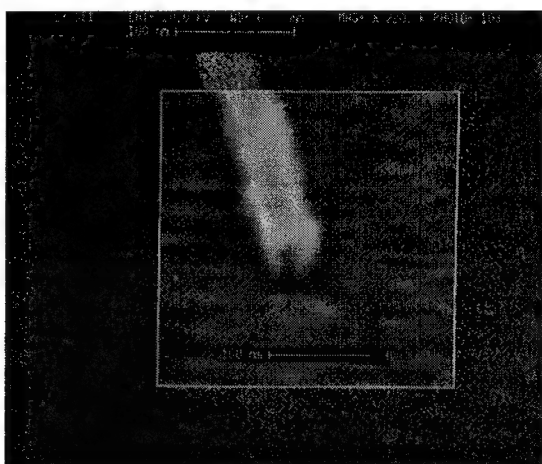
(a)

(b)

Figure 2 - (a) SEM of a 15 nm shallow wet-etched QWR fabricated using crystallographic wet-etching. (b) SEM of deep-etched QWR structures fabricated using crystallographic wet etching.
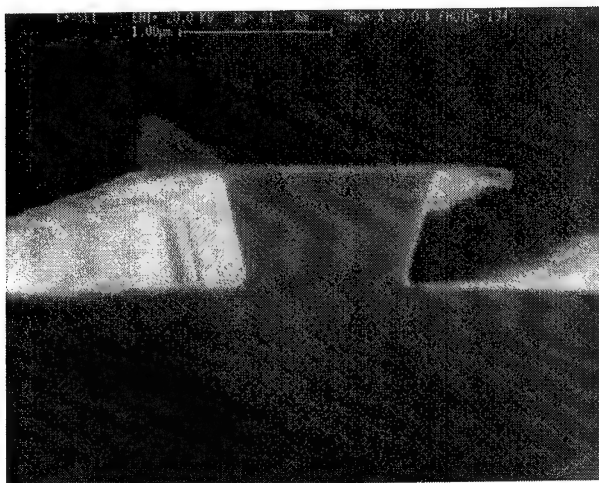
(a)
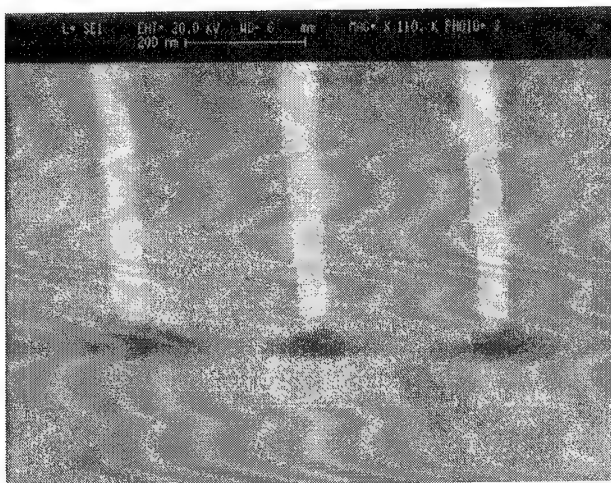
(b)

Figure 3 - (a) SEM of a typical profile for the FCE of InP etched at 200 °C and 6 sccm of Cl₂, the mask material is SiO₂. (b) SEM of a QWR with active region width of 30 nm fabricated using FCE.

fluctuation in the wire present in the original mask [4]. The InGaAs quantum well region is then etched as above, defining a shallow-etched QWR. Figure 2(a) shows a SEM of a 15 nm shallow wet-etched QWR. A further step consisting of the selective crystallographic etch of InP in a solution of $HCl:CH_3COOH$ (1:20) allows us to obtain deep-etched QWR structures as shown in Fig. 2(b).

Free Cl_2 etching is based on the thermal desorption of indium and gallium chlorides that are formed on the semiconductor surface when it is exposed to Cl_2. FCE is an attractive technique for the fabrication of buried structures because there are no energetic ions involved. In addition, it is possible to selectively overgrow the etched structures *in-situ* if a compatible mask material is used. We have characterized the free Cl_2 etching of InP and InGaAs as a function of temperature and pressure in order to investigate the application of this technique to the fabrication of quantum structures [10]. Figure 3(a) shows a SEM of a typical profile for the FCE of InP. Quantum wires were defined by high resolution electron beam lithography followed by Ti or SiO_2 evaporation and lift-off. The etching was performed in a modified Varian/Extrion RE580 chemically assisted ion beam etching (CAIBE) system described elsewhere [12]. Chlorine flow during etch was 6 sccm and the sample temperature was 175 °C. Figure 3(b) shows a QWR with a width of ~ 30 nm fabricated using FCE.

Optical Characterization

The quantum wire samples were studied by low temperature photoluminescence. The samples were cooled in flowing helium vapor to ~5 K in a Janis Super Varitemp liquidhelium cryostat. Photoluminescence (PL) was excited by a focused 514.5-nm Ar+ laser beam and detected through a 1-m focal length single-grating monochromator with a 77 K Ge pin photodiode. The laser was focused onto the sample surface by a single-element lens through a small prism which guided the laser beam onto the surface of the sample at normal incidence. The laser spot size at the sample surface was approximately 50 μm. Details of the setup are described elsewhere [13]

Figure 4 shows a plot of normalized intensity versus wire width for the fabricated wires and a comparison to the results obtained by Maile et al [14] which used Ar/O_2 reactive ion beam etching (RIBE). The normalized intensity is obtained by normalizing the integrated PL intensity to the area filling factor and to the integrated PL intensity of the

reference quantum well emission. As shown in Fig. 6, previously reported studies [14] of dry-etched InGaAs/InP open quantum wires have demonstrated no significant reduction in
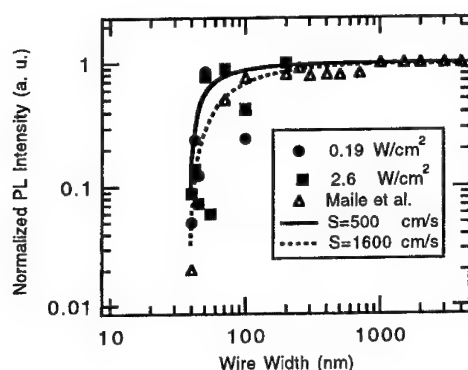
Fig. 4 - Normalized PL efficiency as a function of wire width for RIE QWRs.

PL efficiency for wire widths down to 100 nm; at 80 nm the efficiency begins to decrease, and falls by nearly two orders of magnitude in 40 nm wires. The reduction of the PL efficiency for the narrowest wires (40 nm) fabricated by CH_4/H_2 is about a factor of four less severe than that reported for the dry-etched wires fabricated using Ar/O_2 RIBE. To facilitate quantitative comparison of these results with those of previously published studies of QWRs, we have used a model involving the sidewall non-radiative surface recombination and a "dead layer" [14]. The width of the "dead layer" obtained for the present wires was 19 nm. The surface recombination velocity for the present wires is about 500 cm/s (see the solid curve in Fig. 4), which is significantly smaller than the 1600 cm/s obtained by Maile et al [14] for Ar/O_2 dry-etched wires. However, the optically inactive layer is an obstacle that prevents this etching technique from achieving active structures with dimensions much less than 40 nm. In order to overcome this barrier, QWRs fabricated exclusively by wet-etching were investigated.

Figures 7 and 8 shows the excitation intensity dependence of the PL spectra for a 40-nm RIE wire array and for a 37-nm shallow wet-etched wire array, respectively. In order to facilitate the comparison of the PL line shapes as a function of excitation intensity, all spectra are arbitrarily normalized to their strongest intensities. The evolution of the
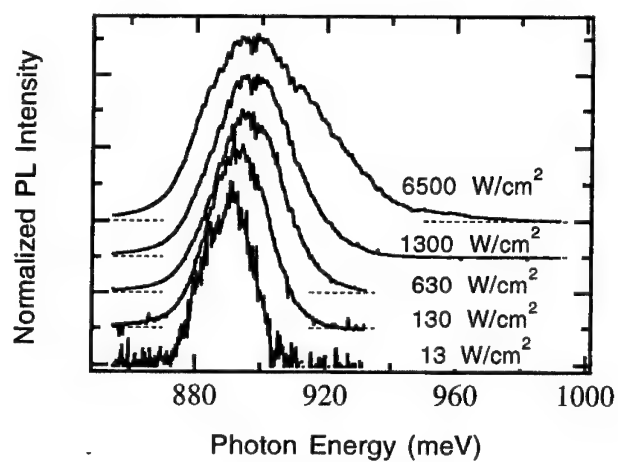
(a)
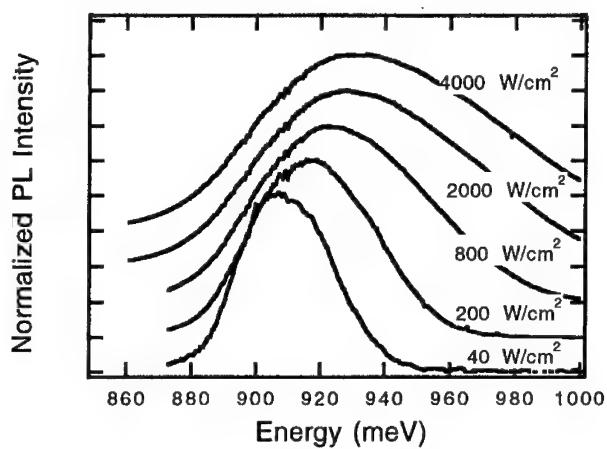
(b)

Figure 5 - PL spectra for (a) 40 nm RIE etched InP/InGaAs QWRs and (b) 37 nm wet-etched InP/InGaAs QWRs as a function of increasing excitation power. Intensities were normalized to unity.

spectra as a function of excitation intensity is quite distinct for the two samples. The wet-etched sample has a substantially larger broadening and also a larger shift of the peak to higher energies. In addition, the same trend with increasing excitation intensity was observed for wires as small as 15 nm. The high luminescence intensity obtained from these narrow WE wires is consistent with previous observations [11,15] and shows that the extent of optical inactive sidewalls is much smaller than that observed for RIE wires. Also, it shows that the wet-etched structures have significantly fewer non-radiative recombination centers. Effective carrier lifetime (τ) is increased when compared to the dry-etched structure, thus allowing a larger concentration of carriers to be maintained. In addition, a change in excitation intensity (ΔP) induces a change in carrier concentration (Δn) given by $\Delta n = \Delta P \, \tau$. This change is larger for the wet-etched wires, consistent with a longer lifetime. The shifts to high energies of the peak position with increasing excitation and the broadening on the high energy side are possibly due to band filling in k -space as well as real space filling [16, 17].

In spite of the improvement in the recombination at the sidewalls and a reduction or elimination of the "dead layer" observed in the wet-etched samples over the dry-etched samples, it is desirable to perform an epitaxial overgrowth step to fully passivate the sidewalls of the quantum structures. This prevents degradation of the active region allowing the investigation of phenomena intrinsic to the fabricated quantum structures. Overgrowth is also required for the practical implementation of these structures in suitable device geometries. We propose to use FCE as a technique by which the patterning of the structure can be done *ex-situ* using a regrowth-compatible mask such as SiO_2 , and the etching and regrowth of the sample be performed using a dedicated chamber. As an initial step in this direction, we have investigated the fabrication of QWRs as described above. Figure 9 shows the excitation intensity dependence of the PL spectra for the 30-nm FCE wire array depicted in Fig. 5 and for the QW reference mesa on the sample. The peak energy shift of the 30-nm QWR with respect to the reference QW is approximately 11 meV and is consistent with previous reports for similar QWRs [11,15]. From Fig. 6, the normalized PL intensities reported by Maile *et al* [14] and Gu *et al* [13] for dry-etched 40 nm wires regrowth of the sample be performed using a dedicated chamber. As an initial step in this direction, we have investigated the fabrication of QWRs as described above. Figure 9 shows the excitation intensity dependence of the PL spectra for the 30-nm FCE wire array depicted in Fig. 5 and for the QW reference mesa on the sample. The peak energy shift of the 30-nm QWR with respect to the reference QW is approximately 11 meV
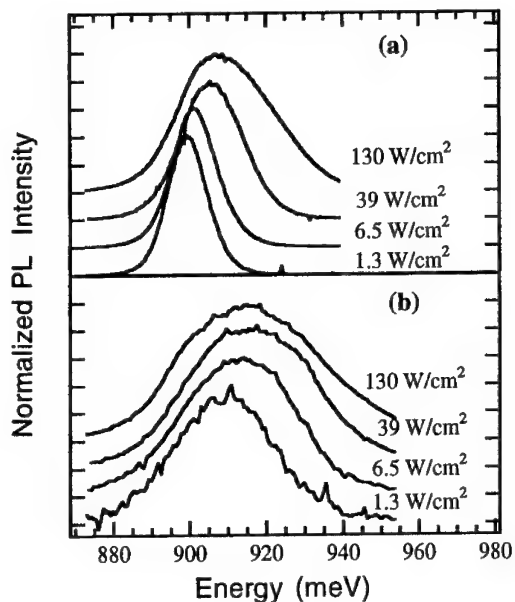
Figure 6 - PL spectra for (a) 30 nm FCE etched InP/InGaAs QWRs and (b) reference QW, for increasing excitation power. Intensities were normalized to unity.

and is consistent with previous reports for similar QWRs [11,15]. From Fig. 6, the normalized PL intensities reported by Maile *et al* [14] and Gu *et al* [13] for dry-etched 40 FCE had an integrated intensity of 0.5 [10]. The broadening of the photoluminescence peak in Fig. 6(b) is also larger than that observed at similar excitation powers in the spectra of dry-etched wires of Fig 5(a). As discussed above for the WE-wires, the explanation of this disparity is that for equivalent excitation intensities a much higher electron-hole plasma (EHP) density is achieved in the free Cl_2 wires than in the dry-etched wires due to reduced non-radiative recombination at the sidewalls.

Summary

The fabrication of quantum wires using reactive ion etching (RIE), selective crystallographic wet etching and free Cl_2 etching were reviewed. Quantum wires fabricated by RIE were shown to have optically inactive layers and high surface recombination

velocities in agreement with previous observations. Wet etching was used to achieve quantum wires with significantly fewer non-radiative recombination centers as inferred from a comparative analysis of the evolution of the PL lineshape as a function of optical excitation intensity. Furthermore, the wet-etched QWRs presented no evidence of an optically inactive layer down to 15 nm. Free Cl_2 etching of quantum structures was proposed as a fabrication procedure suitable for *in-situ* etch followed by regrowth. This technique allows the lithography and deposition of a mask compatible with regrowth to be performed *ex-situ*. Finally, the fabrication of QWRs with free Cl_2 and PL results for a 30-nm wire fabricated with this technique were presented. We conclude that free Cl_2 etching is a technique with attractive characteristics for the fabrication of nanostructures in the $In_{0.53}Ga_{0.47}As/InP$ system.

ACKNOWLEDGMENTS

References

[1] U. Meirav, M. A. Kastner, and S.J. Wind, Phys. Rev. Lett., 65, 771 (1990).
[2] T. Arakawa, M. Nishioka, Y. Nagamune and Y. Arakawa, Appl. Phys. Lett. 64, 2200 (1994).
[3] D. Jovanovic, J.P. Leburton, H. Chang, R. Grundbacher, and I. Adesida, Phys. Rev. B 50, 5412 (1994)
[4] M. Notomi, M. Nakao, and T. Tamamura, Appl. Phys. Lett. 62, 2350 (1993)
[5] K. Cheng, K. Hsieh, and J. Baillargeon, Appl. Phys. Lett 60, 2892 (1992)
[6] P.M. Petroff, A.C. Gossard and W. Wiegmann, Appl. Phys. Lett. 45, 621 (1984)
[7] E. Kapon, M.C. Tamargo, and D.M. Hwang, Appl. Phys. Lett. 50, 347 (1987).
[8] R. Panepucci, M.L. Osowski, D.A. Turnbull, S. Gu, S.G. Bishop, J.J. Coleman and I. Adesida, to be published in Superlat. Microstruct.
[9] K. T.Sung, S. W. Pang, M. W. Cole, and N. Pearce, J. Electrochem. Soc. 142, 206 (1995)

[10] R. Panepucci, C. Youtsey, D. A. Turnbull, S.Q. Gu, C. Caneau, S.G. Bishop and I. Adesida, J. Vac. Sci. Technol. B 13, 2752 (1995)

[11] M.Notomi, M. Naganuma, T. Nishida, T. Tamamura, H. Iwamura, S. Nojima, and M. Okamoto, Appl.Phys. Lett. 58, 720 (1991).

[12] C. Youtsey, R. Grundbacher, R. Panepucci, I. Adesida, and C. Caneau, J. Vac. Sci. Technol. B 12, 3317 (1994)

[13] S. Q. Gu, X. Liu, M. Covington, E. Reuter, H. Chang, R. Panepucci, I. Adesida, C. Caneau, R. Bhat and S. G. Bishop, J. Appl. Phys. 75, 8071 (1994).

[14] B. E. Maile, A. Forchel, R. Germann, D. Grützmacher, H.P. Meier and J. -P. Reithmaier, J.Vac.Sci. Technol. B 7, 2030 (1989)

[15] P.Ils, M. Michel, A. Forchel, I. Gyuro, M. Klenk, and E. Zielinski, J.Vac.Sci. Technol. B 11, 2584 (1993).

[16] V. D. Kulakovskii, E. Lach, A. Forchel, and D. Grützmacher, Phys. Rev. B 40, 8087 (1989).

[17] A. Gustafsson, X. Liu, I. Maximov, L. Samuelson, and W. Seifert, Appl. Phys. Lett. 62, 1709 (1993).

HIGH-QUALITY, NON-STOICHIOMETRIC MULTIPLE QUANTUM WELLS

M. R. Melloch[*,a], I. Lahiri [b], D. D. Nolte [b]
J. C. P. Chang [a], E. S. Harmon [a], and J. M. Woodall [a]
[a] School of Electrical Engineering
[b] Department of Physics
and the MRSEC for Technology-Enabling Heterostructure Materials
West Lafayette, IN 47907

ABSTRACT

A 150 period mutiple quantum well (MQW) consisting of 10 nm GaAs wells and 3.5 nm AlAs barriers was grown at low substrate temperatures by MBE so as to incorporate 0.2 % excess arsenic. With anneal this excess arsenic precipitates turning the MQW semi-insulating with a carrier lifetime of 15ps. Despite the excess arsenic, sharp optical transitions of quantum-confined excitons (10 meV FWHM for the heavy-hole transition) comparable to those in highly stoichiometric MQWs were observed. This combination of sharp excitonic transitions and ultrafast recombination lifetimes has exciting possibilities for photorefractive, electro-optic sampling, and saturable absorption applications.

When arsenides-such as GaAs or AlGaAs are grown at low substrate temperatures by molecular beam expitaxy (MBE), excess arsenic can be incorporated into the lattice [1]. In spite of excess arsenic volume fractions as high as $1-2\%$, the crystal can exhibit high-structural quality [2]. With anneal, the excess arsenic precipitates forming a composite of semi-metallic arsenic clusters in an arsenide semiconductor matrix [3]. With further anneal, the arsenic clusters coarsen [4]. Figure 1 illustrates the control one has over the composite by use of the substrate temperature during MBE to set the amount of excess arsenic in the crystal [5, 6] and the anneal temperature to determine the final spacing of the arsenic clusters [4, 7].

When the average spacing between the arsenic clusters is about three Bohr diameters, these composites exhibit enhanced electro-optic properties [4, 8]. Shown in Fig.2 is a comparison of the differential transmission for a $1~\mu m$ thick AlGaAs epilayer containing arsenic clusters with the differential transmission for the quantum-confined Stark effect in a high-quality, highly-stoichiometric, $1~\mu m$ thick, multiple-quantum well (MQW) structure. Even at an electric field a factor of 5 lower, the AlGaAs epilayer with the arsenic precipitates displays a larger differential transmission then the quantum-confined Stark effect in the MQW, and also exhibits a much broader bandwidth due to the inhomogeneity in the material.

Arsenic precipitates in MQW structures preferentially coarsen to the narrow band gap material with anneal [7, 9, 10]. Since the arsenic clusters are semi-metallic and deplete the surrounding semiconductor [11, 12], this would result in a semi-insulating MQW that would also have picosecond lifetime [13] - an attractive material for eelctro-optic applications. However, previous repoerts of low-temperature-grown MQW structures indicated the excitions were too severely broadened for useful applications [14]. We have recently achieved sharp optical transitions of quantum-confined excitons in AlAs/GaAs quantum wells grown at low substrate temperatures [15].

These MQWs were grown at a substrate temperature around $310^\circ C$ and contained about 2% excess arsenic. The MQW consisted of 150 periods with 10nm thick GaAs quantum wells and with 3.5 nm thick AlAs barriers, and was incorporated as the i-region in a PiN structure. The structure was grown in a GEN II MBE system using the tetramer from of arsenic, As_4, and an As_4 to Ga beam-equivalent pressure of about 20. The growth rate for the GaAs wells was $1\mu m/h$ and the growth rate for the AlAs barriers was $0.3\mu m/h$. The p- and n-regions did not contain excess arsenic. The top p-regions, which consisted of 200 nm of p-$Al_{0.3}Ga_{0.7}As$ and 200 nm of p-GaAs, were grown at a substrate temperature of $450^\circ C$, which acted as a precipitation anneal of 24 min. for the exces arsenic in the LTG-MQW.

Shown in Fig.3 is the absorption spectra for the low temperature-grown (LTG) MQW. For comparison, the absorption spectrum for an identical MQW, except

grown at a substrate temperature of $600°C$, a normal temperature growth (NTG), is shown in Fig.4. The heavy-hole transition in the LTG-MQW has a FWHM of 10 meV while the heavy-hole transtion for the NTG-MQW is slightly narrower at 6 meV. The carrier lifetime in the LTG-MQW was measured using a pump/probe change in absorption technique [12] and is 15 psec. This combination of sharp excitonic transitions and ultra-fast recombination lifetimes is unique to these LTG-MQWs, and has exciting possibilities for photorefractive , electro-optical sampling, and saturable absorption applications.

ACKNOWLEDGEMENT

REFERENCES

1. M. Kaminska, E. R. Weber, Z. Lilental-Weber, R. Leon, and Z. U. Reak, J. Vac. Sci. Technol. B7, 710 (1989).

2. R. J. Matyi, M. R. Melloch, and J. M. Woodall, Appl. Phys. Letters 60, 2642 (1992).

3. M. R. Melloch, N. Otsuka, J. M. Woodall, A. C. Warren, and J. L. Freeouf, Appl. Phys. Lett. 57, 1531 (1990).

4. M. R. Melloch, D. D. Nolte, N. Otsuka, C. L. Chang, and J. M. Woodall, J. Vac. Sci. and Technology B10, 795 (1991).

5. K. Mahalingam, N. Otsuka, M. R. Melloch, J. M. Woodall, and A. C. Warren, J. Vac. Sci. and Technology B9, 2328 (1991).

6. Z. Liliental-Weber, A. Claverie, J. Washburn, F. W. Smith, and A. R. Calawa, Applied Physics A 53, 141 (1991).

7. M. R. Melloch, J. M. Woodall, N. Otsuka, K. Mahalingam, C. L. Chang, and D. D. Nolte, Materials Science and Engineering B22, 31 (1993).

8. D. D. Nolte, M. R. Melloch, J. M. Woodall, and S. J. Ralph, Appl. Phys. Lett. 62, 1356 (1993).

9. K. Mahalingam, N. Otsuka, M. R. Melloch, and J. M. Woodall, Appl. Phys. Lett. 60, 3253 (1992).

10. T. M. Cheng, A. Chin, C. Y. Chang, M. F. Huang, K. Y. Hsieh, and J. H. Huang, Appl. Phys. Lett. 64, 1546 (1994).

11. A. C. Warren, J. M. Woodall, J. L. Freeouf, D. Grischkowsky, D. T. McInturff, M. R. Melloch, and N. Otsuka, Appl. Phys. Lett. 57, 1331 (1990).

12. N. Atique, E. S. Harmon, J. C. P. Chang, J. M. Woodall, M. R. Melloch, and N. Otsuka, Appl. Phys. Lett. 57, 1331 (1990).

13. E. S. Harmon, M. R. Melloch, J. M. Woodall, D. D. Nolte, N. Otsuka, and C. L. Chang, Appl. Phys. Lett. 63, 2248 (1993).

14. W. H. Knox, G. E. Doran, M. Asom, G. Livescu, R. Leibenguth, and S. N. G. Chu, Appl. Phys. Lett. 59, 1491 (1991).

15. I. Lahiri, D. D. Nolte, E. S. Harmon, M. R. Melloch, and J. M. Woodall, to appear in Appl. Phys. Lett. (1995).
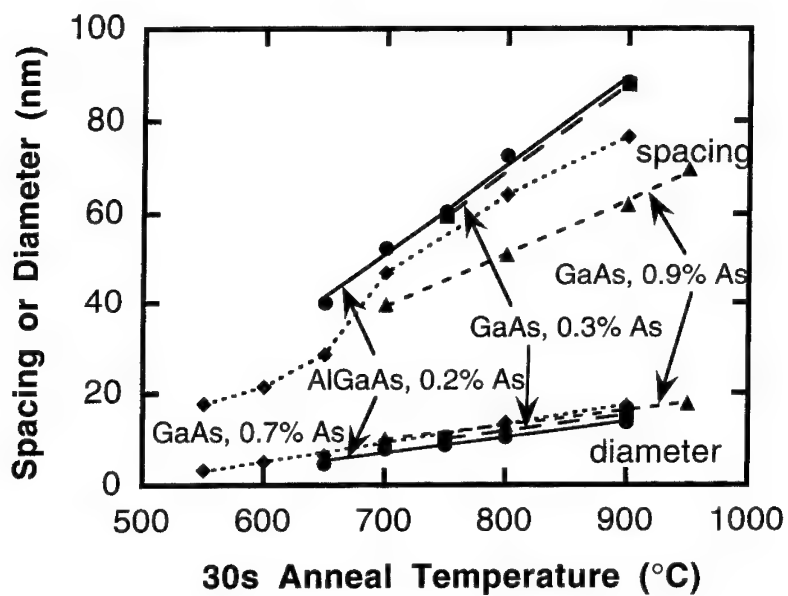
Figure 1: Density and average size of As clusters in four different epilayers as a function of temperature for a 30 s anneal. Three of the epilayers are GaAs, one containing 0.3 % excess As, one containing 0.7 % excess As, and one containing 0.9 % excess As. The fourth epilayer is $Al_{0.25}Ga_{0.75}As$ containing 0.2 % As.
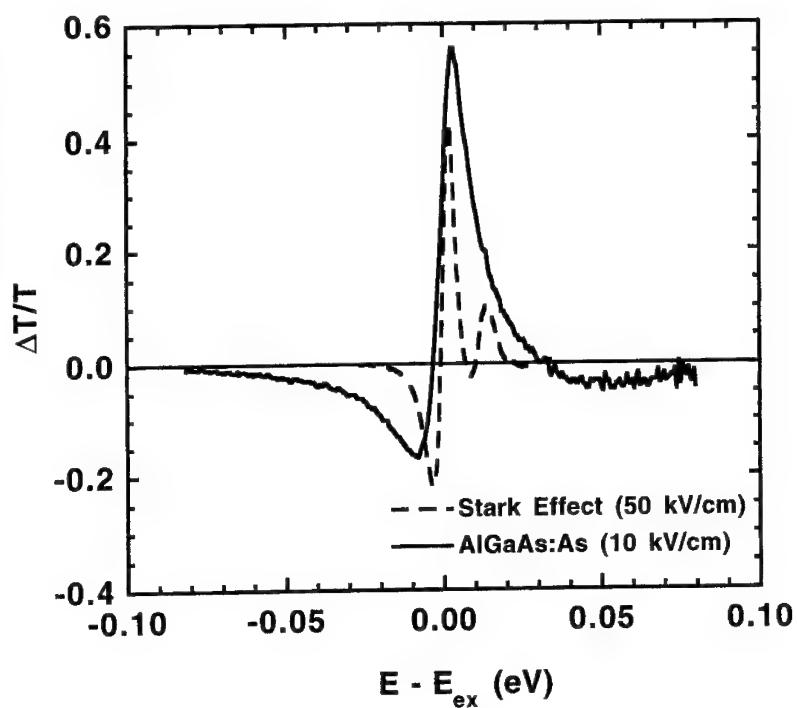
Figure 2: Comparison of the differential transmission for the quantum- confined Stark effect in a high-quality, highly-stoichiometric multiple quantum well structure and the differential transmission in an AlGaAs epilayer As clusters.
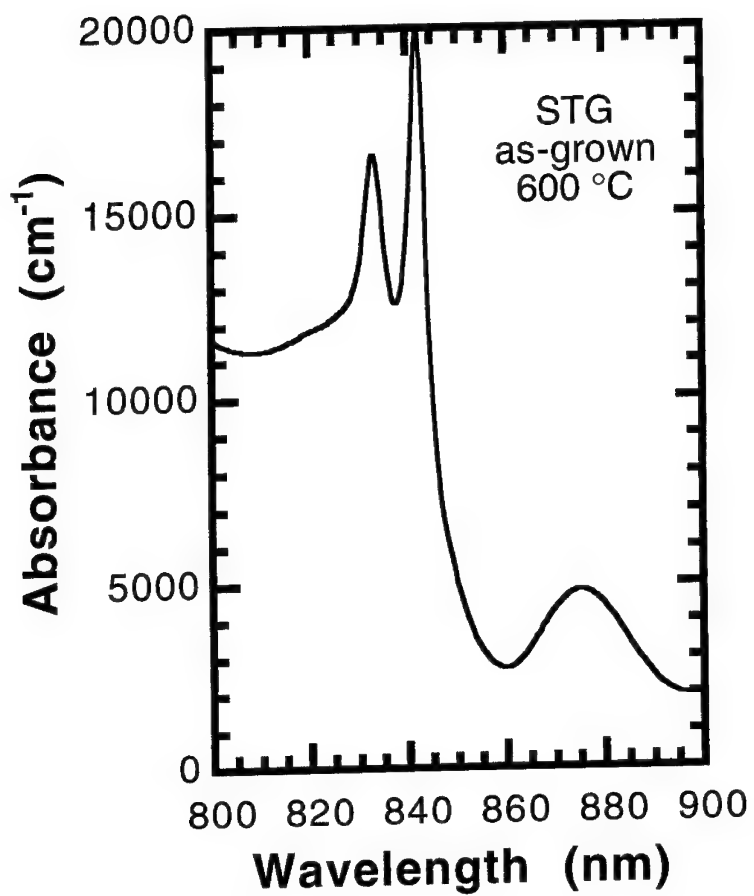
Figure 3: Absorption spectra for low-temperature-grown (LTG) multiple quantum well samples.
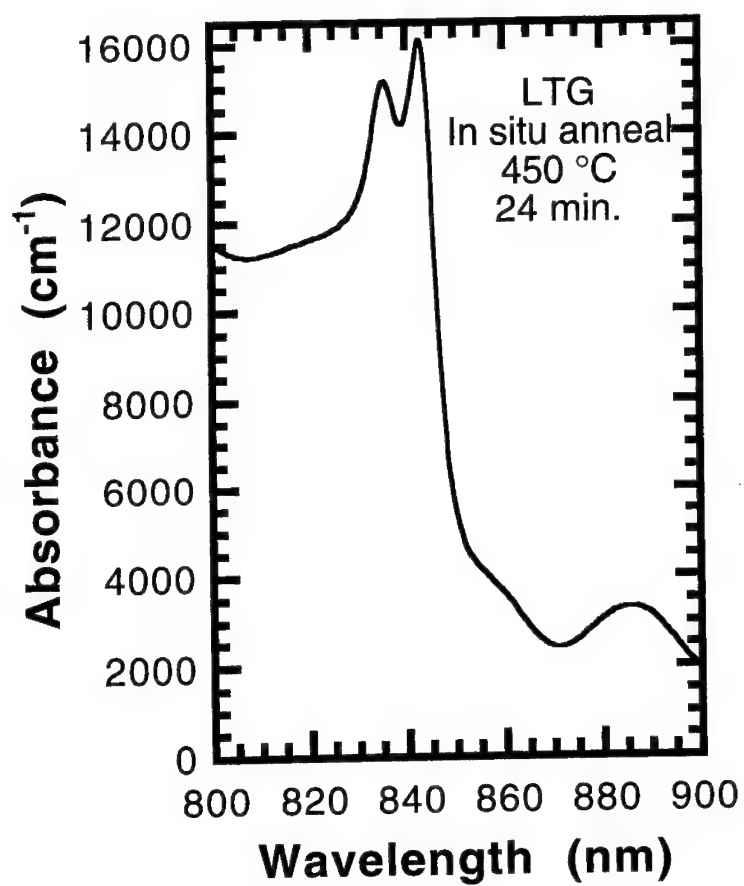
Figure 4: Absorption spectra for standard temperature grown (STG) multiple quantum well samples.

CHEMICAL CONTROL OVER SIZE, SHAPE, AND ORDER ON A NANOMETER LENGTH SCALE

James R. Heath
Department of Chemistry and Biochemistry
UCLA, Los Angeles, CA 90095-1569

ABSTRACT

Chemical control of size and shape is not bounded by size limits and presents an alternative to semiconductor processing approaches. Furthermore, weak interparticle attractions scale geometrically with particle size, and provide a handle for the fabrication of structurally and chemically complex structures. These concepts are demonstrates for Group IV, III-V, and metallic nanocrystal systems.

Chemical control of size and shape is not bounded on either the large and small extremes by size limits and presents an interesting alternative to semiconductor processing approaches. Chemical approaches readily access structures over the size range from 1 - 20 nm, and over this range the electronic structure and phase behaviour are strong functions of crystallite size and shape.

Furthermore, weak interparticle attractions)dispersion forces) scale geometrically with crustallite size from the molecular limit to $\sim$ 20 nm, and provide a handle for the fabrication of structurally and chemically complex assemblies of nanocrystals. The theory and practice of these concepts have beem demonstrated for Group IV (Si,Ge,Sn, and Pb), III-V (InP), and metallic (au,Ag,Pt,Pd) nanocrystal systems. Chemical techniques for controlling size and shape in these systems include separation of the nucleation and crystallization steps, crystal growth within a template, and/or chromatographic separations of nanocrystal sizes following synthesis. Physical approaches toward obtaining positional ordering in these systems include controlled nucleation and growth within a lithographically or electrochemically defined template. Approaches toward obtaining local order within these systems include the exploitation of weak interactions to induce size dependent phase separations followed by 1-,2-,and 3-dimensional opal formation.

These various have been characterized by frequency and/or time resolved absorption, luminescence, and Raman spectroscopies, XPS, conductivity measurements, electron microscopy, and other techniques.

SEMICONDUCTORS IN THE DISORDERED STATE
FROM BULK TO NANOSCALE

P. Armand, L. Iton, D. L. Price, and M. L. Saboungi
Argonne National Laboratory
Argonne, Illinois 60439

ABSTRACT

Clusters of the elemental semiconductor Se and compound semiconductors RbSe and CsSe have been incorporated in Nd-substituted Y-zeolite by vapor deposition techniques. TEM measurements indicate that the semiconductor material resides principally within the cage structure of the zeolite host, while high-resolution neutron and x-ray powder diffraction show that the incorporated material is out of registry with the zeolite host. Using anomalous x-ray scattering it has been possible to measure the internal structure of the semiconductor clusters and compare it with the structure of these materials in the crystalline and liquid states.

Quantum confinement of materials is known to produce significant changes on the physical and chemical properties. In this work, we present results obtained on semiconductors confined in zeolites. The choice of zeolites was motivated by the fact that they have porous structures with about 30-50 % void space after dehydration, offering an alternative mechanism of confining materials in a controlled fashion. The semiconductors were chosen as Se, RbSe, and CsSe since they are well suited for study by anomalous x-ray diffraction and for their unusual properties in the bulk in both crystalline and liquid states. The structure of Se in the amorphous and liquid state is still not well understood. Both RbSe and CsSe are expected to retain their semiconducting behaviour in the disordered state. Recent neutron scattering experiments have shown that Se_2^{2-} Zintl ions are present in both crystalline and liquid states.

In this work, Y zeolite of the faujasite type was used with Nd^{3+} ions exchanged with the Na^+ ions. Se was introduced into this material by vapor diffusion. The resulting material had a uniform orange color. To make the RbSe and CsSe clusters, the Se-loaded zeolite was inserted into glass containers with sufficient quantities of alkali metals to form the stoichiometric compounds. The tubes were heated at $320C$ and annealed until a homogeneous brown material was obtained. The exact compositions were defined by chemical analysis and corresponded to 6.5 Se, 6.0 Rb, and 5.4 Cs atoms per supercage. The observed colors are suggestive of quantum confinement effects.

The internal structures of the clusters were determined by anomalous wide angle x-ray scattering (AWAXS) measurements at the Se and Rb edges, carried out on the X-7A beam line at NSLS. With this technique, the structure factor associated with a specific element a is determined from the difference of the scattered intensities for two diffraction measurements at x-ray energies E_1, just below an absorption edge of element a, and E_2, a little further below: It can be easily shown that the structure factor obtained in this way is a simple combination of the partial structure factors involving element a. By Fourier transformation the real-space correlation function for the environment of element a can be determined. The application of this method to elements (Se or Rb) in the cluster makes it possible to distinguish the environments of these elements from those of the atoms of the zeolite host, which make a much larger contribution to the total scattering.

In the case of the Se-loaded zeolite, comparison of the results obtained with both crystalline and amorphous Se leads to the following observations. First, the nearest-neighbor bond length (2.32 Å) and coordination number (1.9 ±0.1) in the Se-loaded zeolite are similar to that of the bulk phases. Second, the second-neighbor bond length (3.63 Å) is also similar, while its coordination number (3.2 ± 0.3) is greatly reduced suggesting that the selenium is present in the form of isolated short Se_n chains.

In the case of the RbSe and CsSe, the nearest-neighbor Se-Se bonds are found

with bind lengths of 2.44 $\mathring{A}$ and coordination numbers between one and two. This suggests that $Se_2{}^{2-}$ Zintl ions similar to those obtained in the bulk phases as well as short Se_n chains are present. Second neighbor Se-Se and alkali-selenium bonds are observed with bond lengths of 3.6-3.7 $\mathring{A}$.

In conclusion, quantum confinement of a new class of semiconductors has been successfully demonstrated. The AWAXS technique has been shown to be an extremely promising and powerful technique to probe the environment of a selected element. Furthermore, the structure of isolated microclusters in the cages of the zeolite has been measured beyond the first coordination shell. Additional measurements are underway to study the influence of temperature and pressure on these confined materials.

ACKNOWLEDGEMENT

Superlinear energy dependence of photoluminescence from CdS$_x$Se$_{(1-x)}$ nanocrystallites in glass

E.B. Stokes[*], P.D. Persans, and K.L. Stokes,

Department of Physics, Rensselaer Polytechnic Institute, Troy, NY

[*] also of General Electric Corporate Research and Development, Schenectady, NY

Abstract

We measured time–resolved photoluminescence from CdS$_{0.48}$Se$_{0.52}$ doped glass as a function of temperature and excitation pulse energy density. The photoluminescence has a fast component near the absorption band edge and a slow broader component in the far red. At 77 K and low excitation pulse energy density, emitted photoluminescence energy is a linear function of excitation pulse energy density. At higher excitation pulse energy density ($> 1.1 \times 10^{-3}$ J/cm^2, 3 ns pulses, 566 nm) we observe a superlinear transition. At 200 K the superlinear transition is shifted to higher excitation pulse energy density (1.6×10^{-3} J/cm^2). The slow photoluminescence at 77 K is linear in excitation pulse energy density over the range of this investigation ($0 - 1 \times 10^{-2}$ J/cm^2).

Introduction

The photoluminescence properties of crystals in the (Zn,Cd)(S,Se) system have long been investigated, both in bulk materials[1,2] and in composite glasses[3,4]. Photoluminescence emission in powdered phosphors, superlinear in excitation intensity over a certain range, has been reported.[5,6] The superlinear behavior is a function of temperature, and is enhanced (or quenched) by activation (or poisoning) with certain specific transition metal dopants. In bulk materials, superlinearity can be attributed to the presence of more than one class of traps.[7,8,9]

Photoluminescence of CdS$_x$Se$_{(1-x)}$ nanocrystallites is the focus of much recent investigation. Herron et al.[10] report a single broad emission band at 500 nm for Cd$_{32}$S$_{14}$(SC$_6$H$_5$) clusters in THF solu-

tion at 77K. Tanaka et al.[11] also report a single broad emission band for small $CdS_xSe_{(1-x)}$ particles (3.8 nm) in a germanium oxide glass. This band evolves into a broader red peak and a sharper peak near the absorption band edge for larger particles (8.1 nm). The quantum efficiency of both emission bands decreases as temperature is increased. Nogami and Nakamura[12] report sharp and broad emission bands at 500 and 650 nm respectively for 5.5 nm CdS particles in sol–gel derived glass. The lifetime of the 500 nm peak is 2 ns, while that of the 650 nm peak is 50 ns. The 500 nm emission band is attributed to direct band–band recombination, and the 650 nm emission band is attributed to recombination through surface sulfide vacancies.

Many other groups report the same basic photoluminescence emission spectrum for nanocrystallites larger than 5 nm in solution[13], sol–gel glass[14,15], and borosilicate glass[16]. The general form of the spectrum is a sharp emission band near the absorption band edge and a red shifted broad emission band. The sharp fast blue emission band is usually attributed to direct band–band recombination or recombination through shallow traps, while the broad slow red emission band is universally attributed to deeper traps. Several groups[17,18] report that the sharp emission band near the absorption band edge actually consists of a doublet.

Superlinear photoluminescence emission in the fast component has been reported recently in $CdS_xSe_{(1-x)}$ doped glasses. Kull and Coutaz[19] report a superlinear transition at room temperature in Schott OG570. The transition occurs at an excitation pulse energy density of 8.0×10^{-4} J/cm^2 using 80 ps pulses at 300 Hz from a Q–switched frequency–doubled (532 nm) Nd:YAG excitation source. The superlinearity is explained by a band filling model that differentiates between geminate and non–geminate recombination of excited electron–hole pairs. Zheng et al.[20] report a superlinear transition at room temperature in Corning CS 2–58. The transition occurs at an excitation pulse energy density of 1.2×10^{-4} J/cm^2 using 70 ps pulses at 80 MHz from a mode–locked frequency–doubled (532 nm) Nd:YAG excitation source. Tomita et al.[21] report a continuous superlinear range at 77 K of fast photoluminescence at much lower excitation pulse energy density ($0 - 10^{-6}$ J/cm^2) using 90

ps pulses at 80 MHz from a mode–locked frequency–doubled (532 nm) Nd:YAG excitation source. The same group also reports sublinearity in the slow photoluminescence component over the same range.

Experimental

We used a low repetition rate pulsed dye laser to pump as–received samples of Schott RG630 at 77K and 200K. The pulse length was on the order of the lifetime of the fast photoluminescence component. The time between pulses (>50 ms) was longer than the lifetime of the slowest photolumines-cence component, therefore the ensemble, after absorption of one excitation pulse, was allowed a full return to thermal equilibrium prior to the advent of further excitation.

The experimental setup is depicted in figure 1. A nitrogen pumped dye laser (Models VSL–337ND and 337220, Laser Science Inc., Newton, MA) was used with various dyes to generate 3 ns pulses at maximum 1 µJ per pulse at a low frequency repetition rate, typically 1 to 20 Hz. A 100 mm focal length lens was used to collimate the light prior to passing through a variable attenuator and an aper-ture for spatial filtering. A quartz flat at 45 degrees was used to split the beam. The primary fraction of the split was focused by a 50 mm focal length lens onto the sample surface. The beam energy profile at the position of the sample was quantified using a CCD beam characterization system (Big Sky, Bozeman, MT). The beam cross section has an elliptical profile with an area at half maximum of 6.2×10^{-3} mm^2. The secondary fraction of the split was split again by a quartz neutral density filter (OD=0.3, Newport Corp.). The forward fraction was incident on a high speed photodiode; the output was used as a trigger for the data acquisition system. The backward fraction, after passing through the quartz beamsplitter again, was incident on a large area photodiode for pulse energy measure-ment.

A sample of RG630 (Schott Glass Technologies, Duryea, PA) with particle size of 19 nm and com-position $CdS_{0.48}Se_{0.52}$ was mounted on the cold finger of a cryostat. Light from the dye laser was

focused onto the sample surface through a quartz window in the cryostat housing. Photoluminescence emission was collected by a 2 mm diameter bundle of fused silica optical fibers (C technologies, Short Hills, NJ). The other end of the fiber bundle was placed at the entrance slit of a 0.275 m grating monochromator. To prevent reflected laser light from entering the fiber (1) the end of the bundle was set at approximately 20 degrees skew from the plane of the incident and reflected laser beam and (2) a small piece of OG590 cutoff filter (Schott Glass Technologies, Duryea, PA) was placed between the output of the fiber bundle and the input slit of the monochrometer. Light from the exit slit of the monochrometer was incident on the photocathode of a photomultiplier tube (PMT) with a rise time of 2 ns and a transit time spread of 1.2 ns.

The output currents of the photomultiplier tube and the large area photodiode were connected to two input channels of a digitizing oscilloscope (TDS644A, Tektronix, Inc, Beaverton, OR) and digitized at 2 GHz. All oscilloscope inputs were 50 ohms. The oscilloscope traces were recorded and integrated over time.

Results and discussion

The photoluminescence emission at 77 K of RG630, excited with a 514 nm, 1 W/cm^2, cw argon ion laser, shows two primary features: a broad emission band centered at 670 nm and a sharper emission band centered at 595 nm (figure 2). The temporal characteristics of the two bands were investigated by exciting with 3 ns, 566 nm pulses from a nitrogen pumped dye laser. Under pulsed excitation, the 595 nm band splits into a doublet as previously reported, and undergoes a blue shift to 590 nm (figure 3). The 3 ns excitation pulses, when characterized with the same monochromator/PMT system, are broadened by the PMT and electronics to about 10 ns. The 590 nm emission band (figure 4) is broadened to 20 ns, so the actual photoluminescence lifetime is on the order of a few nanoseconds. The 670 nm emission band (figure 5) has an observed lifetime on the order of 1 μs.

Figure 6 shows the normalized relative dependence of emitted photoluminescence energy on excitation pulse energy density. Each data point on figure 6 was obtained by first averaging 256 pulses of excitation, then averaging 256 pulses of photoluminescence, for a number of different average excitation pulse energies. Figure 6 clearly shows that the fast component is superlinear in excitation pulse energy density, while the slow component is linear over the same range. The excitation pulse energy density range of figure 6 is approximately $0 - 1 \times 10^{-2}$ J/cm^2.

The spread of excitation pulse energy and photoluminescence for 4096 simultaneously acquired excitation/photoluminescence pulse pairs is shown in figure 7. The pulse–to–pulse variation in dye laser pulse energy is greater than +/–10%. Since the pulse energy can be *measured* more accurately than it can be *predicted*, both noise and pump energy measurement resolution are reduced by (1) binning the data according to power level, and (2) averaging the photoluminescence in each bin (figure 8). Such an approach was used to generate figure 9, which contains data from just under 10^5 single pulse measurements, 2^{16} pulses at 77 K, and another 2^{15} pulses at 200 K. Note that the superlinear transition at 200 degrees occurs at a higher excitation pulse energy density than at 77 K. The slight non–linear fluctuations at the higher energy levels are due to small mechanical alignment variations over the course of the experiment.

From figure 9, we determine the excitation pulse energy density at the observed superlinear transitions. At 77 K the superlinear transition occurs at 1.1×10^{-3} J/cm^2, while at 200 K, the transition is shifted to 1.6×10^{-3} J/cm^2. These are slightly higher than the results at 298 K of Zhang[20] (1.2×10^{-4} J/cm^2) and Kull[19] (8.0×10^{-4} J/cm^2), and significantly higher than the superlinear range reported at 77 K by Tomita.[21]

Summary

We have performed a time–resolved pulsed photoluminescence experiment which can tell us about recombination, wavefunctions, and traps. The observed superlinearity of photoluminescence sug-

gests that there are three (or more) competing channels for excited carrier recombination, at least two radiative (a doublet) and one non–radiative. A trap associated with the non–radiative channel saturates at excitation pulse energy density greater than the threshold for superlinearity, effectively increasing the rate of recombination through at least one of the radiative channels. The observed temperature dependence of superlinearity suggests that the trap saturation is temperature dependent. This could be because trap capture rate (cross section) decreases with increasing temperature. A more likely mechanism is the thermal excitation of the trap into a competing non–radiative channel.

References

1. Klick, C.C., and J.H. Schulman, "Luminescence in solids", Seitz & Turnbull (Ed.), Solid State Physics, 5, Academic Press, NY, 1957, p.97.

2. Shionoya, S., "Luminescence of lattices of the ZnS type", Goldberg (Ed.), Luminescence of inorganic solids, Academic Press, NY, 1966, p.205.

3. Buzhinskii, I.M., and N.I. Bodrova, Opt. Spect., 12, 212 (1962).

4. Kuwabara, Goro, J. Phys. Soc. Japan, 9, 992 (1954).

5. Nail, N.R., F. Urbach, and D. Pearlman, J. Opt. Soc. Am., 39, 690 (1949).

6. Roberts, Shepard, and Ferd E. Williams, J. Opt. Soc. Am., 40, 516 (1950).

7. Rose, Albert, Phys. Rev., 97, 322 (1955).

8. Duboc, C.A., Brit. J. App. Phys., S4, S107 (1955).

9. Klassens, H.A., J. Phys. Chem. Solids, 7, 175 (1958).

10. Herron, N., and J.C. Calabrese, W.E. Farneth, Y. Wang, Science, 259, 1426 (1993).

11. Tanaka, A., S. Onari, and T. Arai, Z. Phys. D, 26, S222 (1993).

12. Nogami, M., and A. Nakamura, Phys. Chem. Glasses, 34, 109 (1993).

13. Bigham, Shelli R., and Jeffry L. Coffer, J. Phys. Chem., **92**, 10581 (1992).

14. Rajh, T., O.I. Micic, D. Lawless, and N. Serpone, J. Phys. Chem., **96**, 4633 (1992).

15. Reisfeld, R., M. Eyal, V. Chernyak, and C.K. Jorgensen, Proc. SPIE, **1590**, 215 (1991).

16. Uhrig, A., L. Banyai, Y.Z. Hu, S.W. Koch, C. Klingshirn, and W. Neuroth, Z. Phys. B, **81**, 385 (1990).

17. Zheng, J.P., and H.S. Kwok, J. Opt. Soc. Am. B, **9**, 2047 (1992).

18. Hache, F., M.C. Klein, D. Ricard, and C. Flytzanis, J. Opt. Soc. Am. B, **8**, 1802 (1991).

19. Kull, Martin, and Jean–Louis Coutaz, J. Opt. Soc. Am. B, **7**, 1463 (1990).

20. Zheng, J.P., L. Shi, F.S. Choa, P.L. Liu, and H.S. Kwok, App. Phys. Let., **53**, 643 (1988).

21. Tomita, Makato, and Takahiro Matsumoto, Masahiro Matsuoka, J. Opt. Soc. Am. B., **6**, 165 (1989).

Acknowledgements

Figure 1 – The experimental setup

Figure 2: CW Photoluminescence, 514 nm excitation, RG630 at 77K

Figure 3: Fast & slow PL, 566 nm excitation, RG630 @ 77K
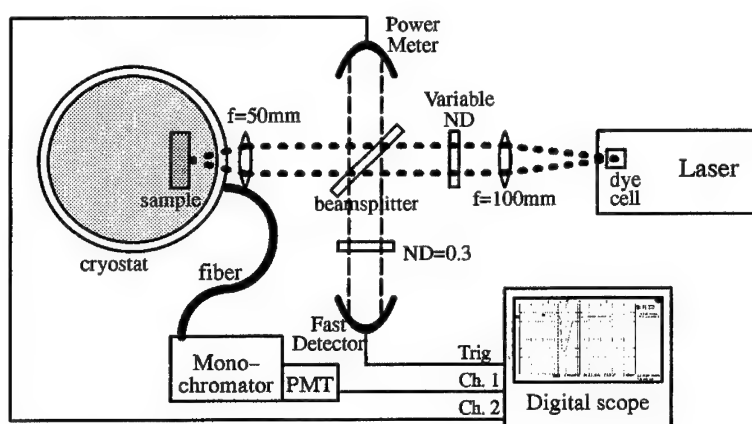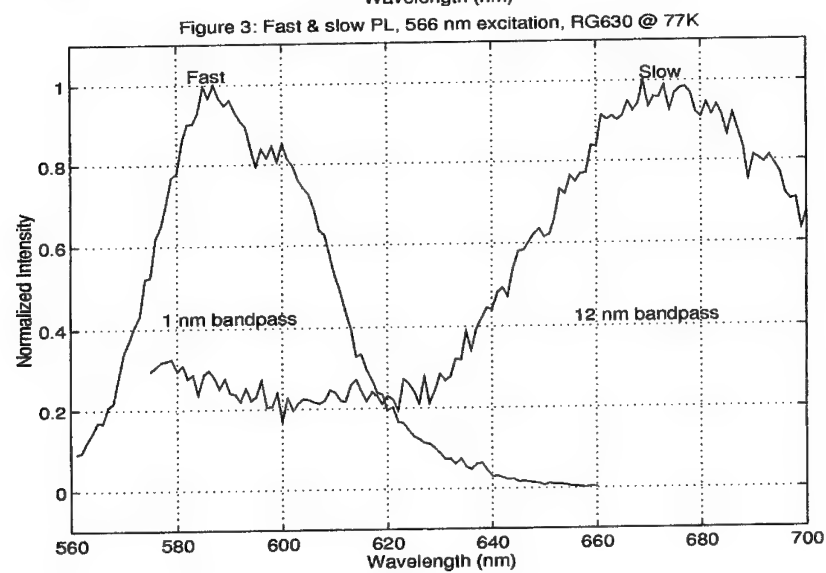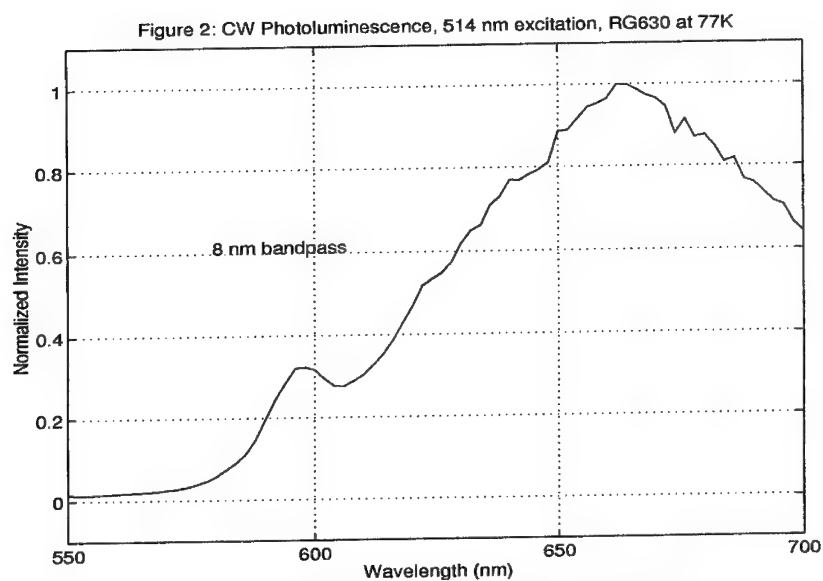
Figure 4 – Fast photoluminescence emission (590 nm) from RG630, temporal response
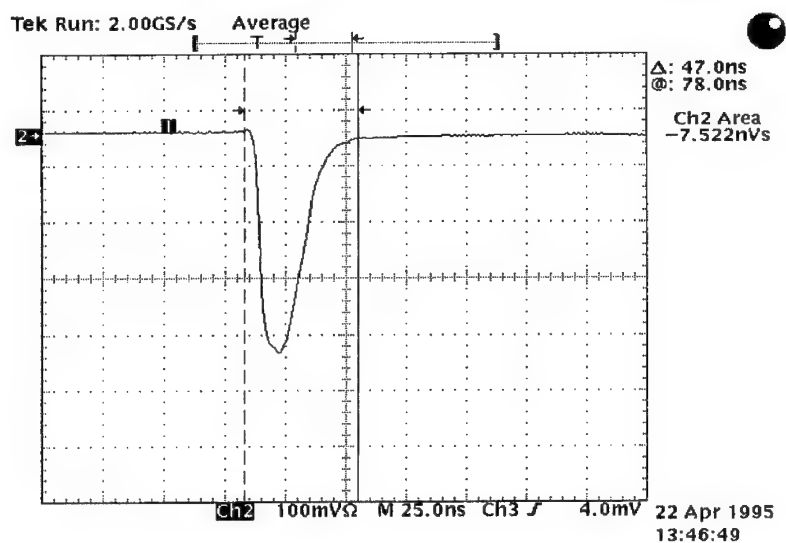
Figure 5 – Slow photoluminescence emission (670 nm) from RG630, temporal response

Figure 6: PL at 590(x) and 670(*) nm, 566x, RG630 @ 77K

Figure 7a – Excitation energy histogram (4096 pulses)

Figure 7b – Photoluminescence energy histogram
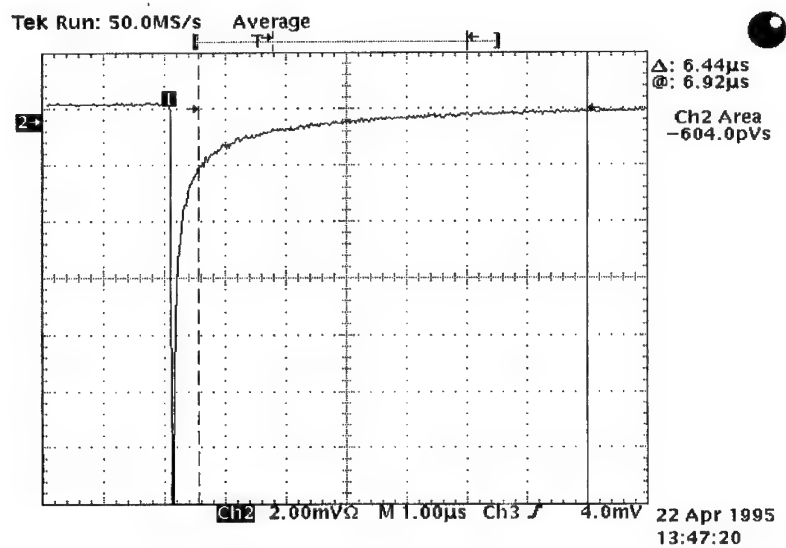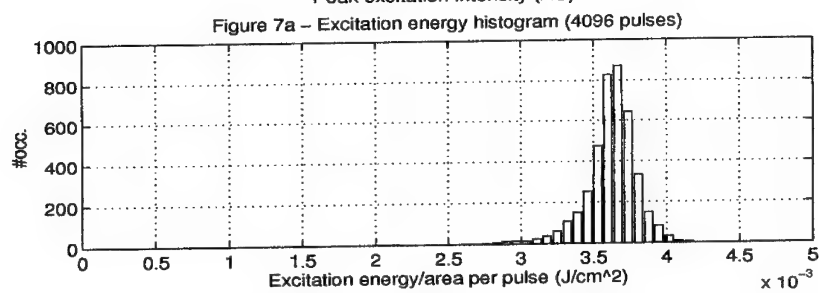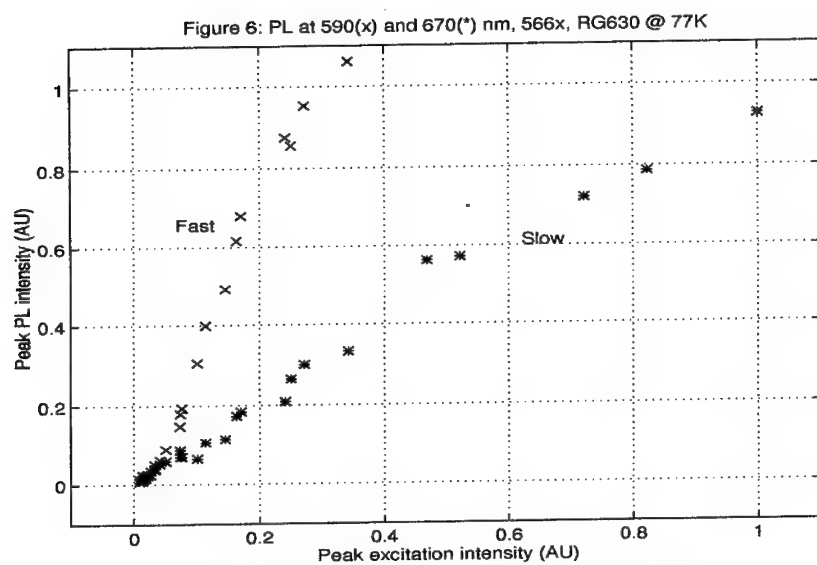
Figure 8a – Photoluminescence vs. excitation energy from fig. 7, raw
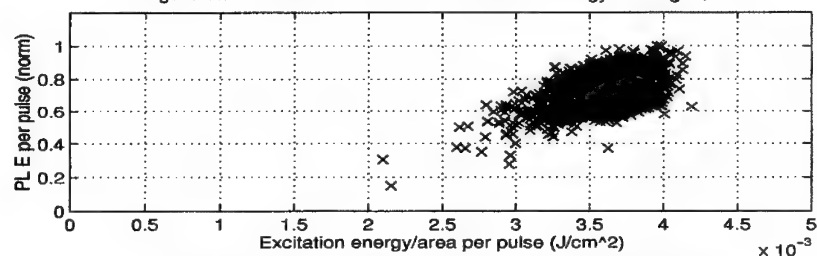
Figure 8b – PL vs. Excitation E from fig. 7, binned & averaged
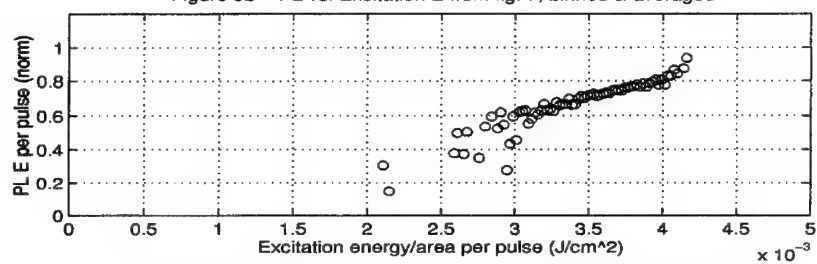
Figure 9 – PL vs. excitation energy for RG630. 77K(x) & 200K(+)
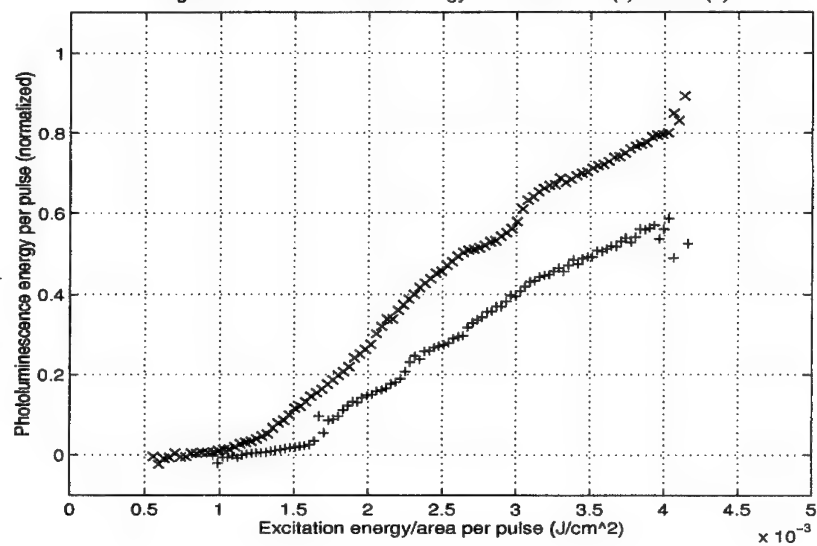
ELASTIC VIBRATIONS OF BIOLOGICAL AND ARTIFICIAL

MICROTUBULES AND FILAMENTS

Yuri M. Sirenko and K. W. Kim

Department of Electrical and Computer Engineering
North Carolina State University, Raleigh, NC 27695, U.S.A.

Michael A. Stroscio

U.S. Army Research Office, Research Triangle Park, NC 27709, U.S.A.

We apply elasticity theory formalism to study long-range, collective vibrations of microtubules (MTs) and filaments, which are major components of cytoskeleton in eukarioutic cells. MTs and filaments are long macromolecules with diameters of order of 10 nm, and are modeled by thin elastic shells and rods. The dispersion relations are obtained analytically for elastic waves propagating along MTs or filaments in presence of a solvent; the numerical calculation of the eigenmodes is performed using the experimentally measured values of Young's modulus. In a long wavelength limit MTs support three acoustic waves with propagation speed in the range of 200 to 600 m/s and set of flexural, helical waves. In the case of filament-water system there exist two acoustic modes with propagation speeds of approximately 800 and 1300 m/s and a single flexural wave with parabolic dispersion law. Our study also draws attention to the parallel existing between the biological and manufactured, free-standing nanotubes and filaments.

I. INTRODUCTION

The search for the new concepts of next generation of ultrasmall electronic devices has resulted in fabrication of a whole set of novel semiconductor nanostructures. In particular, the recent advances in the material growth techniques enabled creation of various self-supporting systems, including free-standing slabs, whiskers [1] and nanotubes [2, 3]. Since in such structures (in contrast to buried wires and wells) the effects of acoustic wave confinement is rather strong, the problem of phonon quantization and confinement in free-standing samples has received much interest [4, 5, 6].

In this study we would like to draw attention to the parallel existing between the artificially made self-supported structures and the filamentous components of cell cytoskeleton. The various filaments of the cytoskeleton have been classified according to their diameter and include microfilaments (5–7 nm), intermediate filaments (8–11 nm), and microtubules (24–28 nm) [7]. MTs are hollow cylinders of approximately 25 nm outer diameter, 15 nm inner diameter, and indefinite length. The wall of a MT cylinder is made up of (usually 13) linear elements termed protofilaments, which are formed of protein subunits known as tubulin dimers. Each 8 nm-long dimer consists of $\alp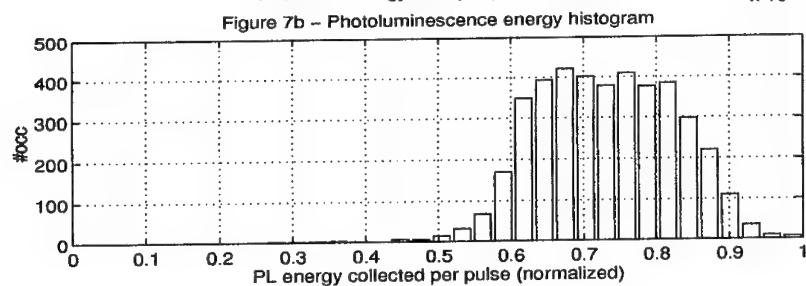ha$ and β tubulin monomers with a molecular weight of 55 kDa. Actin filaments is formed of G-actin monomers arranged in a two-stranded helix, while the intermediate filaments consists of approximately 2-3 nm diameter protofilaments,

twisted together. Though the cytoskeleton has an impact on some purely biological processes (control of gene expression, protein synthesis, and cell cycle regulation), its main functions are based on the mechanical properties such as rigidity and elasticity. The cytoskeleton is responsible for supporting the cell shape and serves as a global framework for the mechanical/functional integration of the whole cell. In a series of experiments the flexural rigidity and elastic Young's modulus for microtubules and actin filaments has been obtained from the measurement of thermal fluctuations in end-to-end distance of the proteins. In more recent works, the elastic parameters of the cytoskeleton components were determined using Fourier-analysis of thermal fluctuations in shape [8], hydrodynamic flow [9], and direct measurements [10].

In this investigation we apply the formalism of classical elasticity theory to describe the vibrational modes and mechanical wave propagation in filamentous cytoskeleton components, such as microtubules (MTs), actin filaments (AFs), and intermediate filaments. This investigation arises in the context of the general problem of protein dynamics and connection between protein dynamics and function [11], as well as available experimental results [12].

The simplest possible description of filament and MT vibrations is based on a linear model and is used extensively for analysis of fluctuations in shape [8, 9, 10]. Further elaborations of the one-dimensional model have addressed the problem of instabilities in vibrations of AFs [13] and soliton propagation in MTs [14] due to inclusion of nonlinear terms in Hamiltonian and polarization effects. Despite the universality and simplicity of the linear model, its applicability is restricted to a limit of extremely large wavelengths of the propagating waves, where all the diversity of the vibrational spectrum is reduced to pure longitudinal, torsional, and bending modes.

On the other hand, the most exhaustive information about internal motion of all constituent elements of the protein can be obtained from microscopic calculations, such as normal mode analysis. Most recently, ben-Avraham and Tirion [15] considered propagation of elastic waves in long AFs. Ignoring the internal motion in actin monomers and allowing for quasiperiodicity (helicity) of the F-actin structure, the authors obtained six vibrational branches, corresponding to three translational and three rotational degrees of freedom for each actin monomer. Assigning a thermal energy of $k_B T/2$ to each mode, the authors calculated the average fluctuations in the filament shape.

Though the normal mode analysis, based on the solution of equations of motion for all microscopic degrees of freedom, provides detailed information on both large-scale and local conformal motion, it lacks some attractive features of the linear model, such as universality and simplicity. Each protein configuration requires separate *ad hoc* calculations, which become rather cumbersome with the increase in protein size. Besides, the detailed information on each vibrational mode is often not required, since many fundamental features of conformal motion can be explained using only the slowest, large-scale collective vibrations. Finally, the inclusion of solvent effects into the microscopic calculations is not straightforward, especially under conditions when there is radiation of acoustic energy from the vibrating protein into the surrounding water. Description of such processes requires consideration of large volumes of the solvent, which therefore can not be treated microscopically, but rather as a continuos medium.

In this study we extend the applicability of a simple linear model, by taking into account the internal motion of proteins by treating the interior as a continuos medium. In Sec. II we apply the formalism of elasticity to find the vibrational spectrum of MTs in the presence of water. Sec. III deals with wave propagation in a water-filament system, treating the latter as an elastic cylinder. The obtained results are summarized in Sec. IV.

II. VIBRATIONS OF MICROTUBULES

We model MTs with an infinitely long cylindrical shells of radius R and wall thickness h. In cylindrical coordinates (r, φ, z), the shell is chosen to be located in the region $R - h/2 < r < R + h/2$; both the inner and outer parts of the shell are filled with a water. We assume the MT material to be isotropic and characterized by bulk Young's modulus E, Poisson's ratio ν, and density ρ.

To derive equations of motion of MTs, we apply the standard formalism of the elasticity theory [16]. Taking into account the boundary conditions at the inner and outer surfaces of a MT, as well as Hooke's law, we find the following set of equations for the displacement vector $\mathbf{u}$ of the shell:

$$-\frac{u_r + u_{\varphi,\varphi}}{R^2} - \frac{\nu\, u_{z,z}}{R} + \frac{p_i - p_o}{\rho h s^2} = \frac{\ddot{u}_r}{s^2},$$

$$\frac{u_{r,\varphi} + u_{\varphi,\varphi\varphi}}{R^2} + \nu_- u_{\varphi,zz} + \frac{\nu_+ u_{z,\varphi z}}{R} = \frac{\ddot{u}_\varphi}{s^2}, \qquad (1)$$

$$\frac{\nu\, u_{r,z} + \nu_+ u_{\varphi,\varphi z}}{R} + \frac{\nu_- u_{z,\varphi\varphi}}{R^2} + u_{z,zz} = \frac{\ddot{u}_z}{s^2}.$$

Here $p_{i,o}$ are water pressures at the inner and outer surface of MT, $s = \sqrt{E/\rho(1 - \nu^2)}$ is so-called longitudinal "thin plate" sound speed of the shell, and $\nu_\pm = (1 \pm \nu)/2$.

To obtain the equations of motion of the water-shell system in a closed form, the pressure terms $p_{i,o}$ need to be related to the shell displacement vector $\mathbf{u}$. The displacement vector $\mathbf{u}_w$ of water can be expressed in terms of the scalar potential Φ through the relationship

$$\mathbf{u}_w = \text{grad } \Phi; \qquad (2)$$

Φ satisfies the wave equation with a propagation speed equal to speed of sound s_w in water. Then, using the relation between the scalar potential and pressure, $p = -\rho_w \ddot{\Phi}$ (ρ_w is a water density), we can express the pressures p_i and p_o in terms of shell displacement vector $\mathbf{u}$.

We seek the solution of the equations of motion (1) as a superposition of harmonic waves with longitudinal wavevector $k_z \equiv k/R$ and azimuthal number m, and take scalar potentials of water corresponding to evanescent *interface* vibrations localized in the vicinity of the shell:

$$\begin{bmatrix} u_r \\ u_\varphi \\ u_z \\ \Phi_i \\ \Phi_o \end{bmatrix} = \begin{bmatrix} -ic_r \\ c_\varphi \\ c_z \\ c_i\, I_m(\kappa r/R) \\ c_o K_m(\kappa r/R) \end{bmatrix} \exp\left(im\varphi + ikz/R - i\omega t\right), \qquad (3)$$

Here I_m and K_m are modified Bessel's functions; the inverse confinement length κ (normalized by the radius R) is given by

$$\kappa^2 = k^2 - (\omega R/s_w)^2 \,, \tag{4}$$

Interface vibrations of water, localized near the shell surface, occur provided that $\kappa^2 > 0$ (i.e. $\omega < s_w k_z$). The opposite case of $\omega > s_w k_z$ corresponds to radiation of acoustic energy from the shell and can be formally treated with the help of Eq. (3) using analytical properties of Bessel's functions.

Substituting Eq. (4) into Eq. (1), and taking into account the continuity of displacement, we obtain the eigenequation for the interface acoustic vibrations of the shell-water system:

$$\mathcal{D} \, [c_r, \ c_\varphi, \ c_z]^{\mathrm{T}} = 0 \,, \tag{5}$$

where the dynamical matrix $\mathcal{D}$ is given by

$$\mathcal{D} = \begin{bmatrix} (\omega R/s_w)^2(1 + V_{m\kappa}) - 1 & m & \nu k \\ m & (\omega R/s_w)^2 - m^2 - \nu_- k^2 & -\nu_+ m k \\ \nu k & -\nu_+ m k & (\omega R/s_w)^2 - \nu_- m^2 - k^2 \end{bmatrix} \,, \tag{6}$$

and the coupling term between the shell and water is equal to

$$V_{m\kappa} = \frac{\alpha}{\kappa} \left[\frac{I_m(\kappa)}{I'_m(\kappa)} + \frac{K_m(\kappa)}{-K'_m(\kappa)} \right] \,. \tag{7}$$

Here $\alpha = \rho_w R/\rho h$ is a dimensionless constant of shell-water coupling.

From Eq. (5) we can find the dispersion relation for confined waves in a shell-water system by equating the determinant of the dynamic matrix $\mathcal{D}$ to zero:

$$\det \mathcal{D} = 0 \,. \tag{8}$$

As follows from Eqs. (6), $\mathcal{D}$ is a real symmetric 3×3 matrix which depends on the azimuthal number m. Therefore, for each given m the dispersion relation specifies three positive vibrational modes ω_{mj} which are identified by $j =$I, II, and III in decreasing order:

$$\omega_m^{\mathrm{I}}(k_z) > \omega_m^{\mathrm{II}}(k_z) > \omega_m^{\mathrm{III}}(k_z) \,. \tag{9}$$

Qualitatively the nature of vibrations in a coupled water-MT system can be understood from the analysis of two limiting cases, corresponding to long wavelength ($k \ll 1$) case and short wavelengths ($k \gg 1 + m$) case. Since at large κ the coupling term $V_{m\kappa} \simeq 2\alpha/\kappa$ tends to zero, we deduce that in a *short wavelength* limit ($R/h \geq k \gg m + 1$), the vibration spectrum of the shell-water system does not depend on azimuthal number m and tends to that of a free shell:

$$\omega_m^{\mathrm{I}}(k_z) \simeq s k_z, \qquad \omega_m^{\mathrm{II}}(k_z) \simeq \sqrt{\nu_-} s k_z, \qquad \omega_m^{\mathrm{III}}(k_z) \simeq \sqrt{1 - \nu^2} s/R \,. \tag{10}$$

Analysis of coefficients c_r, c_φ, c_z in Eq. (5) shows that in the limit of large k the modes I, II, and III correspond to pure *longitudinal, torsional,* and *radial* vibrations, as in the case of a free shell vibration.

Except of the limit of short wavelength waves the behavior of vibrational modes in the MT-water system is qualitatively different for *axisymmetric* waves ($m = 0$) and *flexural* modes In case of **axisymmetric vibrations** ($m = 0$), the mode

$$\omega_0^{II} = \sqrt{\nu_-}sk_z \tag{11}$$

corresponds to pure *torsional* vibrations of the MT only, and is decoupled from the rest of modes in the whole range of k_z.

The axisymmetric modes I and III correspond to coupled *radial-longitudinal* vibrations; their frequencies should be found from the remaining 2×2 determinant in Eq. (6) involving the coupling term $V_{0\kappa}$. Since this term diverges at small κ, the frequencies $\omega_0^I(k_z)$ and $\omega_0^{III}(k_z)$ at small k_z should approach zero maintaining phase velocities less than s_w to avoid crossing the $\omega = s_w k_z$ line. Analysis shows that in the limiting case of small k the frequencies $\omega_0^I(k_z)$ and $\omega_0^{III}(k_z)$ are proportional to the wavevector, $\omega_0^{I,III}(k_z) \simeq s_{I,III}k_z$.

In the case of **flexural modes** ($m \neq 0$), the coupling term $V_{m\kappa}$ reaches a finite value $V_{m0} = 2\alpha/m$ at $\kappa = 0$, and dispersion curves for the modes I and II touch the line $\omega = s_w k_z$ at finite frequencies, while the localization length R/κ diverges. However, in case of $\text{Re}(\omega) > s_w k_z$ the frequency ω has a negative imaginary part, and the amplitudes of vibrations decay as a result of the radiation of acoustic energy out of the shell.

At long wavelength the frequency of the mode III preserves its parabolic dependence on k_z pertinent to vibrations of the free shell [17], though with a renormalized coefficient:

$$\omega_{m \neq 0}^{III}(k) \simeq \sqrt{\frac{1 - \nu^2}{m^2 + 2\alpha m + 1} \frac{s}{R} \frac{k^2}{m}} \ . \tag{12}$$

In order to find the vibrational spectrum of the shell-water system in the whole range of k, we have to solve numerically the transcendental dispersion relation given by Eqs. (6)-(8). In our calculations, the most recent value of Young's modulus, $E = 0.5 \pm 0.1$ GPa [9], is used; we set the Poisson's ratio to its typical value $\nu = 0.3$. Approximation of a microtubule by a hollow cylinder with ideal surfaces, used [8, 9] to calculate the geometric moment of inertia, required the use of "contact" inner radius R_i of 11.5 nm and wall thickness h of 2.7 nm for 14-protofilament MT. Thus, the outer radius R_o of MT in our calculation is 14.2 nm and the mean radius $R \equiv (R_i + R_o)/2$ is approximately 12.8 nm. At the same time, by taking the mass of a tubulin dimer to be $M = 110$ kDa $= 1.83 \times 10^{-19}$ g, and the length $\ell = 8$ nm, we find the density $\rho = 14M/\pi(R_o^2 - R_i^2)\ell \approx 1.47$ g/cm^3 and the "thin-plate" sound speed $s = \sqrt{E/\rho(1 - \nu^2)} \approx 610$ m/s which is 2.5 times less than a speed of sound in water, $s_w = 1.50$ km/s.

We present the results of numerical calculations of dispersion $\omega_{0j}(k)$ for the axisymmetric modes ($m = 0$) on Fig. 1. Thick solid lines correspond to vibrations of MT interacting with water both outside and inside of MT. The eigenfrequencies of *free* MT are presented for comparison and are marked by thick dashed lines. The thin line is specified by the equation $\omega = s_w k_z$ and separates the region of interface vibrations in MT-water system from that of radiative waves. Note that the dimensionless frequency $\omega R/s = 1$ corresponds to a cyclic frequency of $f_0 \approx 7.6$ GHz.

As can be seen from Fig. 1, the frequencies of vibrations for the MT-water system tend to those of a *free* MT at large wavevectors k. In a short-wavelength limit, the modes I and II have a linear dispersion with velocities $s \approx 610$ m/s and $s\sqrt{(1-\nu)/2} \approx 360$ m/s, while the cyclic frequencies of the type-III modes tend to a constant value of 7.2 GHz [see Eq. (10)]. In the limit of large k, modes I, II, and III correspond to pure longitudinal, torsional, and radial vibrations. Note that because of our assumption of homogeneous MT walls, the results at $k \geq 1$ are only of qualitative character (the length of the tubulin dimer, 8nm, is comparable to the radius of MT, 13 nm).

The mode $\omega_0^{\mathrm{II}}(k_z) = \sqrt{(1-\nu)/2}sk_z$ with the velocity 360 m/s involves the pure torsional vibrations of the shell *only* and is decoupled from other modes. The other two modes in Fig. 1 (I and III) cannot touch the line $\omega = s_w k_z$, because the shell-water coupling term $V_{0\kappa}$ diverges when phase velocity of a wave approaches to sound speed in a water s_w. At large wavelength, the radial-longitudinal modes I and III depend linearly on k and are characterized by speeds of propagation eqal to 614 m/s and 225 m/s.

III. VIBRATIONS OF CYLINDRICAL FILAMENTS

We model intermediate filaments and actin filaments with an infinitely long elastic cylinder immersed in water and occupying the region $r < R$. The general solution of the elasticity equations for displacement vector **u** inside the cylinder ($r < R$) can be written in the form [16]

$$\mathbf{u} = \nabla\phi + \nabla \times (\mathbf{e}_z\psi) + R\,\nabla \times \nabla \times (\mathbf{e}_z\chi) . \tag{13}$$

Here $\mathbf{e}_z$ is a unit vector along the axis z, and potential(s) ϕ (ψ, χ) satisfy scalar wave equation with a propagation speed equal to longitudinal (transverse) sound speed s_l (s_t) in cylinder material, where

$$s_l^2 = \frac{(1-\nu)E}{(1-2\nu)(1+\nu)\rho}, \qquad s_t^2 = \frac{E}{2(1+\nu)\rho} .$$

For the outer region, $r > R$, the displacements of water is specified by a scalar potential Φ according to Eq. (2).

In order to describe harmonic vibrations (with frequency ω and wavevector $k_z \equiv k/R$) in a coupled cylinder-water system, localized near the surface of the filament, we set

$$
\begin{bmatrix} \Phi \\ \phi \\ \psi \\ \chi \end{bmatrix} = \frac{1}{R} \begin{bmatrix} ic_0\,K_m(\kappa_w r/R) \\ ic_1\,I_m(\kappa_l r/R) \\ c_2\,I_m(\kappa_t r/R) \\ c_3\,I_m(\kappa_t r/R) \end{bmatrix} \exp(im\varphi + ikz/R - i\omega t) , \tag{14}
$$

where $\kappa_t^2 = k^2 - (\omega R/s_t)^2$, $\kappa_l^2 = k^2 - (\omega R/s_l)^2$, and $\kappa_w^2 = k^2 - (\omega R/s_w)^2$. Note that in the case of $\kappa_w^2 < 0$ (i.e. $\omega > s_w k_z$) the acoustic energy is radiated from the filament into surrounding water. Also, if $\kappa_{l,t}^2 < 0$, the corresponding scalar potentials

specify *confined* vibrations, which do not decay exponentially towards the center of the filament.

Applying standard boundary conditions [16] for a stress tensor at $r = R$, and expressing the water pressure on the filament in terms of **U**, we arrive at the eigenequation for elastic vibrations of coupled water-filament system:

$$\mathcal{D} \, [c_1, \ c_2, \ c_3]^{\mathrm{T}} = 0 \, , \tag{15}$$

where the matrix $\mathcal{D}$ is equal to

$$\begin{bmatrix} 2m(I_{l0} - I_{l1}) & -(\kappa_t^2 + 2m^2)I_{t0} + 2I_{t1} & 2mk(I_{t0} - I_{t1}) \\ -2kI_{l1} & -mkI_{t0} & -(\kappa_t^2 + k^2)I_{t1} \\ (2m^2 + k^2 + \kappa_t^2)I_{l0} - 2(1+W)I_{l1} & 2m[I_{t1} - (1+W)I_{t0}] & 2k[(m^2 + \kappa_t^2)I_{t0} - (1+W)I_{t1}] \end{bmatrix} . \tag{16}$$

Here we use notations $I_{l,t0} \equiv I_m(\kappa_{l,t})$ and $I_{l,t1} \equiv \kappa_{l,t}I'_m(k_{l,t})$; the term

$$W \equiv \frac{\rho_w}{\rho} \, \frac{K_m(\kappa_w)}{-2\kappa_w K'_m(\kappa_w)} \, \left(\frac{\omega R}{s_t}\right)^2 \tag{17}$$

describes the effect of water on the vibration of the filament. In absence of water, Eqs. (15) and (16) reduce to these for elastic vibrations of a free cylindrical rod [16]. The dispersion relation of the vibrations in a water-filament system is obtained by requiring that the determinant of matrix $\mathcal{D}$ equals zero, and specifies formally infinite set of modes for each azimuthal number m.

In the case of **axisymmetric vibrations** ($m = 0$) the characteristic equation specified by the matrix $\mathcal{D}$ in Eq. (16), defines two uncoupled sets of modes corresponding to pure torsional and radial-longitudinal vibrations. The *torsional* vibrations of the filament are decoupled from the water motion and are characterized by the dispersion law

$$\omega_{0j}^{(t)} = s_t\sqrt{(\xi_j/R)^2 + k_z^2} \tag{18}$$

and the displacement vector with components $u_r = u_z = 0$, and $u_\varphi \propto J_1(\xi_j r)$, where the integer index j numerates nonzero solutions of equation $J_2(\xi_j) = 0$. Besides the generic set of solutions in Eq. (18), there exists also a special mode with a linear dispersion law, $\omega_{00}^{(t)} = s_t k_z$, and the displacement $u_\varphi \propto r^2$.

The *radial-longitudinal* are specified by a characteristic equation

$$4k^2\kappa_t^2 \, \frac{I_0(\kappa_t)}{\kappa_t \, I_1(\kappa_t)} = (k^2 + \kappa_t^2)^2 \, \frac{I_0(\kappa_l)}{\kappa_l \, I_1(\kappa_l)} + 2(1+W)(k^2 - \kappa_t^2) \, , \tag{19}$$

where the filament-water coupling factor W given by Eq. (17). In absence of water, $W = 0$, Eq. (19) is reduced to the Pochhammer equation and was analyzed in much detail [6]. The dispersion relation for the *lowest* longitudinal-radial mode $\omega_{00}^{(lr)}$ in the limits of small and large wavevectors k has the following behavior

$$\omega_{00}^{(lr)}(k) \simeq \begin{bmatrix} \sqrt{E/\rho}k_z, & k \ll 1, \\ s_{\mathrm{surf}}k_z z, & k \gg 1. \end{bmatrix} \tag{20}$$

Thus, in the *long wavelength* limit the acoustic mode $\omega_{00}^{(lr)}(k)$ corresponds to longitudinal waves in thin rods [16] with propagation speed of $\sqrt{E/\rho}$. Since the water-filament coupling term W given by Eq. (17) tends to zero at small frequencies ω, the asymptotic relation $\omega_{00}^{(lr)}(z) \simeq \sqrt{E/\rho}k$ is not changed in the presence of water. In the *short wavelength* limit this mode describes es the surface (interface) Rayleigh (Stonley) wave propagating near cylinder surface (water-cylinder interface). Corresponding propagation speed s is found as a solution of standard algebraic equations for Rayleigh or Stonley velocities [16].

In absence of water [6], the dispersion of *higher order* longitudinal-radial modes, $\omega_{0j}^{(lr)}(k_z)$ with $j \geq 1$, can be characterized by the following interpolation formula, valid in the limits of $k \ll 1$ and $k \gg j + 1$:

$$\omega_{0j}^{(lr)}(k_z) \simeq s_t\sqrt{(\zeta_j/R)^2 + k_z^2}\,, \tag{21}$$

where constants ζ_j are given by nonzero roots of equations

$$J_1\left(s_l\zeta_j/s_t\right) = 0 \qquad \text{or} \qquad \left(s_l\zeta_j/2\right)J_0\left(\zeta_j\right) = J_1\left(\zeta_j\right)\,.$$

In the intermediate region, $1 \ll k \ll j + 1$, the waves propagate with a bulk longitudinal sound speed, $\omega \propto s_l k_z$.

Thus, at $k = 0$, the modes with $j \geq 1$ have finite cutoff frequencies equal to $\zeta_j R/s_t$. The situation is changed when water is present. When $W \neq 0$, the region $\omega > s_w k_z$ corresponds to radiation of acoustic waves out of the filament, and is characterized by a complex frequency spectrum. Analysis of Eq. (19) shows that, with decrease of k_z, the branches $\omega_{0j}^{(lr)}$ enter the radiational sector $\omega > s_w k_z$ at frequencies ω_j, given by nonzero solutions of either of the following two equations:

$$J_1\left(\omega_j R\sqrt{s_w^{-2} - s_t^{-2}}\right) = 0, \qquad \text{or} \qquad J_1\left(\omega_j R\sqrt{s_w^{-2} - s_l^{-2}}\right) = 0\,.$$

Finally, in the limit of large wavevector k_z, independent of presence of water, the dispersion relation takes the form $\omega \simeq s_t k_z$, corresponding the confined transverse waves in the filament.

Vibrations with $m \geq 1$ describe the **flexural waves** of the filament, and are specified by Eqs. (15) and (16). It has been shown [6] that, in absence of water, there exists only one flexural mode, emanating from the origin (i.e. $\omega(0) = 0$). This branch corresponds to azimuthal number $m = 1$ and is characterized by a parabolic dispersion at $k_z \ll 1$:

$$\omega_{10}(k_z) \simeq \sqrt{E/\rho}\,Rk_z^2/2\,. \tag{22}$$

Such a type of vibrations corresponds to the bending mode of very thin rods and is predicted by a simple linear model [16]. Since the water-cylinder coupling term, defined by Eq. (17), vanishes at small ω and k_z, the long wavelength asymptotics, given by Eq. (22), holds in the presence of water as well.

The rest of the flexural modes, in absence of water, have finite cutoff frequencies at $k_z = 0$. With water present, their frequencies gain a negative imaginary part at

$\omega > s_w k_z$, and the acoustic energy is radiated from the wire. At large wave vector, $k_z \gg m+1$, all flexural modes behave like transverse waves, $\omega_{mj} \simeq s_t k_z$, while in the intermediate region of $1 \ll k_z \ll m+1$ the dependence $\omega_{mj} \simeq s_l k_z$ is revealed.

In order to visualize the dispersion relations, we present the calculated dependence $\omega(k)$ for axisymmetric radial-longitudinal waves on Fig. 2. To emphasize on the *universal* properties of filament vibration, independent on absolute values of radius R and material propagation speed s_t, we use the dimensionless frequency $\omega R/s_t$ and the dimensionless wave vector $k = k_z R$. The frequencies of the filament vibrations in presence of water and without the surrounding water, are marked by solid and dashed lines, respectively; the dotted straight lines correspond to $\omega = s_l k_z$ and $\omega = s_t k_z$; Poisson's ratio is taken as $\nu = 0.3$.

As seen from Fig. 2, the free vibrations of the filament (dashed lines) are characterized by one acoustic mode and a set of higher modes with finite cutoff frequencies. In the long wavelength limit, the acoustic wave propagates with a speed $\sqrt{E/\rho} \approx 1.61\, s_t$, in agreement with results of a simple linear theory; at large k the acoustic mode becomes a surface wave with a propagation speed equal to Rayleigh velocity, $s_{\text{surf}} \approx 0.93 s_t$. The higher modes demonstrate an anticrossing behavior in the region $s_l k_z < \omega < s_t k_z$, and have a phase velocity approaching s_t at higher wavevector k_z.

For numerical calculation of dispersion relation in filament-water system (solid lines) we choose the parameters of actin filaments (AFs). As for elastic constants, the experimentally measured quantity is ES, where S is an effective cross-section of a filament. Recent measurements of the parameter ES for AFs gave the values of 43.7 ± 4.6 nN [8] and 46.8 ± 2.8 nN [10]. Using the value $ES = 46$ nN, the mass of the tubulin monomer $M = 43$ kDa, and the rise per monomer $\ell = 2.75$ nm, we find the propagation speed of acoustic radial-longitudinal wave equal to $\sqrt{E/\rho} = \sqrt{ES\ell/M} \approx 1.3$ km/s. Then, using the value $\nu = 0.3$, we find a transverse sound speed, $s_t \approx 800$ m/s, and a longitudinal sound speed, $s_l \approx 1.5$ km/s, of the AF material. The bulk longitudinal propagation speed s_l of AF material practically coincides with the sound speed in water, $s_l \approx s_w$. Finally, to find the AF radius R and density ρ, we should introduce a somewhat arbitrarily defined cross-section area S. Taking $S = 25$ nm^2 [8], we obtain the radius $R = \sqrt{S/\pi} \approx 2.8$ nm and filament density $\rho = M/\ell S \approx 1.05$ g/cm^3. We also find that the dimensionless frequency, $\omega R/s_t$, of Fig. 2 corresponds to a cyclic frequency $f_0 = s_t/2\pi R \approx 45$ GHz when $\omega R/s_t = 1$.

The dispersion relations for the axisymmetric radial-longitudinal modes correspond to solid lines on Fig. 2. The most important effect of water on the vibration of the filament is that the acoustic energy is radiated by those waves with the phase velocities, ω/k_z, exceeding the speed of sound in water, s_w. The lowest, acoustic mode has, in the long wavelength limit, a propagation speed $\sqrt{E/\rho} \approx 1300$ m/s, lower than the sound speed in water, and is not affected by presence of solvent for $k \ll 1$. At large wavevector k, the lowest mode corresponds to interface vibrations and has a propagation speed s_{surf}, lower than the Rayleigh speed in absence of water. In the region $\omega > s_w k_z$, the higher-order modes are radiated from the filament and are not shown on Fig. 2, since their frequencies are complex. The frequencies of the higher-order modes coincide with those for a free filament at $\omega = s_w k_z$, and in the region of $\omega > s_w k_z$ the vibrational frequencies in the coupled water-filament system are slightly

lower than those for a free filament. At large wavevector, $k_z > \omega/s_t$, the propagation speeds for waves in both filament-water system and free filament approach the bulk transverse speed s_t. We do not present the numerical results for the flexural modes ($m \geq 1$), since qualitatively the behavior of these modes is similar to higher-order modes in Fig. 2. The only exception occurs in the case of $m = 1$, where an additional bending mode arises with the parabolic dispersion law, given by Eq. (22).

IV. CONCLUSION

In this paper we described the general, universal properties of long protein dynamics, treating the protein as a continuos medium and using the formalism of classical elasticity theory. While this model does not provide the detailed information about microscopic movements of each constituent element, such an approach can describe adequately the most important long-range, collective conformal motion of the protein. Relative simplicity of the obtained results, their independence on specific structure of the protein, emphasis on the most universal properties of vibrations, and inclusion of the solvent effects in the natural way, allows this approach to complement *ad hoc*, microscopic study of protein dynamics.

For specific implementation of our model, we have chosen two types of structures: long cylindrical rods and hollow cylindrical shells filled with a solvent. These two topologically different geometries serve as a physically reasonable approximations for a large variety of filamentous structures, such as microtubules, microfilaments, and intermediate filaments. The elastic parameters of the model have been taken from measurements of flexural rigidity of these objects. The waves propagating near the shell (filament) interface were classified and characterized according their pattern, and the dispersion of these waves was analyzed both analytically and numerically. In the long wavelength limit, the results of simple linear theory for thin elastic rods has been reproduced.

In particular, for cylindrical geometry (filaments), two acoustic waves and one helical wave have been found. As for water-shell system (microtubules), there exist three acoustic modes (one of them appears due to interaction with solvent) and a set of helical, flexural waves. Both structures support also higher frequency waves which become radiative at large wavelength with mechanical energy leaking to surrounding solvent. The results obtained in this paper are of general, universal character and complement detailed microscopic calculations of long protein dynamics.

References

[1] A. K. Viswanath *et al.*, Microwave Optical Technol. Lett. **7**, 94 (1994).

[2] S. Iijima, Nature **354**, 56 (1991).

[3] Science and technology of fullerene materials. Edited by P. Bernier *et al.* (MRC, Pittsburgh, 1995).

[4] N. Bannov, V. Mitin, and M. Stroscio, Phys. Stat. Sol. (b) **183**, 131 (1994); N. Perrin, Phys. Rev. B **48**, 12151 (1994); N. Bannov, V. Aristov, and V. Mitin, Solid State Commun. **93**, 483 (1995).

[5] M. A. Stroscio and K. W. Kim, Phys. Rev. B **48**, 1936 (1993); S. Yu *et al.*, *ibid.* **50**, 1733 (1994); M. A. Stroscio *et al.*, J. Appl. Phys. **76**, 4670 (1994).

[6] V. G. Grigoryan and D. G. Sedrakyan. Sov. Phys. Acoust. **29**, 281 (1984).

[7] L. A. Amos and W. B. Amos. Molecules of cytoskeleton (Guilford Press, New York, 1991).

[8] F. Gittes *et al.*, J. Cell. Biol. **120**, 923 (1993).

[9] P. Venier *et al.*, J. Biol. Chem. **269**, 13353 (1994).

[10] H. Kojima *et al.*, Proc. Natl. Acad. Sci. **91**, 12962 (1994).

[11] H. Fraunfelder *et al.*, Ann. Rev. Biophys. Biophys. Chem. **17**, 451 (1988).

[12] E. L. de Beer *et al.*, Biophysical J. **68**, 70 (1995); H. E. Huxley *et al.*, *ibid.* **67**, 2411 (1994); K. Wakabayashi *et al.*, *ibid.* **67**, 2422 (1994).

[13] K. Sekimoto *et al.*, Phys. Rev. Lett. **75**, 172 (1995).

[14] M. Satarić *et al.*, J. Molecular Electronics **6**, 63 (1990); M. V. Satarić, J. A. Tuszyński, and R. B. Žakula, Phys. Rev. E **48**, 589 (1993).

[15] D. ben-Avraham and M. M. Tirion, Biophysical J. **68**, 1231 (1995).

[16] K. F. Graff. Wave motion in elastic solids (Clarendon Press, Oxford, England, 1975).

[17] S. Markuš. The mechanics of vibrations of cylindrical shells (Elsevier, Amsterdam, 1988).
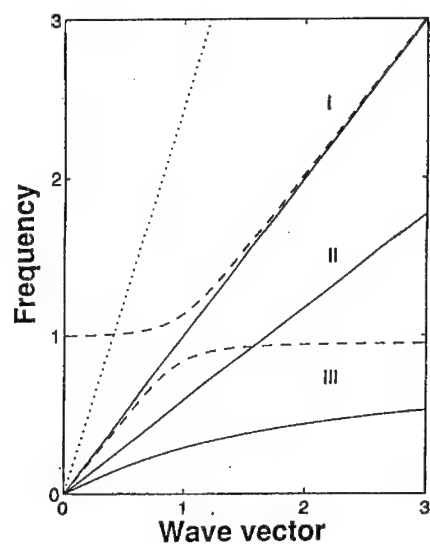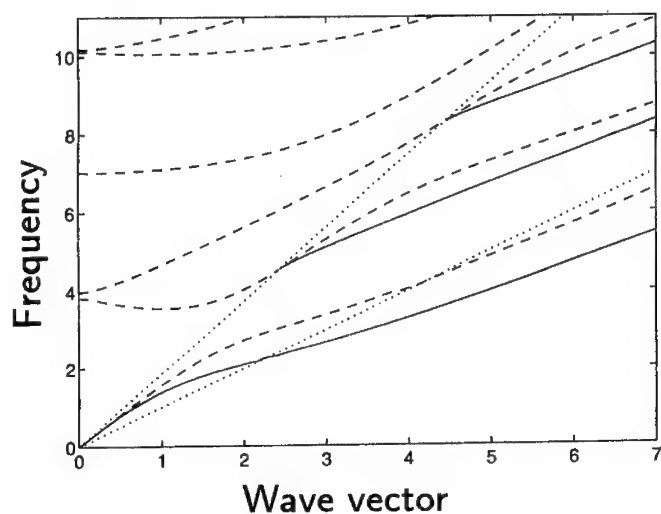
Fig. **2.** Dimensionless frequency $\omega R/s_t$ vs. wavevector $k_z R$ for axisymmetric *radial-longitudinal* vibrations of a cylindrical filament. Solid and dashed lines correspond to vibrations of the filament with and without water, respectively. Dotted lines corrspond to $\omega = s_l k_z = s_w k_z$ (upper line) and $\omega = s_t k_z$ (lower line).

272

Devices

OPERATING MODES OF COUPLED QUANTUM WIRES

O. Vanbésien, L. Burgnies and D. Lippens

Institut d'Electronique et de Microélectronique du Nord (IEMN)
Université des Sciences et Technologies de Lille, Avenue Poincaré BP 69
59652 Villeneuve d'Ascq Cedex, France

ABSTRACT

We report on the operating modes of electron waveguide structures including single- and dual-branch coupling schemes. The analysis of ballistic transport is carried out using mode matching techniques with special attention on wave function patterns and phase conditions. Various configurations are investigated by means of conductance spectra in order to determine how the electron streams can be driven towards the output terminals. For single-branch structures, a backward operating mode was pointed out by a proper breaking of the wave function symmetry. For dual-branch structures, equal sharing (3-dB coupler) and full transfer conditions (electronic switch) were obtained due to interference phenomena. Finally, by viewing the charge transfer as a resonant process, sub-picosecond time response of coupling mechanisms are found.

INTRODUCTION

Electronic transport in confined semiconductor geometries has received increasing interest in the past few years with the potential for a new class of devices whose functionality appears promising for the future. Therefore, a T-shaped quantum wire was proposed as a quantum transistor [1] and a double waveguide structure as the basic cell for an analogue-digital converter [2]. Basically, these new devices take advantage of the extremely high mobility at low temperature[3] of a two-dimensional (2D) electron gas which preserves a ballistic transport of charges over submicron distances. Moreover, recent advance in electron lithography at the nanometer scale made it possible to control the lateral extent of the 2D gas in such a way that the motion is solely along one direction. Such electron waveguide structures have been widely studied in the literature with notably the demonstration of conductance quantization [4]. A next step in the understanding of electron transport in these ultra-

small one-dimensional structures is to study their junctions. This can be done either in a two terminal configuration with stub-like or resonator-like structures as example [5] or in a multi-access scheme as it is the case for a directional coupler by analogy with optics and microwave components. For the latter, an extremely narrow gate controls the height and the width of a tunneling barrier which interconnects two waveguides in close proximity [6]. In this paper, another approach is considered with open windows interconnecting two quantum wires [7]. Beyond the search of new degree of freedom in the design, one of the major advantage of such structures is the openness of the system. In terms of time response, this feature appears favorable by avoiding the use of electrostatic tunneling barrier with highly selective transmissivity. The paper is organized as follows: the numerical procedure is briefly presented. Then we analyzed various operating modes both for single- (SBC) and dual- (DBC) branch coupling schemes including backward wave operation, 3-dB coupling and lateral real space transfer. Finally, the characteristic times of coupling mechanisms are discussed.

NUMERICAL PROCEDURE

The topology of the structure we proposed is schematized in Figure 1. Here we assume that a 2D gas, as it observed at the interface of a conventional GaAs/AlGaAs heterostructure, was laterally confined by split gates implemented on top of the high-gap layer. Figure 1 depicts the undepleted paths where the electron gas is free to move ballistically. Under these conditions, the conduction properties are solely determined by the geometry of the structure which consists of four terminals, labelled port 1 to 4, acting as access regions of two quantum wires and of an active quantum region interconnecting them.
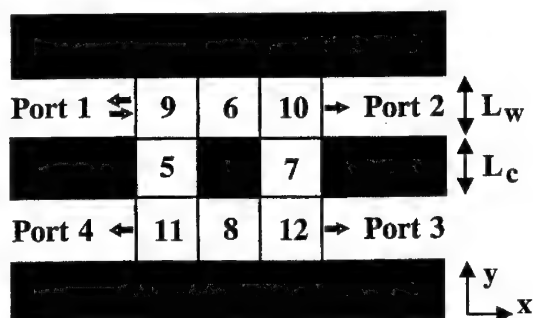

Figure 1: Schematic view of the quantum directional coupler

In this work, two coupling structures have been considered: a Single Branch Coupler (SBC) and a Dual Branch Coupler (DBC). For both designs, the numerical procedure is quite the same and differs solely by the number of sub-regions used for partitioning the coupling waveguide region (3 sub-regions for a SBC and 8 for a DBC). To solve the time-independent Schrödinger equation, we use the following assumptions: the confining potentials are considered as hard walls and square corners. Moreover, we assume near-equilibrium conditions for the 2D gas. The numerical method is based on a mode matching technique first introduced by Kühn [8] for electromagnetic waveguides and recently used by Weisshaar et al [9] for analyzing two port electron waveguide structures. We have extended this procedure in order to study four port structures with the associated benefit of a wide range of possible designs. Port 1 was taken as the reference port with forward and backward waves for describing the wave injection and return resulting from reflexion of the wave function interacting with the coupling region. In contrast, perfect matching was assumed in the output ports, that is to say that we consider only leaving waves in the regions numbered 2, 3 and 4. In each sub-region of the simulation domain, the 2D wave function can be expanded in a set of orthogonal functions. This series expansion, theoretically infinite, is indexed by the quantum levels of the waveguide and weighted by a propagating or attenuating term depending on the energy considered. After truncation, the application of continuity conditions for the wave function and for its normal derivative at each interface leads to a set of linear equations which can be solved to determine completely the wave function Ψ. Once Ψ is known, transmission coefficients as well as conductance at each output arm, according to the Landauer-Büttiker formula [10], can be deduced. Finally, as it is done for microwave couplers, we define the coupling coefficient as the sharing of Ψ between port 1 and port 3, and the directivity as the measure of the unbalance between the electron waves at the output ports of the coupled waveguide namely port 3 and port 4. In practice, the coupling and directivity coefficients can be expressed as a function of conductance values. Details of the numerical procedure can be found in reference [11].

SINGLE-BRANCH COUPLER

Figure 2 shows the conductance evolution as a function of the waveguide widths (L_w) in the case of a SBC. In an experiment, varying L_w corresponds to a variation of the confinement induced by a biasing of outer gates in the y direction. The characteristic dimensions of the active region are 30 nm in the x direction (quantum wires) and 20 nm in the y direction (branch-line) according to the notation of Figure 1. For a fixed energy of 30 meV, the first propagating mode appears for $L_w = 13.7$ nm. With respect to an uniform electron waveguide which exhibits conductance plateaus in units of $2e^2/h$, one can note that the variations of the conductance G_2, which describes the straight-through conduction between the feeding port 1 and the output port 2, is strongly perturbed by the coupling process.
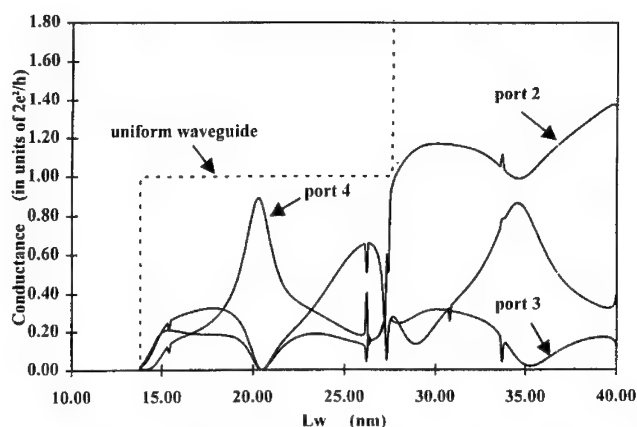
Figure 2 : Conductance characteristics at the three output ports for a single branch coupler as a function of L_w

A full transfer is only recovered at each cut-off length for which a higher mode is accommodated. This is notably the case for $L_w = 27.4$ nm which corresponds to a propagating second order mode. Concerning the values of G_3 and G_4, which reflect the conductance levels within the coupled waveguide, the highest values are always lower than $2e^2/h$ even for a bi-mode operation. Indeed, a careful analysis of coupling processes in waveguides with several propagating modes shows that only the highest order mode contributes to the coupling. On this basis, it seems preferable to work in a monomode situation and hence for L_w between 13.7 and 27.4 nm which is now detailed. Therefore, for a value of L_w close to 21 nm, one can note that the stream of electrons is driven almost entirely towards port 4. The conductance at this output port is equal to $0.9 \times 2e^2/h$ (and not $1 \times 2e^2/h$ due to significant return loss as it will seen hereafter) whereas values at port 2 and 3 are almost zero. This is the typical situation of a backward wave regime where a quasi-full transfer occurs between the two parallel waveguides along with a reversal in the direction of propagation.

In order to have a better understanding of this turnaround process, Figure 3a shows a three-dimensional plot of the modulus of the wave function $|\Psi|$. First of all one, can note that $|\Psi|$ exhibits a node in the two quantum regions connecting ports 3 and 4. Such a pattern is characteristic of a two-order mode which cannot propagate in the quantum wires owing to cut-off considerations. This explains the rapid evanescence of the probability waves in these two output ports. On the other hand, it can be seen that the wave function is highly asymmetric in the coupling branch with an accumulation in the presence probability density close to the confinement wall located on the right hand side of the figure. By systematically varying the ratio between wire

and branch widths (here this ratio is 0.66:1), it was found that this asymmetry was a key feature for successful backward operation, the confinement wall aforementioned acting as a repelling barrier. Illustration of the bending of the wave front can also be found by plotting the iso-phases of the wavefunction reported in Figure 3b.
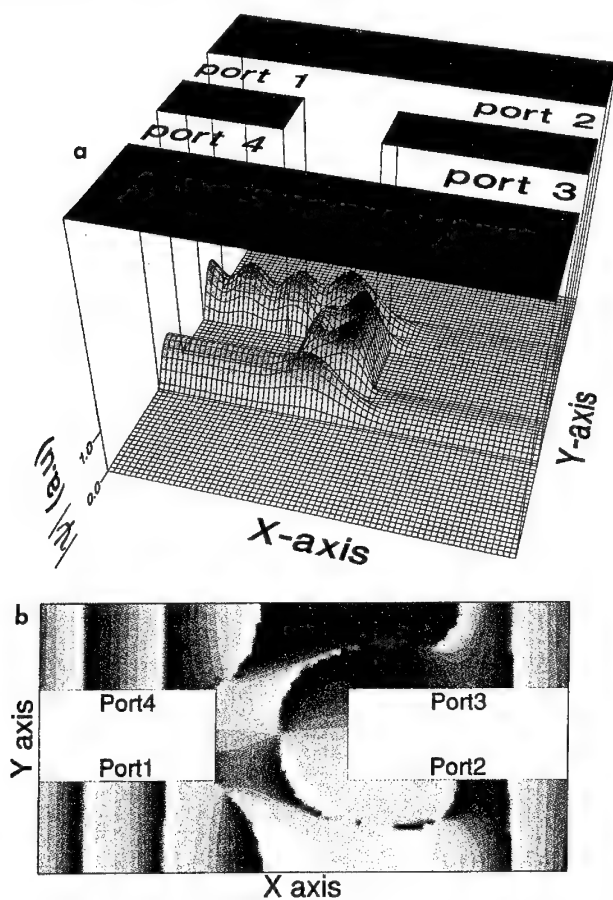

Figure 3 : Illustration of a backward wave operation in a single branch coupler : (a) 3-D view of the modulus of the wave function, (b) 2-D plotting of the phase of the wave function

At the entrance of the coupling region starting from a well defined propagating mode with regular phase front and phase rotation between $-\pi/2$ and $+\pi/2$, one can note a first bending of the wave front which initiates the coupling process. Within the interconnecting region, the curvature is reverse. Such a pattern emphasizes the role played by the right-hand side wall which behaves, due to quantum reflexion, as a virtual source inducing two streams towards port 1 and 4 respectively. These two probability waves are responsible for the ripple observed in the feeding wire and for the transfer in the opposite direction towards the output port 4. In the wires corresponding to the output ports 3 and 2, the phase is seen almost constant over a sizeable distance. This is explained by the predominance in this region of an evanescent two-order mode superimposed onto the ground propagating mode. Far away from the coupling region the wave function is practically quenched. Again the phase front becomes comparable to those observed in ports 1 and 4. However this propagating contribution is negligible and hence the conductance, because the magnitude of the probability density is very low in this region.

Another frequent use of microwave couplers is the "so-called" hybrid coupler or 3-dB coupler where the incident flux is equally shared between two of the three output ports. Such a configuration can be obtained using a SBC by using a large interconnecting branch, at least three times wider than the incident wire. However, such relatively large dimensions imply the existence of many propagating modes in the coupling region resulting in a rather low directivity. This drawback can be alleviated by the use of a double branch coupler (DBC) with characteristic dimensions for the wires and for the interaction region of the same order preserving by this means a monomode operation.

DOUBLE-BRANCH COUPLER

Figure 4 shows the results obtained for the coupling coefficient (C) and the directivity (D) as a function of L_w in the case of a DBC calculated at an energy of 20 meV. Here, except L_w, all the dimensions (branch length and width, inter-branch distance) are fixed to 20 nm. The directivity in most cases appears positive and hence with a preferential transfer towards port 3. Over the wire width investigated and in the monomode regime, values as high as 30 dB can be reached. Concerning the coupling coefficient values close to 0 dB, they correspond to a full transfer of the carrier stream from the first wire towards the second one. This gives rise to various operating regimes illustrated just after. If we consider now a multimode operation, one can note a decrease of D, with maximum values around 12 dB. Moreover, C does not exceed 6 dB in agreement with the argument of coupling mechanisms dominated by the highest order propagating mode. In the same way, a monomode operation seems preferable here and we will focus on two operating regimes namely the 3 dB coupler and the electronic switch.
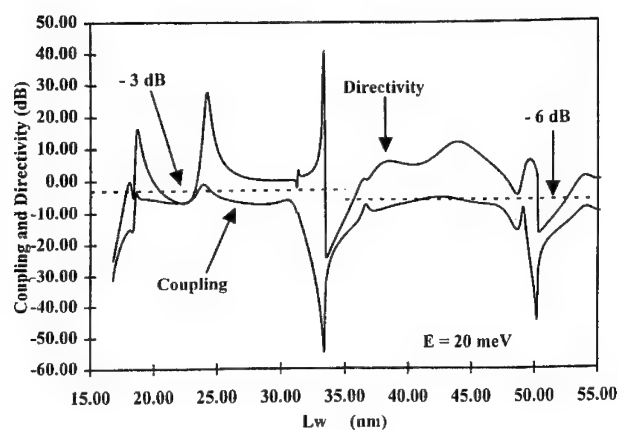
Figure 4 : Coupling coefficient and Directivity as a function of Lw for a double branch coupler at an energy of 20 meV

Figure 5 gives the two dimensional plots of the probability density (Figure 5a) and of the iso-phases of the wave function (Figure 5b) for a 3-dB coupling. In this case the reference energy is 31 meV and all the dimensions are fixed to 20 nm. The directivity is here 17 dB. Let us note that an optimization of D can be undertaken by varying systematically the quantum wire dimensions at a given energy. On this basis, directivity coefficients starting from 15 up to 35 dB in the 20-40 meV energy range can be obtained.

From Figure 5a, one can see that an equal sharing of the presence probability is apparent at the output ports 1 and 3 along with a low reflection coefficient at the feeding port 1 (quantitatively lower than 0.01), characterized by very small changes of grey depth at the center of the incident wire due to the ripple in the probability maxima. Conversely, the conductance value at port 4 is very low (less than $0.01 \times 2e^2/h$ in best cases). As before, such a low transmissivity is due to a rapid decay in the wave function due to excitation of a higher-order evanescent mode (a node is apparent in the middle of the channel at port 4). However, the situation is a little bit complicated with respect to the single branch structure due to interference effects. Such effects are a direct consequence of the two distinct coupling paths and one can expect that the electron waves are in-phase in the sub-region near port 3 and out-of-phase in the vicinity of port 4.
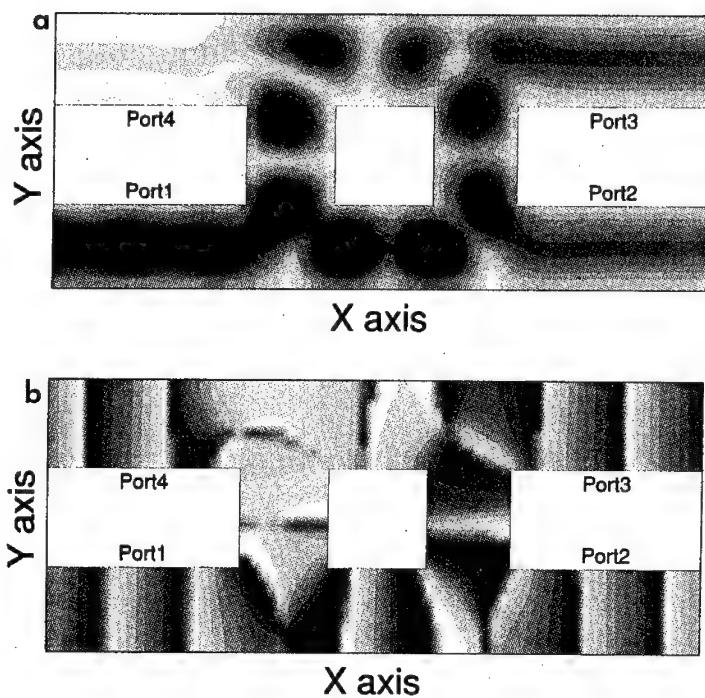
Figure 5 : 2-dimensional views of the presence probability (a) and of the phase (b) for a 3-dB coupling operating mode using a double branch scheme.

This interpretation based on constructive and destructive interferences can be supported by analyzing the iso-phase pattern displayed in Figure 5b. It can be seen that the two branches behave differently with well defined phase rotation for the second branch whereas the phase in the first branch is almost constant.The fact that the phase front is lost for the latter can be explained by the superimposition of a primary electron stream transmitted by the first branch and a back-scattered wave issued from the second branch.

In order to illustrate how the DBC can also be used as a quantum interference electronic switch, we have reduced the lengths of both interconnecting branches down to 15 nm. The other dimensions remain unchanged and the energy was equal to 25 meV. Figures 6a and 6b show the presence probability within the simulation domain for the two opposite states of the switch. Figure 6a corresponds to the case of a straight-through transmission, obtained for $L_w = 29$ nm (conductance at port 2 is 0.994 x $2e^2/h$). Two accumulation density dots of second order kind are apparent in the coupled wire explaining a rapid evanescence of electron wave and thus forbidding an efficient coupling process.
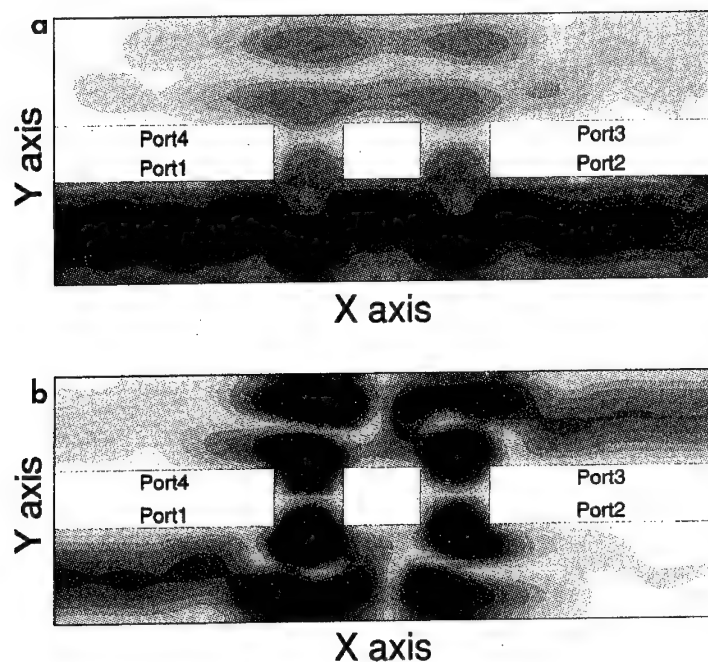
Figure 6 : 2-dimensional views of the presence probability for the switching process using a double branch scheme: (a) straight-through transmission, (b) lateral real space transfer

In contrast, for $L_w = 27.4$ nm, we obtained the results shown in Figure 6b which illustrates the case of lateral real space transfer with a high transfer ratio (conductance at port 3 close to $0.95 \times 2e^2/h$). As in the 3-dB coupling case, the high directivity of this wave control stems from constructive and destructive inferences of the scattered waves in phase in port 3 and out-of-phase in port 2 and 4. By use of this two possible scenarios, the concept of a switching action, relying entirely on quantum interference, can be supported. As a last comment, we have to emphasize that the four terminal configuration appears promising from the return-loss point of view, since the electron flux is transferred and not reflected during the switching process. This point could be checked by calculating the reflexion coefficient at port 1 whose magnitude was found very low.

TIME RESPONSE OF COUPLING MECHANISMS

In this last section, we try to estimate the time response of the coupling mechanisms involved both in DBC's and SBC's. Indeed, by viewing the transfer of electrons from one wire to the another as a resonant process, it is possible to calculate the characteristic time as example for the switching process described above. To this aim, we use the transmission probabilities versus electron energy calculated mode by mode at each port of the structure rather than the conductance data versus L_w.

Figure 7 : Quantum transmission probabilities for the switching process as a function of energy

By way of illustration, Figure 7 shows the variations of the transmission coefficients in the single mode limit at the three output ports of a DBC. The dimensions used correspond to the case of the lateral real space transfer analyzed previously. The energy has been varied around 25 meV. With respect to the analysis made before, the same tendencies can be noted: an upward cusp for channel 3 with resonant peak at 25 meV and a downward cusp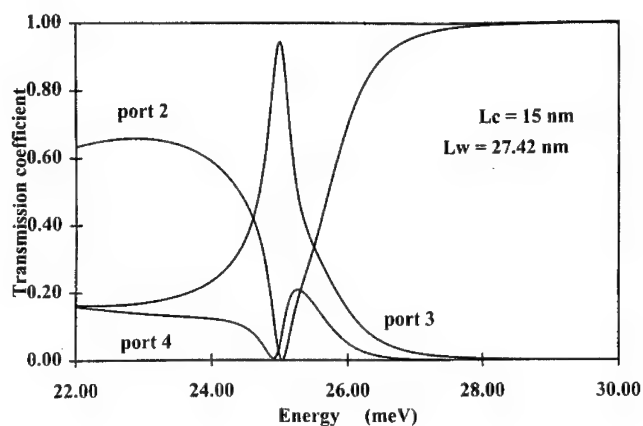 for the other ports. Using now the width at half maximum of the peak (labelled Γ), it is possible to determine the dwelling time (τ) within the coupling region by : $\tau = \hbar/\Gamma$. In this case, we obtain $\Gamma = 1.2$ meV or $\tau = 0.55$ ps, which validates the expectation of a very fast transfer process. The same procedure can be used for the backward wave operating mode using the single branch structure. In that case, the time response obtained is lower with $\tau = 0.15$ ps. In fact, for the latter, the coupling process appears relatively straight forward whereas the coupling phenomena involve a more complex wave pattern for a DBC.

CONCLUSION

In summary, we have investigated theoretically the potential of quantum couplers in a four-port configuration which consist of two parallel electron waveguides connected by one or two branch-lines. For this analysis, a numerical code for solving the 2-dimensional Schrödinger equation, based on a mode-matching technique, has been successfully developed. As the topology of the structure is varied, various operating modes have been pointed out: (i) a backward wave regime using a single branch coupler, (ii) a 3-dB coupler using a dual branch scheme, (iii) a quantum interference electronic switch. Using an open coupling window instead of a tunneling barrier appears a welcome feature in terms of time response. Preliminary estimates of the dwelling time in the coupling region indicate that sub-picosecond time constants can be expected. In anticipation of future improvements in fabrication techniques and higher quality material, it is believed that this new class of quantum components can find application in extremely low-power-consumption and ultra-fast devices.

ACKNOWLEDGMENTS

REFERENCES

[1]   F. Sols, M. Maccuci, U. Ravaioli and K. Hess, Appl. Phys. Lett, **54**, 350 (1989)

[2]   C. Eugster, P.R. Nuytkens and J.A. del Alamo, International Electron Device Meeting, 495, (1992)

[3]   K. Hirakawa and H. Sakaki, Phys. Rev. B, **33**, 8291, (1986)

[4]   S.J. Koester, C.R. Bolognesi, M.J. Rooks, E.L. Hu and H. Kroemer, Appl. Phys. Lett., **62**, 1373, (1993)

[5]   F. Sols, M. Maccuci, U. Ravaioli and K. Hess, J. Appl. Phys., **66**, 3892, (1989)

[6]   CC. Eugster, J. A del Alamo, M. J. Rooks and M. R. Melloch, Appl. Phys. Lett., **60**, 642, (1992)

[7]   O. Vanbésien and D. Lippens, Appl. Phys. Lett, **65**, 2439, (1994)

[8]   E. Kühn, Arch. Elek. Übertragung., **27**, 511, (1973)

[9]   A. Weisshaar, J. Lary, S.M. Goodnick and V.K. Tripathi, J. Appl. Phys., **70**, 355, (1991)

[10] M. Büttiker, Phys. Rev. Lett., **57**, 1761, (1986)

[11] O. Vanbésien and D. Lippens, Phys. Rev. B, **52**, (1995)

RESONANT TUNNELING DEVICES WITH DIRECT SIDEWALL GATES

D.B. Janes, V.R. Kolagunta, G.L. Chen, K.J. Webb, and M.R. Melloch
School of Electrical and Computer Engineering
Purdue University
West Lafayette, IN 47907-1285

ABSTRACT

Gated resonant tunneling devices are developed for applications including vertical one-dimensional quantum dot arrays and resonant tunneling transistors. Schottky gate deposition directly on the mesa sidewall allows submicron device dimensions and provides vertically uniform modulation of the quantum well region and access channels.

INTRODUCTION

Developments in nanofabrication have facilitated the understanding of the tunneling process in small area two-terminal Resonant Tunneling Diodes (RTDs) [1,2]. Features such as fine structure corresponding to the discrete density of states of a zero-dimensional systems and single electron charging effects have been observed [1,2]. Interesting electron charging and coherence effects caused by the interaction between the electrons in three barrier/ two quantum wells have been predicted [3]. Resonant tunneling transistors (RTTs) have also attracted interest as high functionality devices [4]. The use of a third terminal (gate) should make it possible to switch a RTD from the large area regime to one where low-dimensional or Coulomb charging effects occur. Several gating topologies have been developed for RTDs, including gates formed by in-plane Schottky metallization, in-plane implanted gates and Schottky metallization in etched recesses [4-7]. The applicabilities of these techniques for low-dimensional structures are limited by the vertical asymmetry in the gating action, minimum size restrictions ($2\mu m$) due to the lateral straggle of the implantation process and poor device performance in the depletion (pinch-off) regime, respectively.

We present a new self-aligned, sidewall gating technique for applications in the fabrication of controllable quantum dot arrays and RTTs. The application of a gate directly to the nearly vertical sidewall should provide uniform gating of the double barrier region and both access channels. The technique developed herein can be used to fabricate devices of physical dimensions in the submicron regime in order to realize high perfomance RTTs as well as the small area vertical structures proposed for the study of linear response conductance through triple barrier/double quantum well structures [3].

DEVICE DESCRIPTION

The epilayer structure shown in Fig. 1 was grown on a semi-insulating substrate in a GEN II molecular-beam epitaxy (MBE) system at a growth temperature of $600^\circ C$ for all layers except the 35 Å cap. The double-barrier (DB) heterostructure consists of two $AlGaAs$ barriers of thickness 45 Å separated by an i-GaAs well of thickness 50 Å. The gradation in the doping near the DB prevents the formation of a conduction path between the drain and the source through the breakdown of either the gate-source or the gate-drain Schottky diodes. The top-contact layer structure consists of a 1000 Å heavily doped GaAs layer capped by a 35 Å low temperature grown ($250^\circ C$) GaAs layer (LTG:GaAs). To define the device mesa structure shown in Fig. 2, 50 Å Ti/ 1500 Å Au non-alloyed top contacts (Drain) are patterned on the surface by electron beam lithography and liftoff. The non-alloyed contact structure on LTG:GaAs provides good control of the vertical structure and

a specific contact resistance reported to be as low as $1-2x10^{-7}$ $\Omega-cm^2$. [8] Contact to the bottom n-type GaAs layer (Source) is made by optical lithography, with a metallization of 300 Å Ge / 900 Å Au / 100 Å Ni annealed in a rapid thermal annealer for 30 sec at $465^{\circ}C$. The mesa etching is a dual step procedure; i) 0.3 μm etch using a Chemically Assisted Ion-Beam Etching (CAIBE) followed by ii) 0.2-0.3 μm isotropic wet chemical etch in a 1:8:1000 $H_2SO_4 : H_2O_2 : DI$ water solution. The CAIBE etch period was 50 sec with an etch rate of 363 nm/min, the etch gas was Cl_2, the accelerating voltage was 100V, the ion current was 100mA and the sample temperature was $60^{\circ}C$. The CAIBE etch defines a clean vertical sidewall and the wet etching step is used to obtain the controlled undercut necessary to isolate the gate metal from the top-contact metal. Using the top-contact metal as the shadow mask, the gate (100 Å Ti / 100 Å Ni / 200 Å Au) is then deposited in an electron-beam evaporator with the substrate mounted on a continuously rotating chuck and aligned at an angle between 30 and 50 degrees away from the normal incidence of the metallization flux. The inclination determines the proximity between the gate and the top-contact along the sidewall of the mesa. Contact to probe pads from the top-contact is made using a 0.6-0.8μm Au thick airbridge, which is aligned to the top-contact metal by opening windows in a PMMA photoresist layer using the electron-beam lithography system.

ELECTRICAL CHARACTERIZATION

Fig. 3 shows the drain currents for a device with an active area of 1.2μm x 1.2μm, along with the corresponding gate leakage currents. The peak current at zero gate bias is 220μA, giving a peak current density of $1.5x10^4$ A/cm^2, and the peak transconductance, g_m, is 42μS. at $V_{DS} = 0.76$V. The device shows gating for both positive and negative gate biases with a maximum efficiency (g_m normalized to current) near zero gate bias, as expected for a depletion mode device. Earlier work on the in-plane Schottky devices showed an increase in gating efficiency with increasing drain-source bias, which indicates that modulation of the area of one of the access channels, rather than modulation of the DB region, could be the cause for pinchoff of the device [6]. Since the gating efficiency in the sidewall gated devices is almost independent of the gate to drain bias, we conclude that the gating is not dominated by the pinching of the drain channel. Discounting the gate leakage currents due to the large area of the parasitic gate-source Schottky (about 3300μm^2 for these devices), reduction in peak currents up to 36 percent of the zero gate bias values was achieved for gate biases of $V_{GS} = -3$V, from which we estimate a depletion thickness of 230nm at each edge. Interesting quantum confinement effects would therefore be expected for devices with minimum mesa widths below 0.6μm. Since the leakage current is independent of the gate to drain bias and is determined mainly by the gate-source bias, it is concluded that most of

the leakage contribution is due to the reverse/forward saturation currents through the gate-source Schottky. Restricting the deposition of the Schottky gate to within several microns of the mesa along with the use of thicker, lower-doped access layers should greatly reduce this leakage current and reduce the gate capacitance to 0.5 to 1 pF/mm. A second device, which consists of two $1\mu m$ x $1\mu m$ RTDs connected through a thin $0.3\mu m$ region, has been characterized to illustrate the application of the sidewall gating technique for RTTs with larger channel widths. Near zero gate bias, this device shows a peak g_m of $95\mu S$ (42mS/mm) at $V_{DS} = 0.87$V and a peak current which is larger than that of the first device by a factor equal to the area ratio, as expected for large area two terminal RTDs.

CONCLUSIONS

The self-aligned technique can be used to fabricate devices with submicron widths and relatively complex active area structures, to realize novel three terminal vertical mesoscopic devices and fabricate RTT structures with high perimeter to active area ratios. It is expected that increasing the peak current by reducing the barrier thicknesses (45 Å in the present devices) coupled with biasing of the RTT in the negative differential resistance regime would result in higher effective g_m and thus higher cut-off frequencies.

ACKNOWLEDGEMENT

References

[1] M. A. Reed, J. N. Randall, R. J. Aggarwal, R. J. Matyi, T. M. Moore, and A. E. Wetsel, Phys. Rev. Lett. 60 (6), 535-537 (1988).

[2] S. Tarucha, T. Honda, T. Saku, and Y. Tokura, Surf. Sci. 305 (1-3), pp. 547-552 (1994).

[3] G. Klimeck, G.L. Chen, and S. Datta, Phys. Rev. B 50 (4), pp. 2316-2324 (1994).

[4] W. C. B. Peatman, E. R. Brown, M. J. Rooks, P. Maki, W. J. Grimm, and M. Shur, IEEE Elect. Dev. Lett. 15 (7), pp. 236-238 (1994).

[5] P. Gueret, N. Blanc, R. Germann, and H. Rothuizen, Semicond. Sci. Technol. 7, pp. B462-B464 (1992).

[6] P. H. Beton, M. W. Dellow, P. C. Main, T. J. Foster, L. Eaves, A. F. Jezierski, M. Henini, S. P. Beaumont, and C. D. W. Wilkinson, Appl. Phys. Lett. 60 (20), pp. 2508-2510 (1992).

[7] C. J. Goodings, H. Mizuta, J. R. A. Cleaver, and H. Ahmed, J. Appl. Phys. 76 (2), pp. 1276-1286 (1994).

[8] M. P. Patkar, T. P. Chin, J. M. Woodall, M. S. Lundstrom, and M. R. Melloch, Appl. Phy. Lett. 66 (11), pp. 1412-1414 (1995).

i-GaAs		3.5 nm
n-GaAs	5×10^{19} cm^{-3}	10 nm
n-GaAs	5×10^{18} cm^{-3}	100 nm
n-GaAs	2×10^{17} cm^{-3}	200 nm
n-GaAs	1×10^{17} cm^{-3}	50 nm
n-GaAs	5×10^{16} cm^{-3}	50 nm
n-GaAs	1×10^{16} cm^{-3}	10 nm
i-Al$_{0.3}$Ga$_{0.7}$As		4.5 nm
i-GaAs		5 nm
i-Al$_{0.3}$Ga$_{0.7}$As		4.5 nm
n-GaAs	1×10^{16} cm^{-3}	10 nm
n-GaAs	5×10^{16} cm^{-3}	50 nm
n-GaAs	1×10^{17} cm^{-3}	50 nm
n-GaAs	2×10^{17} cm^{-3}	0.6 μm
n-GaAs	$1-2\times10^{18}$ cm^{-3}	1.5 μm
semi-insulating GaAs substrate		

Growth Temperature 250 °C

Growth Temperature 600 °C

Figure 1: MBE grown structure showing gradation in doping of the access layers
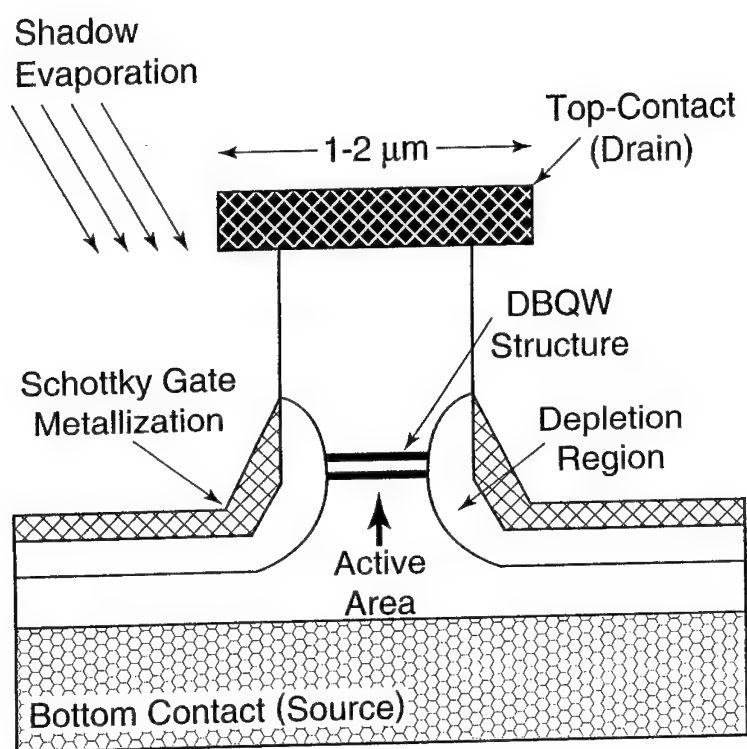
Figure 2: Illustration of the mesa structure and the deposition of the Schottky gate using the top-contact as the shadow evaporation mask.
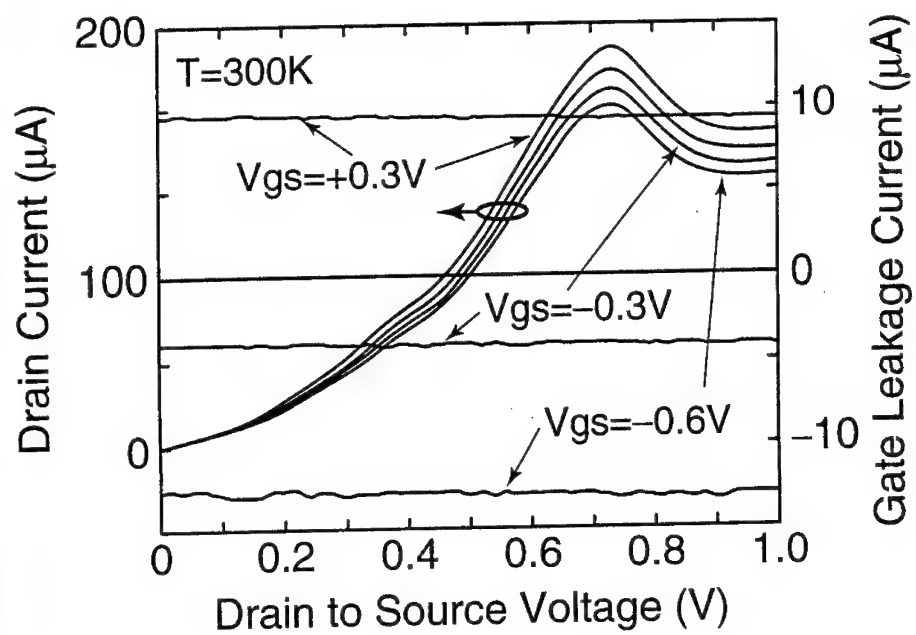
Figure 3: Drain current and gate leakage current versus drain to source voltage at various gate biases for device with a square active area of $1.2\mu m \times 1.2\mu m$.

EFFECTIVE DIFFUSION COEFFICIENT
OF MINORITY CARRIERS IN THE BASE OF
GRADED HETEROJUNCTION BIPOLAR TRANSISTORS
IN THE PRESENCE OF SELF-HEATING EFFECTS

T. Kumar, M. Cahay, and K. Roenker
Department of Electrical Engineering
University of Cincinnati, Cincinnati, Ohio 45221

ABSTRACT

A model to simulate electron transport through the base region of graded Heterojunction Bipolar Transistors (HBTs) is developed which takes into account the temperature rise in the device as a result of self-heating effects. The temperature rise in the structure is shown to increase the ramp energy at the emitter-base junction for a fixed emitter-base bias. This leads to an incident electron energy flux in the base shifted towards higher energy with respect to the bottom of the conduction band in the base. Using this incident energy flux in a regional Ensemble Monte Carlo simulator, the average base transit time is calculated as a function of the emitter-base bias V_{BE} and temperature using the impulse response technique. For a typical graded $AlGaAs/GaAs$ HBT operated at large V_{BE}, the average base transit time is found to decrease as the temperature through the base region rises. This trend is equivalent to an increase with temperature of the effective diffusion coefficient of electrons in the base. This temperature dependence is opposite to the one commonly assumed in the literature, which is based on Einstein's relation and a temperature dependence of the electron mobility as measured in bulk samples with an impurity concentration equal to the base doping.

INTRODUCTION

During the last ten years, $AlGaAs/GaAs$ HBTs have received increased interest for possible use in microwave and millimeter wave monolithic integrated circuits [1, 2, 3]. The ability of these transitors to carry high current densities $(10^4 - 10^5 A/cm^2$) at high frequencies also makes them attractive for microwave power amplifiers. However, at large current densities, due to the limited thermal conductivity of the $GaAs$ substrate, self-heating effects in HBTs with multiple emitter fingers become increasingly important. There are a variety of experimental [4, 5, 6] and theoretical studies [7, 8, 9, 10] showing that self-heating effects in the device can lead to a substantial temperature rise in the device accompanied by a degradation of the device performance.

These self-heating effects seriously reduce the current and power gain of the device and impose a substantial limit on the current and voltage range of device operation. The phenomenon of current gain collapse in HBTs with multiple emitter fingers operated at high power density has been reported experimentally by several groups [4, 5, 6] and analyzed theoretically by others [7, 8, 9, 10]. The current gain collapse is characterized by a sudden drop of the collector current in the common-emitter current-voltage characteristics of the device at large value of V_{CE}. The physical origin of this phenomenon was identified to be thermally induced nonuniform current conduction among the various emitter fingers of the device. To alleviate this problem, Bayraktaroglyu et al. [11] have recently demonstrated that a thermal metal bridge can be fabricated on top of the device to shunt heat away thereby allowing a more uniform temperature for the various emitter fingers during higher power operation. In the absence of these metal bridges, self-heating effects can lead to the formation of local hot spots which can cause current collapse through one of the central fingers [6].

Thermal effects in single emitter HBTs have been modeled in the past using one-dimensional analytical treatments [6, 10] or multi-dimensional numerical schemes [9] based on coupled electrical and thermal models of the device. Under the assumption that the heat generated in the device is conducted primarily through the semi-insulating substrate, these theoretical treatments have shown that the temperature rise inside HBTs can be considered as nearly uniform within the device and can be quite substantial for devices carrying collector current densities in excess of a few times $10^4 A/cm^2$.

These models fail to discuss self-heating effects from a microscopic point of view which will be addressed in this paper. More specifically, we will focus on the model of carrier transport through the emitter and base regions of a typical graded $AlGaAs/GaAs$ HBT in the presence of self-heating effects. Rather than trying to simulate the temperature rise in the device using one of the analytical or numerical models already existing in the literature [7, 8, 9, 10], we assume that the temper-

ature of the device is known and is constant throughout the structure. As stated above, actual calculations have shown that this is indeed a good approximation for the emitter and base regions of typical graded HBTs (The temperature decreases while moving through the collector and subcollector regions upon approaching the substrate usually modeled as a heat sink at room temperature). In this paper, we use a hybrid model of carrier transport to compute the effective diffusion coefficient of electrons through the base as a function of temperature and emitter-base bias. The range of emitter-base bias considered here typically corresponds to collector current densities in excess to $10^4 A/cm^2$, the minimum required for self-heating effects to play a major role on the device performance as shown by others [7, 8, 9].

In this work, we show the inadequacy of some previously used models [7] to describe the diffusion of minority carriers through the base of HBTs in the presence of self-heating effects.

THE MODEL

Our approach to characterize electron transport through the emitter-base junction proceeds as follows. First, the program FISH1D [12] is used to predict the shape of the conduction band energy profile throughout the entire structure for a given forward emitter-base bias and reverse biased base-collector junction. This simulation is performed assuming a uniform temperature across the structure, while including the temperature dependence of all the material parameters throughout the device.

Next, we use the flux method of Das and Lundstrom [13, 14] to calculate exactly the energy spectrum of the injected electron flux into the base using a rigorous quantum-mechanical treatment of tunneling through the spike at the emitter-base junction and thermionic emission above the spike. More specifically, we calculate the energy dependence of the function $f(E)$ defined as follows

$$J_n = \int_{E_c}^{+\infty} f(E)dE \qquad (1)$$

where J_n is the net current flow from emitter to base, E_c is the energy at the bottom of the conduction band in the base (taken as the zero of energy hereafter), and E is the longitudinal energy of the electron (i.e. in the direction of current flow).

The resulting flux f(E) is then used as an initial electron energy distribution to simulate electron transport through the base using a regional Ensemble Monte-Carlo simulator. Our Ensemble Monte-Carlo simulator includes three important features in the electron transport across the base. First, an exact quantum-mechanical treatment of electron tunneling through and thermionic emission above the spike at the emitter-base junction is used to calculate the energy distribution

of the electron flux injected into the base. Next, this electron flux is used as an initial energy distribution in a regional Ensemble Monte-Carlo simulation of electron transport through the base which includes the possibility for carriers to tunnel back into the emitter. Finally, a realistic electric field profile inside the base region is used, including the decelerating electric field due to the conduction band notch on the base side of the emitter-base junction, the accelerating field (towards the base) for electrons in the graded portion of the emitter, and the accelerating field close to the collector side of the base due to the reverse base-collector bias. In this work, electrons moving from the base towards the emitter are allowed to reenter the emitter only if their energy is above the conduction band spike. Details of the Ensemble Monte Carlo code have been reported elsewhere [15, 16].

To compute the effective diffusion coefficient D_{eff} of electrons through the base, we use the results of Dodd and Lundstrom [17] and Ritter et al. [18] who have shown that for the base width considered in this paper, base transport appears diffusive and that the average base transit time can be approximated as follows

$$\tau_B = W_B{}^2/2D_{eff} \tag{2}$$

where W_B is the base width.

The average base transit time is then computed using the impulse response technique [16, 17]. This technique consists in monitoring the current that exits the base region after injecting a delta function (in time) of electrons at t=0 at the emitter edge of the base. The current response h(t) is then computed by recording the number of electrons that exit the base region during a sampling time, ΔT (typically equal to a few tens of femtoseconds). The average base transit time is then calculated from the first moment of the current response, i.e,

$$\tau_B = \int_0^{+\infty} h(t)t\,dt / \int_0^{+\infty} h(t)\,dt. \tag{3}$$

RESULTS

The structure analyzed here consists of a graded $Al_{0.3}Ga_{0.7}As/GaAs$ HBT with the epitaxial layer structure summarized in Table I. The simulation procedure outlined in the previous section was carried for various emitter-base biases V_{BE} (1.4, 1.43, and 1.46 V), while keeping the collector-emitter bias V_{CE} to 4.5 V. Figure 1 shows the conduction band energy profile across the graded portion of the emitter-base junction and across the base region at a fixed value of V_{BE} while increasing the temperature in the device. A similar trend in the conduction band energy profile versus temperature was also observed for all the other values of V_{BE} considered here.

Figure 1 shows the conduction band energy profile across the emitter-base junction at a fixed value of V_{BE} while increasing the temperature in the device.

The conduction band diagram was determined using the program FISH1D [12]. Figure 2 indicates that a temperature rise in the device leads to an increase of the conduction band discontinuity at the emitter-base junction. The minimum of the conduction band rises by approximately 50 meV as the temperature of the device increases from 300K to 350 K. This results from a decrease in the built-in potential across the emitter base-junction with rising temperature when the junction is operated at a fixed V_{BE}.

Figure 2 indicates that the electron energy flux injected into the base region will be shifted towards higher energy with respect to the minimum of the conduction band in the base. This is illustrated in Fig. 2 where we plot the electron energy flux defined in Eq.(1) as a function of temperature for the case where $V_{BE} = 1.46V$. Figure 3 illustrates the electric field profile across the graded portion of the emitter and the base region for temperature ranging from 300 to 350 K. This figure clearly shows that electrons entering the graded portion of the emitter from the base are quickly slowed down and pushed back towards the base. Furthermore, the intensity of the electric field in the graded region is larger as the junction temperature rises.

Ensemble Monte-Carlo simulations combined with the impulse response technique were then carried to determine the average base transit time and effective diffusion coefficient through the base as a function of V_{BE} and temperature. The results are depicted in Fig.4. Also shown for comparison is the temperature dependence of the diffusion coefficient for electrons through the base region as modeled by Liou et al. [7] in their modeling of self-heating effects in graded HBTs. Liou et al. assumed that the diffusion coefficient for minority carriers can be modeled using Einstein's relation while using the temperature dependence of the electron mobility as reported in the literature for bulk samples with impurity concentration equal to the base doping concentration. More explicitely, Liou and coworkers use the following expression for the effective diffusion coefficient of electrons through the base region [7, 19]

$$D_{eff} = \frac{kT}{q}(7200/(1 + 5.5X10^{-17}N_A)^{0.233})(\frac{300}{T})^{2.3} \qquad (4)$$

where q is the magnitude of the charge of the electron, k is Boltzmann's constant, T the temperature, and N_A is the doping concentration in the base region.

Figure 4 clearly indicates the shortcomings of an equation such as Eq.(4). This equation fails to predict the bias dependence of the effective diffusion of minority carriers through the base region. This bias dependence should be expected since the electron flux injected across the emitter-base junction is obviously a function of V_{BE}. Furthermore, Eq. (4) predicts a decrease of the diffusion coefficient of carriers as the temperature through the device increases, whereas our simulations indicate that the effective diffusion coefficient through the base region is increasing

slightly with temperature for all V_{BE}. This can be understood as follows. As illustrated in Figures 1 and 2, the effect of temperature rise on the emitter-base conduction band energy profile is to increase the probability for electrons through the base to be injected at higher energy, enhancing the probability for ballistic transport of electrons through the base region. However, a trade-off resulting from the temperature rise in the base is that the various scattering rates in the base region are also enhanced. Our simulations show that for large emitter-base biases, the benefit of electron injection in the base at a higher energy prevails over the detrimental effect of the higher scattering rates in the base as the temperature through the device rises.

CONCLUSIONS

In this paper, we have shown that the effective diffusion coefficient through the base of graded AlGaAs/GaAs HBTs is quite different from the one predicted using Einstein's relation and a temperature dependence of the electron mobility as measured in bulk samples with an impurity concentration equal to the base doping [7]. For a typical graded $AlGaAs/GaAs$ HBT operated at large V_{BE}, the effective diffusion coefficient is found to increase slightly as the temperature through the base region rises.

ACKNOWLEDGEMENT

REFERENCES

1. M. E. Kim, B. Bayraktaroglu, and A. Gupta, "HBT Devices and Applications", Chapter 5 in **HEMTs and HBTs: Devices, Circuits, and Applications**, edited by F. Ali and A. Gupta, Artech House, Boston (1991).

2. P. Asbeck, M. F. Chang, J. A. Higgins, N. H. Sheng, G. J. Sullivan, and K. C. Wang, IEEE Transactions on Electron Devices, **ED-36**, 2032 (1989).

3. M. B. Das, IEEE Transactions on Electron Devices, **ED-35**, 604 (1988).

4. D. E. Dawson, A. K. Gupta, and M. L. Salib, IEEE Transactions on Electron Devices, Vol. 39, 2235 (1992).

5. J. R. Waldrop, K. C. Wang, and P. M. Asbeck, IEEE Transactions on Electron Devices, Vol. 39, 1248 (1992).

6. W. Liu, S. Nelson, D. Hill, and A. Khatibzadeh, IEEE Transactions of Electron Devices, Vol. 40, 1917 (1993).

7. J. J. Liou, L. L. Liou, C. I. Huang, and B. Bayraktaroglu, IEEE Transactions on Electron Devices, Vol. 40(9), 1570 (1993).

8. L. L. Liou, C. I. Huang, and J. Ebel, Solid State Electronics, Vol.35(4), 579 (1992).

9. L. L. Liou, J. L. Ebel, C. I. Huang, IEEE Transactions on Electron Devices, Vol. 40(1), 35 (1993).

10. A. Samelis and D. Pavlidis, "Modeling HBT self-heating", Applied Microwave & Wireless, p. 56 (1995).

11. B. Bayraktaroglu, J. Barrette, L. Kehias, C. I. Huang, R. Fitch, R. Neidhrad, and R. Sherer, IEEE Electron Device Letters, Vol.14(10), 493 (1993).

12. FISH1D is a software package released by Purdue University for the analysis of carrier transport in compound semiconductors.

13. A. Das and M. S. Lundstrom, IEEE Electron Device Letters, 12(6), 335 (1991).

14. A. Das and M.S. Lundstrom, Journal of Applied Physics, 66(5), 2168 (1989).

15. T. Kumar, M. Cahay, S. Shi, K. Roenker, and W. E. Stanchina, Journal of Applied Physics, Vol.77(11), 5786(1995).

16. T. Kumar, M. Cahay, S. Shi, K. Roenker, to appear in Journal of Applied Physics, December 1995.

17. P. Dodd and M. S. Lundstrom, Appl. Phys. Lett., 61(4), 465 (1992).

18. D. Ritter, R.A. Hamm, A. Feygenson, M.B Panish and S. Chandrashekhar Appl. Phys. Lett., 59(26), 3431(1991). Journal of Applied Physics, 68(2), 621 (1990).

19. D. A. Sunderland and P. L. Dapkus, IEEE Transactions on Electron Devices, Vol. ED-34, 367 (1987).

Table I: Layer parameters of the graded $Al_{0.3}Ga_{0.7}As$ HBT structure analyzed in the text.

Layer	Material	Thickness ($\mathring{A}$)	Doping (cm^{-3})
Emitter	$n - Al_{0.3}Ga_{0.7}As$	1700	$5 X 10^{17}$
Grading Layer	$n - Al_xGa_{1-x}As(x = 0.3 \text{ to } 0.0)$	300	$5 X 10^{17}$
Base	$p - GaAs$	1000	$1 X 10^{19}$
Collector	$n - GaAs$	2700	$5 X 10^{16}$
Sub-collector	$n^+ - GaAs$	1000	$5 X 10^{18}$
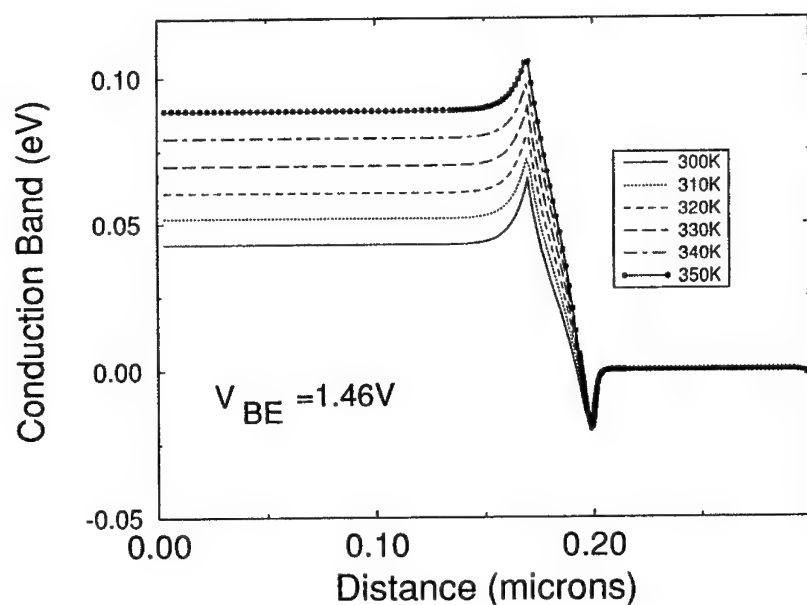
Figure 1: Temperature dependence of conduction band energy profile across the graded portion of the emitter and across the base region of the $AlGaAs/GaAs$ HBT described in Table I. The voltage across the emitter-base (V_{BE}) and emitter-collector (V_{CE}) regions are set equal to 1.46 V and 4.5 V, respectively.
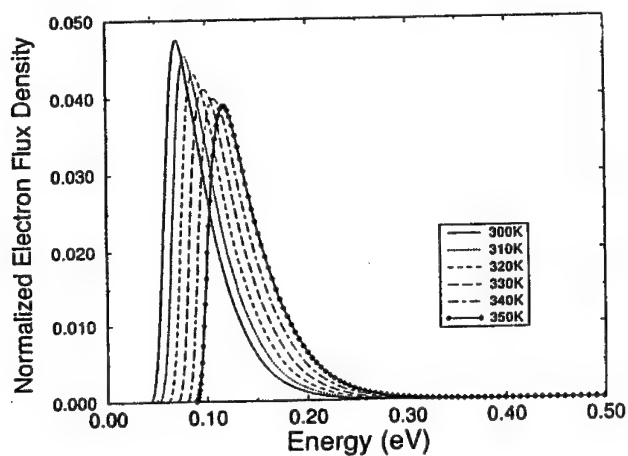
Figure 2: Temperature dependence of electron flux injected from emitter into the base region of the graded HBT described in Table I. Energy is measured with respect to the minimum of the conduction band in the base region. The emitter-base voltage is equal to 1.46 V.
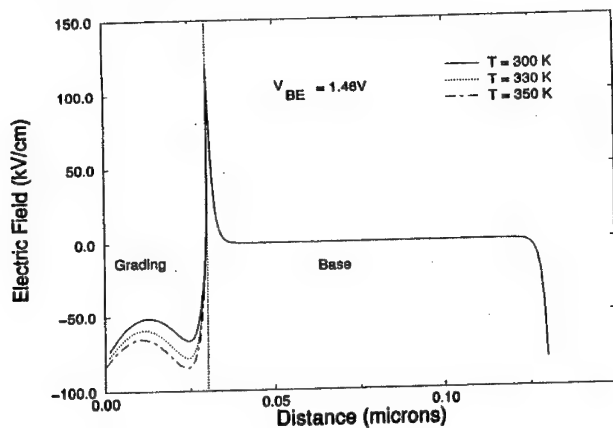
Figure 3: Temperature dependence of electric field profile through the graded portion of the emitter and through the base region of the HBT described in Table I. The emitter-base voltage V_{BE} is equal to 1.46 V. V_{CE} is equal to 4.5 V.

Figure 4: Temperature dependence of effective diffusion coefficient of electrons through the base region of the graded HBT described in Table I, for various values of the emitter-base bias. Also shown for comparison (filled circles) is the effective diffusion coefficient used in the analytical model of self-heating effects in [7].

THEORETICAL STUDY OF GATE
CURRENT DEPENDENCE ON GATE VOLTAGE IN HIGFET

S.V.Maheshwarla and R. Venkatasubramanian
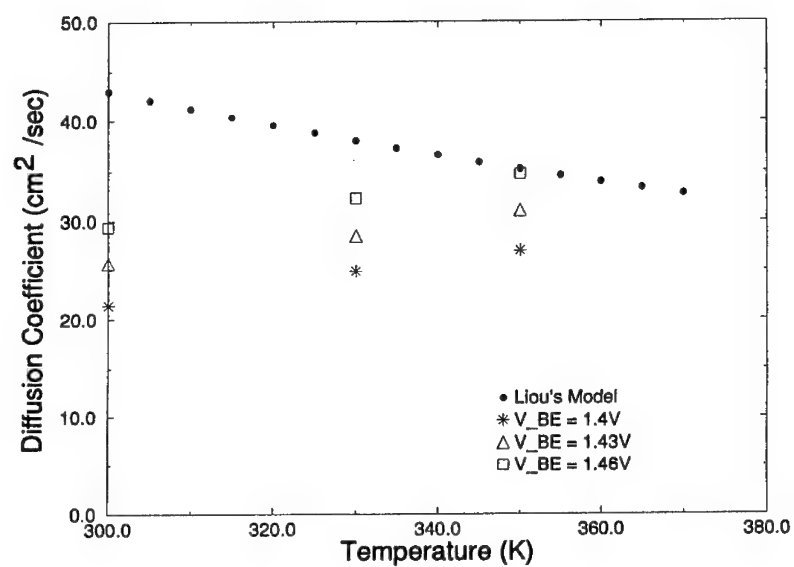Department of Electrical and Computer Engineering
University of Nevada, Las Vegas, Las Vegas, NV 89154

ABSTRACT

The gate current (I_g) dependence on gate voltage (V_g) is studied, with tunneling through a hetero-barrier theoretically assumed as the dominant mechanism in a $Ga_{0.47}In_{0.53}As$ / $Al_{0.47}In_{0.53}As$ / WSi heterostructure insulated gate field effect transistor (HIGFET). Two components of tunneling currents, one from the decay of the quasi-bound resonant states in the accumulation well and the other from the tunneling electrons with kinetic energy above the bulk energy level, were considered. Moreover, the possibility of the electrons being hot is addressed. The tunneling current is obtained as a function of V_g for two device structures, and are compared with the experimental results. The calculated currents are within a factor of 2 of the experimental results for most voltage range of study with electron temperature is equal to $450^\circ K$. The reason for the larger discrepancies between the experimental values and the theoretical values reported in earlier literatures is attributed mainly the exclusion of the hot electron mechanism and neglecting of the contribution to current from the decay of the resonant states in the accumulation well.

1 Introduction

Lattice matched hetero-structures involving $AlInAs$ and $GaInAs$ have found use in integrated circuit (IC) applications through heterostructure insulated gate field effect transistors (HIGFETs) due to their excellent properties [1-4]. Since the layers are usually undoped in HIGFETs, the threshold voltages are just dependent on the Schottky barrier height,(Φ_s) and the conduction band discontinuity, (ΔE_c) between the $AlInAs$ and $GaInAs$ which results in uniform threshold voltage values; a highly desirable device property in IC applications.

The gate current, I_g, in $GaAs$ MISFETs has been shown to control the negative differential resistance in the drain current, (I_D), when the gate is moderately forward biased [8]. Thus, the gate current has become one of the important parameters characterizing the quality of heterostructure field effect transistors. The negative differential resistance observed in $GaAs/AlGaAs$ hetero- field effect transistor has been demonstrated to be due to the dramatic change of the channel electric field with an increase of the field at the source end and to the saturation of the density of the 2D electron gas in the channel [9,10] and possibility of hot electrons at the drain end [11].

The I_g versus V_g characteristics of heterostructure devices has been modeled primarily based on thermionic emission [7] and quantum tunneling mechanisms [12-15]. These models have been shown to be good for certain heterostructure devices. The tunneling current model employed in the past has used the WKB approximation in the derivation of transmission coefficient as a function of incident energy of the electron [12-15]. As the WKB approximation has limitations [16], this manuscript avoids it and derives the transmission coefficient as a function of energy analytically using Airy functions.

This article is organized as follows. The procedure used to obtain the accumulation band bending at the interface between semiconductor and insulator as a function of V_g is discussed in section 2.1. The procedure for obtaining transmission coefficient and resonant levels of electrons in the accumulation well as a function of the incident energy of the electron are presented in sections 2.2 and 2.3, respectively. A procedure to compute tunneling current components due to the carriers in the accumulation well and above the bulk energy is discussed in section 2.4. The results for the two experimentally studied structures are obtained and discussed in section 3. Conclusions are presented in section 4.

2 Theoretical Calculation of I_g versus $\mathcal{V}_g$

2.1 Surface Band Bending

Consider the heterostructure shown in Fig. 1. Let the conduction band discontinuity and the Schottky barrier height be ΔE_c and $q\Phi_s$, respectively. Let us assume that the semiconductor is doped n-type. Under forward bias conditions, an electron accumulation layer forms in the semiconductor at the semiconductor-insulator interface as shown in Fig. 1. The surface band bending, $q\Psi_s$ at the semiconductor-insulator interface is related to the gate voltage, $\mathcal{V}_g$ as [17]:

$$qV_g = q\Psi_s + qW\mathcal{E}_s\frac{\epsilon_s}{\epsilon_i} - \Delta E_c + q\Phi_s + E_c - E_F \tag{1}$$

where W is the width of the insulator, $\mathcal{E}_s$ is the semiconductor electric field at the semiconductor-insulator interface, and ϵ_s and ϵ_i are the permittivities of the semiconductor and the insulator, respectively.

The electric field $\mathcal{E}_s$ in semiconductor is given by Poisson's equation as:

$$\frac{d\mathcal{E}_s}{dx} = \frac{\rho(x)}{\epsilon_s} \tag{2}$$

where $\rho(x)$ is the charge density which is given by [17]:

$$\rho(x) = -qN_{c,3D}\mathcal{F}_{\frac{1}{2}}\left(\frac{E_F - E_c(x)}{kT}\right) \tag{3}$$

with

$$N_{C,3D} = \left(\frac{2\pi mkT}{h^2}\right)^3 \tag{4}$$

k is the Boltzmann constant, T is the temperature in $^\circ K$ and $\mathcal{F}_{\frac{1}{2}}$ is the Fermi-Dirac integral of order $\frac{1}{2}$. It is noted that Equation 3 assumes that the carriers are 3-dimensional and that in reality, 2-dimensional carrier behavior should be considered for electrons within the accumulation well. The electric fields at the interface satisfy:

$$\mathcal{E}_s\epsilon_s = \mathcal{E}_i\epsilon_i \tag{5}$$

Solving Eqs.(1-5) self-consistently yields the band bending and the electric field in the semiconductor accumulation layer.

2.2 Derivation of Transmission Coefficient

The WKB approximation used in theoretical analysis of gate current reported in the earlier literature [12-13] is based upon the assumption that the potential

varies very slowly over lengths compared to the wavelength of the electron. This assumption is not valid for very high gate biases, when the potential drop on the insulator can be very sharp, and the accumulation well is sharp and narrow.

Thus, we avoid using the WKB approximation due to its limitations and obtain the transmission coefficient as a function of E_x from first principles as follows. In the case of device structures considered in the present study, the potential profile of the accumulation layer was computed using Eqs. (1-5). The accumulation layer is approximated by a triangle as shown in Fig. 1 for the derivation of transmission coefficient. It is noted that the electrons were injected from the bulk E_c of the semiconductor.

The following is the derivation of the transmission coefficient for the device structure whose E_c profile is shown in Fig. 1. The solutions to Schrodinger's equation can be written in terms of the Airy functions, $Ai[f(x)]$ and $Bi[f(x)]$ as:

$$\Psi_1(x) = e^{ik_1 x} + Ae^{-ik_1 x} \cdots\cdots\cdots\cdots\cdots\cdots\cdots\cdots\cdots\cdots\cdots\cdots\cdots x < 0, \tag{6}$$

$$\Psi_2(x) = BAi\left[\rho_1(V_{11} - s_1 x - E)\right] + CBi\left[\rho_1(V_{11} - s_1 x - E)\right] \cdots\cdots\cdots 0 < x < d_1, \tag{7}$$

$$\Psi_3(x) = DAi\left[\rho_2(V_{21} - s_2 x - E)\right] EBi\left[\rho_2(V_{21} - s_2 x - E)\right] \cdots\cdots\cdots d_1 < x < d_2, \tag{8}$$

$$\Psi_4(x) = Fe^{ik_2 x} \cdots\cdots\cdots\cdots\cdots\cdots\cdots\cdots\cdots\cdots\cdots\cdots\cdots\cdots\cdots\cdots x > d_2, \tag{9}$$

where k_1 and k_2 are the propagation vectors in the bulk semiconductor and the metal and are given by:

$$k_1 = \sqrt{\frac{2m_s(E - V_{11})}{\hbar^2}} \tag{10}$$

and

$$k_2 = \sqrt{\frac{2m_o E}{\hbar^2}} \tag{11}$$

respectively, where m_o is the rest mass of the electron. The quantity ρ_1 in Eq. (7) is given by:

$$\rho_1 = \left(\frac{2m_s}{\hbar^2 s_1^2}\right)^{\frac{1}{3}} \tag{12}$$

where s_1 is the slope of the triangulated accumulation layer. ρ_2 in Eq. (8) is given by:

$$\rho_2 = \left(\frac{2m_i}{\hbar^2 s_2^2}\right)^{\frac{1}{3}} \tag{13}$$

and s_2 is the electric field in the insulator, E_s. m_i is the effective mass of the electron in the insulator. Using the typical boundary conditions, (i.e., continuity

of the wave functions and their derivatives divided by the spatially dependent effective mass of electron across the boundary), we obtain at the boundary between the bulk semiconductor and the accumulated semiconductor, $x = 0$,

$$1 + A = BAi[\rho_1(V_{11} - E)] + CBi[\rho_1(V_{11} - E)] \tag{14}$$

$$\frac{ik_1}{m_s}(1 - A) = -\frac{\rho_1 s_1}{m_s}\left(BAi'[\rho_1(V_{11} - E)] + CBi'[\rho_1(V_{11} - E)]\right), \tag{15}$$

where m_s is the effective mass of the electron in the semiconductor. At the boundary between semiconductor and the insulator, $x = d_1$,

$$BAi[\rho_1(V_{12} - E)] + CBi[\rho_1(V_{12} - E)] = DAi[\rho_2(V_{21} - E)] + EBi[\rho_2(V_{21} - E)] \tag{16}$$

$$\frac{-\rho_1 s_1}{m_s}\left(BAi'[\rho_1(V_{12} - E)] + CBi'[\rho_1(V_{12} - E)]\right) = -\frac{\rho_2 s_2}{m_i}\left(DAi'[\rho_2(V_{21} - E)] + EBi'[\rho_2(V_{21} - E)]\right) \tag{17}$$

where m_i is the effective mass of the electron in the barrier region. Similarly, at the boundary between the insulator and the right contact, (i.e.), $x = d_2$, we have:

$$Fe^{ik_2 d_2} = DAi[\rho_2(V_{22} - E)] + EBi[\rho_2(V_{22} - E)] \tag{18}$$

$$\frac{ik_2}{m_o}Fe^{ik_2 d_2} = \frac{-\rho_2 s_2}{m_i}\left(DAi'[\rho_2(v_{22} - E)] + EBi'\rho_2(V_{22} - E)\right) \tag{19}$$

where m_o is the rest mass of the electron. Solving Eqs. (14-19) simultaneously, we obtain:

$$F = \frac{2\Delta_2 \Delta_3}{e^{ik_2 d_2}}\frac{1}{\Delta_1} \tag{20}$$

where

$$\Delta_2 = X\left(Ai[\rho_1(V_{12} - E)]Bi'[\rho_1(V_{12} - E)] - Ai'[\rho_2(V_{12} - E)]Bi[\rho_1(V_{12} - E)]\right) \tag{21}$$

with

$$X = \frac{\rho_1 s_1 m_i}{\rho_2 s_2 m_s} \tag{22}$$

Δ_3 and Δ_1 in Eq. (20) are given by:

$$\Delta_3 = \left(Ai[\rho_2(V_{22} - E)]Bi'[\rho_2(V_{22} - E)] - Ai'[\rho_2(V_{22} - E)]Bi[\rho_2(V_{22} - E)]\right) \tag{23}$$

and

$$\Delta_1 = P\left(Ai\left[\rho_1(V_{11} - E)\right] - \frac{\rho_1 s_1 m_s}{ik_1 m_i} Ai'\left[\rho_1(V_{11} - E)\right]\right)$$
$$- Q\left(Bi\left[\rho_1(V_{11} - E)\right] - \frac{\rho_1 s_1 m_s}{ik_1 m_i} Bi'\left[\rho_1(V_{11} - E)\right]\right) \tag{24}$$

respectively. The terms P, and Q in Eq. (24) are given by:

$$P = -p_{11}p_{12} + p_{13}p_{14} \tag{25}$$

and

$$Q = -p_{11}q_{12} + p_{13}q_{14} \tag{26}$$

with p_{11}, p_{12}, p_{13}, p_{14}, q_{12} and q_{14} given by:

$$p_{11} = Bi'\left[\rho_2(V_{22} - E)\right] + \frac{ik_2 m_i}{\rho_2 s_2 m_o} Bi\left[\rho_2(V_{22} - E)\right] \tag{27}$$

$$p_{12} = Ai\left[\rho_2(V_{21} - E)\right] Bi'\left[\rho_2(V_{12} - E)\right] X - Bi\left[\rho_2(V_{12} - E)\right] Ai'\left[\rho_2(V_{21} - E)\right] \tag{28}$$

$$p_{13} = Ai'\left[\rho_2(V_{22} - E)\right] + \frac{ik_2 m_i}{\rho_2 s_2 m_o} Ai\left[\rho_2(V_{22} - E)\right] \tag{29}$$

$$p_{14} = Bi\left[\rho_2(V_{21} - E)\right] Bi'\left[\rho_2(V_{12} - E)\right] X - Bi\left[\rho_2(V_{12} - E)\right] Bi'\left[\rho_2(V_{21} - E)\right] \tag{30}$$

$$q_{12} = Ai\left[\rho_2(V_{21} - E)\right] Ai'\left[\rho_2(V_{12} - E)\right] X - Ai\left[\rho_2(V_{12} - E)\right] Ai'\left[\rho_2(V_{21} - E)\right] \tag{31}$$

and

$$q_{14} = Bi\left[\rho_2(V_{21} - E)\right] Ai'\left[\rho_2(V_{12} - E)\right] X - Ai\left[\rho_2(V_{12} - E)\right] Bi'\left[\rho_2(V_{21} - E)\right] \tag{32}$$

respectively. The transmission coefficient, $T(E_x)$ is related to the amplitude transmission coefficient, $F(E_x)$, as:

$$T(E_x) = \frac{k_2 m_s}{k_1 m_o}|F(E_x)|^2 \tag{33}$$

2.3 Derivation of Resonant Levels in the Accumulation Potential and their Lifetimes

Approach similar to that employed in section 2.2 is used with a modified wave function for region $x < 0$ given by:

$$\Psi_{1,2D}(x) = Ae^{\alpha x} + Be^{-\alpha x} \tag{34}$$

To evaluate the relative strengths of the resonant states for various energies the following strength function, $S(E)$, was evaluated:

$$S(E) = \int_{x=0}^{x=d_1} \Psi_{1,2D}^*(x)\Psi_{1,2D}(x)dx \tag{35}$$

The location and relative strength of the resonant states are obtained by analyzing $S(E)$. The escape time, $\tau_{e,i}(\mathcal{V}_g)$ is obtained as [20]:

$$\tau_{e,i}(\mathcal{V}_g) = \frac{\hbar}{\Delta E_i} \tag{36}$$

where ΔE_i is the full width at half maximum(FWHM) of the resonant state 'i' in the accumulation well.

2.4 Tunneling current

Tunneling current is assumed as the dominant conduction current mechanism for the device under forward bias. Two tunneling current components, one resulting from the carriers with kinetic energy higher than the bulk-energy, $I_{g,b}$ and the other resulting from the carriers with kinetic energy lower than the bulk-energy occupying the resonant states, $I_{g,r}$. The total current, I_g is given by:

$$I_g = I_{g,b} + I_{g,r} \tag{37}$$

The bulk current $I_{g,b}$ can be related to the transmission coefficient, $T(E_x)$, and the gate voltage, $\mathcal{V}_g$, by [1]:

$$J_{g,b}(\mathcal{V}_g) = \int_{E_{low}}^{E_{high}} q N_b(E_x) T(E_x) dE_x \tag{38}$$

with

$$N_b(E_x) = \left(\frac{4\pi m_s q k T}{h^3}\right) \ln\left(\frac{1 + exp\left(\frac{E_F - E_x}{kT}\right)}{1 + exp\left(\frac{E_F - \mathcal{V}_g - E_x}{kT}\right)}\right), \tag{39}$$

where E_x is the kinetic energy of the electron in the direction perpendicular to the semiconductor-insulator interface, h is the Planck's constant and m_s is the effective mass of electron in the semiconductor.

The current density, $J_{g,r}(\mathcal{V}_g)$ is given by [21]:

$$J_{g,r}(\mathcal{V}_g) = \sum_{i=1}^{i=n} q N_{2D,i}(\mathcal{V}_g)/\tau_{e,i}(\mathcal{V}_g) \tag{40}$$

where $N_{2D,i}(\mathcal{V}_g)$ is given by:

$$N_{2D,i}(\mathcal{V}_g) = \frac{4m\pi kT}{h^2} \ln\left(1 + exp\left(\frac{E_F - E_i}{kT}\right)\right) \tag{41}$$

where E_i are the 'i' resonant levels of the wave function in the accumulation well.

3 Results and Discussion

3.1 HIGFET

In this work we considered two cases of $In_{0.53}Ga_{0.47}As/In_{0.53}Al_{0.47}As/WSi$ HIGFETs which have been experimentally studied and reported in the literature [1,13]. The parameters describing the device structures are obtained from [1,13,19] for two cases and are listed in Table I.

Eqs.(1-5) were solved numerically to compute $E_c(x)$ and $\mathcal{E}_s$ as a function of $\mathcal{V}_g$. The $\mathcal{E}_s$ versus x and E_c versus x are shown in Figs. 2 and 3, respectively, for $\mathcal{V}_g$ is 0.5V and 1.5V Due to the failure of non-degenerate statistics in this case, a Fermi integral table was created for the energy range of -20.0 eV to 20.0 eV and employed in the numerical solution. Then $E_c(x)$ in the accumulation layer was triangulated with the $\mathcal{E}_s$ at the interface deciding the slope of the triangle for each case of solution to Schrodinger's equation. The energy depth of the accumulation well is the range of (0.2 eV to 0.3 eV) and the width is in the range of (75 Åto 200 Å). The bulk current $I_{g,b}$ was obtained by integrating between $InGaAs$ bulk E_C level to $E_C + 7ev$ using Eqs. (38,39). The $S(E)$ was obtained using Eq. (35) for various $\mathcal{V}_g$'s and analyzed for resonant states E_i and their . The function $S(E)$ versus E is shown in Fig. 4 for various $\mathcal{V}_g$'s. It is noted that the resonant energy levels move up in energy with $\mathcal{V}_g$. The FWHM's obtained for various $\mathcal{V}_g$ are in the range 10^{-4} to 10^{-8} eV. Eqs. (36,40,41) were employed to compute the $J_{g,r}$ as a function of $\mathcal{V}_g$ using the FWHM's and E_i. Since the electrons are accelerated through higher electric field (10^7 V/m) within few hundred $Å$s in the accumulation layer before tunneling, the electron may not have enough time to achieve thermal equilibrium with the lattice. Therefore, it is possible that the electrons tunneling through may be somewhat hot. Thus, we have hypothesized that the electrons tunneling are somewhat hot and employed the temperature of the electron, T_e, as a model parameter for the current computation. Fig. 5 shows I_g versus $\mathcal{V}_g$ for various T_e's. The experimental data shows excellent fit to the theoretical data with $T_e = 450°K$ for most voltage range. The agreement between the results of the present theory and the experiments (case 1) is within a factor of 2 for most $\mathcal{V}_g$'s for $d = 300$ $Å$ [13]. For the case of $d = 400$ $Å$ [1], the agreement between the experimental data (case 2) of 4 A and our results (with a $T_e = 400$ K) of 3.7 A is excellent.

The transmission coefficient derived in this work is general and avoids the WKB approximation. It can be applied to device structures for which the conduction or valence band discontinuity can be linearized, that is the band bending at the interfaces can be approximated by a linear variation. There are many heterostructure devices such as heterostructure bipolar transistor (HBT) and high electron mobility transistor (HEMT) for which the approach discussed in section

2.1 and 2.2 or a modified version of it can be applied. The approach adopted for the computation of tunneling current contribution from the resonant states in the accumulation well may be applicable for other compound semiconductor heterostructure systems as well. It is important to note that carriers in the accumulation well are treated as 3-D and that 2-D nature of the electron is ignored. The 3-D assumption results in an overestimation of carrier concentration very close to the interface by a factor of 4 to 5 and within a factor of 1 to 2 in about 80-90 % of the well. This overestimation results in about 60-80 % deeper well and attendant errors in rest of the results. The error estimation results are in agreement with the work of Zimmermann et al [22] and Ref.[21]. Even though, the possibility of hot electrons in the accumulation well is hypothesized and the hot electron temperature is employed as a model parameter, it needs to be thoroughly studied theoretically and experimentally. It is noted that the escape of electrons from the resonant states requires continuous replenishing of these states by bulk electrons through collision processes. It is believed that the number of collisions required for this process is much smaller than that required for achieving thermal equilibrium. Thus, it is justified that in spite of collisions, the electron can be some what hot. It may be important for many other heterostructure systems. Since there is a flow of current through the insulator, the presence of charge in the insulator should be taken in to account for the solution of Poisson's equation and in the current computation. It is noted that this particular issue is not addressed in this article.

4   Conclusion

The I_g versus V_g is studied theoretically assuming that tunneling through a heterobarrier is the dominant mechanism in heterostructure field effect transistors. The transmission coefficient is derived as a function of the kinetic energy of the electrons using Airy functions solution to Schrodinger's equation. The agreement obtained between the experiment and theory is excellent, and the currents are within a factor of 2 for most voltage ranges of the two sets of experimental results obtained from the literature. The reason for the discrepancy between the experiments and the theory reported in [13] is mainly due to the exclusion of the current from the tunneling of electrons from the resonant state and the possibility of hot electrons.

Acknowledgment:

References

[1] M.D. Feuer, D.M. Tennant, J.M. Kuo, S.C. Shunk, B. Tell and T.Y. Chang, *IEEE Electron Device Lett.*, vol. 10, p.70, 1989.

[2] D.M. Tennant, S.C. Shunk, M.D. Feuer, J.M. Kuo, R.E. Behringer, T.Y. Chang and R.W. Epworth, *J. Vac. Sci. Tech.*, vol. B(7), p.1836, 1989.

[3] M.D. Feuer, Y. He, S.C. Shunk, J.-H. Huang, T.A. Vang, K.F. Brown-Goebeler and T.Y. Chang, *IEEE Electron Device Lett.*, vol. 12, p.98, 1991.

[4] M. Kamada, and H. Ishikawa, *Electron Lett.* vol. 28, p.1494, 1992.

[5] K. Arai, T. Mizutani and F. Yanagawa, *Japan. J. Appl. Phys.*, vol 24, p.623, 1985.

[6] T. Mizutani, S. Fujita and F. Yanagawa, *Electron, Lett.*, vol. 21, p.1116, 1985.

[7] S. Fujita and T. Mizutani, *IEEE Trans. Electron Devices*, vol. ED-34, p.1889, 1987.

[8] Danneville, P. Godts, J. Zimmermann and E. Constant, "Modeling of negative differential resistance (NDR) in HIGFET and SISFET GaAs/AlGaAs structures and possible application in microwave integrated circuits", *Int. Symp. on GaAs and Related Compounds*, (Jersey, UK, 1990)(in IOP Conf. Ser., 112, K.E. Singer Ed. Bristol, UK, Inst of Physics, 1990), p.438.

[9] Junho Baek and Michael Shur, *IEEE Trans. Electron Devices*, vol ED-37, p.1917, 1990.

[10] P. P. Ruden, M. Shur, A.I. Akinwande and P.Jenkins, *IEEE Trans. Electron Devices*, vol ED-36, p.453, 1989.

[11] Michael S. Shur, D.K. Arch, R.R. Daniels and Jonathan K. Abrokwah, *IEEE Elect. Device Letts.*, vol EDL-7, p.78, 1986.

[12] I. Hase, H. Kawai, K. Kaneko and N. Watanabe, *J. Appl. Phys.*, vol. 59, p.3792, 1986.

[13] M. Kamada, H. Ishikawa and M. Feng, *IEEE Trans. Electron Devices*, vol ED-40, p.1358, 1993.

[14] Hussein Fawaz, Joel Gest and Jacques Zimmermann, *IEEE Trans. Electron Devices*, vol ED-40, p.846, 1993.

[15] E.B. Abbott, M. Lee, R.S. Mand, M. Sweeny and J.M. Xu, *IEEE Trans. Electron Devices*, vol ED-40, p. 1022, 1993.

[16] A.T. Fromhold, *Quantum Mechanics for Applied Physics and Engineering*, New York, Academic Press, 1981.

[17] R.F. Pierret and G.W. Neudeck, *Modular Series on Solid State Devices*, vol.IV, Massachusetts, Addison Wesley, 1987.

[18] S.M. Sze, *Physics of Semiconductor Devices*, New York, Wiley-Interscience, 1981.

[19] M. Kamada, *Private Communication*.

[20] Claude Cohen-Tannoudji, Bernard Diu, Franck Laloe, *Quantum Mechanics, volume II*, John Wiley & Sons, 1977.

[21] L. Burgnies, O. Vanbesien, V. Sadaune and D. Lippens, J.Nagle and B. Vinter *to be published*.

[22] B. Zimmermann, E. Marclay, M. LLegems and P. Gueret, *J. Appl. Phys.*, vol. 64, p.3581, 1988.

TABLE I Parameters of the *InGaAs/InAlAs* heterostructure system obtained from [13,19] and used for various calculations.

Parameter name	Parameter symbol	Value
Conduction band discontinuity	ΔE_c	0.52 eV
Schottky barrier height	$q\Phi_s$	0.57 eV
Thickness of the insulator (case 1)	d	300 $\mathring{A}$
Thickness of the insulator (case 2)	d	400 $\mathring{A}$
Energy gap	E_g	0.75 eV
Effective mass of electron in *InGaAs*	m_s	0.041 m_o[1]
Effective mass of electron in *InAlAs*	m_i	0.084 m_o[1]
Donor concentration in *InGaAs* (case 1)	N_D	4.3 x $10^{15}/cm^3$
Donor concentration in *InGaAs* (case 2)	N_D	1.0 x $10^{15}/cm^3$

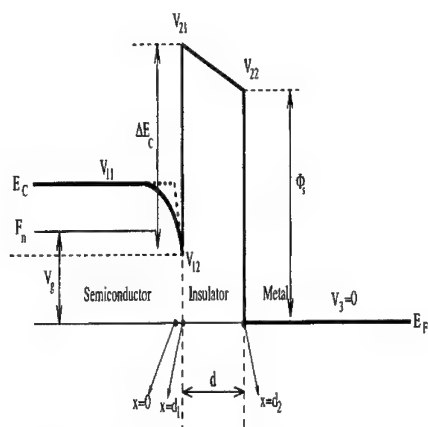[1] m_o is the rest mass of the electron.

Figure 1. A schematic picture of the E_c profile of semiconductor-insulator-metal HIGFET with band bending at the accumulated interface. Note the triangulated accumulation well.
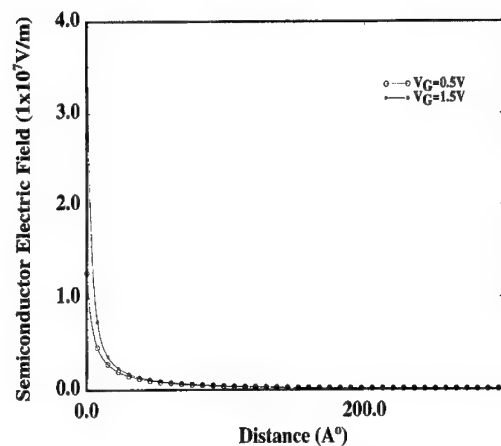

Figure 2. The $\mathcal{E}_s$ profile of accumulation well in $InGaAs$. The $x = 0$ corresponds to the semiconductor-insulator interface.
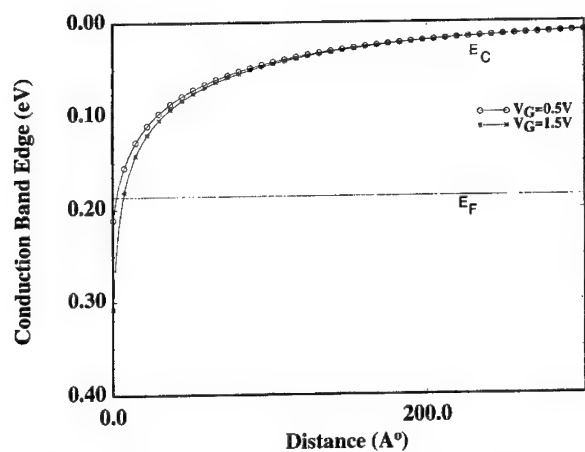
Figure 3. The E_c profile of accumulation well in the $InGaAs$. The $x = 0$ corresponds to the semiconductor-insulator interface.
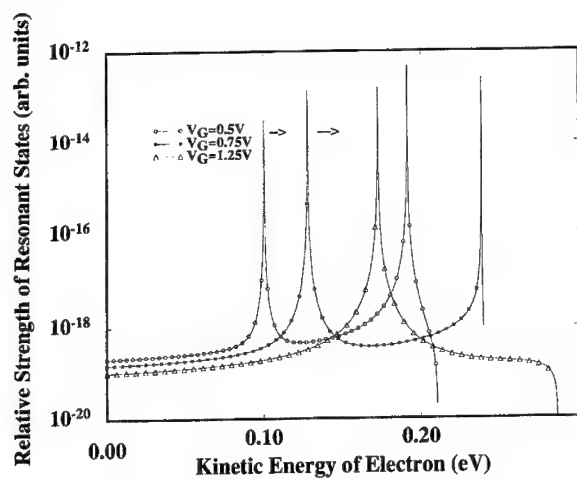

Figure 4. The relative strength of the resonant states, in the accumulation well, $S(E)$, showing the presence and movement of resonant states with $\mathcal{V}_g$.
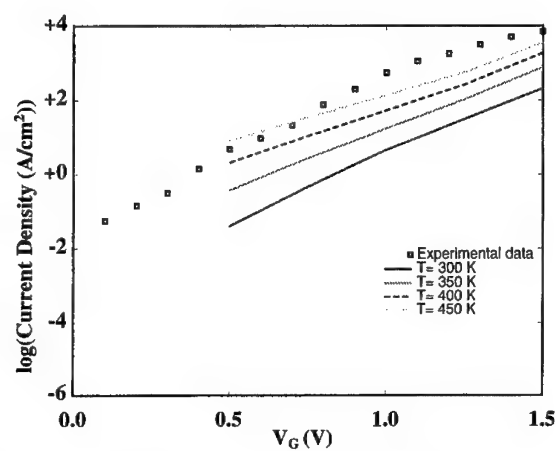
Figure 5. Plots of I_g versus V_g for $Ga_{0.47}In_{0.53}As/\ Al_{0.47}In_{0.53}As/\ WSi$ HIGFET at room temperature with d $= 300\mathring{A}$ for various T_e's along with experimental data from [13].

High-T_c Superconductivity

Physics of High-Temperature Superconductors

J. C. Phillips

AT&T Bell Laboratories

600 Mountain Avenue

Murray Hill, NJ 07974

Abstract

A short summary of some of the author's views on this subject is given.

There are many puzzling aspects of this subject which have been discussed previously in this interesting symposium. It seems that many of these aspects have been discussed in my book and various papers on this subject, but these discussions are unknown to many-body theorists who are generally not interested in materials science. This is unfortunate, because there can be little doubt that the remarkable superconductive properties of multilayered cuprates arise directly from unique materials characteristics. It was the realization of the uniqueness of these materials that led Bednorz and Muller to study them in the first place, and now, more than 40,000 papers later, little doubt about this point should remain, even in the minds of many-body theorists.

Dow and Blackstead, in their contributions to this symposium, have emphasized that strong superconductive interactions do not originate in the metallic CuO_2 planes, ubiquitous though these may be, but rather at or near secondary metallic planes containing oxygen vacancies or interstitials, such as the CuO_{1-x} planes in YBCO, the BiO planes in BSCCO, and HgO_δ planes in HBCCO. Their viewpoint is in close agreement with mine, as expressed in several recent papers [1-3]. Some people wonder, however, why the CuO_2 planes are necessary if this is the case.

The general answer to this question was given by Wells long ago [4], as pointed out in my book [5]. Wells stated that the structural chemistry of cupric compounds is exceptionally complex; "in one oxidation state this element shows a greater diversity in its stereochemical behavior than any other element". This is a very economical and powerful statement, but its implications are generally lost on many-body theorists who confine their chemistry to the distinction between bosons and fermions. The reader may therefore forgive me for explaining what Wells' statement means in the present context. The complexity of cupric coordination environments (compared, for example, to Ni) means that it is possible in the cuprates to have a very high density of resonant pinning states which pin E_F and produce a very high density of states at E_F (represented by $N_r(E_F)$) in addition to the band density of state $N_b(E)$ expected in

an effective medium model which is associated primarily with the CuO_2 planes. It is $N_r(E_F)$, not $N_b(E_F)$, which explains the high values of T_c observed in these materials. Such defects are the O_δ atoms in HBCCO, or the O_x vacancies in $YBCO_{7-x}$. The pinning occurs because of the anti-Jahn-Teller effect [6].

While we are on this subject, we take the opportunity to emphasize that there is strong evidence for large $N_r(E_F)$ in angle-resolved photoemission experiments [7-9]. Curiously enough, the defect character of these bands (which are flat and lie at E_F within the resolution limits of the experiment [10]) is not mentioned in the discussions of these data. Similar data have been used to interpret the anisotropy of the small tail in $N(E)$ as reflecting d-wave anisotropy of the superconductive energy gap $\Delta(\mathbf{k})$ [11]. This is one possible interpretation of the data, but it can scarcely be taken seriously, as such d-wave symmetry always produces very small values of T_c, not very large values!

What, then, is the correct interpretation of these data? The first point to notice is the energy scale involved: the values of Δ are $\lesssim 10^{-2}$ eV, whereas the width Γ of the peak to which the foot is attached is ~ 0.1 eV. Generally speaking it is difficult to compare features of two peaks (here measured for $T \succ T_c$ and for T close to zero) on a scale $\lesssim \Gamma/5$, no matter how carefully measured, but here we are talking about variations on a scale of $\Gamma/10$! Nevertheless, we may choose to be optimistic and to suppose that, all experience to the contrary, the resolution and reproducibility do somehow exist to make such comparisons meaningful. Does this mean that the variations we somehow recognize, in spite of final-state interactions [10], must be associated with $\Delta(\mathbf{k})$? Not at all. The variations could, and probably would, be associated with effects on $N_r(E)$ associated with the kinds of defect relaxation ordering which are observed by ion channeling, but not by neutron diffraction [12]. (This means that such relaxations modify $N_r(E)$ not only at $E = E_F$, but also at other energies as well.) Between the high value of $T > T_c$ and the low $T \sim 0$ considerable defect relaxation occurs [12], and this must surely strongly affect resonant pinning states

near E_F. It would then be easy (but very näive) for an optimistic observer to assign this behavior to an anisotropy of $\Delta(\mathbf{k})$, whereas most of the observed anisotropy need not involve $\Delta(\mathbf{k})$ at all, at least directly. There is, by the way, strong evidence [9] that a small amount of Co impurity in YBCO has a huge effect on ARPE measurements of this peak, not on an energy scale of 10^{-2} eV, but on an energy scale of 0.1 eV! Such a large effect can occur in several ways (for example, by surface segregation), but whatever its explanation, it certainly cannot be explained by an effective medium model.

Another example of an experiment whose significance has been exaggerated by misinterpretation is the study of temperature dependence of microwave penetration depths. These can easily be explain by two-phase models of partly superconductive and partly normal metals [13].

REFERENCES

[1] J. C. Phillips, Phys. Rev. Lett. **72**, 3863 (1994).

[2] J. C. Phillips, Physica C **221**, 327 (1994).

[3] J. C. Phillips, Physica C **252**, 188 (1995).

[4] A. F. Wells, *Structural Inorganic Chemistry* (Oxford Univ. Press, Oxford, 1984), p. 1116.

[5] J. C. Phillips, *Physics of High-T_c Superconductivity* (Academic Press, New York, 1989), p.77.

[6] J. C. Phillips, Phys. Rev. B **47**, 11615 (1993).

[7] K. Gofron, J. C. Campuzano, A. A. Abrikosov, M. Lindroos, A. Bansil, H. Ding, D. Koelling and B. Dabrowski, Phys. Rev. Lett. **73**, 3302 (1994).

[8] D. M. King, Z.-X. Shen, D. S. Dessau, D. S. Marshall, C. H. Park, W. E. Spicer, J. L. Peng, Z. Y. Li and R. L. Greene, Phys. Rev. Lett. **73**, 3298 (1994).

[9] P. Alm'eras, H. Berger, G. Margaritondo, J. Ma, C. Quitmann, R. J. Kelley and M. Onellion, Solid State Commun. **91**, 535 (1994).

[10] N. V. Smith, P. Thiry and Y. Petroff, Phys. Rev. B **47**, 15476 (1993).

[11] Z.-X. Shen et al., Phys. Rev. Lett. **70**, 1553 (1993). In the caption to Fig. 1 it is flatly stated that "the spectral changes above and below T_c are caused by the opening of the superconducting gap." This statement is misleading because it neglects the effects of lattice relaxation, which are only indirectly related to the gap in $N_b(E)$.

[12] R. P. Sharma, F. J. Rotella, J. D. Jorgensen and L. E. Rehn, Physica C **174**, 409 (1991).

[13] J. C. Phillips, Physica C **228**, 171 (1994).

Effects of Exchange-Correlation on the Superconductivity of a Layered Two-Dimensional System

Y.M. Malozovsky[+] and S.M. Bose

Department of Physics and Atmospheric Science
Drexel University, Philadelphia, PA 19104

ABSTRACT

The influence of the Hubbard exchange-correlation term $G(k)$ on the normal and superconducting state properties of a layered 2D electron gas has been investigated. It is shown that the local field correction can induce a metal-insulator phase transition when the condition $p_F \approx 1/c$, where c is the interlayer separation, is satisfied. At carrier densities lower than that for the metal-insulator phase transition, the plasmon-mediated superconductivity is suppressed, whereas at higher carrier densities superconductivity can exist with T_c having a bell-shape dependence on the carrier density.

Since the discovery of the high-T_c superconductivity various microscopic models have been proposed for the explanation of the unusual normal and superconducting state properties of the cuprates. The small isotope effect[1] and unusual doping density[2] dependence of the phase diagram raise doubts that only phonons are responsible for such high T_c's. The existence of the metal-insulator phase transition at low doping density indicates that cuprates are closely related to the Mott-Hubbard systems. The absence of calculations resulting in the prediction of high-T_c superconducting transition with such an unusual phase diagram[3], requires a search for an alternative mechanism for the explanation of the anomalous behavior of the layered cuprates. Among potential nonphonon mechanisms of high-T_c superconductivity the plasmon exchange model[4-6] is a good candidate to explain the dramatic increase of the superconducting transition temperature with an unusual phase diagram. There are a number of reasons which seem to favor the plasmon-mediated high-T_c superconductivity. In a layered 2D cuprate the plasmon spectrum is gapless[7] due to 2D nature of the electron spectrum, and the interlayer Coulomb coupling splits the plasmon spectrum into a pseudo-optical 'band' with appropriate acoustic and optic limits[8]. In recent related papers[9,10], we have shown that in the framework of the standard Fermi-liquid approach in the RPA, the electron-plasmon interaction in a layered 2D electron gas leads to results which are similar to the phenomenology of 'marginal' Fermi-liquid model in both normal and superconducting states[11,12]. However, in those papers we did not investigate the influence of the exchange and correlation on the normal state and

plasmon-mediated superconducting state properties of a layered 2D Fermi liquid.

In this paper we show that the local field correction or the exchange-correlation effects in the Hubbard approximation can induce a metal-insulator phase transition at a certain carrier density and suppress plasmon-mediated superconductivity near this phase transition. However, for higher carrier densities, our calculation shows that T_c has a bell-shape behavior, thus verifying experimental observations[2].

It can be shown that the local field factor is related to the Landau Fermi-liquid interaction function $f_{p,p'}^{\sigma,\sigma'}$ and in the charge channel it takes the form[13]

$$G(k) = - \frac{Z(0)}{2V(k)} \left\langle f_{p,p'}^{\uparrow\uparrow} + f_{p,p'}^{\uparrow\downarrow} \right\rangle,$$ (1)

where <...> means average over the angle between $\mathbf{p}$ and $\mathbf{p}'$, $Z(0) = Z(p,\omega)|_{\omega=0,|p|=pF} = 1 - \partial\Sigma(p,\omega)/\partial\omega|_{\omega=0,|p|=pF}$ is the well-known Fermi-liquid renormalization parameter, and $V(k)$ is the bare Coulomb interaction.

In a layered two-dimensional (2D) metal, with cylindrical topology of the Fermi surface, the contribution of the bare Coulomb interaction to the exchange part of the self-energy can be written as[14,15]

$$\Sigma_{ex}^{n}(\mathbf{p}) = 2\sum_{k} \int_{-\infty}^{\infty} \frac{d\omega}{2\pi} V(\mathbf{p}-\mathbf{k}) \, \text{Im} \, G(k,\omega) \, n_F(\omega),$$ (2)

where $n_F(\omega) = [\exp(\omega/T) + 1]^{-1}$ is the Fermi distribution function, and G is the normal electron Green's function

$$G(p,\omega) = [\omega Z(p,\omega) - \xi_p]^{-1},$$ (3)

with $\xi_p = \varepsilon_p - \varepsilon_F$ as the energy measured relative to the Fermi energy, and $\varepsilon_p = p^2/2m^*$ being the 2D single-particle energy. In Eq. (2) $V(\mathbf{k})$ is the bare Coulomb interaction in a layered crystal which has the well-known form[8]

$$V(\mathbf{k}) = V_0(k_{\parallel}) \frac{\sinh c\, k_{\parallel}}{\cosh c\, k_{\parallel} - \cos c k_z} = V_0(k_{\parallel})\, f(\mathbf{k}) \qquad (4)$$

Here $\mathbf{k}_{\parallel}$ and k_z are the momentum components in the plane and normal to the plane of the layers, respectively; c is the separation between successive layers, and $V_0(k_{\parallel}) = 2\pi e^2/k_{\parallel}\kappa$ is the Coulomb interaction in a pure 2D case with κ as the dielectric constant of the background lattice.

Calculation of Eq. (2) with the use of Eqs. (3) and (4) yields, in a form similar to that of a strict 2D case[16],

$$\Sigma_n^{ex}(p)_{|T=0} = -\frac{2e^2}{\pi Z(0)\kappa}\, p\, [E(p_F/p) - (1 - p_F^2/p^2)K(p_F/p)]\,,\ p \geq p_F \qquad (5)$$

where $E(x)$ and $K(x)$ are the complete elliptic integrals of the second and first kind, respectively. Use of Eq. (5) in the following definition[17] of $\left\langle f_{\mathbf{p},\mathbf{p}'}^{\uparrow\uparrow} \right\rangle$ gives

$$\left\langle f_{\mathbf{p},\mathbf{p}'}^{\uparrow\uparrow} \right\rangle = \delta_{\sigma,\sigma'} \left\langle \frac{\delta\Sigma_\sigma(p)}{\delta n_{\sigma'}(p')} \right\rangle \approx 2\, \frac{\delta\Sigma^{ex}(k)}{\delta n_s} = \begin{cases} -4e^2/\kappa Z(0)p_F\,,\ k = p_F \\[2mm] -2\pi e^2/\kappa Z(0)k,\ k \gg p_F \end{cases}$$

where $k = k_{\parallel}$, $p_F = \sqrt{2\pi n_s}$ is the 2D Fermi momentum and coefficient 2 appears due to the fact that $n_\sigma = n_s/2$. Substituting this expression into Eq. (1) we have

$$G(k) \approx -\frac{Z(0)}{2V(k)} \left\langle f_{\mathbf{p},\mathbf{p}'}^{\uparrow\uparrow} \right\rangle = \begin{cases} k/\pi\, f(k)p_F\,,\ k < p_F, \\[2mm] 1/2\, f(k),\qquad k \gg p_F \end{cases}$$

This expression for the local field factor neglects the correlation of electrons with opposite spins. Taking into account the fact that correlation of electrons with antiparallel spin increases the local field factor, and combining the above two limiting cases together ($k < p_F$ and $k \gg p_F$), we arrive at the following Hubbard-like expression for the local field factor in a layered system[18]

$$G(k) = \frac{k}{2\, f(k)\, \sqrt{k^2 + p_F^2}} \ ,$$
(6)

We will now consider the effect of the exchange correlation term on the superconductivity of layered systems. Concentrating in the region of momenta close to the Fermi surface ($|p- p_F|/p_F \ll 1$), we can express the Eliashberg equations for a layered system in the form[10]

$$Z(\omega)\,\Delta(\omega) = \int_0^{\infty} d\omega' \mathrm{Re}\left\{\frac{\Delta(\omega')}{\sqrt{\omega'^2 - \Delta^2(\omega')}}\right\}\int_0^{\infty} d\Omega\, S(\Omega,\omega)\, Q_+(\omega',\Omega),$$
(7)

$$\omega\,[\,1 - Z(\omega)] = \int_0^{\infty} d\omega' \mathrm{Re}\left\{\frac{\omega'}{\sqrt{\omega'^2 - \Delta^2(\omega')}}\right\}\int_0^{\infty} d\Omega\, S(\Omega,\omega)\, Q_-(\omega',\Omega),$$
(8)

where

$$Q_\pm(\omega',\Omega) = (\,\tanh\tfrac{\omega'}{2T} + \coth\tfrac{\Omega}{2T})[(\omega'+\omega+\Omega+i\delta)^{-1}\pm(\omega'-\omega+\Omega-i\delta)^{-1}]\pm$$
$$(\coth\tfrac{\Omega}{2T} - \tanh\tfrac{\omega'}{2T})[\,(\omega'-\omega-\Omega-i\delta)^{-1}\pm(\omega'+\omega-\Omega+i\delta)^{-1}]$$
(9)

with the kernel of interaction in the form

$$S(\Omega,\omega) = -\frac{1}{(2\pi)^3}\int_{Y(\omega)/v_F}^{2p_F} [\,F(k,\omega) + F(k,-\omega)]\,\overline{S}(k,\Omega)k\,dk,$$
(10)

where $k = k_{||}$, and

$$\overline{S}(k,\omega) = \frac{c}{2\pi}\int_{-\pi/c}^{\pi/c} dk_z V^2(k)\,[\,1 - G(k)]\,\mathrm{Im}\,\chi(k,\omega),$$
(11)

is the average of the kernel of interaction over k_z. In Eq. (10) and (11)

$$F(k, \pm\omega) = \left[\,v_F^2 k^2 - \left(\frac{k^2}{2m^*} \pm Y(\omega)\right)^2\right]^{-1/2},$$

and

$$\chi(k,\omega) = \widetilde{\chi}(k,\omega)/[1 - V(k)\,\widetilde{\chi}(k,\omega)],$$

with

$$\widetilde{\chi}(k,\omega) = \chi_0(k,\omega)\Gamma(k,\omega) = \frac{\chi_0(k,\omega)}{1 + V(k)G(k)\chi_0(k,\omega)},$$
(12)

where $\chi_0(k,\omega)$ is the usual free-electron response function in a pure 2D case

$$\chi_0(k,\omega) = -\frac{m^*}{\pi} \{ 1 - [1 - v_F^2 k^2/\omega^2]^{-1/2} \}, \tag{13}$$

and

$$Y(\omega) = Z(\omega) \, \text{Re} \, \sqrt{\omega^2 - \Delta^2(\omega)}.$$

The sign $\pm$ in $F(k,\pm\omega)$ corresponds to inelastic electron scattering with absorption (emission) of an excitation quantum.

Let us first consider the contribution of plasmon excitations. Following the method of Ref. 10 it can be shown that the average kernel of interaction in region of plasmon excitation is

$$\overline{S}_{pl}(k,\omega) = \frac{c}{2\pi} \int_{-\pi/c}^{\pi/c} dk_z V^2(k)[1 - G(k)] \, \text{Im} \, \chi_{pl}(k,\omega) =$$
$$- \frac{V_0(k)[1 - V_0(k)G_0(k)\widetilde{\chi}(k,\omega)]}{\sqrt{[V_0(k)\widetilde{\chi}(k,\omega) \coth \frac{ck}{2} - 1][1 - V_0(k)\widetilde{\chi}(k,\omega)\tanh \frac{ck}{2}]}} \tag{14}$$
$$= - \frac{V_0(k)\omega^2}{\sqrt{(\omega_+^2 - \omega^2)(\omega^2 - \omega_-^2)}}$$

where $G_0(k) = 0.5k/\sqrt{k^2 + p_F^2}$ is the local field factor in a pure 2D case[18], and $\widetilde{\chi}(k,\omega) = \chi_0(k,\omega)/[1 + V_0(k) G_0(k)\chi_0(k,\omega)]$ is the irreducible response function in a pure 2D case (see Eq. (12)). In Eq. (14)

$$\omega_+^2 = \omega_p^2(k) [\coth \frac{ck}{2} - G_0(k)] + \frac{3}{4} v_F^2 k^2 + \frac{v_F^2 a^*_B k^3}{16(\coth \frac{ck}{2} - G_0(k) + a^*_B k/4)} \approx$$
$$\omega_p^2(k) \coth \frac{ck}{2} + \frac{3}{4}(1 - \frac{2}{3} \alpha) v_F^2 k^2 \tag{15}$$

is the pure optical plasmon frequency, and

$$\omega_-^2 = \omega_p^2(k) [\tanh \frac{ck}{2} - G_0(k)] + \frac{3}{4} v_F^2 k^2 + \frac{v_F^2 a^*_B k^3}{16(\tanh \frac{ck}{2} - G_0(k) + a^*_B k/4)} \approx$$
$$\omega_p^2(k) \tanh \frac{ck}{2} + \frac{3}{4}(1 - \frac{2}{3} \alpha) v_F^2 k^2 \tag{16}$$

is the proper acoustic plasmon frequency. Here $\omega_p^2(k)= e^2\, v_F p_F k/\kappa$ is the plasmon frequency for a pure 2D system, $a^*_B = \kappa/e^2 m^*$ is the effective Bohr radius, and $\alpha = e^2/v_F\kappa$ is the interelectron interaction constant.

It follows from Eq. (16) that the acoustic plasmon frequency for small p_F ($\approx 1/c$) overlaps with the region of the single-particle excitations, and thus, in this region the acoustic mode does not exist. It will be shown below that when $p_F \approx 1/c$, the homogeneous state of electron liquid in the layers becomes unstable and the layered 2D electron liquid undergoes the metal-insulator phase transition due to the charge density wave instability.

Substituting Eq. (14) into Eq. (10) and carrying out the integration, we find that for a layered system ($cp_F \geq 1$), the kernel for the electron-plasmon interaction is

$$S_{pl}(\Omega,\omega') \approx \frac{\alpha\Omega}{2\pi^2\sqrt{\omega_{pl}^2 - \Omega^2}}\, K\!\left[\sqrt{1 - (\gamma - \alpha/2 + 3/4)Y^2(\omega')/\Omega^2}\,\right], \qquad (17)$$

$$\sqrt{\gamma - \alpha/2 + 3/4}\ Y(\omega') \leq \Omega \leq \min\{\omega_{pl},\ \sqrt{\gamma - \alpha/2 + 3/4}\ \varepsilon_F\},$$

where $K(x)$ is the complete elliptic integral of the first kind, $\gamma = c/2a^*_B$ is the interlayer plasmon coupling constant, $\omega_{pl}= (4\pi e^2 n_s/\kappa m^* c)^{1/2} = \omega_c/\sqrt{\gamma}$ is the bulk plasmon frequency for a layered 2D system, and $\omega'Z(\omega') \leq \varepsilon_F$.

Using the single-particle contribution of Eqs. (12) and (13) into Eq. (11) we find for the layered system

$$\overline{S}_{s\text{-}p}(k,\omega) \approx -\frac{\pi e^2}{\sqrt{2}\,k}\, \frac{(1+2c/a^*_B)}{(1+c/a^*_B)^{3/2}}\, \frac{\omega}{\omega_{pl}}, \qquad (18)$$

The contribution from the single-particle excitations and bare Coulomb interaction to the equation for the gap has the form[10]

$$Z_{cl}\Delta_{cl} = -\int_0^\infty d\omega'\, \mathrm{Re}\left\{\frac{\Delta(\omega')}{\sqrt{\omega'^2 - \Delta^2(\omega')}}\right\} \mu(\omega')\ \tanh\frac{\omega'}{2T}, \qquad (19)$$

where

$$\mu(\omega) = \frac{c}{(2\pi)^3} \int_{-\pi/c}^{\pi/c} dk_z \int_{Y(\omega)/v_F}^{2p_F} kdk \, [\, F(k,\omega) + F(k,-\omega)] \, V_{scr}(k), \tag{20}$$

is the screened Coulomb repulsion parameter with

$$V_{scr}(k) = \frac{V(k)}{1 - V(k) \, [1 - G(k)] \, \chi_0(k_{\|},0)}, \tag{21}$$

as the screened Coulomb potential in a layered 2D metal. Averaging over k_z in Eq. (20) with the use of Eq. (21), gives the screened Coulomb repulsion parameter near $\omega \approx 0$ as $\mu(0) = \alpha\mu_s/\pi$ where

$$\mu_s = \int_0^1 \frac{dx}{\sqrt{1 - x^2}} \frac{1}{\sqrt{x^2(1 - \frac{\alpha}{\sqrt{1 + 4x^2}})^2 + 2\alpha x(1 - \frac{\alpha}{\sqrt{1 + 4x^2}})\coth \zeta x + \alpha^2}}, \tag{22}$$

with $\zeta = 2p_F c$. In the strong coupling $\alpha \gg 1$(low density) limit when $\zeta = 2p_F c$ --> 2 we get

$$\mu_s \sim \frac{1}{\alpha\sqrt{5}} \ln \frac{4\sqrt{5}}{\sqrt{1 - 2(\alpha-1)/\alpha\zeta}} \sim \frac{1}{\alpha\sqrt{5}} \ln \frac{4\sqrt{5}p_F c}{\sqrt{p_F(c + a^*_B) - 1}}, \tag{23}$$

which shows that μ_s increases infinitely for $p_F(c + a^*_B)$ --> 1. It will be shown below that the system undergoes a metal-insulator phase transition when the condition $p_F (c + a^*_B) = 1$ is satisfied.

Now we evaluate the electron-plasmon interaction constant using the method of our previous paper[10]

$$\lambda_{pl}(\omega) = 4 \int_0^\infty \frac{d\Omega}{\Omega} S_{pl}(\Omega,\omega), \tag{24}$$

Substituting Eq. (17) into Eq. (24) and performing the integration, we can find the electron-plasmon interaction constant as, $\lambda_{pl}(\omega) \approx \frac{\alpha\beta}{\pi} \ln (\Omega_0/\omega Z(\omega))$, where

$$\Omega_0 \propto \begin{cases} \omega_{pl}/\sqrt{\gamma - \alpha/2 + 3/4}, & \xi > 1, \\ \\ \varepsilon_F, & \xi < 1, \end{cases} \tag{25}$$

and $\beta = \min\{\xi, 1\}$, with $\xi = \frac{\varepsilon_F}{\omega_{pl}}\sqrt{\gamma - \alpha/2 + 3/4}$. Thus in a layered 2D system in the vicinity of the instability, i.e., when $p_F(c + a^*_B) \rightarrow 1$, we have $\lambda_{pl} \sim \beta = \xi = \frac{\varepsilon_F}{\omega_{pl}}\sqrt{\gamma - \alpha/2 + 3/4} \approx \frac{\varepsilon_F}{\omega_{pl}}\sqrt{\gamma(1 + a^*_B/c - 1/cp_F)} \rightarrow 0$, which means that the electron-plasmon interaction constant drops rapidly to zero in this region.

Next let us consider the renormalization parameter $Z(\omega)$ which includes contributions of both plasmon and single-particle excitations. Following Ref. 10 we write the renormalization parameter as

$$Z(\omega) = 1 + \overline{\lambda}_{pl}(\omega, T) + \frac{\alpha}{\pi}(1 - \mu_s), \tag{26}$$

where μ_s is defined by Eq. (22) and

$$\overline{\lambda}_{pl}(\omega, T) \approx \begin{cases} \frac{\alpha}{\pi}\beta \ln(\Omega_0/\omega), & \omega \gg T, \\[2mm] \frac{\alpha}{\pi}\beta \ln(\Omega_0/T), & \omega \ll T, \end{cases} \tag{27}$$

is the temperature dependent electron-plasmon interaction constant. It follows from Eq. (26) that when μ_s is finite and less than the plasmon contribution, the quasiparticles are well defined with $Z(\omega) > 1$. In the vicinity of the instability, however, μ_s increases infinitely, the renormalization parameter $Z(\omega)$ decreases rapidly and thus the quasiparticle does not exist. The instability (infinite increase of μ_s) thus corresponds to the metal-insulator phase transition which in this case manifests itself as a drop in the quasiparticle density of states at the Fermi surface. Thus, the exchange-correlation correction in a layered 2D system gives rise to the metal-insulator phase transition when the condition $p_F(c + a^*_B) = 1$ is satisfied. In addition, we note that the metal-insulator phase transition is due to the charge density wave instability which takes place when $\chi^{-1}(k, 0) = 0$ as can be seen from Eq.

(12). The dependence of the renormalization parameter on the doping density (p_F^2) is schematically represented in Fig. 1.

Let us now consider the effects of exchange-correlation on the plasmon mediated superconductivity in a layered 2D metal. Following Ref. 10, we can express the superconducting transition temperature as

$$T_c \approx 1.13 \, \omega_0 \exp(-1/\lambda_{eff}), \tag{28}$$

where

$$\lambda_{eff}^{-1} \approx \frac{\pi\mu^*}{\alpha\beta} + \sqrt{\left(\frac{\pi\mu^*}{\alpha\beta}\right)^2 + \frac{2\pi}{\alpha\beta} + a^2 - b}, \tag{29}$$

with

$$a = \ln(4\gamma_E/\pi), \qquad b = \int_0^\infty \frac{\ln^2 x}{\cosh^2 x} \, dx \tag{30}$$

and $\mu^* = \mu(0)/[1+\mu(0)\ln(\omega_\infty/\omega_0)]$ is the reduced Coulomb repulsion parameter. Here ω_∞ is the cutoff frequency of the Coulomb repulsion, which is of order of ε_F, and $\omega_0 \approx \Omega_0$ is the cutoff frequency of the electron-plasmon interaction.

We now study Eq. (28) in two different limits: $p_F c \gg 1$ and $p_F c \geq 1$. First, let us consider the case when $p_F c \gg 1$ where we have $\omega_0 \approx \Omega_0 \approx \omega_c/\gamma \sim v_F/c \ll \varepsilon_F$ and $\alpha \ll 1$, and we get

$$T_c \sim \frac{v_F}{c} \exp(-\lambda_{eff}^{-1}),$$

where $\lambda_{eff}^{-1} \sim (\pi\mu^*/\alpha\beta) + \sqrt{(\pi\mu^*/\alpha\beta)^2 + (2\pi/\alpha\beta)} \gg 1$ (since α is small and β is finite). Thus, in this case T_c will diminish with the increase of $p_F c$. In the case $1 < p_F c \ll \infty$, we have $\omega_0 \sim \varepsilon_F$, and $\beta \approx 1$ and T_c has the form

$$T_c \sim \varepsilon_F \exp(-1/\lambda_{eff})$$

where λ_{eff}^{-1} is finite. This case which represents strong intra- and inter-plane couplings ($\alpha \gg 1$ and $p_F c > 1$) gives the maximum possible T_c which scales with the Fermi energy ε_F. However, in the vicinity of the metal insulator phase

transition ($p_{FC}=1$), where μ_s increases (see Eq. (23)) and $\lambda_{pl} \sim \beta \approx \xi \ll 1$ (see Eq. (25)), $\lambda_{eff}^{-1} \gg 1$. Thus, in this region, Eq. (28) leads to a sharp drop of T_c, which means that the exchange-correlation correction strongly suppresses plasmon mediated superconductivity near the metal-insulator phase transition.
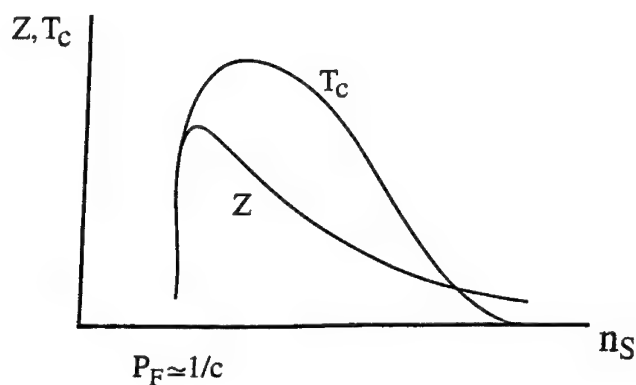

Fig. 1. Schematic representation of the dependence of the renormalization parameter $Z(\omega,T)$ and the superconducting transition temperature T_c on the carrier density n_s.

Our calculation indicates that in a layered 2D system, in the presence of Hubbard-type local field correction, the plasmon mediated superconductivity can explain the bell-shape dependence of T_c on the carrier density[2] as scematically shown in Fig. 1, and that the metal-insulator phase transition takes place when the Fermi momentum is approximately equal to the inverse interlayer spacing. For example, our estimation of the doping parameter x at the metal-insulator phase transition ($p_F c \approx 1$) for the LaSrCuO compounds with $c \approx 6.6\text{Å}$, and $a \approx 3.8\text{Å}$ (where a is the in-plane lattice constant for Cu)

gives $x = a^2 n_s = a^2/2\pi c^2 \approx 0.053$, which is in good agreement with the experimental value for the doping parameter for the insulator-superconductor transition.

In conclusion, in this paper we have shown that the Hubbard-type exchange-correlation correction can induce metal-insulator phase transition in a layered 2D electron gas and thus also has some relevance for the phase separation in the cuprates. It also leads to the bell-shape dependence of T_c of the plasmon mediated superconductivity on the doping density.

REFERENCES

+Present address: Department of Physics, Southern University and A&M College, P.O. Box 10559, Baton Rouge, Louisiana 70813

1.   J.P.Frank, Experimental Studies of the Isotope Effect in High Temperature Superconductors, in *Physical Properties of High Temperature Superconductors* IV, Editor D.M. Ginsberg, 1994.

2.   H.Zang and H. Sato, Phys. Rev. Lett. **70**, 1697 (1993).

3.   P.W. Anderson, Science, **256**, 1526 (1992).

4.   V.Z. Kresin, Phys. Lett. **122A**, 434 (1987); Phys. Rev. **B35**, 8716 (1987); V.Z. Kresin and H.Moravitz,*ibid*. **37**, 7854 (1988).

5.   J. Ruvalds, Phys. Rev. **B35**, 8869 (1987); Y. Ishii, and J. Ruvalds, *ibid*. **48**, 3455 (1993); G.S. Canright and G. Vignale, *ibid*. **39**, 2740 (1989).

6.   E.A. Pashitskii, Sov. Phys.JETP **76**, 425 (1993); E.A. Pashitskii, Y.M. Malozovsky, and A.V. Semenov, *ibid*. **73**, 255 (1991).

7.   F.Stern, Phys. Rev. Lett. **18**, 546 (1967).

8. S.M. Bose and P.Longe, J. Phys. Condens. Matter **2**, 2491 (1990); P.Longe and S.M. Bose, *ibid.* **4**, 1811 (1992).

9. Y.M. Malozovsky, S.M. Bose and P.Longe, Phys. Rev. **B 47**, 15242 (1993).

10. Y.M. Malozovsky, S.M. Bose, P.Longe and J.D. Fan, Phys.Rev. **B48**, 10504 (1993).

11. C.M. Varma, P.B. Littlewood, S.Schmitt-Rink, E.Abrahams, and A.E. Ruckenstein, Phys. Rev. Lett. **63**,1996(1989).

12. P.B. Littlewood and C.M. Varma, Phys. Rev. **B 46**, 405(1992).

13. D. Pines and P. Nozieres, *The Theory of Quantum Liquids* (W.A. Benjamin, Inc., N.Y., 1966).

14. A.A. Abrikosov, L.P. Gorkov and I.E. Dzyaloshinski, *Method of Quantum Field Theory in Statistical Physics* (Prentice-Hall, New Jersey, 1964).

15. G.D. Mahan, Many- Particle Physics (Plenium Press, N.Y., 1990).

16. A.V. Chaplik, Sov. Phys. JETP **33**, 997 (1971).

17. T.M. Rice, Annals of Phys. **31**, 100 (1964); T.K. Lee *et al*, Phys. Rev. Lett. **35**, 1048 (1975).

18. M. Jonson, J. Phys. C **9**, 3055 (1976).

Implications of magnetic pair-breaking
in $YBa_2Cu_3O_7$ homologues

Howard A. Blackstead
Department of Physics,
University of Notre Dame, Notre Dame, Indiana 46556 U.S.A.
and
John D. Dow
Department of Physics and Astronomy,
Arizona State University, Tempe, Arizona 85287-1504 U.S.A.

Abstract

Since (i) 100% substitution of Y by magnetic ions such as Nd and Gd does not disrupt superconductivity in $YBa_2Cu_3O_x$ with x≈7, but (ii) modest substitution of Ba by magnetic Nd or Gd does, one is forced to conclude that the origin of superconductivity is remote from the CuO_2 (cuprate) planes.

I. Introduction

$YBa_2Cu_3O_x$ with x≈7 and its homologues are the most thoroughly studied of the high-temperature oxide superconductors. A striking fact for these materials is that 100% substitution of Y^{+3} by most magnetic rare-earth ions, such as Nd^{+3} or Gd^{+3}, has essentially no effect on the superconductivity [1], despite the fact that magnetic ions are expected to break nearby Cooper pairs and hence should disrupt the superconductivity: the exchange interaction should cause the spin of one partner in a nearby Cooper pair to flip [2]. Recently it has been shown that *Ba-site magnetic* rare-earth ions, such as Nd^{+3} and Gd^{+3}, *do break pairs and degrade superconductivity* [3–7], but that non-magnetic La^{+3} ions on Ba-sites do not [6,8]. There appear to be three conceivable explanations of the absence of pair-breaking by Y-site magnetic rare-earth ions, two of which are inconsistent with the Ba-site pair-breaking observations and other recent data: (i) the Y-site is magnetically isolated from the superconductivity, which purportedly originates in the cuprate (CuO_2) planes adjacent to the Y-site [9], (ii) crystal-field splitting inhibits the pair-breaking [10], and (iii) the root of superconductivity is remote from the Y-site, in the vicinity of the Cu–O chain layers [11]. (The crystal structure is presented in Fig. 1, and has the Y-site sandwiched between two cuprate-planes that are not flat, but "crinkled" by the strain associated with lattice mismatch between them and their adjacent layers. These in turn are sandwiched between Ba–O layers and then Cu–O chain layers.)

II. Magnetic pair-breaking
II.A. Magnetic isolation

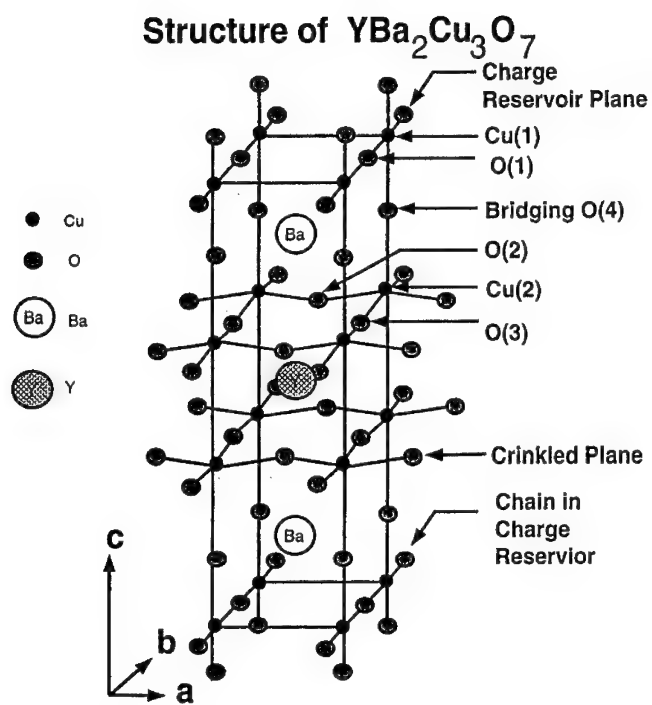The magnetic isolation explanation states that the magnetic moments

Structure of $YBa_2Cu_3O_7$

Fig. 1. Crystal structure of ideal $YBa_2Cu_3O_7$.

on the Y-sites associated with Nd or Gd ions, for example, are effectively *uncoupled* from the Fermi sea, because the (calculated) local electronic density of charge at the Fermi energy is very small [9]. This magnetic isolation explanation has since been convincingly contradicted by the following facts: (i) nuclear spins on Y-sites relax according to Korringa's law, considered to be unimpeachable evidence of coupling between a spin on that site and the Fermi sea [12–14]; (ii) Nd or Gd ions on Ba sites *do break pairs and destroy superconductivity* [3,7], as shown in Fig. 2, where we present the Nd doping data in comparison with data for La doping on the Ba-site as a control [6,8] — since Nd doping of the Y-site in $YBa_2Cu_3O_x$ does not adversely affect the superconductivity, and since La^{+3} is non-magnetic ($J=0$), the *difference between the two curves* of Fig. 2 is the Ba-site *magnetic pair-breaking* effect. Because the theoretical local charge-density at the Ba-site is comparable with that at the Y-site [9], one cannot argue that there is magnetic isolation at one site but not at the other.

The evidence that the pair-breaking is *magnetic* is strong: (i) The effect is experimentally discontinuous in J, since modest concentrations of $J=0$ Ba, Sr, and La ions at Ba-sites do not destroy superconductivity, but $J\neq0$ Nd and Gd do. There is also fragmentary evidence that Ba-site Pr^{+3} [15–17], Ce^{+3} [18], and Sm^{+3} [19] may destroy superconductivity; all have non-zero total angular momentum J. (ii) The charge of the Ba-site ion is not determinative, because Ba^{+2}, Sr^{+2}, and La^{+3} all maintain ≈90 K superconductivity. (iii) The complete passivation and compensation of the excess charge of the Ba-site ion La^{+3} is required, to be sure: inferior materials which fail to achieve such passivation yield degraded superconductivity, while undegraded superconductivity requires samples to be fully oxygenated [4,6,20–23]. But the $Nd_{1+u}Ba_2Cu_3O_x$ samples [3,4] were loaded with excess oxygen, and exhibited hole concentrations virtually independent of the Ba-site doping concentration u [3] — and yet Nd still destroyed the superconductivity, unlike La. Such oxygen loading led to observable occupancy of the O(5) anti-chain sites — demonstrating conversion of the Cu–O chains into cuprate-planes. Thus the planes on either side of the Ba-sites were almost identical to those neighboring the Y-sites [3,7], but Y-site Nd did not destroy superconductivity, while Ba-site Nd did. (iv) The relative charge densities at the Y- and Ba-sites are not responsible for the observed pair-breaking and the difference between the two curves of Fig. 2, as demonstrated by $(La_{Ba})^{+3}$ doping data [6] and double-doping experiments with $(Ca_Y)^{+2}$ and $(La_{Ba})^{+3}$ [21], both of which resulted in ≈90 K superconductivity. (v) Although Ba-site solubility is larger for the larger ionic sizes, the fact that Ba^{+2}, Sr^{+2}, and La^{+3} on that site all preserve ≈90 K superconductivity rules out size as the cause of the Nd and Gd pair-breaking. (vi) $J\neq0$ Pr has been detected on the Ba site in $PrBa_2Cu_3O_x$ [15–17], and is known to destroy supercon-
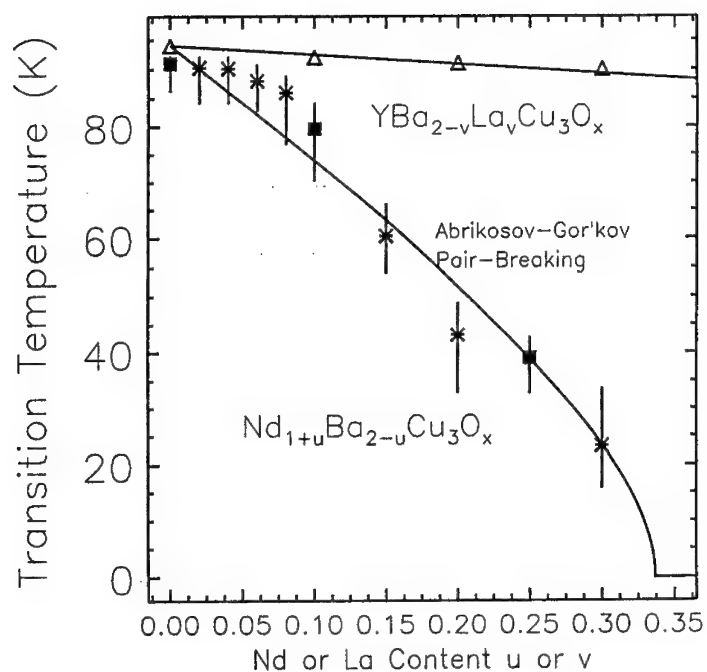
Fig. 2. Superconducting critical temperature (in K) *versus* Ba-site dopant concentration u (of magnetic Nd) or v (of non-magnetic La) in $Nd_{1+u}Ba_{2-u}Cu_3O_x$ (closed squares and asterisks) [3] and in $YBa_{2-v}La_vCu_3O_x$ with x≈7 (open triangles) [6,8]. Only the data of Ref. [3] which are represented here as closed squares are supported by neutron-diffraction measurements of the content u (with uncertainty ~±0.01). The uncertainty is larger yet for the asterisked data. The data for 0<u≤0.04 correspond to multi-phase samples and accordingly should be given less weight.

ductivity (although a quantitative correlation between the site occupancy and the destruction of superconductivity has not been demonstrated yet). (vii) $J \neq 0$ Nd (in $Nd_{1-y}Ce_yBa_2Cu_3O_x$ [18]) and Cm in $CmBa_2Cu_3O_x$ [24] are known to destroy superconductivity, and, by virtue of their sizes, are expected to occupy Ba sites in concentrations large enough to break pairs in the superconducting vicinity of the Cu–O chains. (viii) No electronic or chemical effect can be invoked to explain the data, because the rare-earths are all electronically and chemically virtually identical but magnetically different (due to the very-small-radius 4f electrons), and La on the Ba-site does not destroy superconductivity, while Ba-site Nd does — indicating that the *magnetic* differences are what are important. (ix) To rule out magnetic pair-breaking by Ba-site Nd, one would have to prepare samples of superior quality that eliminate the difference between the two curves of Fig. 2 by *raising* the $Nd_{1+u}Ba_{2-u}Cu_3O_x$ transition temperature to $\approx$90 K. Numerous experiments with various concentrations x of oxygen have failed to achieve undegraded $\approx$90 K superconductivity in $Nd_{1+u}Ba_{2-u}Cu_3O_x$ [3,4,6,20–23]. To escape the conclusion that the pair-breaking in $Nd_{1+u}Ba_2Cu_3O_x$ has a magnetic origin, one would have to experimentally observe such undegraded superconductivity.

II.B. Crystal-field splitting

The crystal-field splitting explanation [10] is invalid in this class of materials. While this mechanism is operative in some superconductors, such as the Chevrels [10], it is inoperative in the $YBa_2Cu_3O_7$-class, as is clearly demonstrated by the fact that $GdBa_2Cu_3O_7$ superconducts at $\approx$90 K [1]. Gd^{+3} has L=0, and so does not experience crystal-field splitting, yet has non-zero J=7/2, and so would break Cooper pairs if the insensitivity of the superconductivity to rare-earth-site magnetic moments were due to crystal-field splitting. The experimental facts are that Y-site Gd does not break pairs [1], but Ba-site Gd does [7]. This is the same behavior exhibited by $L \neq 0$ Nd [3], and so crystal-field splitting, which requires non-zero orbital angular momentum L of the rare-earth ion, is not relevant to this problem.

II.C. Superconductivity originating outside the cuprate-planes

The third mechanism is that the superconductivity is rooted in a plane remote from the Y-site, presumably in the vicinity of the Cu–O chain layers (Fig. 1) [11]. The pair-breaking exchange interaction is very short-ranged, and is effective only when the carrier whose spin is flipped occupies a nearest-neighbor site to the magnetic impurity. Hence Ba-site magnetic impurities would flip spins in the adjacent Cu–O chain layers, but Y-site impurities would be too distant from those superconducting layers to break pairs. This mechanism would rule out the cuprate-planes as the primary

source of superconductivity, and it would undermine most of the theories of high-temperature superconductivity [25].

In our opinion, the data definitely require us to abandon the cuprate-planes as the root of superconductivity, and, when combined with the fact that $Ba_{1-a}K_aPb_{1-b}Bi_bO_3$ superconducts up to 32 K despite having no two-dimensional layers, no cuprate-planes, and no Cu [26], indicate that oxide superconductivity originates in the only common ingredient: under-charged or "neutral" dopant oxygen, not in Cu or cuprate-planes. This oxygen is in the Cu–O chain layers of the $YBa_2Cu_3O_7$ homologues, but is interstitial in many other oxide superconductors [27–30].

We see no other plausible explanation of the fact that magnetic ions on Ba-sites of $YBa_2Cu_3O_7$ homologues destroy superconductivity, but the same ions on Y-sites do not. The superconductivity is rooted in the vicinity of the *dopant oxygen*, which in these materials lies in the Cu–O chains, not in the cuprate-planes [28].

II.D. Experimental confirmation of non-cuprate-plane superconductivity

This picture implies that $PrBa_2Cu_3O_7$ fails to superconduct, not because of Pr-site Pr (as is widely suspected), but because Ba-site Pr destroys the superconductivity [31]. If small regions of $PrBa_2Cu_3O_7$, the size of a coherence length, are free of Ba-site Pr, those regions should superconduct. We have recently observed such patches of inhomogeneous superconductivity in $PrBa_2Cu_3O_7$ [17,32–34].

II.E. Inadequacy of hybridization theories

The usual explanation of the failure of $PrBa_2Cu_3O_7$ to superconduct is that "hybridization" inhibits the superconductivity. Since hybridization involves a mixing coefficient that increases with ionic size and decreases as the magnitude of the energy difference between the f electron and the Fermi energy increases, this concept can be tested. Kim *et al.* [35] applied pressure to $NdBa_2Cu_3O_7$ to shorten the Nd–O distance to the value found for $PrBa_2Cu_3O_7$ — and expected to observe the superconducting critical temperature vanish, but it *increased* (contrary to a hybridization model and consistent with a model that associates the superconductivity with charge-reservoir dopant-oxygen). The possibility that the increase in T_c was associated with the difference between the f electronic energy and the Fermi energy can be excluded, because several different magnetic ions, with different f energies, lead to a breakdown of superconductivity: Pr, Cm, and Ce in $PrBa_2Cu_3O_7$, $CmBa_2Cu_3O_7$, and $Nd_{1-y}Ce_yBa_2Cu_3O_7$ and $Y_{1-y}Ce_yBa_2Cu_3O_7$, respectively [18,24,36–38].

III. The case for non-cuprate-plane superconductivity

Many workers in the field will have difficulty accepting the notion that, in general, the cuprate-planes are not the primary loci of superconductivity, both because so many high-temperature superconductors have such planes, and because the evidence for cuprate-plane superconductivity was accepted so early.

However, most of the efforts to discover new superconductors with higher critical temperatures have concentrated on cuprate-plane materials, and so it is not surprising that many of the new superconductors are of this type. There are relatively few new *classes* of superconductors, however, and one of these few is a copper-less class discovered *before* the search for cuprates began: $Ba_{1-a}K_aPb_{1-b}Bi_bO_3$ [39]. This class has all the earmarks of oxide high-temperature superconductors [26]: (i) a T_c greater than 23 K (32 K), (ii) a Sommerfeld specific heat γ comparable with those of the other oxide superconductors [40] (but not with ordinary superconductors), (iii) the property that it can be converted directly from an insulator to a superconductor by varying the composition indices a and b; (iv) the property that it does not superconduct unless the charge-balance condition for the presence of hypocharged oxygen is met: $a+b \neq 0$ [41–44]; and (v) p-type superconductivity. Therefore, we believe that it is inappropriate to classify $Ba_{1-a}K_aPb_{1-b}Bi_bO_3$ separately from the other high-temperature superconductors, or to extrapolate the cuprate-plane-oriented materials efforts of the last few years and to infer that most high-temperature superconductors must have cuprate-planes.

With regard to the theories based on cuprate-planes, there are basically two types of theories that are now popular, the t–J model [45,46] (or variants of it, such as Hubbard models), and the spin-fluctuation model [47]. Each of these models has some apparent triumphs: The t–J model seems to account for some of the Coulomb-corrections to the quasi-particle dispersion curves (as measured by photoemission [48]), while the spin-fluctuation model seems to account for the nuclear magnetic resonance spin-lattice relaxation time T_1 of $YBa_2Cu_3O_x$ [49]. What remains inadequately explained is the superconductivity, which, in some t–J models relies on non-existent Cu^{+3} [46], and in spin-fluctuation models must be disrupted less by magnetic Ni than by non-magnetic Zn [49] — contrary to the data [30,44,50–52].

In $YBa_2Cu_3O_x$, cuprate-plane models are giving an increasingly accurate picture of the antiferromagnetism [53], and there seems to be some correlation between the antiferromagnetism and the superconductivity — which has caused theorists to be optimistic about extending the cuprate-plane models of antiferromagnetism to predict and describe superconductivity. However, the assumption that the antiferromagnetism and the superconductivity are closely related in general is not valid, since in $La_{2-\beta}Sr_\beta Cu_{1-y}Li_yO_4$

they appear to be unrelated: Li doping suppresses the antiferromagnetic spin-fluctuations, while having little effect on the superconducting critical temperature [54]. And so any cuprate-plane model must demonstrate that it can successfully describe high-temperature *superconductivity,* no matter how successful it might be, for example, at describing antiferromagnetism. To our knowledge, no cuprate-plane theory has successfully done that.

In the early days of the field, before it was realized that the high-temperature superconductors are generally p-type, Cu was identified as the element primarily responsible for the superconductivity, largely because solid Cu is a metal (although n-type). As a result, most theories concentrated on Cu and phenomena related to it, such as charge- or spin-fluctuations, as causing the superconductivity. However, the identification of Cu as the essential element has serious faults, not only for the copper-less high-temperature superconductors $Ba_{1-a}K_aPb_{1-b}Bi_bO_3$, but also for materials such as $YBa_2Cu_3O_7$, where cuprate-plane theories often expect the seven oxygen ions to require a total of about fourteen electrons, and there are only thirteen available — even if the cations are fully ionized to Y^{+3}, Ba^{+2}, and Cu^{+2} [27,44,50]. The fourteenth electron must come from ionization of Cu^{+2} to Cu^{+3} (which has the smallest cation ionization potential), but the nuclear magnetic resonance data show that no Cu^{+3} is present in this material [13] — a fact confirmed by x-ray data [55]. Therefore, a proper model of superconductivity in $YBa_2Cu_3O_7$ must choose between hypercharged Cu^{+3}, although the experiments indicate that none exists, or hypocharged oxygen — presumably in the Cu–O chain layers as O^{-Z}, with Z<2. The fact that oxygen readily leaks out of these materials and can rather easily be added to them (*e.g.,* under pressure) indicates that the oxygen is not in the large-radius O^{-2} state, and is often severely hypocharged, almost neutral, and unbonded — and so it would seem that the data clearly prefer hypocharged oxygen to hypercharged copper. Nevertheless, for historical rather than scientific reasons, most theories have been based on Cu and cuprate-planes — and have devoted considerable effort to explaining why Cu^{+2}, with its magnetic moment, does not destroy the superconductivity thought to be in the cuprate-planes.

The experiment that first appeared to conclusively demonstrate cuprate-plane superconductivity was determination that the charge on cuprate-plane-Cu in $YBa_2Cu_3O_x$ increased suddenly as the oxygen content x increased through x=6.4 [56], the condition for the onset of superconductivity. This result has two serious flaws that have only recently been recognized: (i) a sudden increase in charge corresponds to a first-order phase transition, while superconductivity is supposed to be a second-order transition, and (ii) independent experiments [57] did not detect *any* discontinuous change in the planar-Cu charge or its derivative. Indeed, it is now clear that the correct

increase in planar-Cu charge actually is zero within the uncertainty of the determination. Thus the field of high-temperature superconductivity is now in the awkward state of having a remote-control model of superconductivity (the dopant-oxygen in the charge-reservoir purportedly controls the superconductivity in the cuprate-planes by controlling the hole-transfer to those planes) without there being any experimental proof that the remote-control mechanism actually operates as proposed — an unacceptable situation for a scientific theory.

Clearly, the p-type superconductivity must be where there are holes. Analyses of the bond-lengths of $La_{2-\beta}Sr_\beta CuO_4$ showed that the holes are *not* in the cuprate-planes, but in or between the La–O layers [41,58]. Similarly, analyses of the charge-transfer in the $HgBa_2Ca_{n-1}Cu_nO_{2n+2}$ compounds showed that electrons, not holes are transferred to the cuprate-planes as the superconducting critical temperature T_c increases with pressure p or chemical pressure n [42]. This is the opposite to what is expected on the basis of the remote-control charge-transfer hypothesis. In general, with the exception of $YBa_2Cu_3O_x$ as a function of oxygen content x, the onset of superconductivity and increases of T_c are associated with the transfer of electrons, not holes to the cuprate-planes — the opposite of what is expected for a cuprate-plane model of superconductivity. Even for the case of $YBa_2Cu_3O_x$ which does exhibit considerable hole transfer to the cuprate-planes as x increases and superconductivity sets in, there is $PrBa_2Cu_3O_x$ as a counter-example, generally thought to be an insulator, with the same charges-transferred as a function of x — demonstrating that the charge-transfer is not sufficient for superconductivity. In $T\ell_2Ba_2Ca_{n-1}Cu_nO_{2n+4}$ the dopant oxygen is packed into the crystal-structure so *tightly* that it fits only if it is virtually neutral; O^{-2} does not fit at the dopant site. If this dopant oxygen is virtually neutral, its holes remain near it and do not transfer to the cuprate-planes — and hence cannot induce cuprate-plane superconductivity. In $HgBa_2Ca_{n-1}Cu_nO_{2n+2}$ the dopant-oxygen is packed so *loosely* that it is unbonded to the adjacent Hg ions in the charge-reservoir planes, an indication that the oxygen is hypocharged. Thus analyses of the charge-transfer extractable from bond-lengths reveal that the holes responsible for Cooper-pairing and superconductivity have very different degrees of localization in different materials, are most commonly found in the charge-reservoir regions containing the dopant-oxygen, and do not necessarily readily transfer to the cuprate-planes as originally hypothesized [11,42].

Independent confirmation that the superconductivity originates primarily where the holes are, namely in the charge-reservoirs rather than in the cuprate-planes, is afforded by numerous pair-breaking studies [59]. For example, magnetic impurities located in the cuprate-planes do not break Cooper-pairs and degrade the superconducting transition temperature T_c whenever

they are separated by one or more atoms from the charge-reservoir regions (where the holes and dopant-oxygen reside [51,52,58]). In particular, (nonmagnetic) Zn and (magnetic) Ni doping of cuprate-plane-Cu sites both produce the same weak scattering of pairs whenever the dopant-oxygen regions are remote from the cuprate-planes — indicating that the superconducting region lies outside the cuprate-planes, beyond the range of the magnetic scattering. And the amount of cuprate-plane Zn or Ni required to destroy superconductivity increases exponentially with the distance of the cuprate-planes from the charge-reservoirs — a clear signature that the seat of superconductivity is in the charge-reservoirs, not in the cuprate-planes. Indeed, T_c itself increases with the separation between the cuprate-planes and the charge-reservoirs — indicative that the cuprate-planes are *electronically* deleterious to superconductivity (even though they enhance T_c when they mechanically compress the charge-reservoirs [30]). Indeed, the very fact that almost all (Rare-earth)$Ba_2Cu_3O_7$ materials superconduct is evidence of this sort: Rare-earth-site *magnetic* ions do not adversely affect the superconductivity — because the origin of superconductivity is in the vicinity of the Cu–O chains, in the remote charge-reservoir regions [60,61]. (Ba-site rare-earth ions do break pairs and destroy superconductivity [17,31,32,62].) In $Bi_2Sr_2CaCu_2O_8$, Josephson radiation and critical current studies [63] show that either the cuprate-planes or the Bi–O layers superconduct; and scanning tunneling spectroscopy measurements [64] and photoemission studies (of Au on the surface [65]) both independently show that the surface Bi–O layers superconduct — proving in conjunction with the Josephson studies that the cuprate-planes are not the origin of superconductivity in that material [66], provided, of course, that the various samples studied are chemically the same.

Infrared spectra obtained by Basov *et al.* [67] from unusually defect-free materials demonstrate that more than half of the superconducting condensate in $YBa_2Cu_3O_7$ lies in the Cu–O chains, not in the cuprate-planes; this fraction is even greater than 75% for $YBa_2Cu_4O_8$. Such large condensate fractions are incompatible with a hole-transfer, cuprate-plane picture: How can the holes first be transferred to the cuprate-planes and then induce proximity-effect superconductivity back on the chains from which they came, such that the *majority* of the superconducting condensate is in the chains? This would appear to require a double-remote-control mechanism of superconductivity.

It seems to us that the evidence is overwhelmingly against cuprate-plane models of high-temperature superconductivity and in favor of charge-reservoir superconductivity associated with dopant oxygen. The most popular cuprate-plane models feature either Cu^{+3}, which is known to be absent, or spin-fluctuations that predict the pair-breaking by Ni to be weaker than that by Zn — contrary to virtually all of the data which show the pair-

breaking by Zn and Ni to be the same (impossible if the impurities are immersed in the superconductor and the paired holes are time-reversed).

We acknowledge that it may take some time for these facts to be accepted, but there are so many of them that we cannot understand why cuprate-plane models are still held in general favor. In our opinion, efforts to understand high-temperature superconductivity should focus on the charge-reservoirs and attempt to understand precisely the role of dopant oxygen.

References

[1] Z. Fisk, J. D. Thompson, E. Zirngiebl, J. L. Smith, and S. W. Cheong, Solid State Commun. **62**, 743 (1987); P. Hor, R. L. Meng, Y.-Q. Wang, L. Gao, Z. J. Huang, J. Bechtold, K. Forster, and C. W. Chu, Phys. Rev. Lett. **58**, 1891 (1987).

[2] A. A. Abrikosov and L. P. Gor'kov, Zh. Eksperim. Teor. Fiz. **39**, 1781 (1960); [English transl.: Soviet Phys. JETP **12**, 1243 (1961)].

[3] M. J. Kramer, S. I. Yoo, R. W. McCallum, W. B. Yelon, H. Xie, and P. Allenspach, Physica **C 219**, 145 (1994).

[4] K. Takita, H. Katoh, H. Akinaga, M. Nishino, T. Ishigaki, H. Asano, Jpn. J. Appl. Phys. **29**, L57 (1988); K. Takita, H. Akinaga, T. Oshima, Y. Takeda, and M. Takano, Physica **C 191**, 509 (1992).

[5] While Ref. [3] presents another explanation of the pair-breaking by Ba-site Nd, that explanation is unsatisfactory because it implies that La doping of the Ba-site should produce similar behavior to Nd, which it does not (Ref. [6]).

[6] A. Tokiwa, Y. Syono, M. Kikuchi, R. Suzuki, T. Kajitani, N. Kobayashi, T. Sasaki, O. Nakatsu, and Y. Muto, Jpn. J. Appl. Phys. **27**, L1009 (1988). Structural measurements of such La-doped material are given by P. Karen, H. Fjellvag, A. Kjekshus, and A. F. Andresen, J. Sol. State Chem. **93**, 163 (1991).

[7] V. N. Narozhnyi, private communication; V. N. Narozhnyi, E. P. Khlybov, V. N. Kochetkov, and T. C. Uvarova, *Physica* **C 235-240,** 1349 (1994); and V. N. Narozhnyi, E. P. Khlybeb, V. I. Nizhankovskii, and Z. Bukowski, Proc. XXIX Conference on Low-Temperature Physics, Part 1, p. C2 (Russian Academy of Sciences and Kazan State University, Kazan and Moscow, 1992).

[8] We examine the pair-breaking data primarily at moderate rare-earth doping levels u or v, large enough to discern a statistically significant difference between the two curves of Fig. 2, and both small and large enough to avoid the regimes in which multiple-phase material grows: $u \geq 0.4$ and $u \leq 0.04$. Heavy doping, for example in $Y(Ba_{2-v}La_v)Cu_3O_x$ for $v > 0.4$, can lead to different local crystal structures, and hence to marked deviations from the Abrikosov-Gor'kov behavior [2].

[9] A. J. Freeman (private communication) and co-workers have calculated the local state density at the Fermi energy to be so low near the rare-earth site that they feel the site is magnetically isolated from the Fermi sea. However, the calculated state-density at the Ba-site is comparably low, and Nd ions in $NdBa_2Cu_3O_7$ (Ref. [3]) or Gd ions in $GdBa_2Cu_3O_7$ (Ref. [7]) on Ba sites certainly break pairs. See A. J. Freeman, J. Yu, S. Massidda, and D. D. Koelling, Phys. Lett. **A 122**, 198 (1987).

[10] O. Pena and M. Sergent, Prog. Solid State Chem. **19**, 165 (1989).

[11] H. A. Blackstead and J. D. Dow, Pis'ma Zh. Eksperim. Teor. Fiz. **59**, 262 (1994) [JETP Lett. **59**, 283 (1994)] and references therein.

[12] J. T. Markert, T. W. Noh, S. E. Russek, and R. M. Cotts, Solid State Commun. **63**, 847 (1987).

[13] C. H. Pennington and C. P. Slichter, in *Physical Properties of High-Temperature Superconductors II*, edited by D. M. Ginsberg, (World Scientific, Singapore, 1990), p. 285, and references therein.

[14] For studies of Ba-site spin relaxation, see J. Shore, S.-t. Yang, J. Haase, D. Schwartz, and E. Oldfield, Phys. Rev. **B 46**, 595 (1992).

[15] M. P. Nutley, A. T. Boothroyd, and G. J. McIntyre, J. Magnetism Magnetic Mater. **104-107,** 623 (1992); C.-k. Chen, A. T. Boothroyd, Y.-l. Hu, F. R. Wondre, B. M. Wanklyn, and J. W. Hodby, Physica C **214**, 231 (1993).

[16] Z. P. Han, R. Dupree, D. McK. Paul, A. P. Howes, and L. W. J. Caves, Physica **181**, 355 (1991).

[17] H. A. Blackstead, D. B. Chrisey, J. D. Dow, J. S. Horwitz, A. E. Klunzinger, and D. B. Pulling, Physica C **235-240**, 1539 (1994).

[18] G. Cao, R. J. Kennedy, J. W. O'Reilly, J. E. Crow, P. Pernambuco-Wise, and S. T. Ting, Physica **B 186-188**, 1022 (1993); G. Cao, J. Bolivar, J. W. O'Reilly, J. E. Crow, R. J. Kennedy, and P. Pernambuco-Wise, Physica **B 186-188**, 1004 (1993).

[19] H. Akinaga, H. Katoh, K. Takita, and K. Masuda, Jpn. J. Appl. Phys. **28**, L31 (1989).

[20] Y. Tokura, J. B. Torrance, T. C. Huang, and A. I. Nazzal, Phys. Rev. **B 38**, 7156 (1988).

[21] P. R. Slater and C. Greaves, Superconductor Science and Technology

5, 205 (1992).

[22] Ba-site doping by La^{+3}, Nd^{+3}, or Gd^{+3} is naturally compensated by anti-chain O(5)-site oxygen. Controlled compensation by Ca^{+2} (J=0) on the Y-site, simultaneous with Ba-site La^{+3} (J=0) doping in $Y_{1-\lambda}Ca_{\lambda}Ba_{2-\lambda}La_{\lambda}Cu_3O_x$, produces almost the same minor degradation of T_c (Ref. [21]), proving that details of the compensation do not alter the essential physics discussed here.

[23] P. Karen, F. Fjellvag, and A. Kjekshus, J. Solid State Chem **97**, 257-273 (1992).

[24] L. Soderholm, G. L. Goodman, U. Welp, C. W. Williams, and J. Bolender, Physica **C 161**, 252 (1989).

[25] V. Z. Kresin, H. Morawitz, and S. A. Wolf, *Mechanisms of Conventional and High T_c Superconductivity*, (Oxford University Press, Oxford, 1993).

[26] R. G. Goodrich, C. Grienier, D. Hall, A. Lacerda, E. G. Haanappel, D. Rickel, T. Northington, R. Schwarz, F. M. Mueller, D. D. Koelling, J. Vuillemin, L. Van Bockstal, M. L. Norton, and D. H. Lowndes, J. Phys. Chem. Solids, **54**, 1251 (1993).

[27] H. A. Blackstead and J. D. Dow, J. Superconduct. **8**, 613 (1995).

[28] Interestingly enough, magnetic ions *in the cuprate-planes* of some high-temperature superconductors do not break pairs, a fact which confirms that the origin of superconductivity is not in the cuprate-planes. Magnetic doping of the Cu-sites of the cuprate-planes in $La_{2-\beta}Sr_{\beta}CuO_4$ reveals *no magnetic pair-breaking:* that is, non-magnetic Zn (the control) and magnetic Co or Ni have the same effect on the transition temperature. In contrast, Cu-site doping of $Nd_{1-z}Ce_zCuO_4$ with non-magnetic Zn has only a small effect, almost the same fractional degradation of T_c as in $La_{2-\beta}Sr_{\beta}CuO_4$; but magnetic Co and Ni produce dramatic depression of the transition temperature and strong magnetic pair-breaking [29,30]. These different responses to magnetic dopants show that the superconductivity cannot originate in the cuprate-planes themselves, which are the same in the two materials; the superconductivity must be rooted primarily in other layers. Our explanation is that interstitial oxygen is bonded to the impurity site in $Nd_{1-z}Ce_zCuO_4$, but not in $La_{2-\beta}Sr_{\beta}CuO_4$, so that superconductivity associated with dopant interstitial oxygen is disrupted by the Cu-site magnetic impurities in the former material, but not in the latter.

[29] J. M. Tarascon, E. Wang, S. Kivelson, B. G. Bagley, G. W. Hull, and R. Ramesh, Phys. Rev. **B 42**, 218 (1990).

[30] H. A. Blackstead and J. D. Dow, "Evidence of the direct role of dopant oxygen in high-temperature superconductivity," Philos. Mag., (Jan, 1996) in press.

[31] H. A. Blackstead and J. D. Dow, Phys. Rev. **B 51**, 11830 (1995).

[32] H. A. Blackstead and J. D. Dow, J. Superconduct. **8**, 653 (1995).

[33] H. A. Blackstead, J. D. Dow, D. B. Chrisey, J. S. Horwitz, P. J. McGinn, M. A. Black, A. E. Klunzinger, and D. B. Pulling, "Observation of superconductivity in $PrBa_2Cu_3O_7$," to be published.

[34] H. A. Blackstead, D. B. Chrisey, J. D. Dow, J. S. Horwitz, A. E. Klunzinger, and D. B. Pulling, Phys. Lett. **A 207**, 109 (1995).

[35] C. C. Kim, E. F. Skelton, M. S. Osofsky, and D. H. Liebenberg, Phys. Rev. **B 48**, 6431 (1993).

[36] J. L. Peng, P. Klavins, R. N. Shelton, H. B. Radousky, B. A. Hahn, and L. Bernardez, Phys. Rev. **B 40**, 4517 (1989).

[37] C.-S. Jee, A. Kebede, D. Nichols, J. E. Crow, T. Mihalisin, G. H. Myer, I. Perez, R. E. Salomon, and P. Schlottmann, Solid State Commun. **69**, 379 (1989); C. R. Fincher, Jr. and G. B. Blanchet, Phys. Rev. Lett. **67**, 2902 (1991).

[38] G. Y. Guo and W. M. Temmerman, Phys. Rev. **B 41**, 6372 (1990).

[39] A. W. Sleight, J. L. Gillson, and F. E. Biersted, Solid State Commun. **17**, 27 (1975).

[40] J. C. Phillips, Phys. Rev. **B 36**, 861 (1987).

[41] H. A. Blackstead and J. D. Dow, J. Appl. Phys. **78**, 7175 (1995).

[42] H. A. Blackstead and J. D. Dow, Solid State Commun. **95**, 613 (1995).

[43] H. A. Blackstead and J. D. Dow, Philos. Mag. **72**, 529 (1995).

[44] H. A. Blackstead and J. D. Dow, "Constraints imposed by the data on a successful theory of high-temperature superconductivity," Proc. SPIE **2397**, *Optoelectronic Integrated Circuit Materials — Physics and Devices,* edited by M. Razeghi, Y.-S. Park, and G. L. Witt, p. 617 (1995).

[45] R. Fehrenbacher and T. M. Rice, Phys. Rev. Lett. **70**, 3471 (1993) and references therein.

[46] T. M. Rice, Physics News in 1994, S11 (April, 1995).

[47] A. Millis, H. Monien, and D. Pines, Phys. Rev. **B 42**, 167 (1990); P. Monthoux, A. Balatsky, and D. Pines, Phys. Rev. Lett. **67**, 3348 (1991); Phys. Rev. **B 46**, 14803 (1992); P. Monthoux and D. Pines, Phys. Rev. **B 47**, 6069 (1993); P. Monthoux and D. Pines, Phys. Rev. Lett. **69**, 961 (1992).

[48] Z.-X. Shen, W. E. Spicer, D. M. King, D. S. Dessau, and B. O. Wells, Science **267**, 343 (1995).

[49] D. Pines, in *Strongly Correlated Electronic Materials: Los Alamos Symposium 1993,* edited by K. Bedell, Z. Wang, D. E. Meltzer, A. Valatsky, and E. Abrahams (Addison-Wesley, Reading, Massachusetts, 1994).

[50] H. A. Blackstead and J. D. Dow, in *Proceedings of the Second International Symposium on Quantum Confinement Physics and Applications,*

edited by M. Cahay, S. Bandyopadhyay, J. P. Leburton, A. W. Klein-sasser, and M. A. Osman, Proceedings Volume **94-17**, (Electrochemical Society, Pennington, NJ, 1994), p. 408; p. 419.

[51] H. A. Blackstead and J. D. Dow, "Ni and Zn doping of Cu sites in superconducting $Nd_{2-z}Ce_zCuO_4$, $La_{2-\beta}Sr_\beta CuO_4$, $YBa_2Cu_3O_7$, $YBa_2Cu_4O_8$, and $Bi_2Sr_2CaCu_2O_8$," to be published.

[52] H. A. Blackstead and J. D. Dow, "Pair-breaking as a probe of d-wave high-temperature superconductivity," to be published.

[53] *Strongly Correlated Electronic Materials: Los Alamos Symposium 1993,* edited by K. Bedell, Z. Wang, D. E. Meltzer, A. Valatsky, and E. Abrahams (Addison-Wesley, Reading, Massachusetts, 1994).

[54] J. L. Sarrao, L. S. Cassady, Z. Fisk, and J. D. Thompson, Bull. Amer. Phys. Soc. **40**, 795 (1995), and to be published.

[55] J. M. Tranquada, S. M. Heald, A. R. Moodenbaugh, and M. Suenaga, Phys. Rev. **B 35**, 7187 (1987), and references therein, provide evidence that there is no Cu^{+3} in the $LaCuO_4$ family of high-temperature superconductors. See also J. M. Tranquada, S. M. Heald, and A. R. Moodenbaugh, Phys. Rev. **B 36**, 5263 (1987).

[56] R. J. Cava, A. W. Hewat, E. A. Hewat, B. Batlogg, M. Marezio, K. M. Rabe, J. J. Krajewski, W. F. Peck, Jr., and L. W. Rupp, Jr., Physica C, **165**, 419 (1990); R. Cava, *Synthesis and crystal chemistry of high-T_c oxide superconductors,* in *Processing and Properties of High-T_c Superconductors,* Vol. 1, edited by S. Jin (World Scientific, Singapore, 1993), p. 1 *et seq.*, especially p. 12.

[57] J. D. Jorgensen, B. W. Veal, A. P. Paulikas, L. J. Nowicki, G. W. Crabtree, H. Claus, and W. K. Kwok, Phys. Rev. **B 41**, 1863 (1990).

[58] H. A. Blackstead and J. D. Dow, "Charge-transfer and the location of superconducting holes in $La_{2-\beta}Sr_\beta CuO_4$," J. Phys. Chem. Solids **56**, No. 12 (Dec, 1995) in press.

[59] Cooper pairs have been detected by tunneling experiments, and the existence of a critical current both indicates that they can be broken and suggests that the pairs are time-reversed. See T. Yamashita, A. Kawakami, T. Nishihara, Y. Hirotsu, and M. Takata, Jpn. J. Appl. Phys. **26**, L635 (1987); T. Yamashita, A. Kawakami, T. Nishihara, M. Takata, and K. Kishio, Jpn. J. Appl. Phys. **26**, L671 (1987); T. J. Witt, Phys. Rev. Lett. **61**, 1423 (1988); D. Esteve, J. M. Martinis, C. Urbina, M. H. Devoret, G. Collin, P. Monod, M. Ribault, and A. Revcolevschi, Europhys. Lett. **3**, 1237 (1987); R. H. Koch, C. P. Umbach, G. J. Clark, P. Chaudhari, and R. B. Laibowitz, Appl. Phys. Lett. **51**, 200 (1987); C. E. Gough, M. S. Colclough, E. M. Forgan, R. G. Jordan, M. Keene, C. M. Muirhead, A. I. M. Rae, N. Thomas, J. S. Asbell, and S. Sutton, Nature **326**, 855 (1987); P. Gammel, D. J.

Bishop, G. J. Dolan, J. R. Kwo, C. A. Murray, L. F. Schneemeyer, and J. V. Waszczak, Phys. Rev. Lett. **59**, 2592 (1987).

[60] H. A. Blackstead and J. D. Dow, Solid State Commun. **96,** 313 (1995).

[61] H. A. Blackstead, J. D. Dow, W. E. Packard, and D. B. Pulling, Physica C **235-240**, 1363 (1994).

[62] H. A. Blackstead and J. D. Dow, Superlatt. Microstruct. **14**, 231 (1993).

[63] R. Kleiner and P. Müller, Phys. Rev. **B 49**, 1327 (1994).

[64] E. L. Wolf, A. Chang, Z. Y. Rong, Yu. M. Ivanchenko, and F. Lu, J. Superconduct. **7**, 355 (1994). A. Chang, Z. Y. Rong, Yu. M. Ivanchenko, F. Lu, and E. L. Wolf, Phys. Rev. **B 46**, 5692 (1992).

[65] D. S. Dessau, Z.-X. Shen, B. O. Wells, W. E. Spicer, R. S. List, A. K. Arko, R. J. Bartlett, Z. Fisk, and S.-W. Cheong, D. B. Mitzi, A. Kapitulnik, and J. E. Schirber, Appl. Phys. Lett. **57**, 307 (1990).

[66] H. A. Blackstead and J. D. Dow, "Evidence for superconductivity in the Bi–O layers and not in the cuprate-planes of $Bi_2Sr_2CaCu_2O_8$," Superlatt. Microstruct., in press (1996).

[67] D. N. Basov, R. Liang, D. A. Bonn, W. N. Hardy, B. Dabrowski, M. Quijada, D. B. Tanner, J. P. Rice, D. M. Ginsberg, and T. Timusk, Phys. Rev. Lett. **74**, 598 (1995), and private communication.

Oxide superconductivity:
Integrated, photo-induced, high-temperature superconductivity in confined metallic oxygen

Howard A. Blackstead
Department of Physics,
University of Notre Dame, Notre Dame, Indiana 46556 U.S.A.
and
John D. Dow
Department of Physics and Astronomy,
Arizona State University, Tempe, Arizona 85287-1504 U.S.A.
and
David B. Pulling
Department of Physics,
University of Notre Dame, Notre Dame, Indiana 46556 U.S.A.

Abstract

Oxygen in both the O^{-2} ionic state and the hypocharged O^{-Z} state (with $Z<2$) has been identified as the essential ingredient of superconductivity in $YBa_2Cu_3O_x$ and other high-temperature superconductors. The role of the $YBa_2Cu_3O_{6.5}$ is to act as a box or cage for the additional hypocharged or "neutral" oxygen necessary for superconductivity. Consequently one should be able to fabricate a similar box from semiconductors grown epitaxially, and fill it with oxygen — leading to integrated semiconductor/superconductor microstructures exhibiting high-temperature superconductivity and/or photo-induced superconductivity.

I. Introduction

The discovery of high-temperature oxide superconductivity [1] originally led to visions of room-temperature superconductivity and electrical power transmission over long distances with negligible losses. While the highest temperature at which superconductivity has been reported has been rising toward room temperature [2], the vision of the future appears to have refocussed more on superconducting devices than on power transmission. Until recently, there has been no comprehensive physical picture of the mechanism for high-temperature superconductivity, and so it has not been possible to predict which types of devices will be realizable. Now, however, there is a theory [3] which attributes the superconductivity to hypocharged or "neutral" oxygen interchanging charge with O^{-2} ions, providing p-type superconducting metallic oxygen — a very specific picture of the superconductivity. (Hypocharged oxygen is O^{-Z}, with $Z<2$). This picture not only discards many of the currently accepted features of high-temperature superconductivity, it also provides a simple view of the phenomenon, and

implies that room-temperature superconductors encased in semiconductor microstructures should be achievable: the materials previously thought to be essential to high-temperature superconductivity are now identified as mere cages for oxygen. Thus the superconductivity is a property of a quasi-intercalate, the confined metallic oxygen that results from charge exchange between hypocharged oxygen and ionic O^{-2}. The "material" merely serves as a box or cage for the metallic oxygen superconductor, and so, one should be able to fabricate a cage out of novel materials (such as epitaxial semiconductors) without sacrificing the superconductivity of the oxygen.

The purpose of this paper is to elaborate on this idea of fabricating epitaxial layered structures from semiconductors for use as oxygen cages, hopefully leading to epitaxial high-temperature superconductivity. Furthermore, since high-temperature oxide superconductivity is sometimes accompanied by *photo-induced* superconductivity [4,5], it should be possible to make entire new classes of novel devices whose superconductivity can be turned on by light. Hence, with this paper we hope to stimulate experimental efforts to fabricate such integrated high-temperature superconducting devices.

II. Theory of high-temperature superconductivity

The essential elements of the theory of high-temperature superconductivity [3] are best discussed in terms of the thoroughly-studied, idealized, prototypical material $YBa_2Cu_3O_7$, whose crystal structure is given in Fig. 1. The top plane of the unit cell consists of chains of Cu and O. Following the rules of basic chemistry, we assume Cu to be in the +2 valence state, while O is O^{-2}; hence the layer is neutral. This layer is called the "chain layer" and also the "charge-reservoir layer." The next layer down is the Ba–O layer, and is also neutral, with Ba^{+2} and O^{-2}. The layer beneath the Ba–O layer is a CuO_2 "crinkled cuprate plane" and has a net charge of $-2\,|e|$ (where $|e|$ is the proton's charge): $[CuO_2]^{-2}$. At the center of the unit cell is Y^{+3}, and the planes beneath the Y are mirror images of those above. The sandwich of Y^{+3} and the two crinkled cuprate planes has a net charge of $-1\,|e|$.

The material $YBa_2Cu_3O_7$ has a unit cell that is not charge-neutral when described in terms of the normal valences of its constituents, having a net charge of $-1\,|e|$. Of course, this is unacceptable, and such a material cannot be stable. There are at most 13 electrons per unit cell that can be ionized from the neutral atoms leaving the cations Y^{+3}, Ba^{+2}, and Cu^{+2}, and, with 7 O^{-2} ions, 14 electrons are trapped on oxygen ions — one more than ionized! Clearly the number of electrons trapped by oxygen must equal the number liberated from cations. Therefore one or more elements in the unit cell must have an abnormal valence. Two abnormal valence schemes for restoring charge-neutrality are: (i) the valence-fluctuation scheme [1,6]: the valence of Cu in the chain layer must be Cu^{+3}, not Cu^{+2}; or, alternatively,
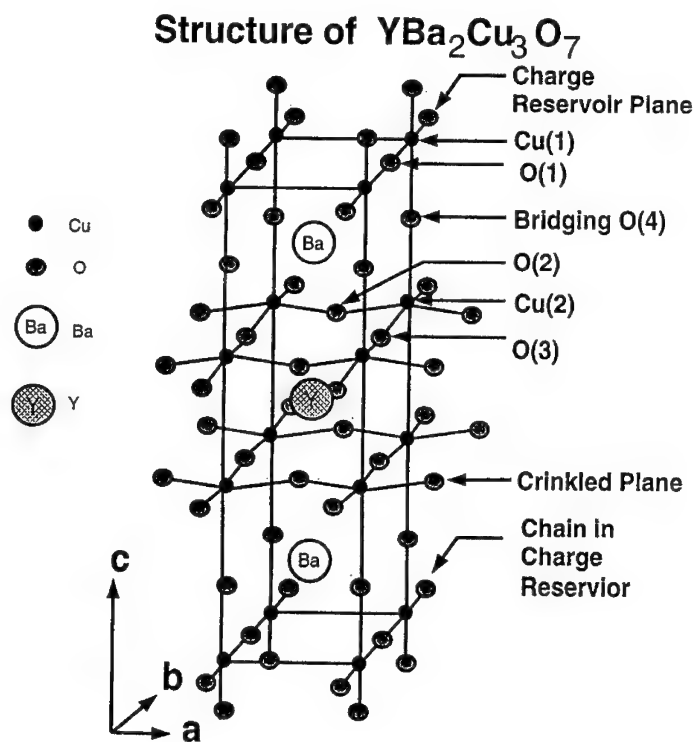
Structure of $YBa_2Cu_3O_7$

Fig. 1. Crystal structure of ideal $YBa_2Cu_3O_7$. The notation for the various atoms is not unique.

(ii) the "neutral" or hypocharged oxygen model [3,7]: all Cu ions should be Cu^{+2}, but the number of oxygen ions O^{-2} in $YBa_2Cu_3O_7$ should be 6.5, not 7. (This number 6.5 will reappear later with the Tokura-Torrance Rule.) The resolution of this abnormal valence problem lies at the heart of mechanisms of high-temperature superconductivity.

Traditionally, the abnormal valence problem has been resolved by postulating the existence of Cu^{+3} rather than Cu^{+2} in the chain layers. However, it is now abundantly clear from many experiments that Cu^{+3} does not occur in solid $YBa_2Cu_3O_x$: There may be some Cu^{+1} and there certainly is Cu^{+2}, but no Cu^{+3}. The evidence for the absence of Cu^{+3} is extremely strong [8].

A recent solution to the abnormal valence problem is that some oxygen occurs as hypocharged or "neutral" oxygen rather than as ionic O^{-2} [3]. In the most simplified version of this model, all Cu is in the Cu^{+2} state and 6.5 oxygen are O^{-2}, while the remaining (x-6.5) oxygen atoms in $YBa_2Cu_3O_x$ are neutral on the average. (These charge assignments should not be taken too literally, because the charges are allowed to redistribute themselves after the assignments. For example, the chain Cu and O can relax from Cu^{+2} and O^{-2} to Cu^{+1} and O^{-1}, leaving chain-Cu without a magnetic moment.) In the simplest version of the oxygen model, there is one O^0 per two unit cells for x=7, or 6.5 O^{-2} and (x-6.5) O^0 per unit cell in general. Each "neutral" oxygen atom, which can be thought of as O^{-2} plus two holes, then exchanges charge with the O^{-2} ions, leading to metallic oxygen confined within a $YBa_2Cu_3O_{6.5}$ cage. The holes can pair according to the pairing reaction $2h^+ + O^{-2} \rightarrow O^0$, and this pairing interaction leads to superconductivity.

Evidence supporting this model includes [3]: (i) The superconductivity in $YBa_2Cu_3O_x$ is observed only for 6.4<x<7, in agreement with the notion that for x<6.5 there is no "neutral" oxygen in the chain layers, and for x=7 the chains are fully occupied. (For 6.4<x<6.5 there is doubtless some "neutral" oxygen because some Cu is in the Cu^{+1} valence state.) (ii) The critical temperature $T_c(x)$ shows steps (Fig. 2 [9,10]) attributed to the onset of superconductivity ($T_c \approx 60$ K) at x≈6.5 and the onset of improved (90 K) superconductivity at x≈6.75 — with the improved superconductivity being associated with a material whose typical unit cell does not contain a vacancy scattering center [3]. (iii) The Tokura-Torrance Rule [11] for the phase boundary between the superconducting and insulating phases, relating the critical oxygen concentration x_c to the critical La concentration y_c in $YBa_{2-y}La_yCu_3O_x$, is predicted by the theory [3]: $x_c = 6.5 + y_c$. Recall that 6.5 is the concentration for the onset of "neutral" oxygen formation in $YBa_2Cu_3O_x$, and that the dependence of x_c on y_c indicates that every pair of La atoms must be passivated by one oxygen before "neutral" oxygen becomes available for superconductivity. (iv) The model provides a natural explana-
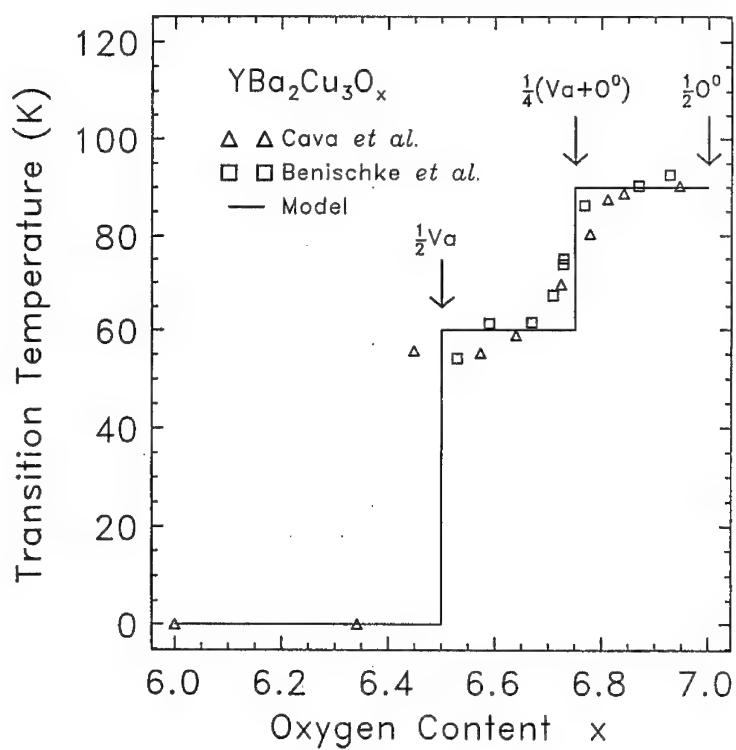
Fig. 2. Superconducting critical temperature (in K) versus oxygen content x of $YBa_2Cu_3O_x$, including the data of Cava *et al.* (triangles; Ref. [9]) and of Benischke *et al.* (squares; Ref. [10]). The arrows indicate the occupancies of chain-layer oxygen sites in a unit cell of typical material: (one-half vacancy, denoted Va) for x=6.5, (one-fourth vacancy and one-fourth neutral oxygen) for x=6.75, and (one-half neutral oxygen) for x=7.

tion of photo-induced superconductivity: O^{-2} is photo-ionized by light, with the photo-electrons being trapped (probably by oxygen vacancies), thereby locally increasing the concentration of "neutral" oxygen to above the critical concentration. (v) Doping studies can be summarized as follows: (a) undercharging the unit cell's cations (*e.g.*, $Y^{+3} \to Ca^{+2}$ or Na^{+1}) does not adversely affect the superconductivity (to lowest order in the dopant concentration) because variations in oxygen concentration compensate the cation charge changes; and (b) A magnetic moment located near or in the cuprate-plane layers (*e.g.*, $Cu \to Ni$) does not breaks pairs and destroy superconductivity in the remote charge-reservoir layers, nor does substitution at the Y site with a magnetic impurity (*e.g.*, $Y \to Dy$, with $J=15/2$) disrupt the superconductivity assumed to originate in the remote charge-reservoirs, not in the cuprate-planes [12].

III. Confined metallic oxygen

This theory of high-temperature superconductivity, if correct, makes it very clear that the oxygen is the superconducting material, not the "cage" $YBa_2Cu_3O_{6.5}$. This picture also applies to a wide class of oxide superconductors (different cages), and so can be used as a basis for imagining new superconductors. The essential ingredients are a cage or box with O^{-2} ions protruding (Fig. 3), and "neutral" oxygen in the box, leading to confined metallic oxygen when the "neutral" oxygen and O^{-2} exchange charge. The other chalcogenides, such as S^{-2} with "neutral" S, should also exhibit superconductivity when appropriately confined. One can imagine a confinement structure fabricated by modern epitaxial methods out of semiconductors, and integrated into some electronic microstructure. The box would probably have to be made of a II-VI chalcogenide, such as MgO or CdS. This would leave O^{-2} (or S^{-2}) ions at the surface of the box, ready to exchange charge with the "neutral" chalcogen atoms. Then "neutral" chalcogen atoms should be deposited in the box, perhaps using the techniques of oxygen deposition employed for $YBa_2Cu_3O_x$ and other high-temperature superconductors. Finally the "neutral" chalcogen would be encapsulated by another oxide or chalcogenide structure.

At the moment, this idea is quite speculative, and awaits demonstration that such epitaxial superconductors can be fabricated. But, if they can, if they exhibit photo-induced superconductivity, and if the confinement of the epitaxial layers can be engineered to produce high superconducting transition temperatures, one can envision entire new classes of devices based on them: these devices could perhaps be integrated into conventional electronics, and would involve room-temperature superconducting elements whose superconductivity could be turned on by light.
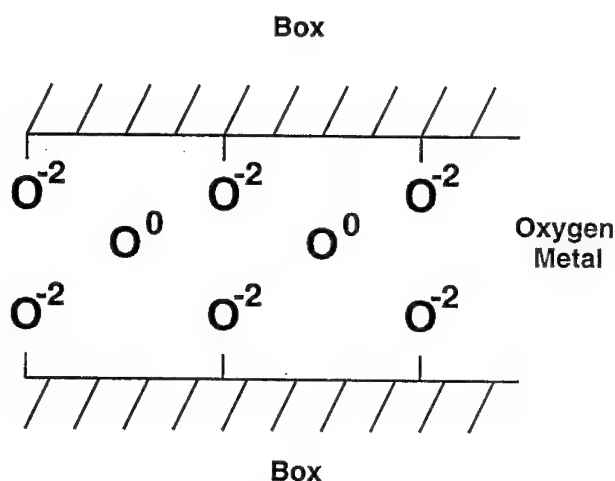
Fig. 3. Schematic illustration of the nature of a confinement box for oxide superconductivity. The O^{-2} ions should be part of the cage or box, and the O^0 atoms should be situated so that they can exchange charge with the O^{-2}.

Interestingly enough, confined high-temperature superconductivity may have been observed years ago in CdS [13]: Brown, Homan, and MacCrone reported a Meissner effect at 77 K on pressure-quenched CdS. The Meissner effect was found only in samples from one vendor, and so their results have failed to receive general acceptance. Nevertheless they applied pressures in excess of 40 kbar, and then released the pressure at rates greater than 1 Mbar/sec, to find dislocations in a material with a mixture of zincblende, rocksalt, and wurtzite structures. The material became black after the pressure quenching, similar to lasers that experience degradation by dark-line defects [14]. We speculate that these results might perhaps be interpreted as follows: The pressure quenching leads to small dislocations or "nano-cracks" in the material, which form with the assistance of some impurity, possibly $C\ell$. The surfaces of these nano-cracks are terminated by S^{-2} ions, and "neutral" S is contained in the cracks. The "neutral" S charge-exchange with S^{-2} then leads to superconductivity.

Of course this interpretation is highly speculative, and should not be taken seriously until more data on pressure-quenched CdS have been reported — but it certainly suggests that the old experiments should be re-examined, repeated, and extended — and that more studies of superconductivity in

semiconducting materials are called for.

References

[1] J. B. Bednorz and K. A. Müller, Z. Phys. **B 64**, 189 (1986).

[2] M. Lagues, X. M. Xie, H. Tebbji, X. Z. Xu, V. Mairet, C. Hatterer, C. F. Beuran, and C. Deville-Cavellin, Science **262**, 1850 (1993).

[3] H. A. Blackstead and J. D. Dow, Pis'ma Zh. Exp. Teor. Phys. **59**, 262 (1994); [Engl. transl., Sov. Phys. — JETP Lett. **59**, 283 (1994).]

[4] V. I. Kudinov, I. L. Chaplygin, A. I. Kirilyuk, N. M. Kreines, R. Laiho, E. Lähderanta, and C. Ayache, Phys. Rev. **B 47**, 9017 (1993). V. I. Kudinov, A. I. Kirilyuk, N. M. Kreines, R. Laiho, and E. Lähderanta, Phys. Lett. **A 151**, 358 (1990); V. I. Kudinov, I. L. Chaplygin, A. I. Kirilyuk, N. M. Kreines, R. Laiho, and E. Lähderanta, Phys. Lett. **A 157**, 290 (1991).

[5] G. Yu, A. J. Heeger, G. Stucky, N. Herron, E. M. McCarron, Solid State Commun. **72**, 345 (1989); G. Yu, C. H. Lee, A. J. Heeger, N. Herron, E. M. McCarron, Phys. Rev. Lett. **67**, 2581 (1991).

[6] Many of the theories assume the existence of Cu^{+3}. See V. L. Kresin, H. Morawitz, and S. A. Wolf, *Mechanisms of Conventional and High T_c Superconductivity,* (Oxford University Press, Oxford, 1993).

[7] For an earlier neutral-oxygen model, see D. I. Khomskii and A. Z. Zvezdin, Solid State Commun. **66**, 651 (1988).

[8] C. H. Pennington and C. P. Slichter, in *Physical Properties of High-Temperature Superconductors,* edited by D. M. Ginsberg, (World Scientific, Singapore), Vol. II, p. 269 *et seq.* (1990), and references therein.

[9] R. J. Cava, A. W. Hewat, E. A. Hewat, B. Batlogg, M. Marezio, K. M. Rabe, J. J. Krajewski, W. F. Peck, Jr., and L. W. Rupp, Jr., Physica **C**, **165**, 419 (1990).

[10] R. Benischke, T. Weber, and W. H. Fietz, Physica **C 203**, 293 (1992).

[11] Y. Tokura, J. B. Torrance, T. C. Huang, and A. I. Nazzal, Phys. Rev. **B 38**, 7156 (1988), Fig. 1.

[12] J. T. Markert, Y. Dalichaouch, and M. B. Maple, in *Physical Properties of High-Temperature Superconductors,* edited by D. M. Ginsberg,

(World Scientific, Singapore), Vol. I, p. 265 *et seq.* (1989), and references therein.

[13] E. Brown, C. G. Homan, and R. K. MacCrone, Phys. Rev. Lett. **45**, 478 (1980); P. J. Cote, C. G. Homan, W. C. Moffatt, S. Block, G. P. Piermarini, and R. K. MacCrone, Phys. Rev. **B 28**, 5041 (1983).

[14] J. D. Dow and R. E. Allen, Appl. Phys. Lett. **41**, 672 (1982).

AUTHOR INDEX

Adesida,I.,224
Agger,J.,14
Alperov,Zh.I.,80
Anderson,M.W.,14
Ando,H.,155
Ando,S.,155
Andres,R.P.,56
Armand,P.,245
Balandin,A.,117
Bandyopadhyay,S.,117
Bayliss,S.C.,178
Bielefeld,J.D.,56
Bimberg,D.,80
Bishop,S.G.,224
Blackstead,H.A.,339,355
Böhrer,J.,80
Bose,L.,326
Burgnies,L.,274
Butko,V.,14
Cahay,M.M.,294
Chang,J.P.C.,236
Chen,A.C.,141
Chen,G.L.,286
Cheng,K.Y.,141
Cooper,S.L.,141
Craighead,H.G.,84
Datta,S.,70
Dennis,B.S.,89
Dow,J.D.,339,355
Dneprovskii,V.,166
Dua,P.,141
Fukatsu,S.,31
Grundmann,M.,80
Gu,S.,224
Gushina,N.,166
Hammersberg,D.O.,129
Harmon,E.S.,236
Hawrylak,P.,89
Heath,J.R.,244
Henderson,D.O.,186
Henderson,J.I.,56,70

Heitz,R.,80
Holland,M.C.,89
Hopkins,F.K.,93
Iton,L.,245
Janes,D.B.,56,286
Johnson,N.P.,14
Kamada,H.,37
Kanbe,H.,155
Karavanskii,V.,166
Kersulis,S.,212
Kim,K.W.,260
Kirstaedter,N.,80
Kolagunta,V.R.,56,286
Kop'ev,P.S.,80
Kubiak,C.P.,56,70
Kumar,T.,294
Kundu,S.,205
Kuramochi,F.,37
Lahiri,I.,236
Leburton,J.P.,156
Ledentsov,N.N.,80
Lippens,D.,274
Lockwood,D.J.,89
Lyanda-Geller,Yu.B.,156
Madarasz,F.L.,93
Maheshwarla,S.V.,304
Malozovsky,Y.M.,326
Melloch,M.R.,236,286
Mu,R.,186
Nishiya,T.,37
Nolte,D.D.,236
Notomi,M.,37,129
Nötzel,R.,37
Mitin,V,V.,197,212
Okamoto,M.,129
Osifchin,R.G.,56
Panepucci,R.,224
Parpia,J.M.,84
Peaker,A.R.,14
Pemble,M.E.,14
Persans,P.D.,248

368

SUBJECT INDEX

absorption band edge,14,248
acoustic wave,260
Aharanov-Bohm,3
anti-Jahn-Teller effect,322
Atomic force microscopy,186
backscattering,84
ballistic transport,274
benzene ring,70
biexciton,93,117
binding energy,117
blue shift,14,129
Boltzman equation,205
chrystolite asbestos,14
confined hole states,156
confined metallic oxygen,355,360
correlation effects,89
Coulomb blockade,3
coupled quantum wires,274
crystal-field splitting,343
CuO_2 planes,339
cupric compounds,321
deformation potential,197
direct sidewall gate,286
dispersion relation,260
dodecanethial molecule,56
dual-branch waveguide,274
edge state,84
Einstein relation,294
elasticity theory,260
electron beam litography,224
electron mobility,197
electron waveguide,274
electronic switch,274
electro-optical sampling,236
EXAFS,178
exciton,93,129
flexural wave,260
gate current,304
glass,248
Green function,70
growth simulation,212

Hall effect,3
Hall resistance,3
Hartree calculations,89
helical wave,260
HEMT,205
heterointerface acoustic vibrations,197
heterojunction bipolar transistor,294
HIGFET,304
hopping transport,156
Hubbard exchange-correlation,326
hybridization theory,344
inelastic light scattering,89
interband resonant tunneling,156
interlevel coupling,84
intersubband relaxation,155
Landau fan chart,129
Landau level,84
Landauer formula,70,276
lateral ordering,141
lattice mismatch,129
magnetic pair-breaking,339
magneto-Raman scattering,89
magnetoresistance,3
magnetotransport,84
many-body effects,321
metal-insulator transition,326
metallic cluster,56
metallic nanocrystal,244
microtubule,260
modulation doped,129
molecular wire,56
Monte Carlo,212,294
nanocluster,178
nanocrystallites,248
nanophase,186
nanoscale electronic device,70
nanostructure,224
non-linear optical properties,93,117,166
one-dimensional hole-gas,205
organic molecule,56,70
PbI_2 quantum dots,186

photoluminescence,14,31,37,141,155,178,224
piezoelectric charges,89
porous silicon,171,186
pulse energy density,248
quantum box superlattice,156
quantum confined excitons,236
quantum confinement,14,129,178
quantum disk layer,37
quantum dot,3,80,89,166,286
quantum well,31,93
quantum wire,14,31,93,117,129
141,155,166,224
Raman line,89
Raman phonon frequencies,14
Raman scattering,141,186
reactive ion etching,224
red-shift,186
resonant pinning states,321
selective epitaxial overgrowth,224
self-assembled,14,56
self-heating effects,294
self-organized,3,37
Shubnikov-de Hass oscillations,84
Si/pure Ge/Si heterostrcuture,31
Stranski-Krastanov growth mode,89
surface phonon polaritons,186
surface recombination velocity,224
strain,129,141
thermal free chlorine etching,224
thermoelectric power,205
transmission electron microscope,31
tunneling current,304
vertically coupled dots,89
Wannier-Stark localized electrons,156
X-ray powder diffraction,245
Young modulus,260
Y-zeolite,245

372